Table 6.4
Fracture toughness results of A36-60-25 specimens

A36 Specimen ID →	60-25-1	60-25-2	60-25-3	60-25-4	60-25-5
Charpy Spec. # 1	48	16	20	16	10
Charpy Spec. # 2	88	51	31	21	14
Charpy Spec. #3	98	64	36	22.5	15
Charpy Spec. #4	175	110	70	32	19.5
Charpy Spec. #5	213	120	75	63	19.5
Charpy Spec. #6	214	173	97	-	20
Mean	139	89.0	54.8	30.9	16.3
95% confidence interval for actual mean	65.18 - 213.5	29.89 - 148.1	23.17 - 86.50	7.5 – 54.31	12.11 – 20.55
Std. Deviation	70.7	56.3	30.2	18.9	4.02
Median	137	87.0	53.0	22.5	17.3
Average absolute deviation from median	61.3	45.3	25.8	11.6	3.33
Probability of null hypothesis (data is statistically similar to undamaged data from t-test)	0.89	0.050	0.0003	<0001	<0001

Table 6.5
Fracture toughness results of A36-60-50 specimens

A36 Specimen ID →	60-50-1	60-50-2	60-50-3	60-50-4	**60-50-5
Charpy Spec. #1	23.5	26	18	18	17
Charpy Spec. #2	39	28	37	28	19
Charpy Spec. #3	50	95	67	30	61
Charpy Spec. #4	143	157	78	32	77
Charpy Spec. #5	148	200	95	33	78
Charpy Spec. #6	157	219	110	45	89
Mean	93.4	121	67.5	31.0	56.8
95% confidence interval for actual mean	28.35 - 158.5	32.40 – 209.3	30.98 – 104.0	21.85 – 40.15	23.89 – 89.77
Std. Deviation	62.0	84.3	34.8	8.72	31.4
Median	96.5	126	72.5	31.0	69.0
Average absolute deviation from median	55.9	71.2	26.8	5.67	24.5
Probability of null hypothesis (data is statistically similar to undamaged data from t-test)	0.087	0.61	0.0018	<0.000 1	0.0004

*Refers to specimens with significant curvature after heat straightening. Data is not entirely reliable.

Table 6.6
Fracture toughness results of A36-90-25 specimens

A36 Specimen ID →	90-25-1	90-25-3	**90-25-5
Charpy Spec. #1	78	15	13.5
Charpy Spec. #2	112	68	20.5
Charpy Spec. #3	115	169	21.5
Charpy Spec. #4	143	242	220
Charpy Spec. #5	236	242	238
Charpy Spec. #6	239	-	242
Mean	154	147	126
95% confidence interval for actual mean	82.44 – 225.2	19.69 – 274.7	2.13 – 249.7
Std. Deviation	68.0	103.0	118.0
Median	129	169	121
Average absolute deviation from median	52.2	80.2	107
Probability of null hypothesis (data is statistically similar to undamaged data from t-test)	0.47	0.73	0.79

Table 6.7
Fracture toughness results of A36-90-50 specimens

A36 Specimen ID →	90-50-1	90-50-2	90-50-3	90-50-4	90-50-5
Charpy Spec. #1	12	21.5	17	92	67
Charpy Spec. # 2	23	24	19	95	74
Charpy Spec. #3	28	89	21.5	109	94
Charpy Spec. #4	28	97	25	230	95
Charpy Spec. #5	29.5	105	30	232	110
Charpy Spec. # 6	32	240	88	240	232
Mean	25.4	96.1	33.4	166	112
95% confidence interval for actual mean	17.86 – 32.97	12.64 – 179.5	4.94 – 61.90	88.22 – 244.4	48.18 – 175.8
Std. Deviation	7.20	79.5	27.1	74.4	60.8
Median	28.0	93.0	23.3	170	94.5
Average absolute deviation from median	4.42	51.3	14.3	67.7	33.7
Probability of null hypothesis (data is statistically similar to undamaged data from t-test)	<0.000 1	0.16	<0.000 1	0.25	0.32

*Refers to speci mens with significant curvature after heat straightening. Data is not entirely reliable.

Table 6.8
Average structural properties of A588 steel

Specimen	σ_y *(ksi)*	*E (ksi)*	ε_y	σ_t	ε_u	ε_u / ε_y	*% Elongation*	*% Reduction*
Undamaged	57.4	28285	0.00203	83.1	0.16	77.7	33.60	71.44
A588-20-25-1	59.7	29580	0.00202	84.1	0.15	76.3	29.71	69.13
A588-20-25-2	58.2	30434	0.00191	83.0	0.15	75.8	30.24	67.65
A588-20-25-3	58.7	30140	0.00195	82.7	0.14	69.7	28.23	68.19
A588-20-25-4	57.3	29852	0.00192	80.8	0.14	72.3	28.29	71.20
A588-20-25-5	59.0	29848	0.00198	81.2	0.13	64.4	27.93	69.35
A588-20-50-1	61.6	30544	0.00202	86.6	0.14	66.9	27.96	68.70
A588-20-50-2	62.2	29245	0.00213	85.7	0.12	54.1	26.45	68.02
A588-20-50-3	61.3	30215	0.00203	84.2	0.12	58.9	26.50	68.52
A588-20-50-4	59.5	29772	0.00200	83.8	0.14	69.5	29.10	70.08
A588-20-50-5	63.5	30132	0.00211	84.9	0.11	53.5	27.12	66.94
A588-40-25-1	56.7	30668	0.00185	81.8	0.13	68.6	27.54	71.52
A588-40-25-2	58.0	30702	0.00189	81.1	0.14	74.7	28.01	69.51
A588-40-25-3	57.4	30832	0.00186	80.6	0.15	82.6	30.87	70.58
A588-40-25-4	59.7	30610	0.00195	81.9	0.14	73.4	28.45	69.19
****A588-40-25-5*	60.4	30615	0.00197	80.5	0.14	71.9	28.11	67.55
A588-40-50-1	61.8	30159	0.00205	84.2	0.11	52.0	25.00	68.06
A588-40-50-2	60.7	29792	0.00204	84.6	0.14	69.2	28.34	67.34
A588-40-50-3	57.3	30834	0.00191	81.3	0.14	71.9	28.19	72.15
A588-40-50-4	57.1	30499	0.00187	81.5	0.13	67.9	26.85	71.12
A588-40-50-5	58.6	30081	0.00195	80.9	0.15	74.9	30.17	70.39
****A588-60-25-1*	57.6	30535	0.00189	82.1	0.14	76.6	28.43	70.72
A588-60-25-2	57.5	29984	0.00192	79.6	0.15	79.9	30.46	71.33
A588-60-25-3	54.9	30252	0.00185	77.7	0.16	88.0	30.66	72.88
****A588-60-25-4*	59.9	30519	0.00193	80.2	0.14	70.9	28.08	66.56
A588-60-25-5	57.6	30643	0.00192	77.8	0.15	79.1	29.77	72.13
A588-60-50-1	60.2	30483	0.00197	85.0	0.14	70.9	28.33	69.18
A588-60-50-2	58.2	30442	0.00191	82.7	0.15	79.4	29.95	70.44
A588-60-50-3	59.2	29977	0.00197	80.6	0.14	72.4	28.56	69.12
A588-60-50-4	62.5	31046	0.00201	82.4	0.12	57.7	25.61	68.55
A588-60-50-5	61.8	30781	0.00201	81.7	0.14	72.0	28.70	69.15

*Refers to speci mens with significant curvature after heat straightening. Data is not entirely reliable.

Table 6.9
Average structural properties of A7 steel

Specimen	σ_y *(ksi)*	*E (ksi)*	ε_y	σ_t	ε_u	ε_u / ε_y	*% Elongation*	*% Reduction*
Undamaged	38.7	31228	0.00124	62.1	0.22	180.53	44.14	61.63
A7-30-25-1	37.6	28972	0.00130	61.2	0.23	173.61	39.36	62.23
A7-30-25-3	36.5	31456	0.00116	60.3	0.18	155.59	35.79	65.07
A7-30-25-5	41.3	26655	0.00155	60.3	0.14	90.13	28.07	58.61
A7-30-40-1	38.7	29125	0.00134	62.2	0.21	155.80	34.95	61.41
A7-30-40-3	41.1	28093	0.00146	62.2	0.22	149.49	35.15	63.33
A7-30-40-5	41.6	26556	0.00156	64.1	0.18	112.50	33.08	59.02
A7-60-25-1	38.4	26869	0.00144	60.5	0.20	142.73	34.12	63.18
A7-60-25-3-1	37.7	31510	0.00120	61.4	0.20	191.73	33.10	58.44
A7-60-25-3-2	35.5	27201	0.00130	58.9	0.20	153.70	33.36	61.50
A7-60-25-5	38.6	27127	0.00142	61.3	0.19	135.57	27.30	59.68
A7-60-40-1	39.8	27440	0.00145	61.3	0.19	132.93	33.82	62.51
A7-60-40-3	37.4	-	-	59.2	0.21	-	35.78	64.88
***A7-60-40-5*	46.7	-	-	62.7	0.12	56.97	25.30	60.46
***A7-90-25-1*	42.7	-	-	60.7	0.20	140.70	38.01	64.76
***A7-90-25-3*	37.2	-	-	60.3	0.20	132.92	32.35	61.36
***A7-90-40-1*	33.3	-	-	59.6	0.24	-	33.86	66.03
***A7-90-40-3*	38.5	-	-	59.7	0.21	-	33.42	63.35

*Refers to speci mens with significant curvature after heat straightening. Data is not entirely reliable.

Table 6.10
Fracture toughness results of A7-30 specimens

A7 Specimen ID →	**30-25-1**	**30-25-3**	**30-25-5**	**30-40-1**	**30-40-3**	**30-40-5**
Charpy Spec. # 1	26.5	15	10.5	13	13	5.5
Charpy Spec. #2	30	16	14.5	25.5	13.5	6.5
Charpy Spec. #3	34	17.5	15	26	23	8
Charpy Spec. # 4	38	24	18	26.5	24	53
Charpy Spec. # 5	39	30	18	32	36	92
Charpy Spec. # 6	40	30	19	33	38	97
Mean	34.6	22.1	15.8	26.0	24.6	43.7
95% confidence interval for actual mean	28.89 – 40.28	14.85 – 29.31	12.50 – 19.16	18.51 – 33.49	13.37 – 35.79	-1.789 – 89.12
Std. Deviation	5.43	6.89	3.17	7.13	10.7	43.3
Median	36	20.8	16.5	26.3	23.5	30.5
Average absolute deviation from median	4.42	5.92	2.50	4.50	8.08	37.0
Probability of null hypothesis (data is statistically similar to undamaged data from t-test)	0.24	0.0001	0.0001	0.002	0.0023	0.65

Table 6.11
Fracture toughness results of A7-60 specimens

A7 Specimen ID →	60-25-1	60-25-3	60-25-3 -r	60-25-5	60-40-1	60-40-3	**60-40-5
Charpy Spec. #1	21.5	13.5	13	62	12	8.5	7.5
Charpy Spec. #2	23	15.5	32	67	22	9.5	8.5
Charpy Spec. #3	24.5	31	60	74	23	11.5	9
Charpy Spec. #4	25	90	79	76	29	27	10
Charpy Spec. #5	26	97	90	78	30	30	13
Charpy Spec. #6	28.5	102	92	96	32	33	21.5
Mean	24.8	58.2	61.0	75.5	24.7	19.9	11.6
95% confidence interval for actual mean	22.1-27.29	13.64 - 102.7	26.92 - 95.08	63.23 - 87.77	16.93 - 32.40	8.11-31.72	6.11 - 17.05
Std. Deviation	2.42	42.4	32.5	11.7	7.37	11.2	5.21
Median	24.8	60.5	69.5	75.0	26.0	19.3	9.50
Average absolute deviation from median	1.75	38.2	26.0	7.83	5.67	10.1	3.25
Probability of null hypothesis (data is statistically similar to undamaged data from t-test)	0.0003	0.082	0.015	<0.0001	0.0009	0.0002	<0.0001

Table 6.12
Fracture toughness results of A7-90 specimens

A7 Specimen ID →	**90-25-1	**90-25-3	**90-40-1	**90-40-3
Charpy Spec. #1	29	23.5	25	10
Charpy Spec. #2	32	24	32	30
Charpy Spec. #3	33	41	46	32
Charpy Spec. #4	38	50	51	34
Charpy Spec. #5	50.5	51	53	44
Charpy Spec. #6	59	62	54	56
Mean	40.3	41.9	43.5	34.3
95% confidence interval for actual mean	27.75 - 52.75	25.57 - 58.26	30.75 - 56.25	18.21 - 50.45
Std. Deviation	11.9	15.6	12.1	15.4
Median	35.5	45.5	48.5	33.0
Average absolute deviation from median	8.92	12.4	9.17	10.3
Probability of null hypothesis (data is statistically similar to undamaged data from t-test)	0.72	0.52	0.28	0.38

*Refers to specimens with significant curvature after heat straightening. Data is not entirely reliable.

Table 6.13
Average structural properties of overheated A36 steel

Specimen	σ_y *(ksi)*	*E (ksi)*	ε_y	σ_t	ε_u	ε_u / ε_y	*% Elongation*	*% Reduction*
Undamaged	39.1	30295	0.00129	66.7	0.20	153.8	38.92	67.29
A36-60-25-1-1400	48	29821	0.00161	71.3	0.18	113.2	32.99	70.57
A36-60-25-3-1400	46.5	29143	0.0016	67.3	0.16	100.9	32.33	72.88
A36-60-50-1-1400	47.1	31570	0.00149	69.8	0.19	124.7	32.74	72.7
A36-60-50-3-1400	47.6	30669	0.00155	69.9	0.16	103.1	32.25	73.49
A36-90-25-1-1400	48.7	30463	0.0016	72.2	0.18	111.4	33.54	67.64
A36-90-25-3-1400	45.7	30421	0.0015	69.8	0.19	127.1	35.1	73.62
A36-90-50-1-1400	49.5	31122	0.00159	71.9	0.19	119.1	36.32	73.29
A36-90-50-3-1400	48.7	29871	0.00163	71.8	0.17	106.4	34.42	72.63
A36-60-25-1-1600	48.6	30543	0.00159	71.5	0.19	121.4	35.8	71.96
A36-60-25-3-1600	48.4	29924	0.00162	70.7	0.14	89.2	28.38	71.74
A36-60-50-1-1600	47.9	29408	0.00163	72.3	0.19	119.1	35.64	71.27
A36-60-50-3-1600	44.5	30766	0.00145	69.8	0.18	125.7	29.5	73.09
A36-90-25-1-1600	47.6	30680	0.00156	71.2	0.16	104.4	29.75	72.85
A36-90-25-3-1600	46.9	31507	0.00149	70.8	0.19	124.8	37.8	70.68
A36-90-50-1-1600	47.1	30305	0.00155	70.9	0.2	127.1	35.75	73.1
A36-90-50-3-1600	47.8	30244	0.00158	70.6	0.13	82.3	28.06	73.13

Table 6.14
Fracture toughness of damaged-repaired overheated A36 steel subjected to damage strains of 60 ε_y and maximum temperatures of 1400 °F

A36 Specimen ID →	A36-60-25-1-1400	A36-60-25-3-1400	A36-60-50-1-1400	A36-60-50-3-1400
Charpy Spec. #1	185	111	131	180
Charpy Spec. #2	189	133	145	185
Charpy Spec. #3	208	175	175	204
Charpy Spec. #4	222	225	179	216
Charpy Spec. #5	241	237	187	216
Charpy Spec. #6	252	250	216	234
Mean	216	189	172	206
95% confidence interval for actual mean	187.6 - 244.8	127.8 - 249.2	140.2-204.1	184.3 - 227.4
Std. Deviation	27.2	57.9	30.4	20.5
Median	225	200	177	210
Average absolute deviation from median	22.2	48.8	21.8	16.2
Probability of null hypothesis (data is statistically similar to undamaged data from t-test)	<0.000 1	<0.000 1	<0.000 1	<0.000 1

Table 6.15
Fracture toughness of damaged-repaired overheated A36 steel subjected to damage strains of 90 ε_y and maximum temperatures of 1400 °F

A36 Specimen ID →	A36-90-25-1-1400	A36-90-25-3-1400	A36-90-50-1-1400	A36-90-50-3-1400
Charpy Spec. #1	75	211	175	109
Charpy Spec. #2	77	216	183	126
Charpy Spec. #3	126	239	206	228
Charpy Spec. #4	159	244	216	243
Charpy Spec. #5	185	263	223	251
Charpy Spec. #6	203	-	238	-
Mean	138	235	207	191
95% confidence interval for actual mean	80.57 - 194.4	208.1 - 261.1	181.6 - 232.1	106.7 - 276.1
Std. Deviation	54.2	21.3	24.1	68.2
Median	44.8	239	211	228
Average absolute deviation from median	143	16	18.8	51.8
Probability of null hypothesis (data is statistically similar to undamaged data from t-test)	<0.000 1	<0.000 1	<0.000 1	<0.000 1

Table 6.16
Fracture toughness of damaged-repaired overheated A36 steel subjected to damage strains of 60 ε_y and maximum temperatures of 1600 °F

A36 Specimen ID →	A36-60-25-1-1600	A36-60-25-3-1600	A36-60-50-1-1600	A36-60-50-3-1600
Charpy Spec. #1	122	170	75	66
Charpy Spec. #2	125	209	125	124
Charpy Spec. #3	128	210	128	170
Charpy Spec. #4	221	248	162	185
Charpy Spec. #5	223	251	198	199
Charpy Spec. #6	230	254	216	228
Mean	175	224	151	162
95% confidence interval for actual mean	117.4 - 232.3	188.7 - 258.6	96.06 - 205.3	100.8 - 223.2
Std. Deviation	54.7	33.3	52	58.3
Median	175	229	145	178
Average absolute deviation from median	49.8	27.3	41.3	42
Probability of null hypothesis (data is statistically similar to undamaged data from t-test)	<0.000 1	<.0001	<.0001	<.0001

Table 6.17
Fracture toughness of damaged-repaired overheated A36 steel subjected to damage strains of 60 ε_y and maximum temperatures of 1600 °F

A36 Specimen ID →	A36-90-25-1-1600	A36-90-25-3-1600	A36-90-50-1-1600	A36-90-50-3-1600
Charpy Spec. #1	90	135	113	30
Charpy Spec. #2	102	177	125	58
Charpy Spec. #3	112	185	126	92
Charpy Spec. #4	217	200	215	200
Charpy Spec. #5	223	212	228	231
Charpy Spec. #6	240	219	251	234
Mean	164	188	176	141
95% confidence interval for actual mean	91.14 - 236.9	156.1 - 219.9	111.8 - 240.9	44.82 - 236.8
Std. Deviation	69.4	30.4	61.5	91.5
Median	165	193	171	146
Average absolute deviation from median	62.7	22.3	55	80.8
Probability of null hypothesis (data is statistically similar to undamaged data from t-test)	<0.000 1	<0.000 1	<0.000 1	0.0003

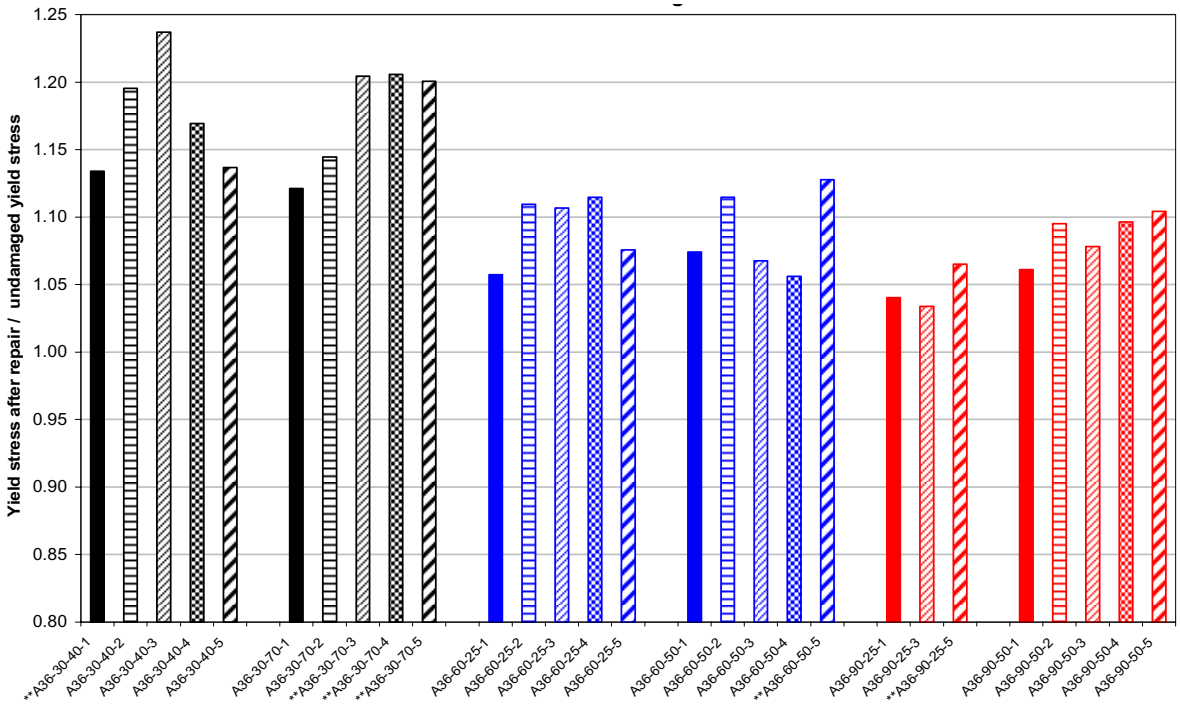

Figure 6.1
Normalized yield stress of damaged-repaired A36 steel

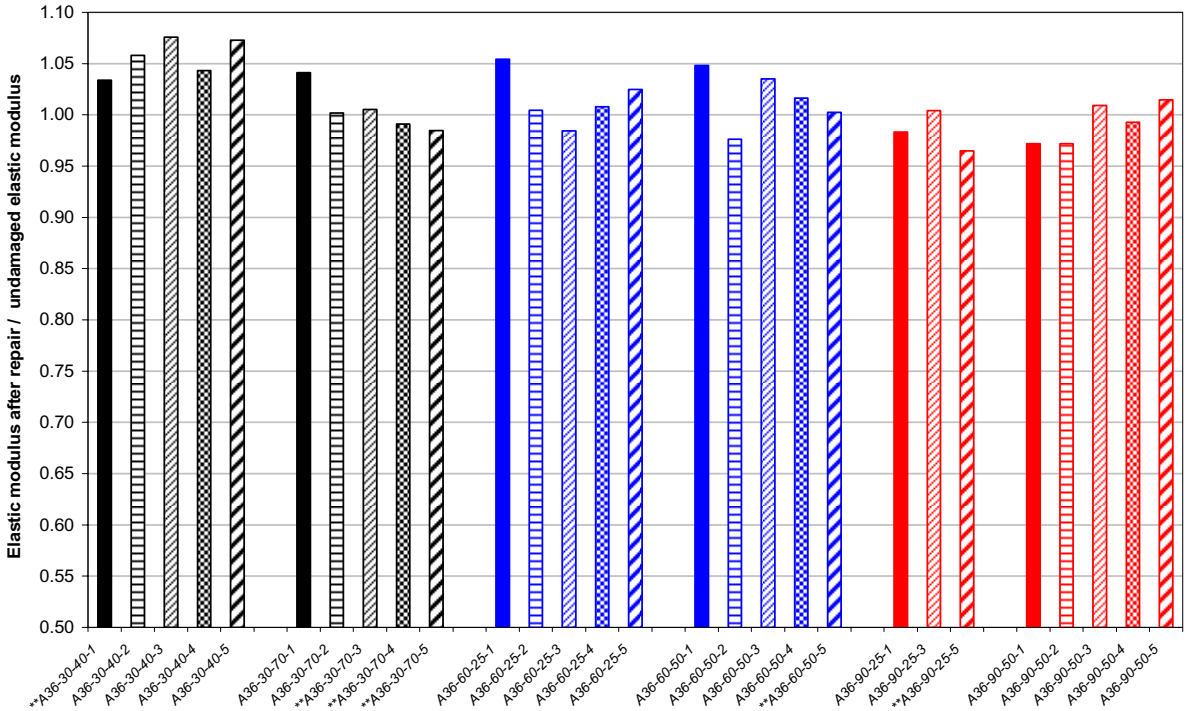

Figure 6.2
Normalized elastic modulus of damaged-repaired A36 steel

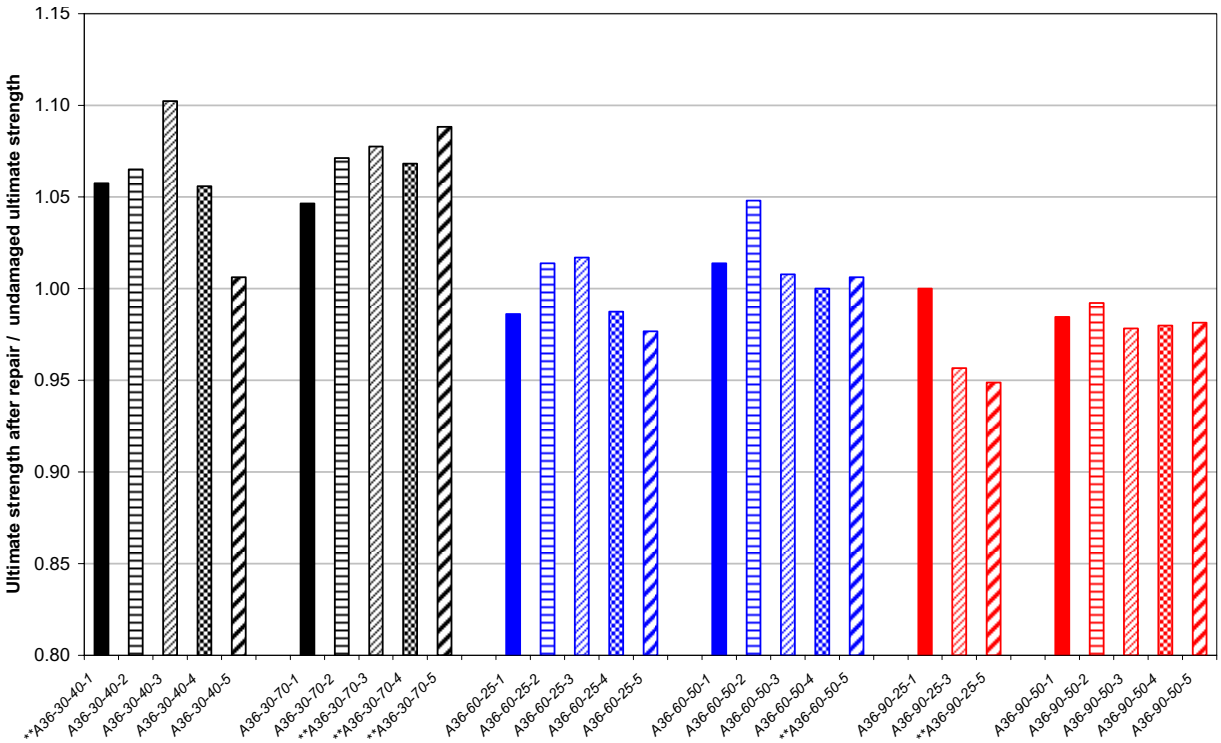

Figure 6.3
Normalized ultimate stress of damaged-repaired A36 steel

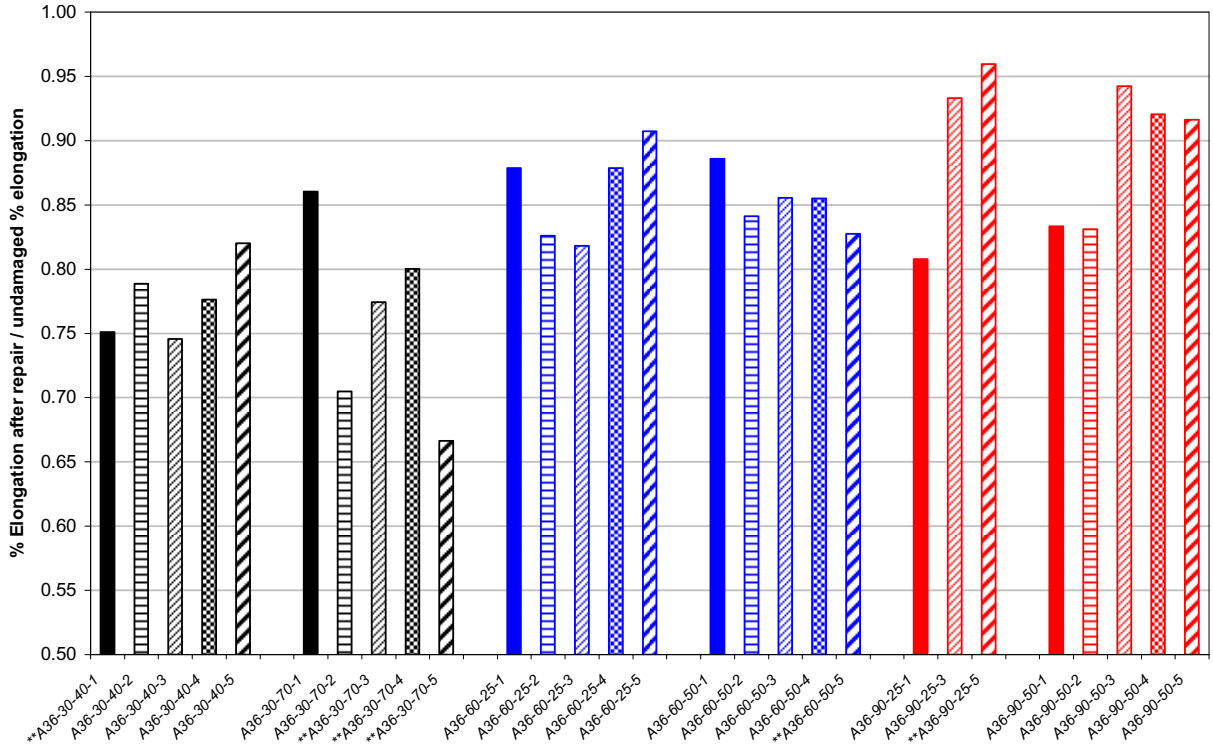

Figure 6.4
Normalized percent elongation of damaged-repaired A36 steel

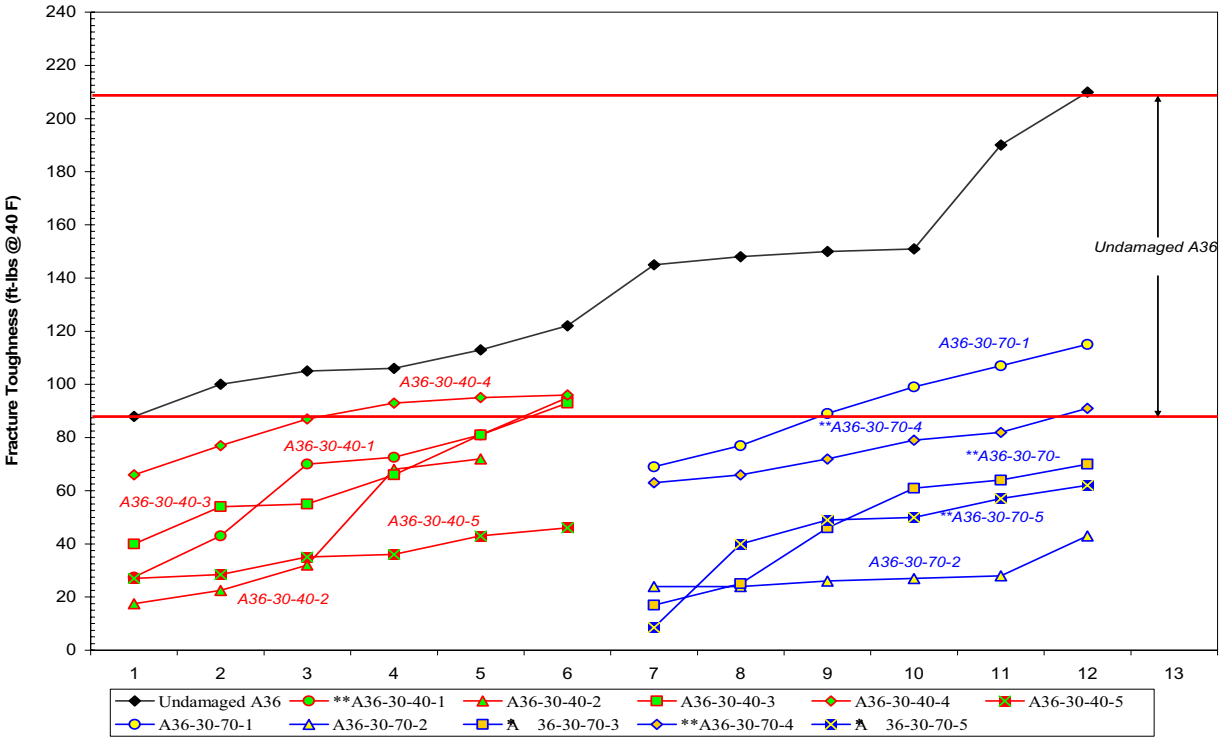

Figure 6.5
Fracture toughness comparisons of A36-30 (ε_d=30 ε_y) specimens

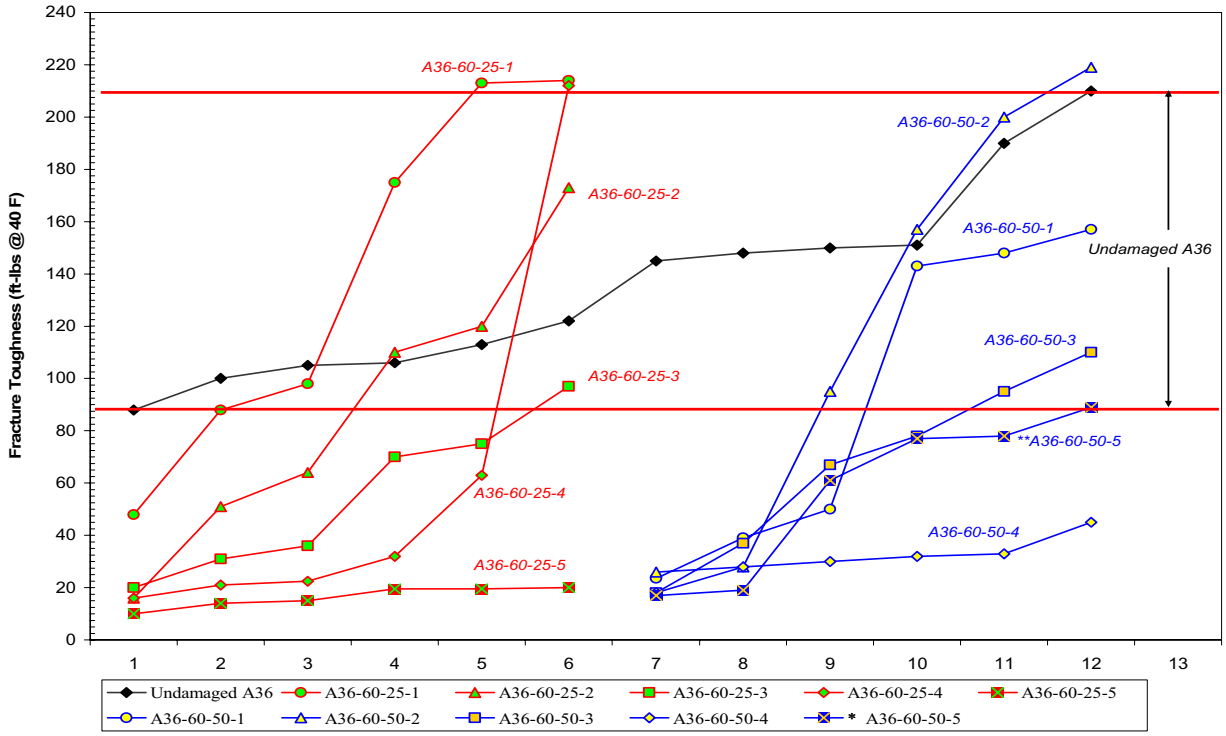

Figure 6.6
Fracture toughness comparisons of A36-60 (ε_d=60 ε_y) specimens

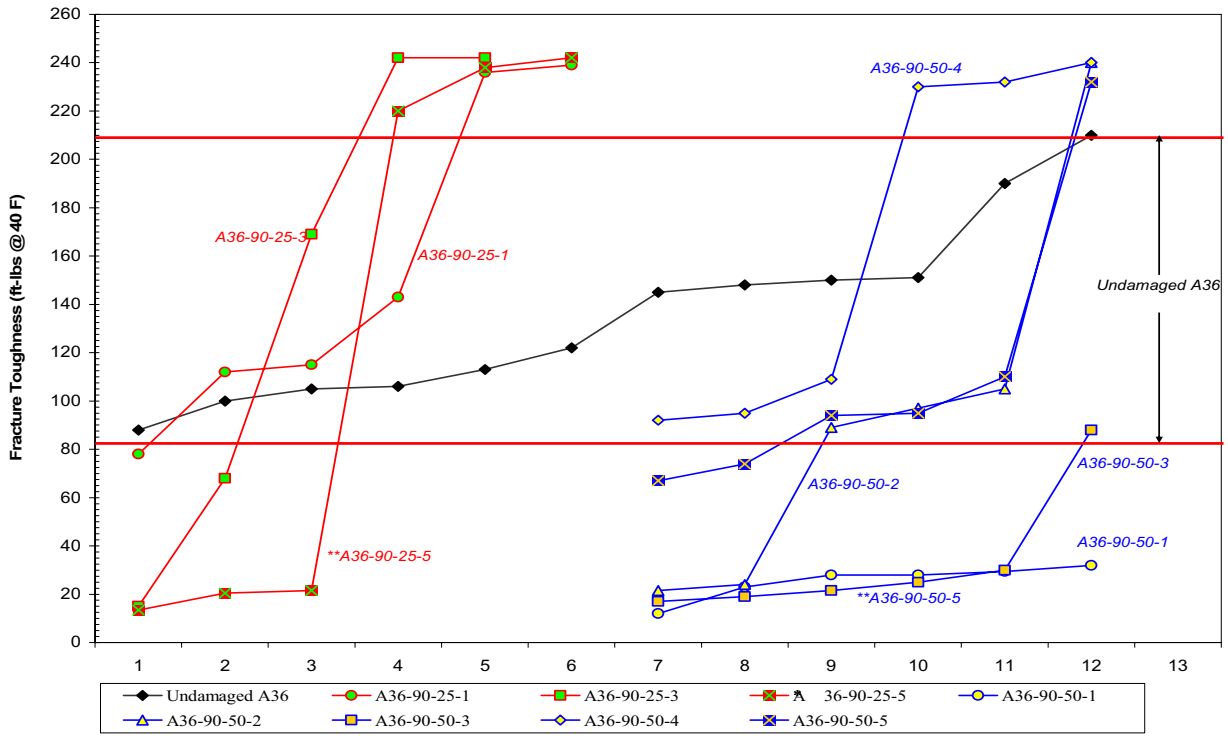

Figure 6.7
Fracture toughness comparisons of A36-90 (ε_d=90 ε_y) specimens

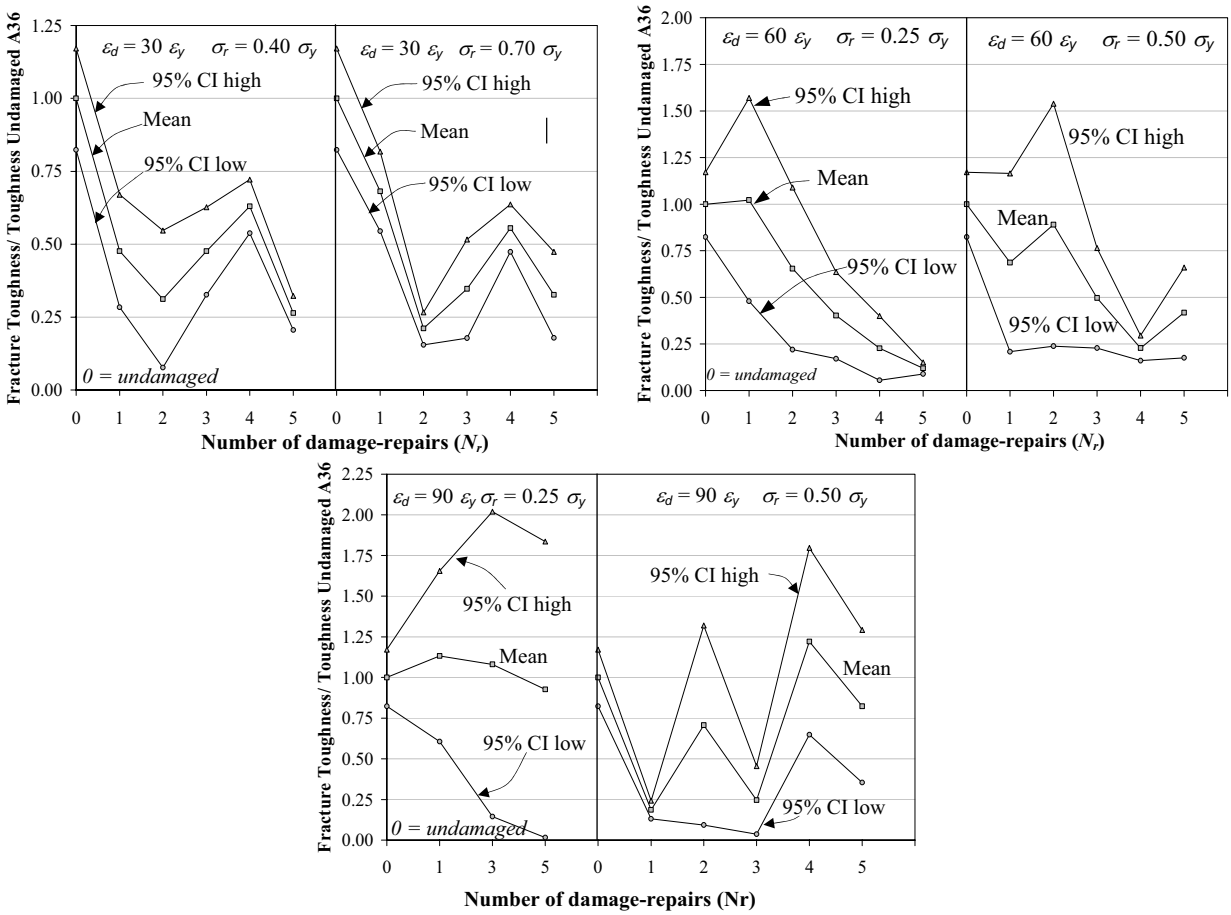

Figure 6.8
Normalized fracture toughness (mean and 95% CI) for damaged-repaired A36 steel

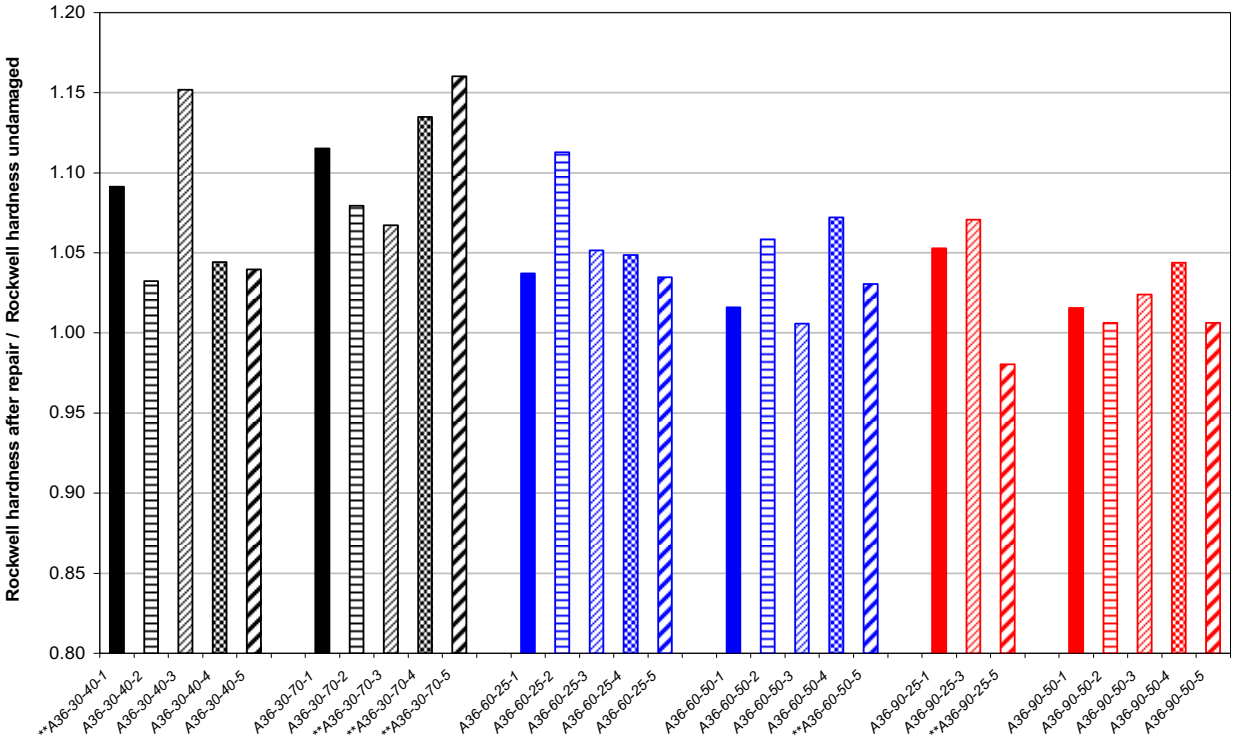

Figure 6.9
Normalized Rockwell hardness of damaged-repaired A36 steel

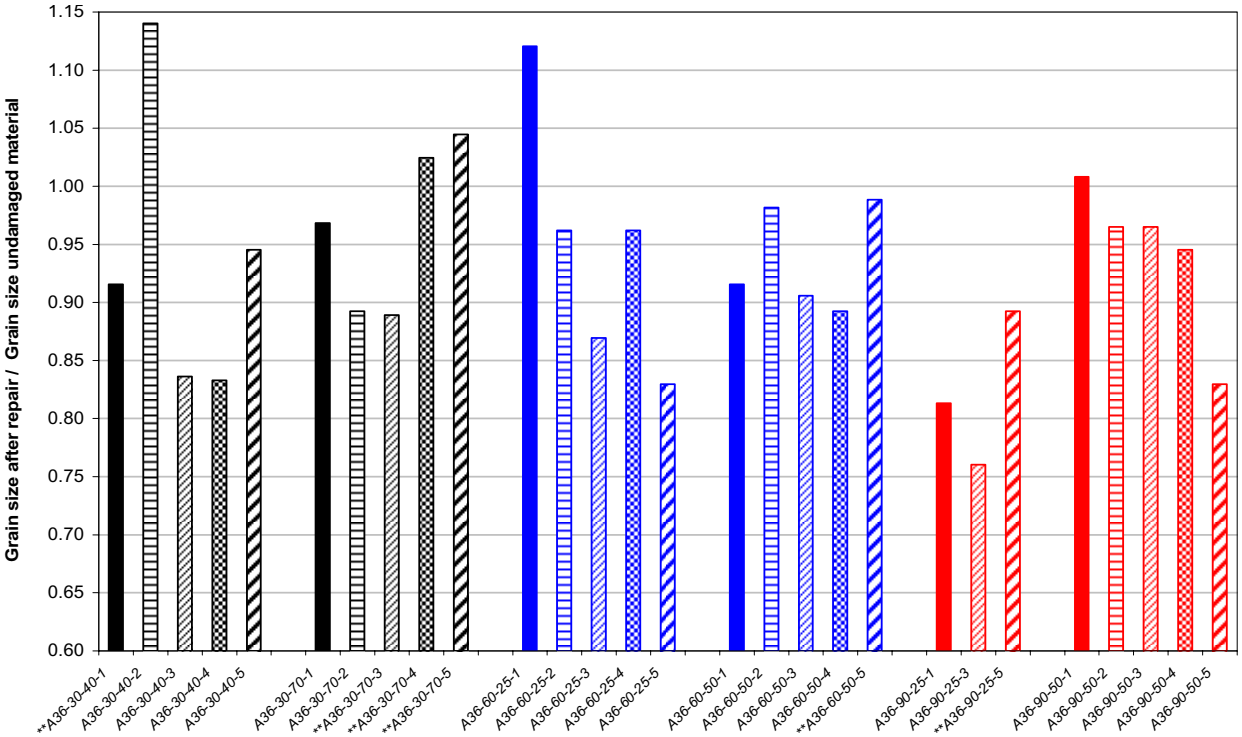

Figure 6.10
Normalized grain size of damaged-repaired A36 steel

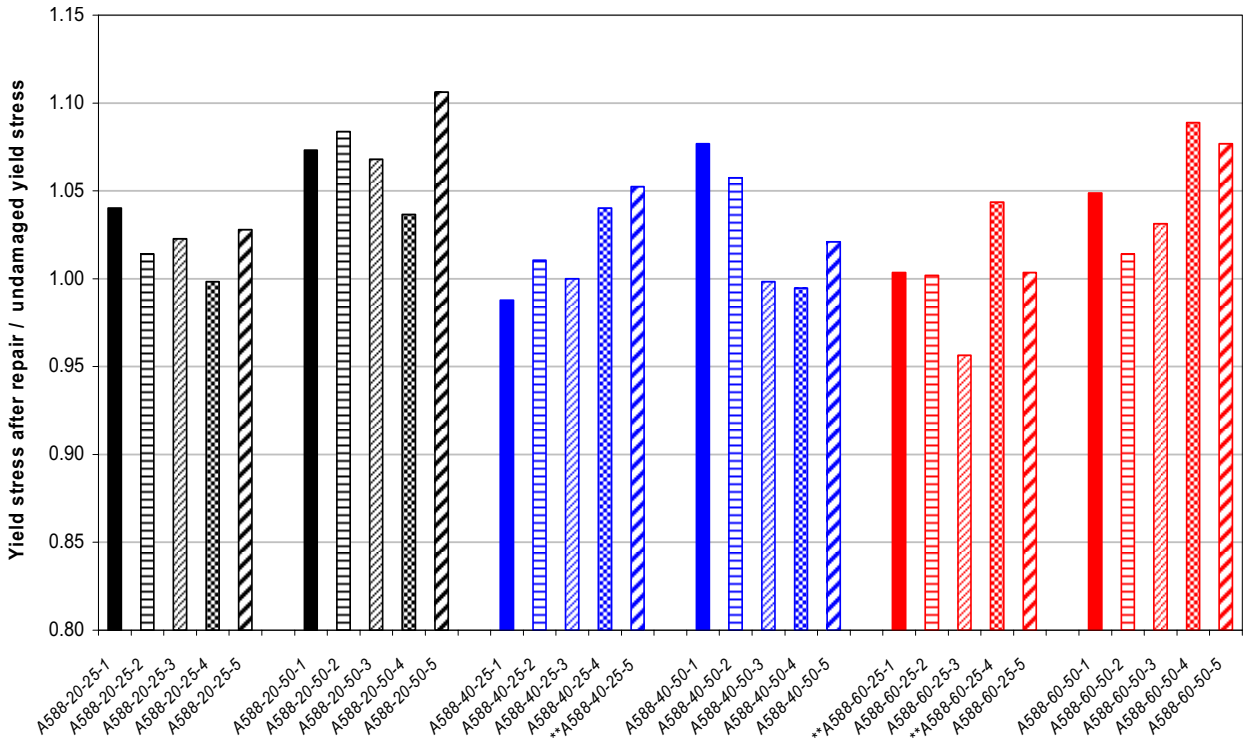

Figure 6.11
Normalized yield stress of damaged-repaired A588 steel

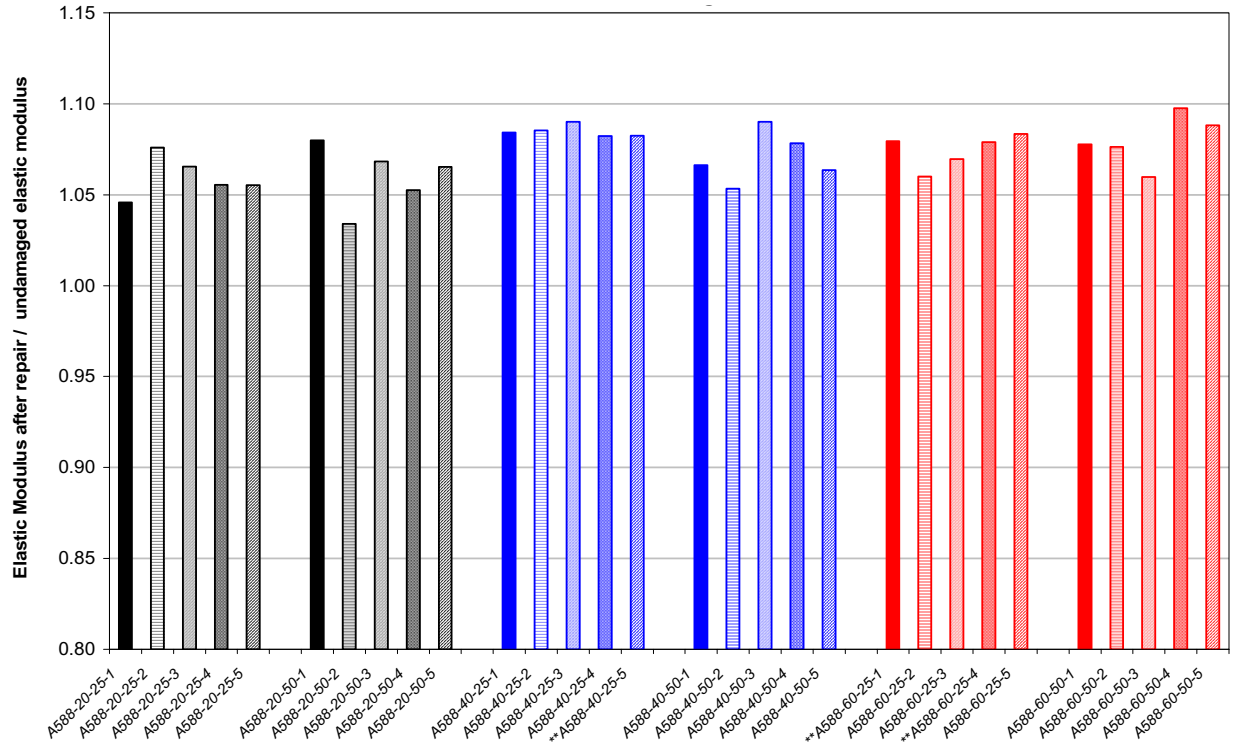

Figure 6.12
Normalized elastic modulus of damaged-repaired A588 steel

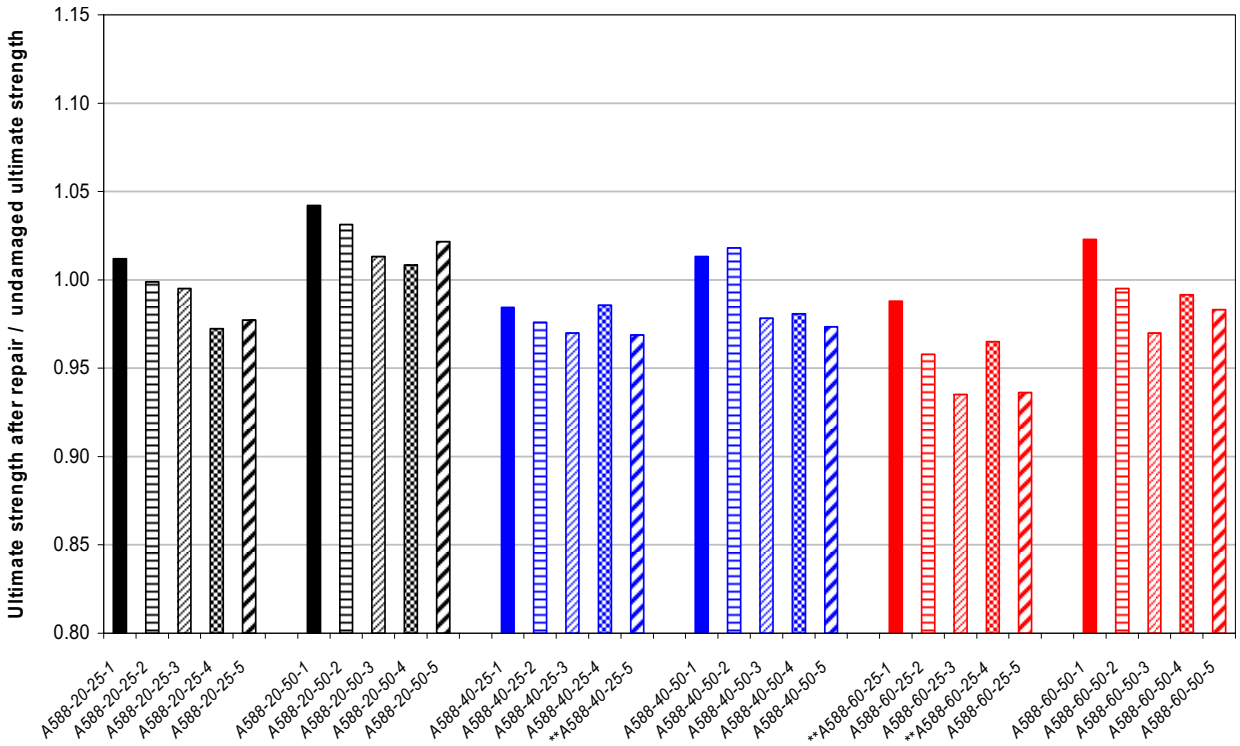

Figure 6.13
Normalized ultimate stress of damaged-repaired A588 steel

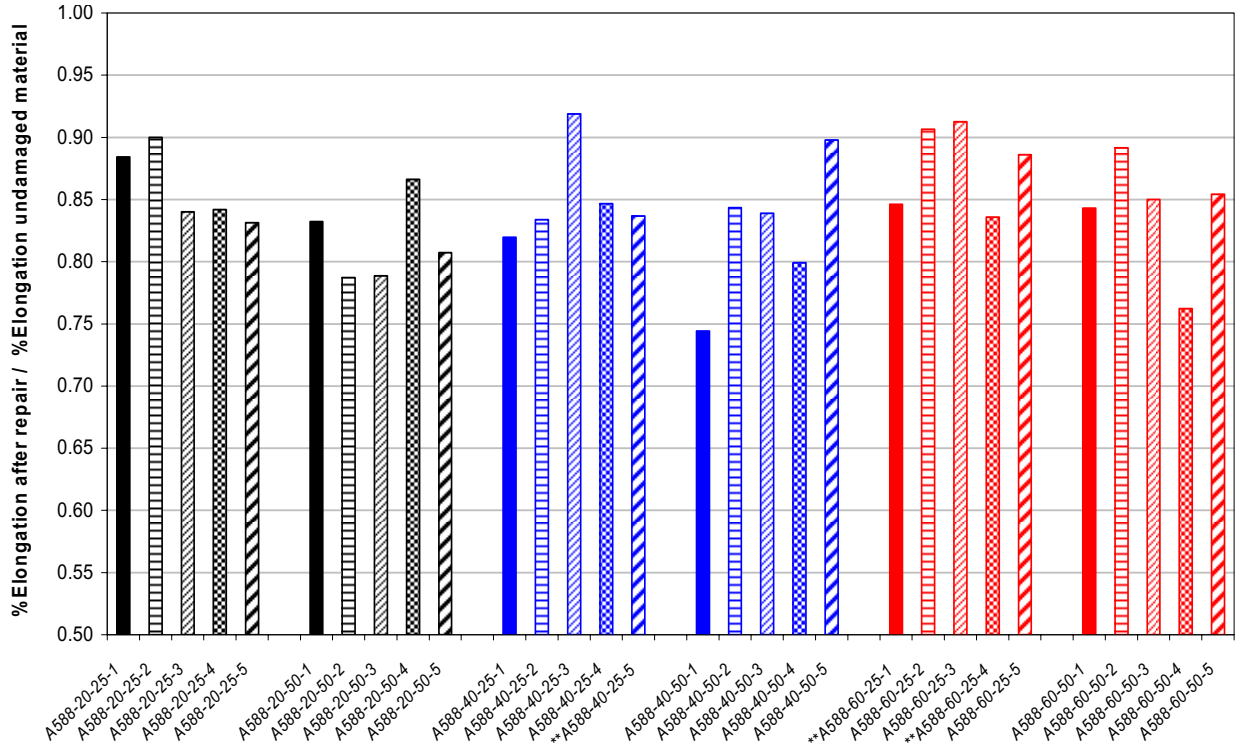

Figure 6.14
Normalized percent elongation of damaged-repaired A588 steel

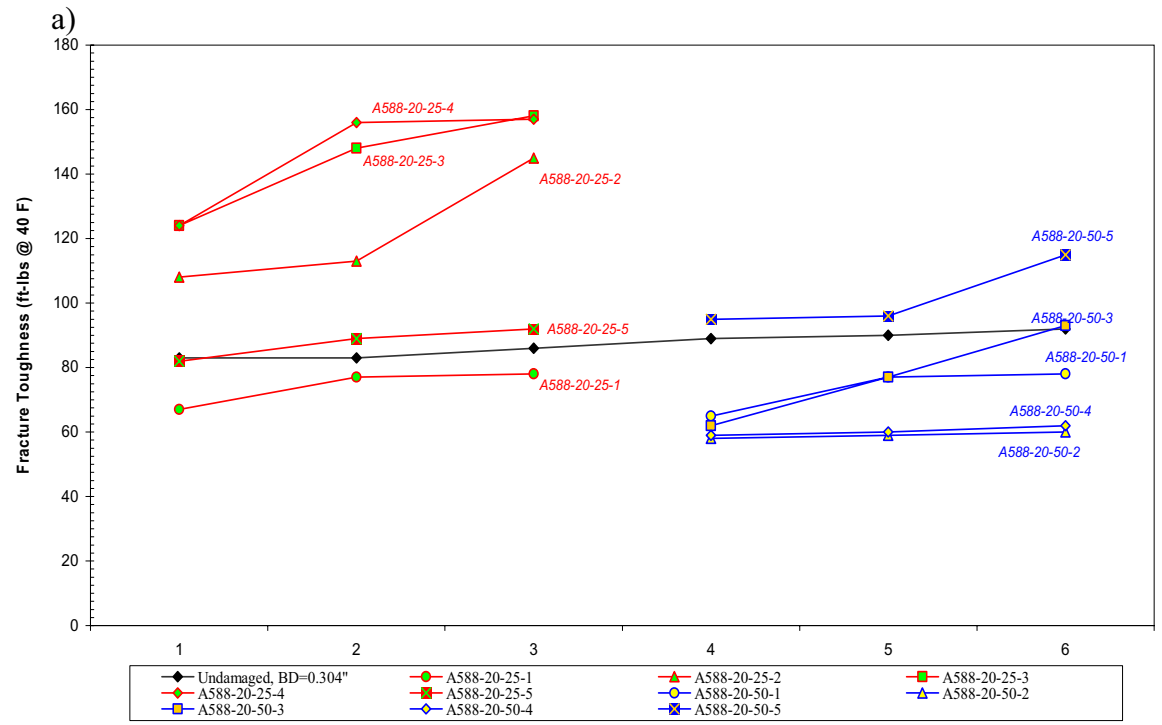

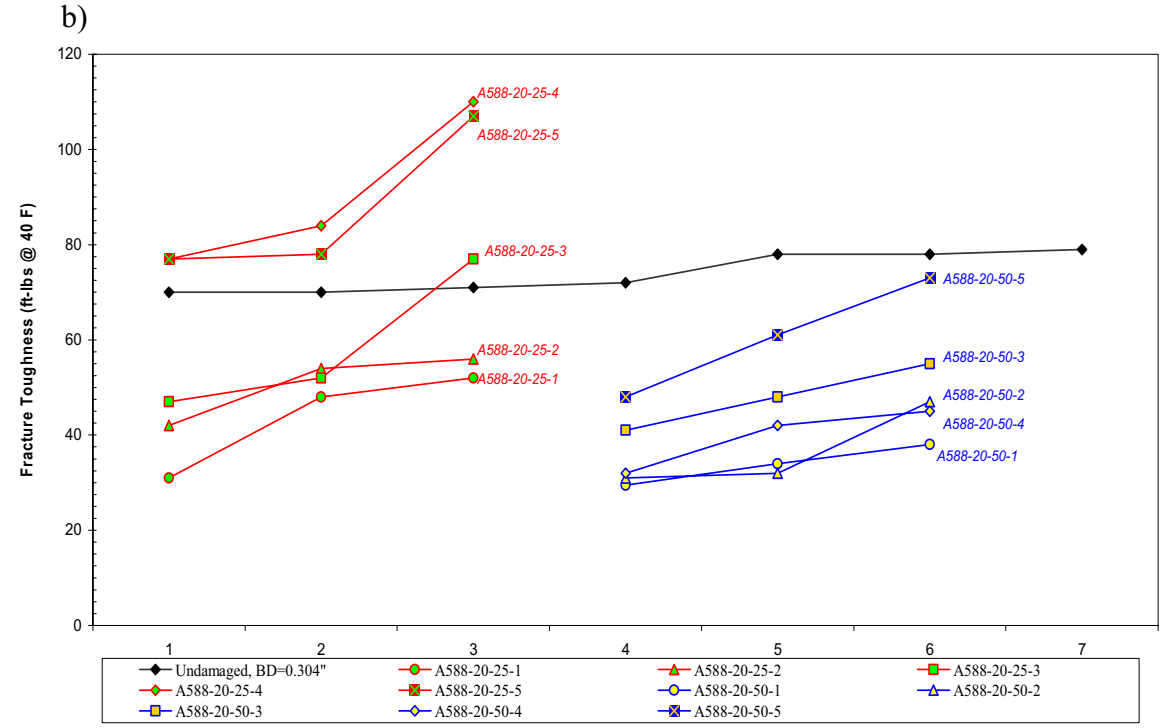

Figure 6.15

Fracture toughness values for A588-20 (ε_u=20 ε_y) specimens: (a) quarter, and (b) mid thickness

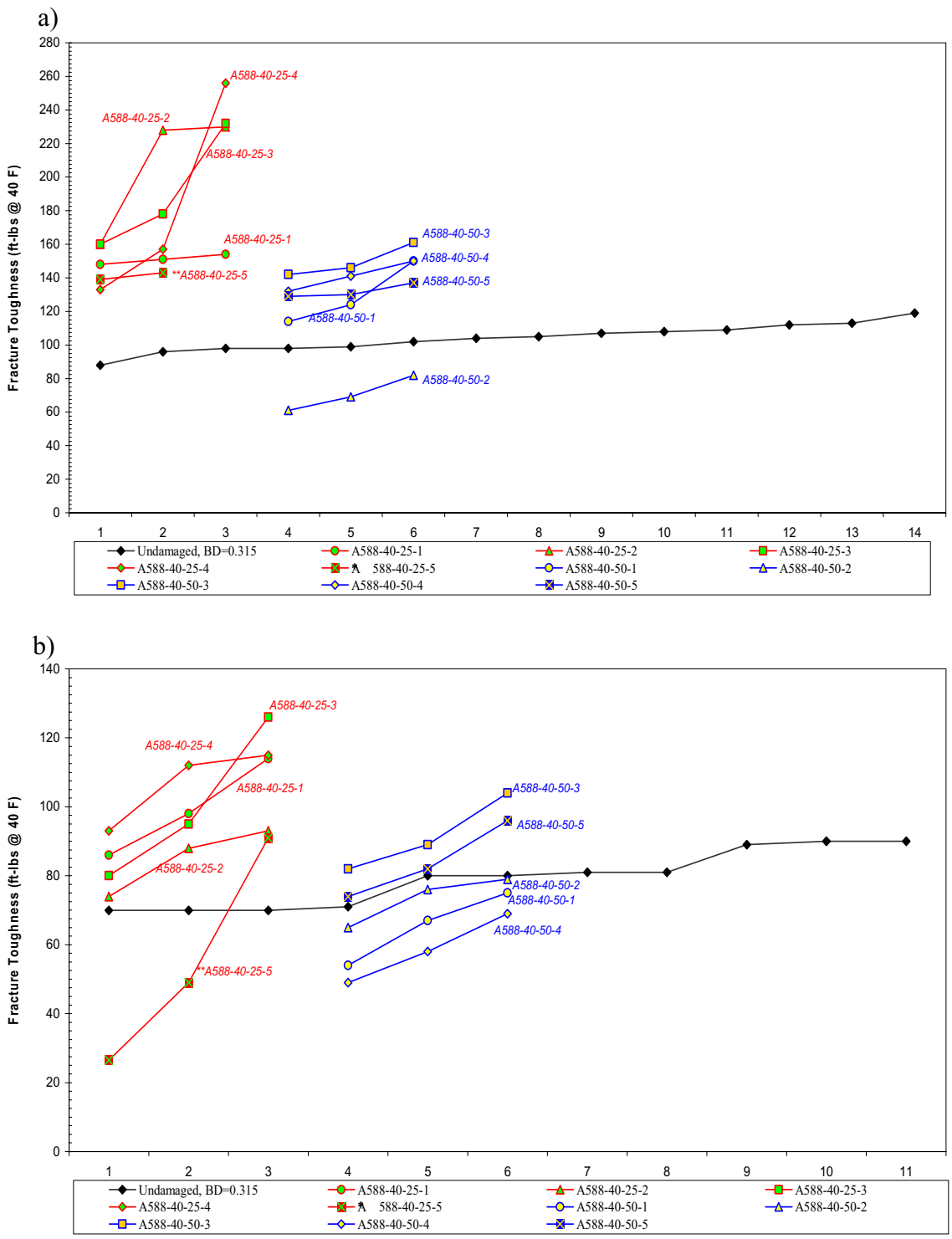

Figure 6.16
Fracture toughness values for A588-40 (ε_u=40 ε_y) specimens: (a) quarter, and (b) mid thickness

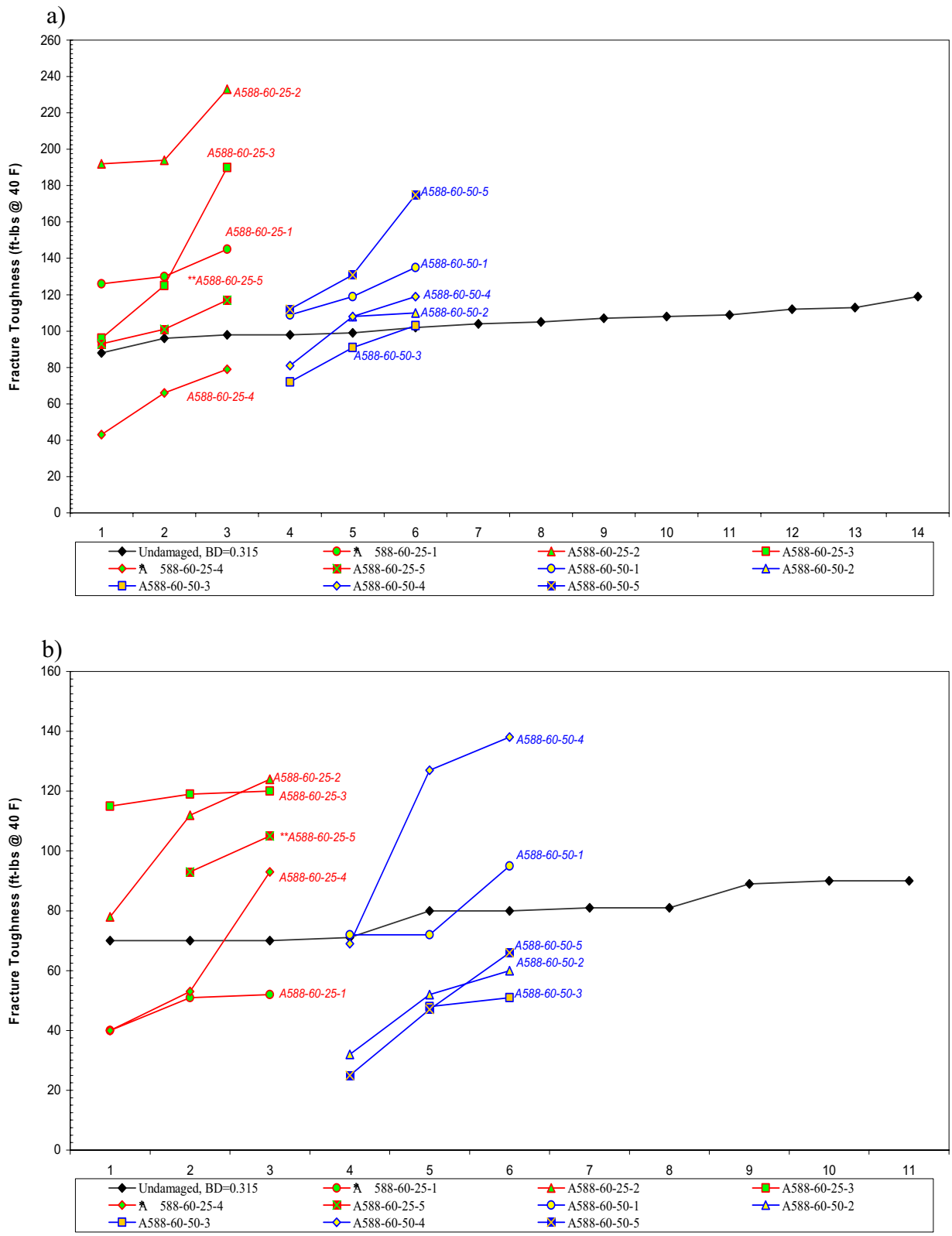

Figure 6.17
Fracture toughness values for A588-60 (ε_d=60 ε_y) specimens: (a) quarter, and (b) mid thickness

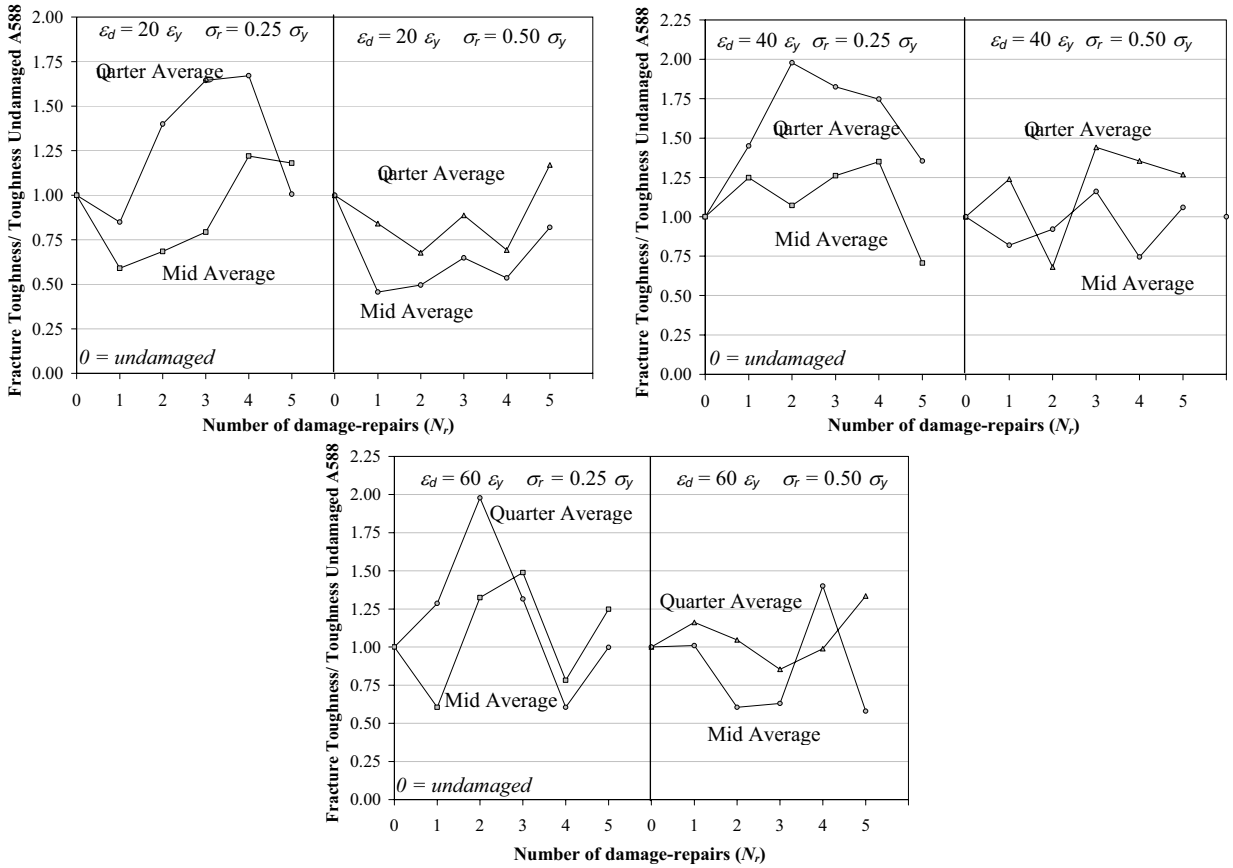

Figure 6.18
Normalized fracture toughness values for damaged-repaired A588 specimens

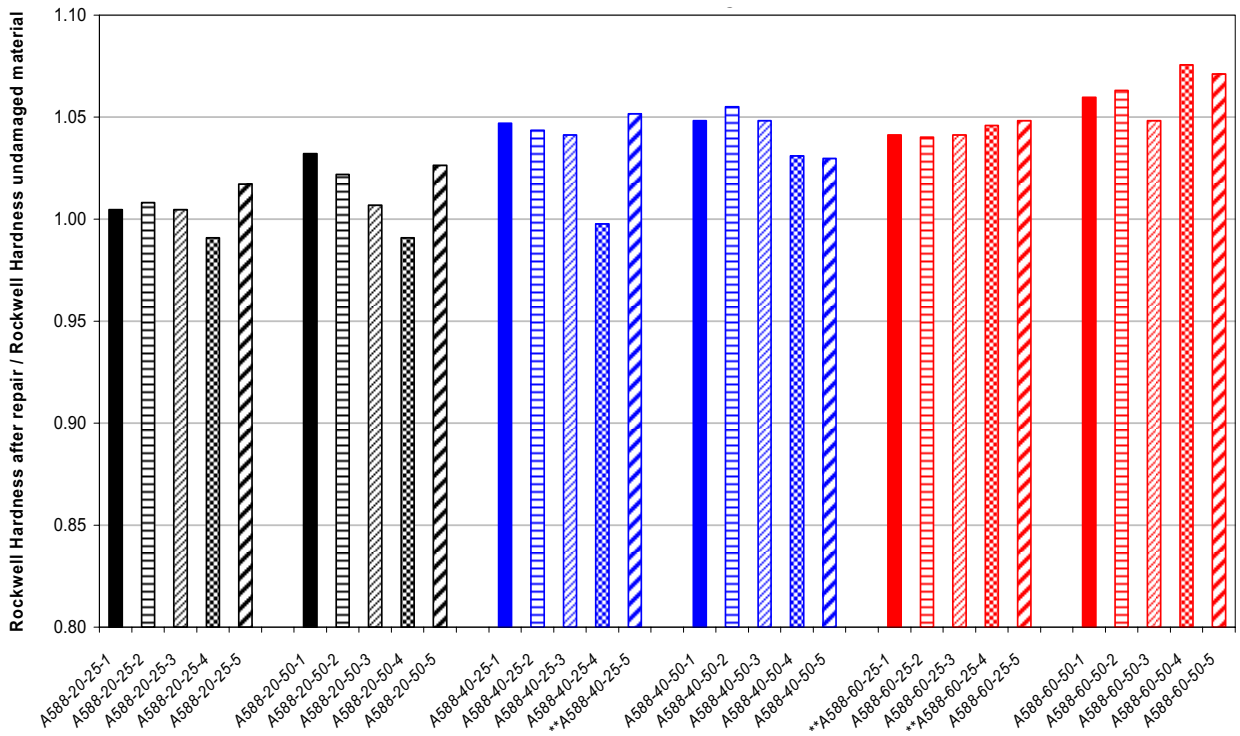

Figure 6.19
Normalized Rockwell hardness of damaged-repaired A588 steel

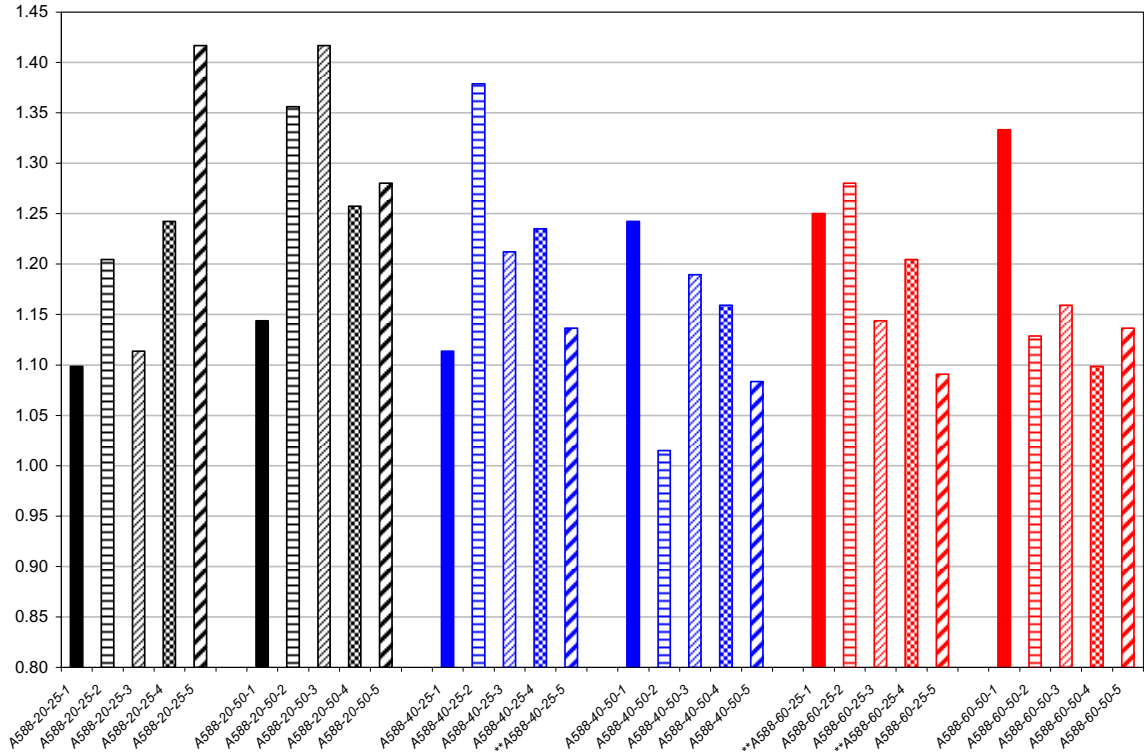

Figure 6.20
Normalized grain size of damaged-repaired A588 specimens

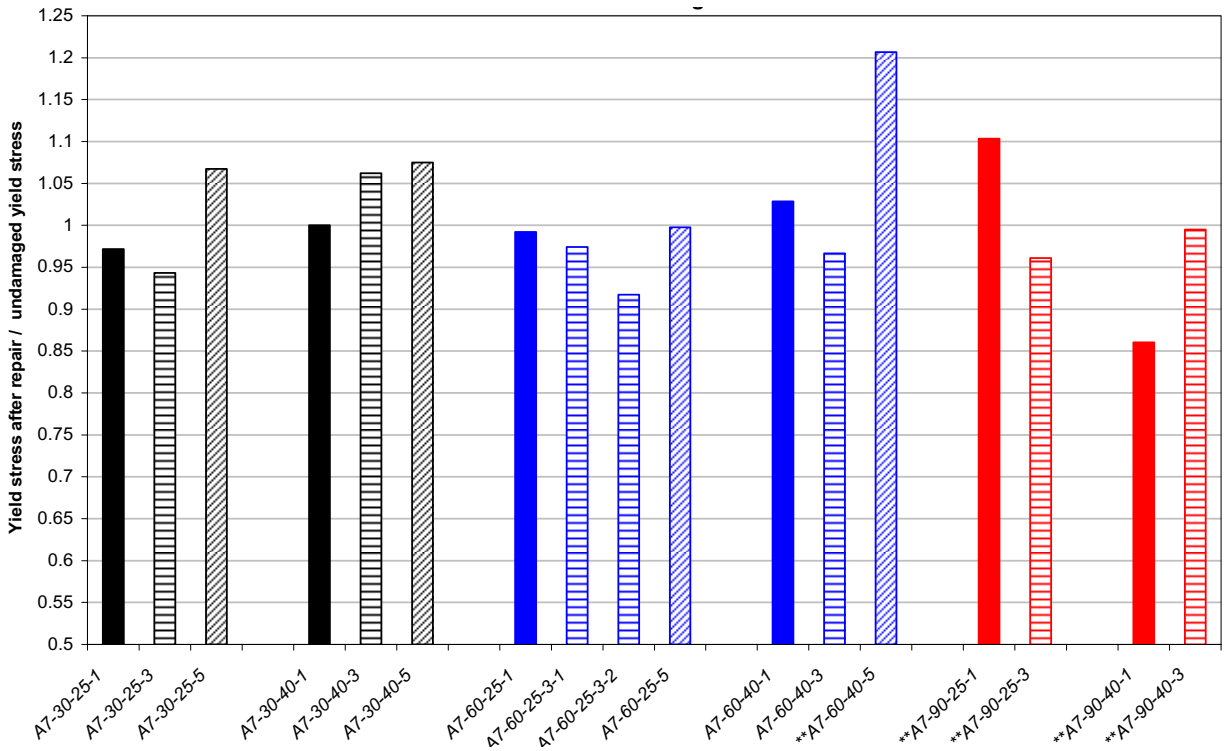

Figure 6.21
Normalized yield stress of damaged-repaired A7 steel

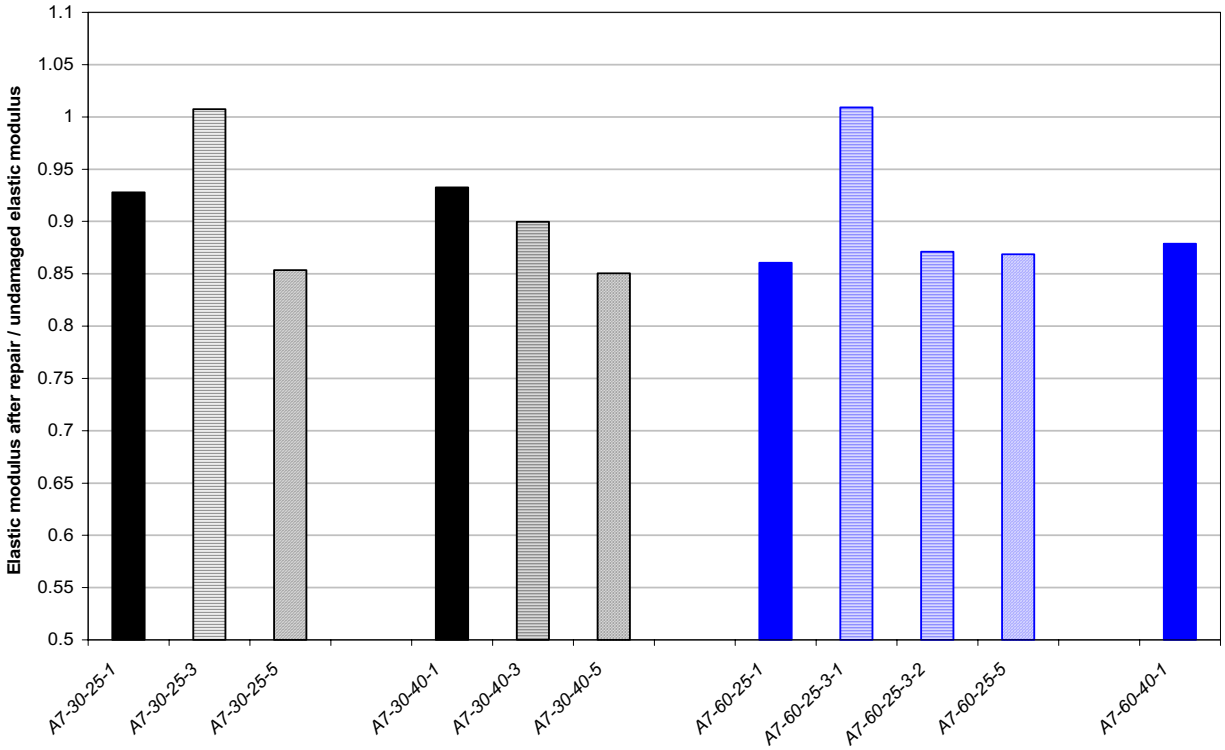

Figure 6.22
Normalized elastic modulus of damaged-repaired A7 steel

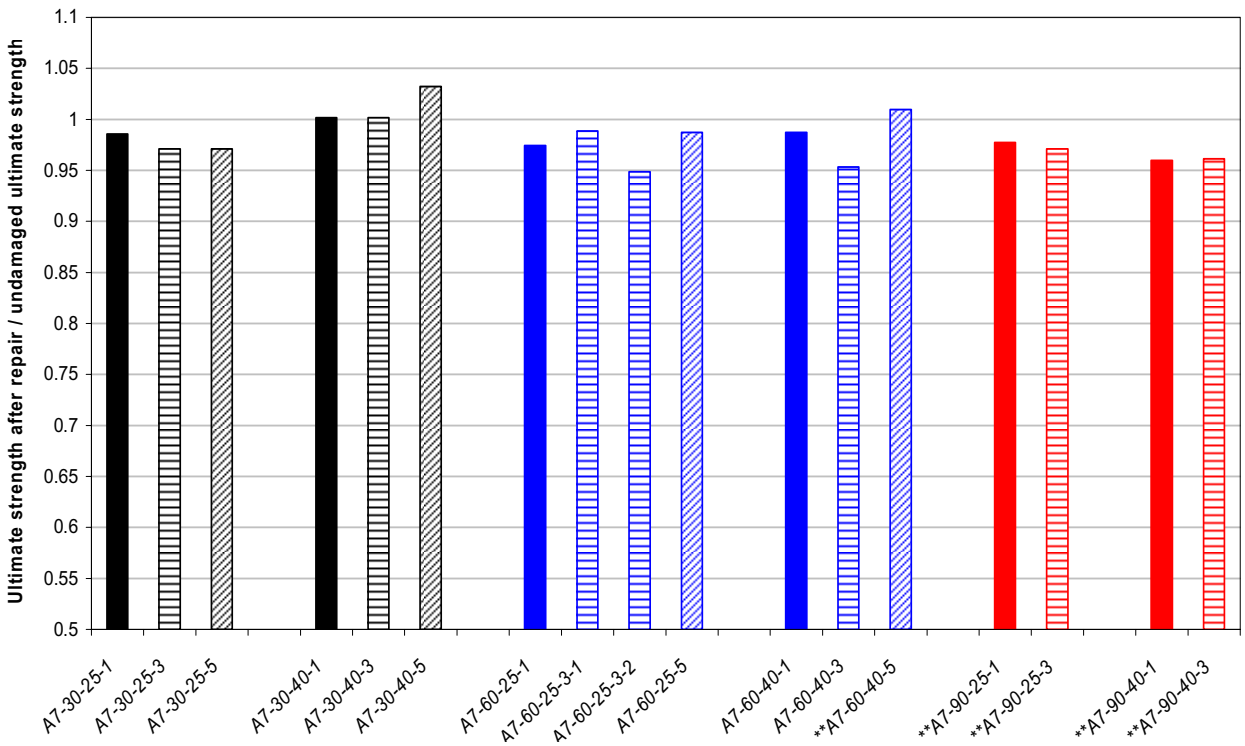

Figure 6.23
Normalized ultimate stress of damaged-repaired A7 steel

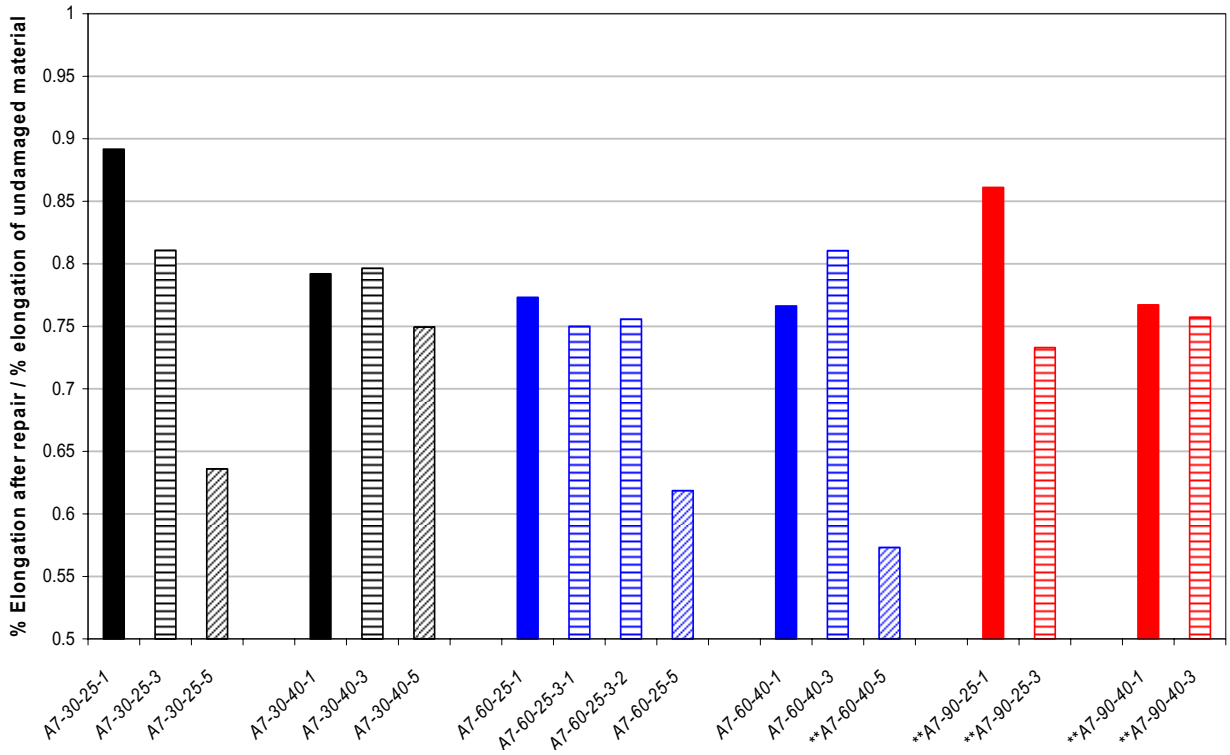

Figure 6.24
Normalized percent elongation of damaged-repaired A7 steel

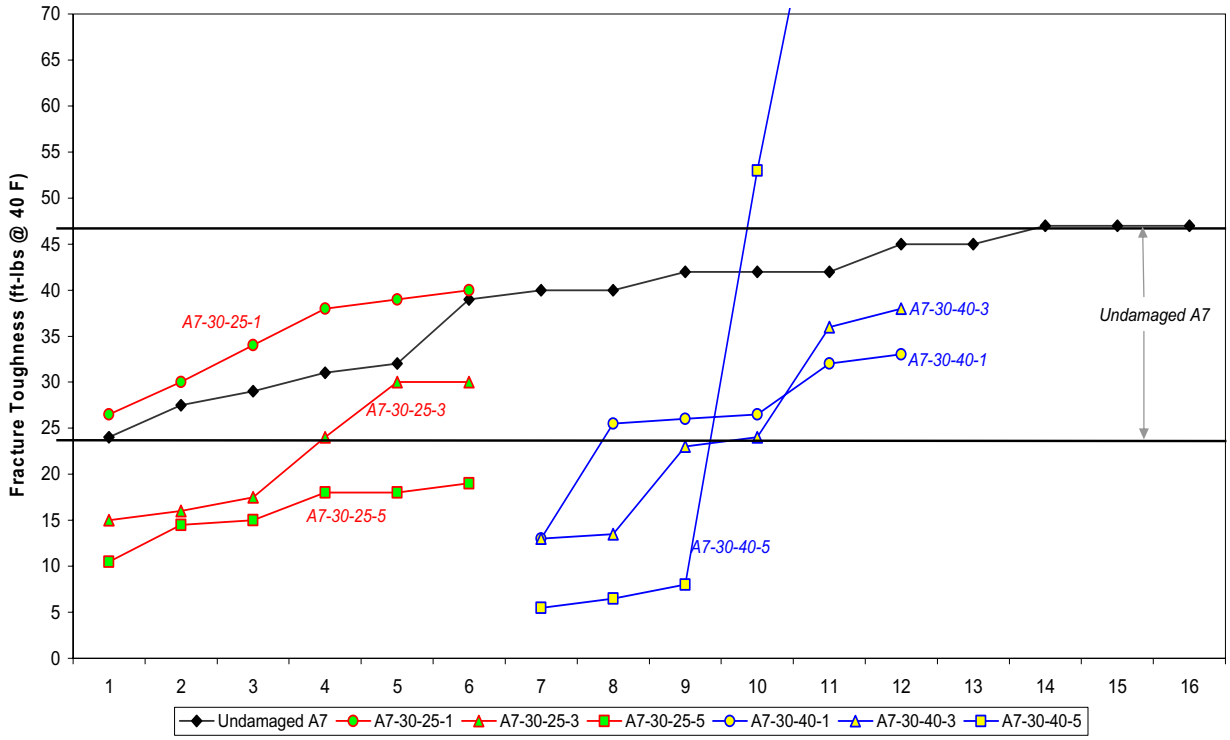

Figure 6.25
Fracture toughness comparisons of damaged-repaired A7-30 (ε_d=30 ε_y) specimens

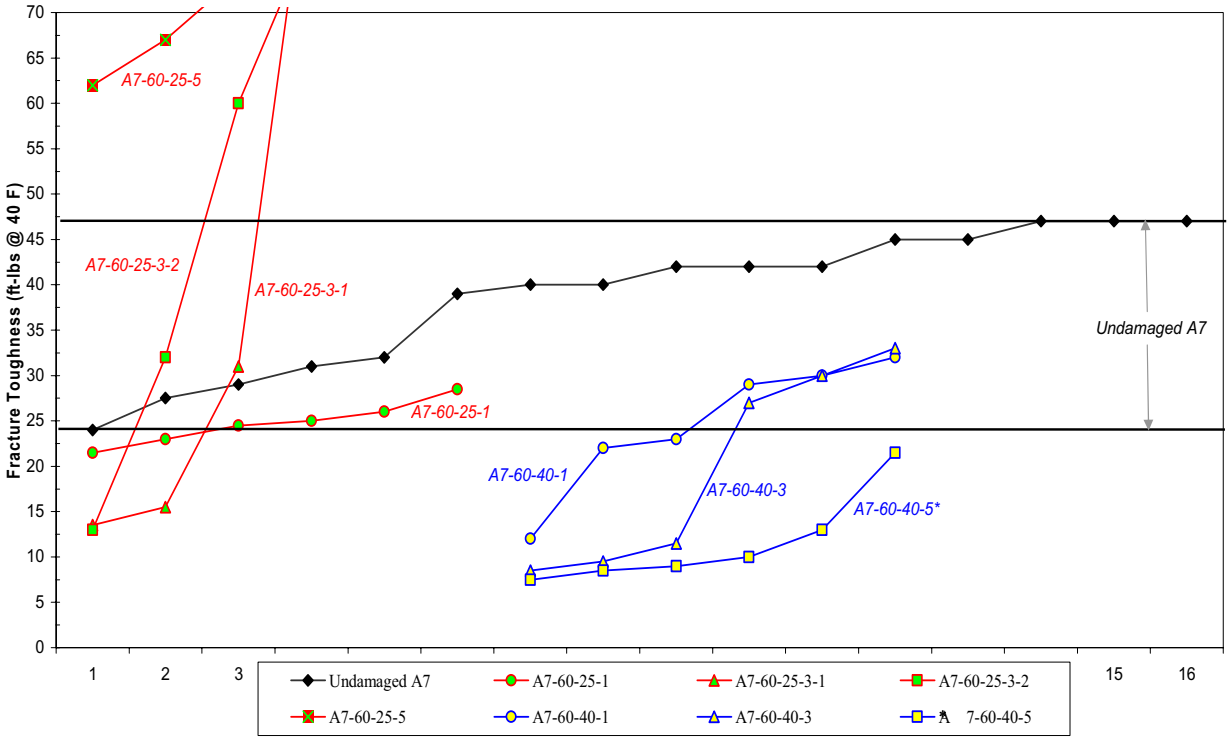

Figure 6.26
Fracture toughness comparisons of damaged-repaired A7-60 (ε_d=60 ε_y) specimens

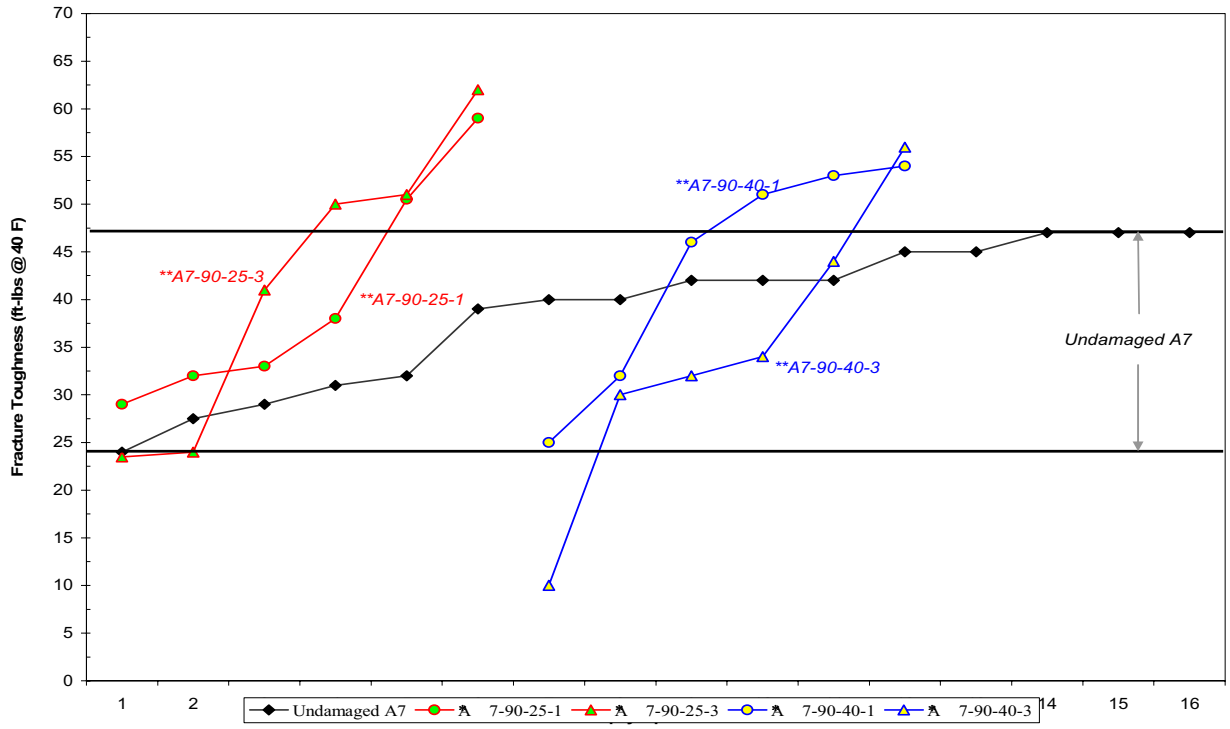

Figure 6.27
Fracture toughness comparisons of damaged-repaired A7-90 (ε_d=90 ε_y) specimens

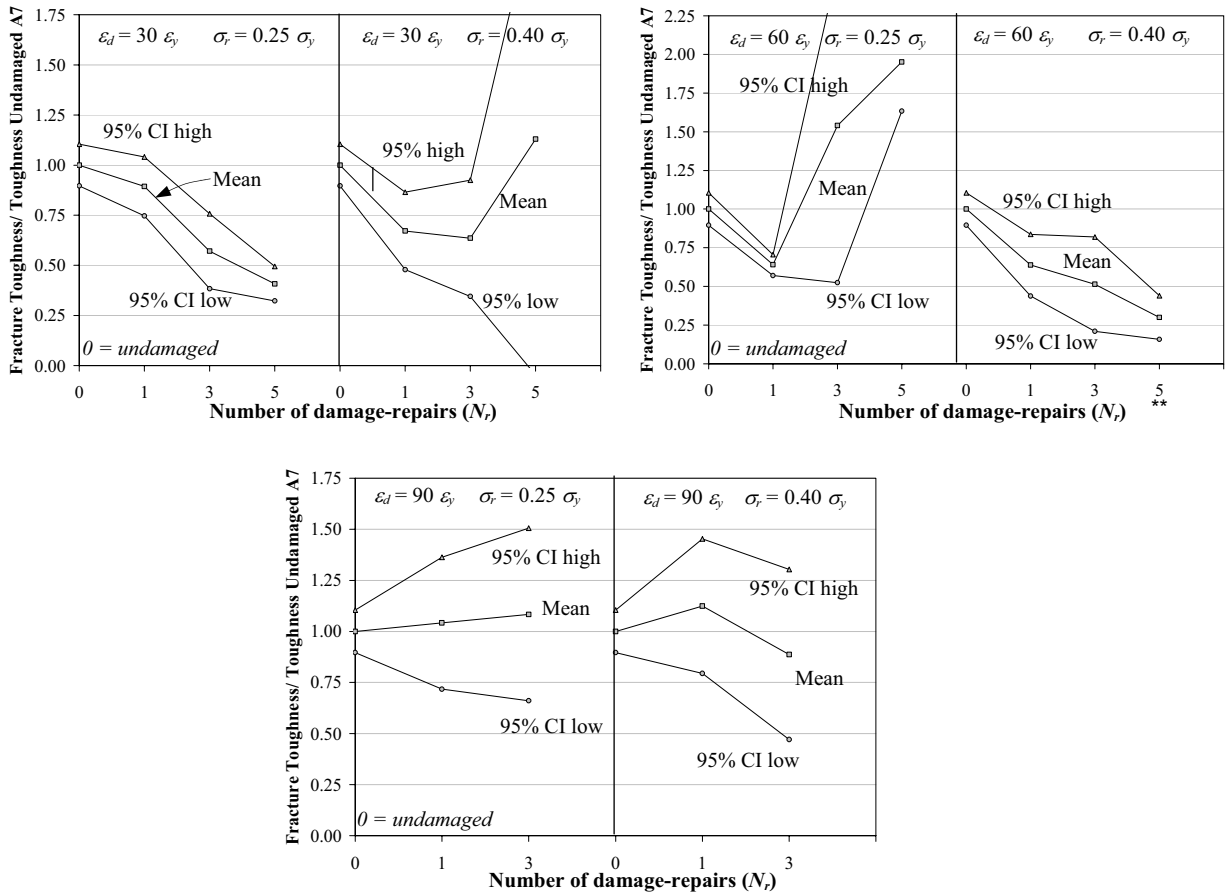

Figure 6.28
Normalized fracture toughness (mean and 95% CI) for damaged-repaired A7 specimens

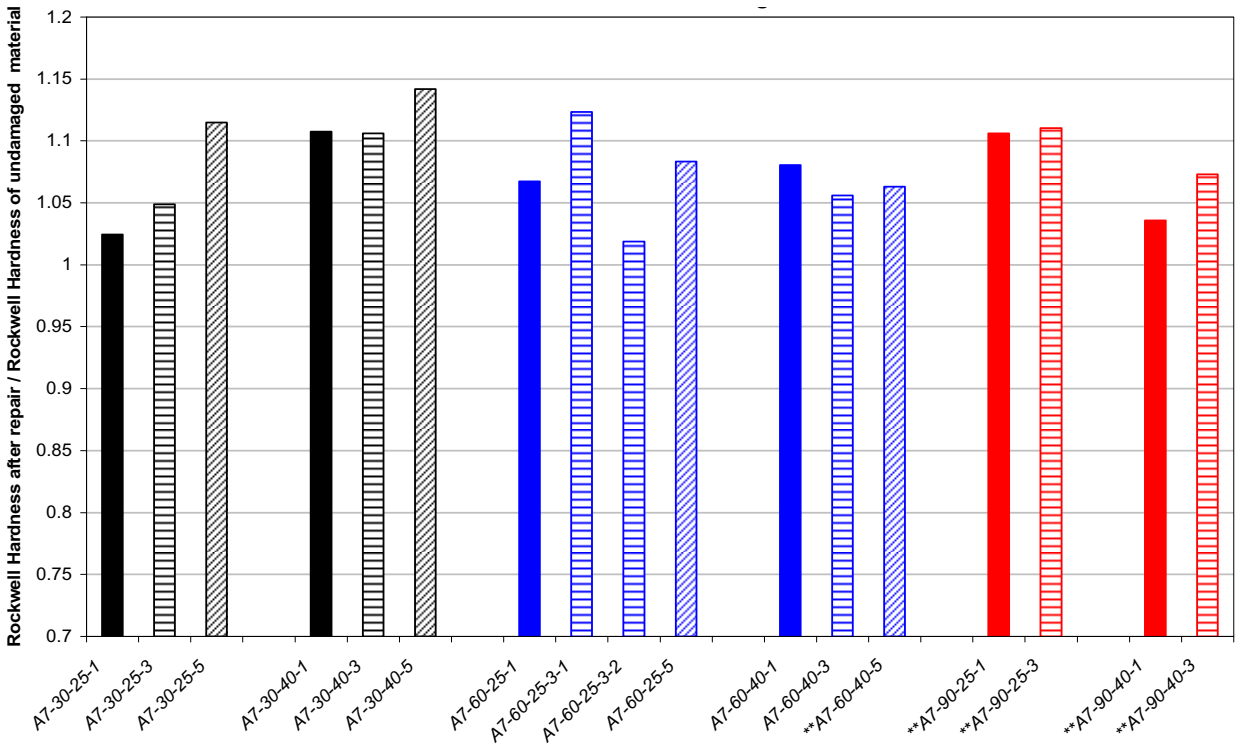

Figure 6.29
Normalized Rockwell hardness of damaged-repaired A7 steel

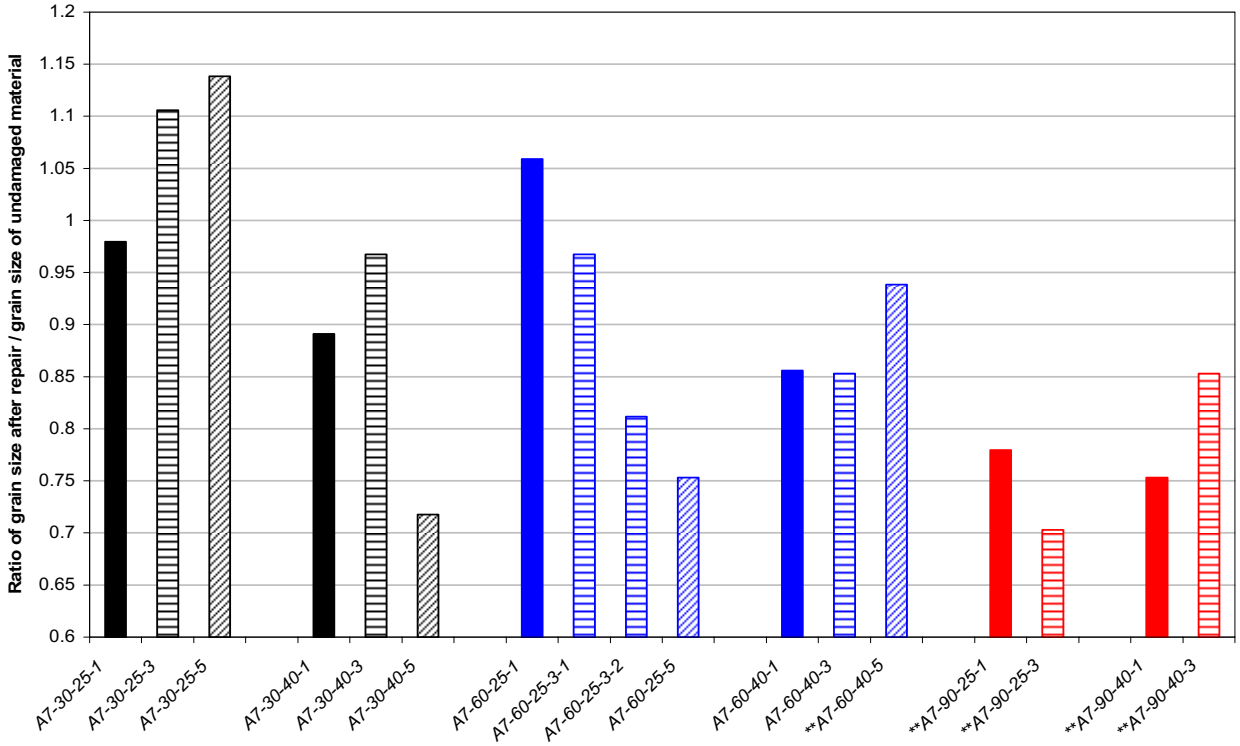

Figure 6.30
Normalized grain size of damaged-repaired A7 steel

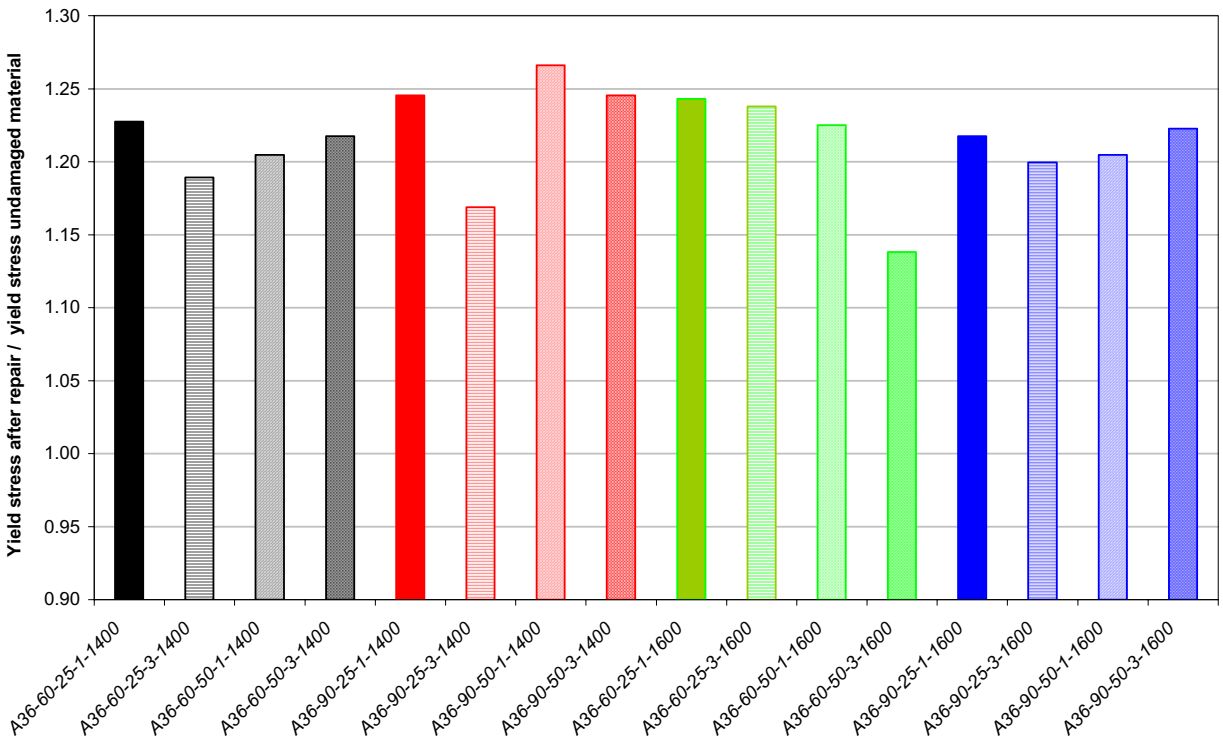

Figure 6.31
Normalized yield stress of damaged-repaired overheated A36 steel

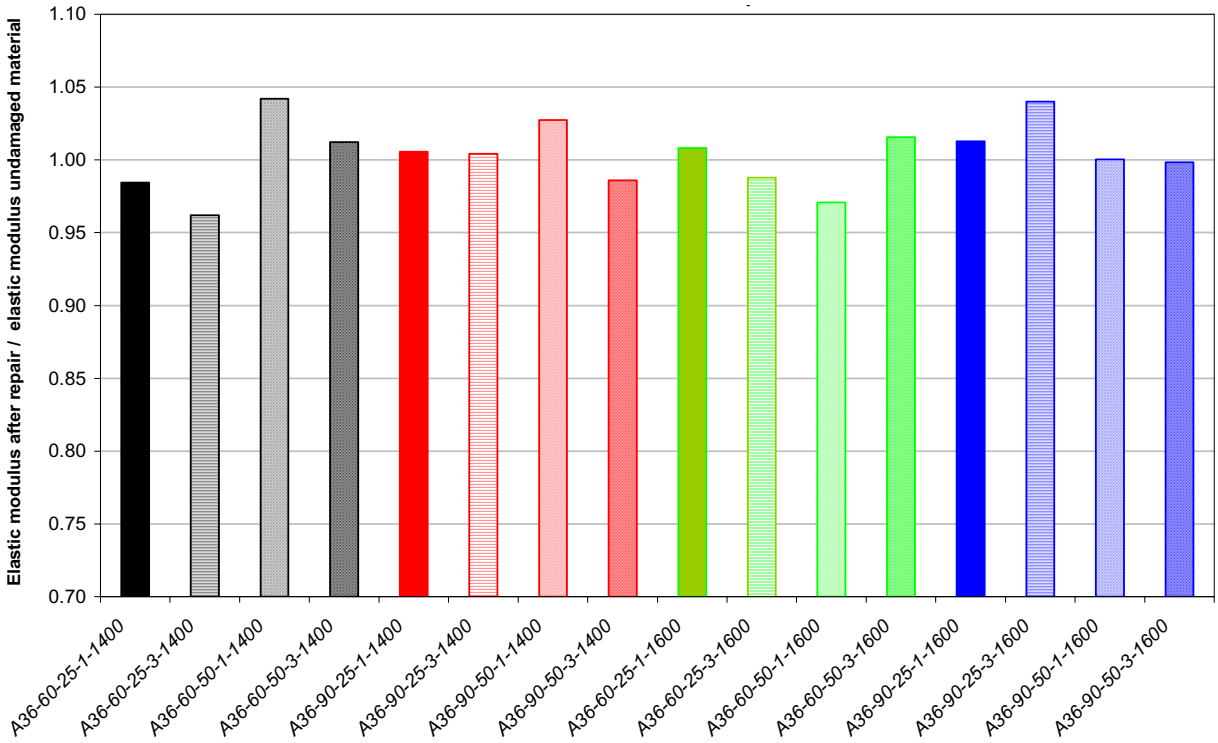

Figure 6.32
Normalized elastic modulus of damaged-repaired overheated A36 steel

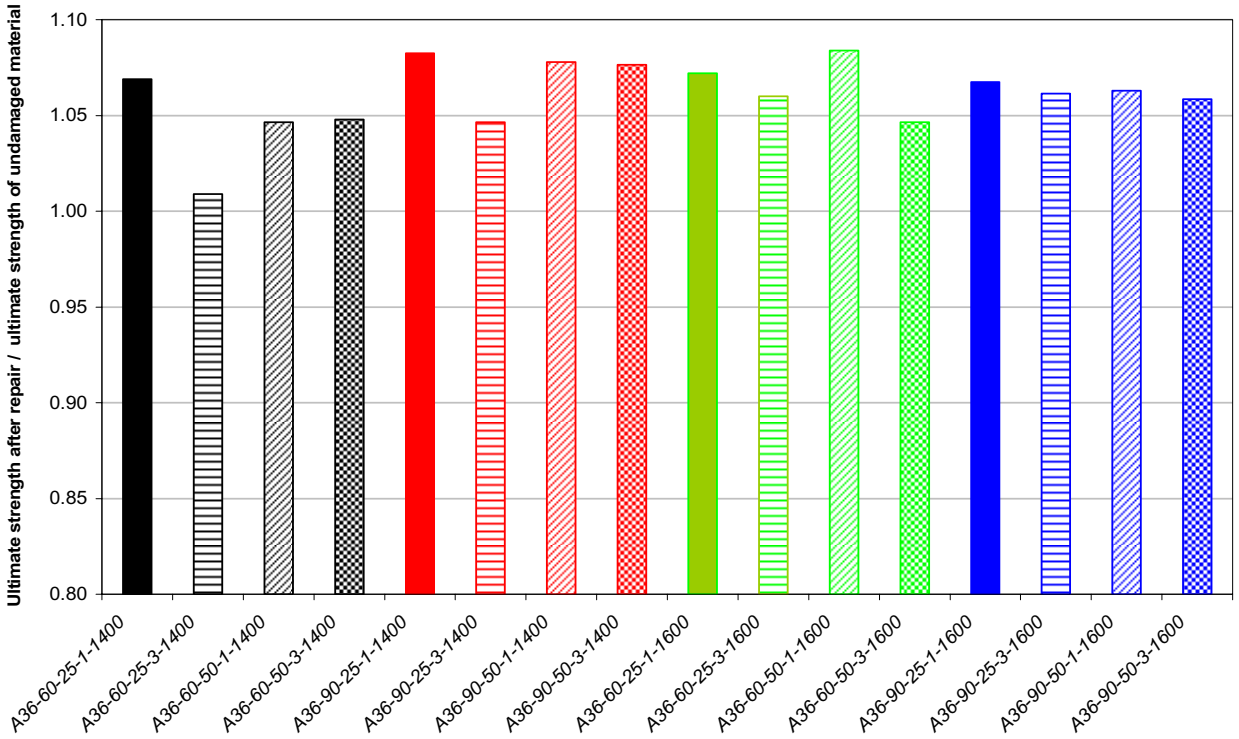

Figure 6.33
Normalized ultimate stress of damaged-repaired overheated A36 steel

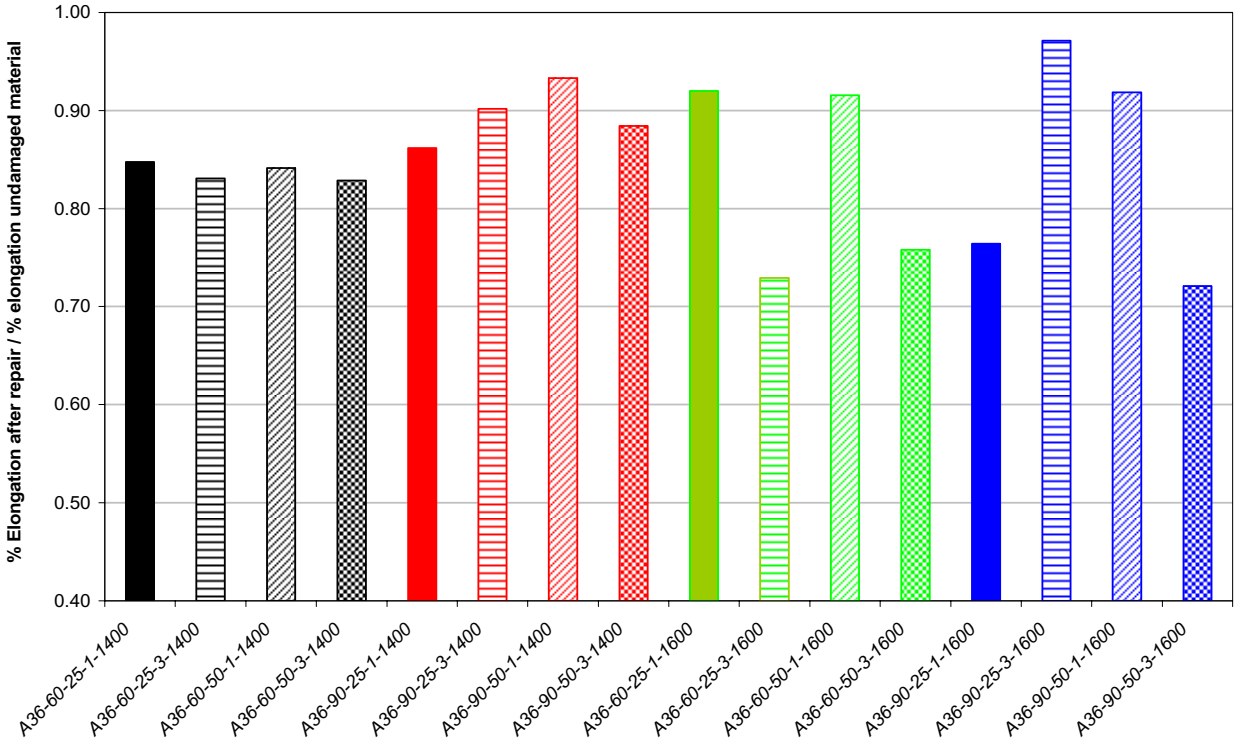

Figure 6.34
Normalized percent elongation of damaged-repaired overheated A36 steel

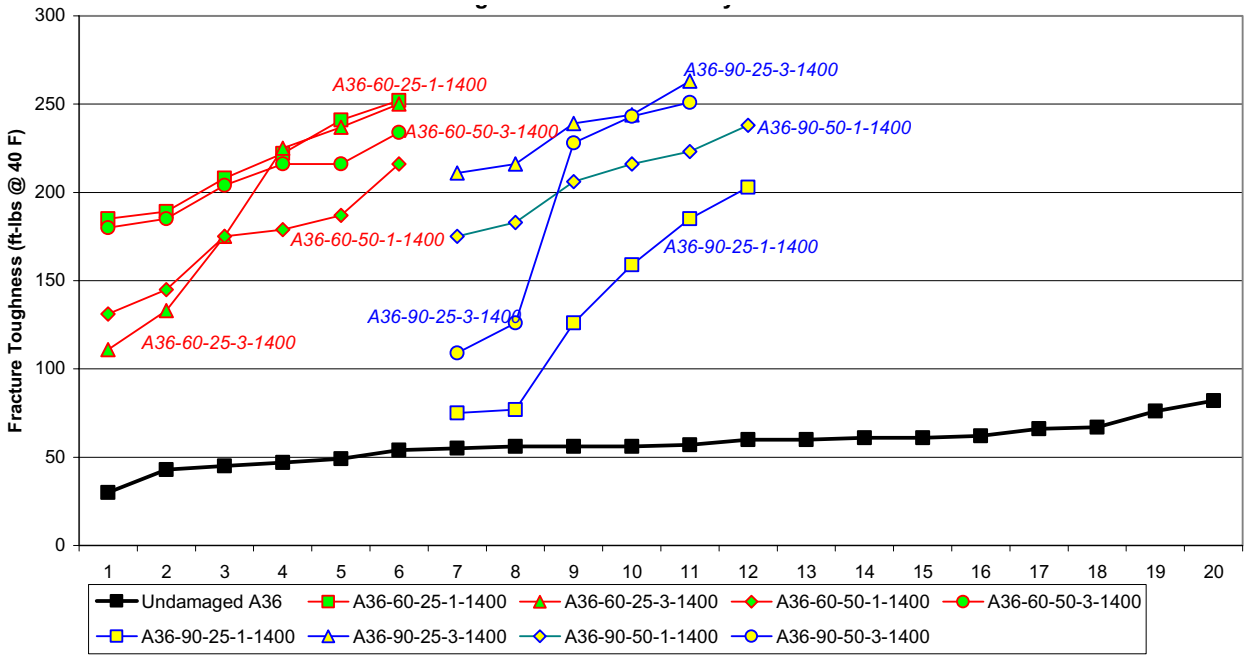

Figure 6.35
Fracture toughness comparisons of damaged-repaired A36 steel overheated to 1400 ºF

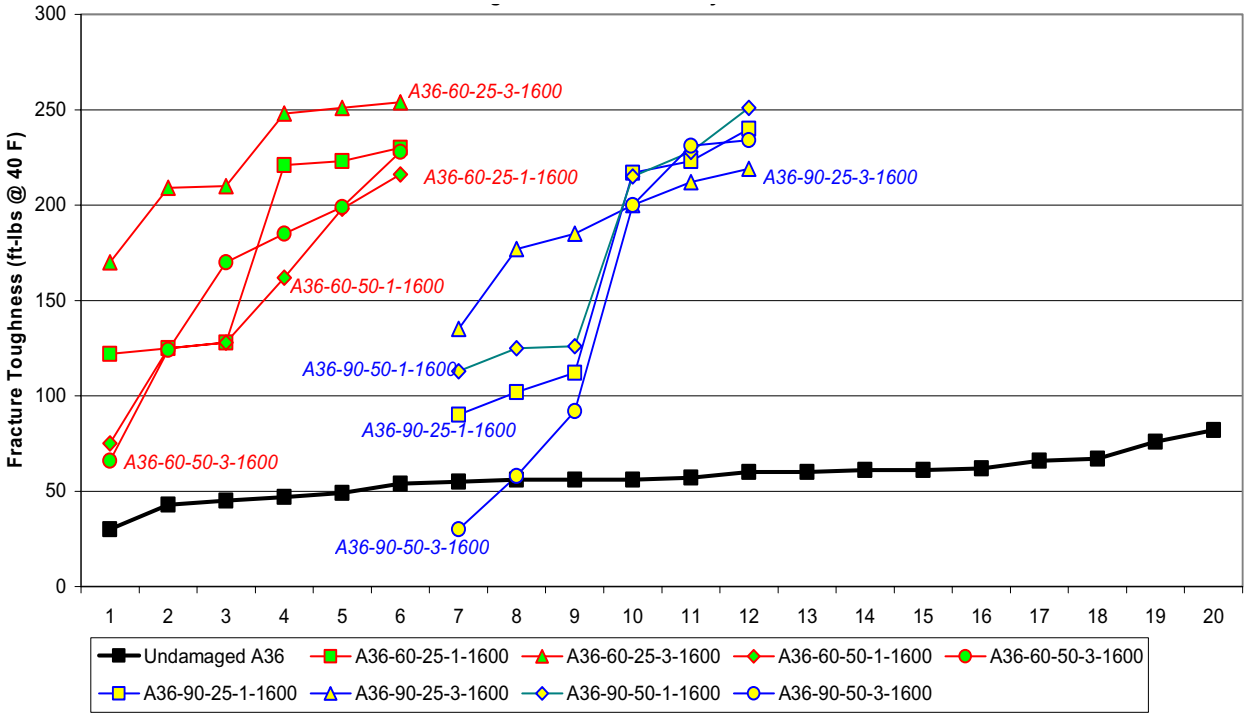

Figure 6.36
Fracture toughness values comparisons of damaged-repaired A36 steel overheated to 1600 ºF

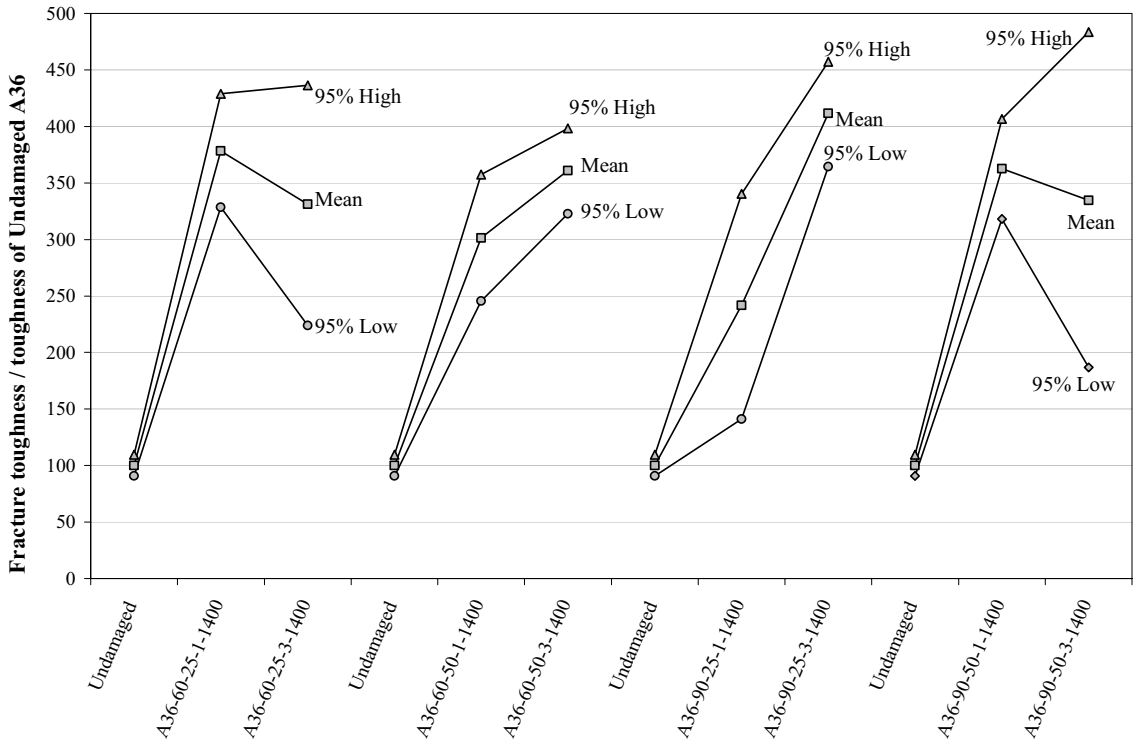

Figure 6.37
Normalized FT (mean and 95% CI) of damaged-repaired A36 steel overheated to 1400 °F

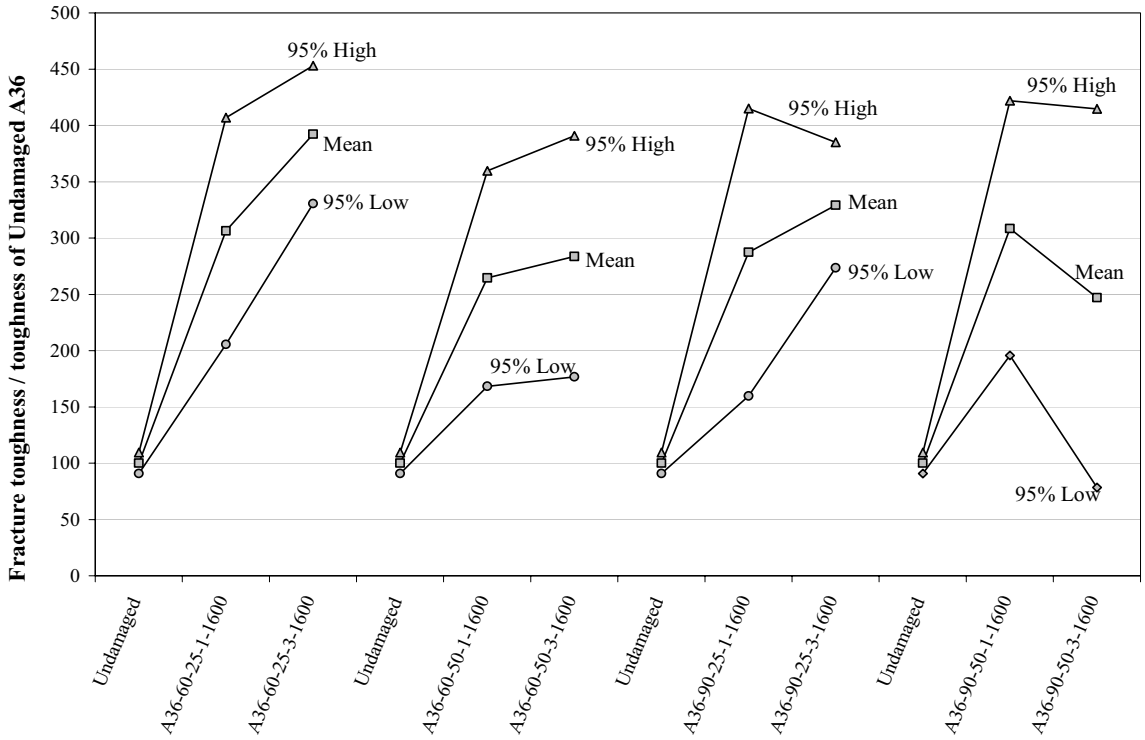

Figure 6.38
Normalized FT (mean and 95% CI) of damaged-repaired A36 steel overheated to 1600 °F

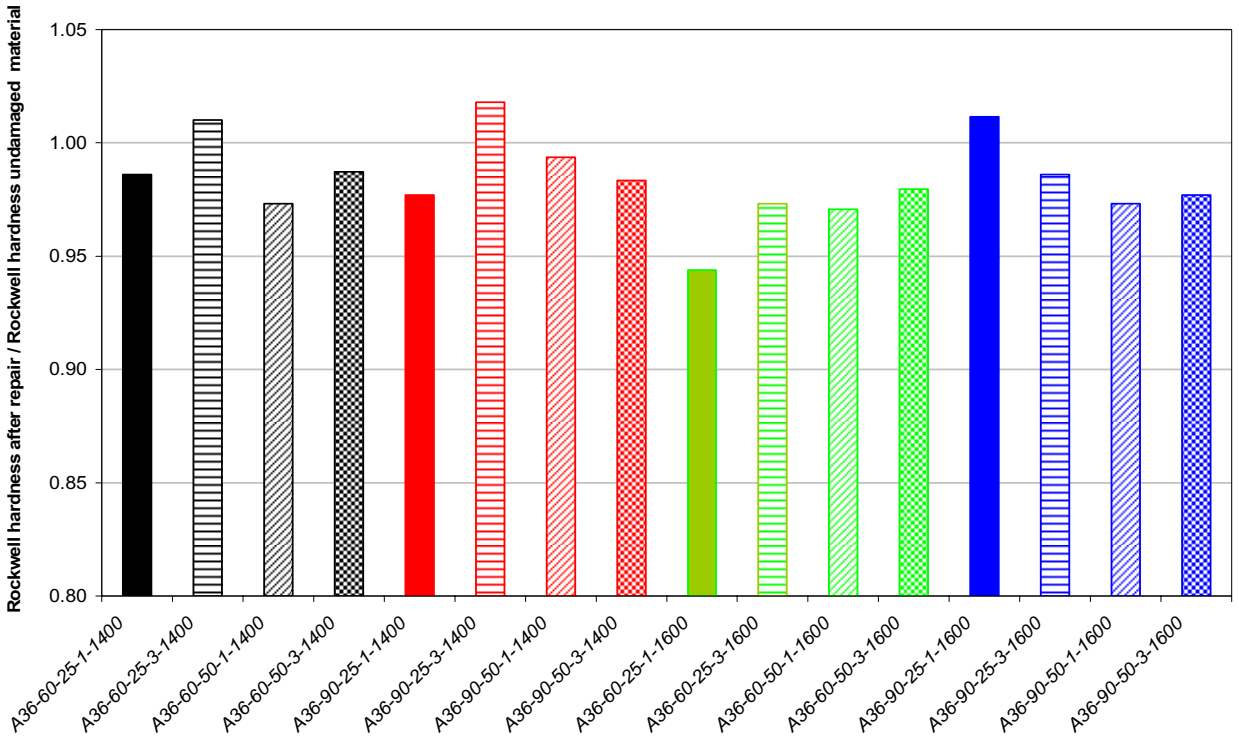

Figure 6.39
Normalized Rockwell hardness of damaged-repaired overheated A36 steel

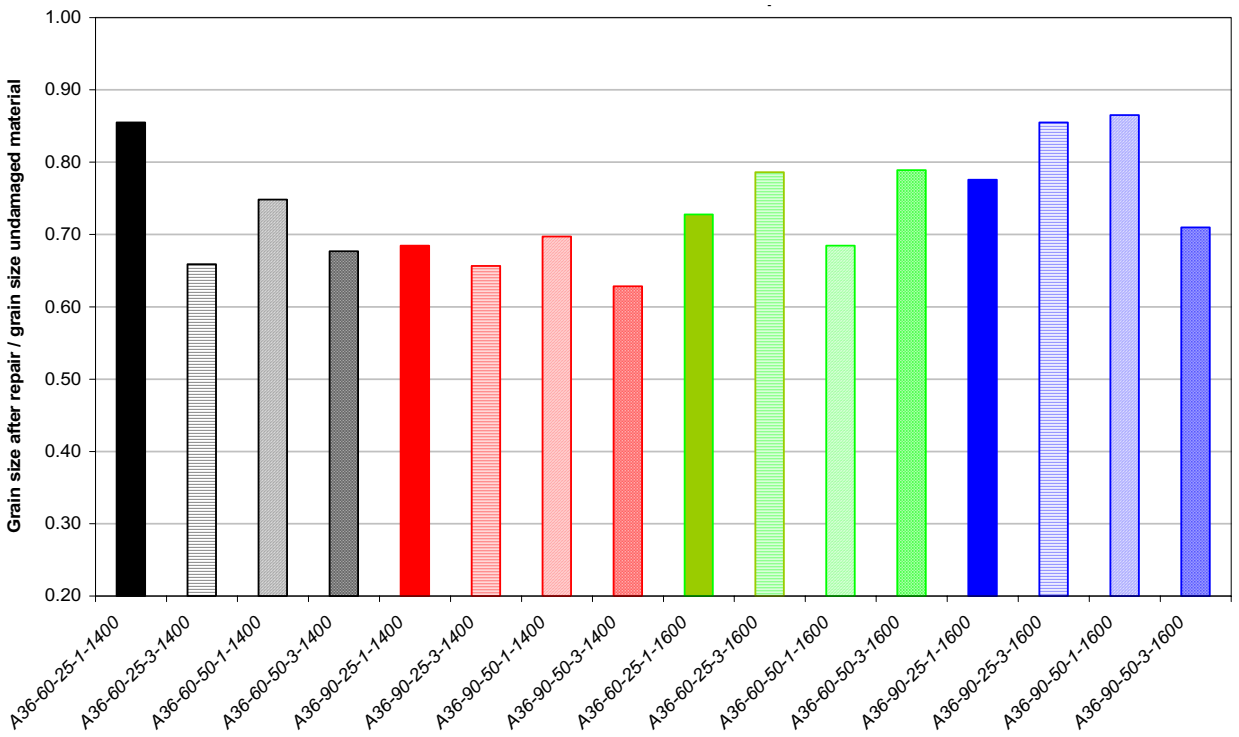

Figure 6.40
Normalized grain size for damaged-repaired overheated A36 steel

[Intentionally Blank Page]

7 EXPERIMENTAL INVESTIGATIONS OF LARGE-SCALE STEEL BEAMS

7.1 INTRODUCTION AND TASK IV OBJECTIVES

The results of Task III offered significant insight into the effects of multiple damage-heat straightening repair cycles on the structural properties of bridge steels. The results were used to develop recommendations for replacing steel beams subjected to multiple damage-repair cycles. These recommendations were evaluated by subjecting large-scale steel beams to multiple damage-repair cycles and determining the structural properties.

Multiple damage-heat straightening repair cycles were conducted on *six* large scale steel beam specimens made from each of the bridge steels studied in Task III. Two beams were made from A36 steel, two from A588 steel, and two from A7 steel. The A7 steel beam specimens were fabricated from one of the two decommissioned W24 x76 steel beams (see Section 4.5.2). The A36 and A588 steel beams were built-up (fabricated) from steel plates similar to the plates used to fabricate the Task III laboratory-scale specimens.

The analysis of the Michigan high-load hits database, presented in Section 2.3, indicated that composite wide-flange steel beams and composite steel plate girders are the most frequently damaged and repaired bridge structure types in Michigan. These structure types are damaged by an overheight truck colliding with the bottom flange of the steel fascia beam. The damage consists of out-of-plane or weak axis bending of the bottom flange combined with twisting of the overall cross-section. This damage is repaired by heat-straightening where several Vee heats are applied to the bottom flange and strip heats are applied to the web. The heat-straightening repair primarily consists of Vee heats applied along the length of the bottom flange. As presented in Sections 3.1.1, 3.1.2, and 3.1.3, all the steel bridges visited in Task II were damaged and heat straightened similarly.

The six steel beam specimens were damaged in weak axis bending (Category W damage) and repaired using several partial-depth Vee-heats along the lengths of both flanges. This damage-repair approach was used for the steel beam specimens for the following three reasons: (1) the damage and repair are similar to that of the bottom flange of a composite beam. (2) The weak axis bending or Category W damage is easier to conduct, control, and repeat in a laboratory type setting as compared to the composite beam damage. (3) Both flanges of the beam are subjected to identical damage-heat straightening repair, which provides twice the material for obtaining consistent material samples.

The steel beam specimens were roller supported at the ends and subjected to concentrated load at midspan to produce weak axis bending (Category W damage). The test setup simulated symmetric loading and boundary conditions, thus allowing the beam to deform freely.

The experimental test matrix for Task IV is summarized in Section 7.2 of this chapter. Section 7.3 describes the fabrication of the experimental beam specimens. Section 7.4 summarizes the experimental test setup. Section 7.5 describes the experimental damage-repair procedures and the instrumentation used to aid the procedures. Section 7.6 describes the material testing procedures on both undamaged and damaged-repaired beam specimens. The undamaged material testing results are provided in Section 7.6. Section 7.7 discusses an analytical fiber analysis procedure used to predict the stress and strain history induced within the experimental beam specimens. Section 7.7 also provides the damage strain-restraining stress history of each material sample removed from the damaged-repaired beam specimens.

7.2 LARGE-SCALE EXPERIMENTAL TEST MATRIX

The test matrix for the large scale investigations of Task IV is summarized in Table 7.1. Table 7.1 identifies each beam specimen by its name and presents the damage-repair histories. The specimens are arranged in the order of testing. Each beam specimen was subjected to three damage-repair cycles, where the damage and repair parameters are: the damage strain (ε_d), the restraining moment (M_r), and the maximum heating temperature (T_{max}). ε_d is defined as the longitudinal strain in the extreme tension fiber of the midspan cross-section. M_r is provided as a ratio of the minor-axis plastic moment capacity (M_p).

The experimental investigations of large-scale A7 steel beams focused specifically on the impact of damage strain and limited to three damage-repair cycles based on the conclusions and recommendations of Task III. The first A7 beam (A7-Beam 1) was subjected to a damage strain of 30 ε_y at the extreme tension fiber of the midspan cross-section for all three damage cycles. Restraining moments of 0.25 M_p, 0.50 M_p, and 0.25 M_p were used for repair cycles 1, 2, and 3, respectively. The second A7 beam (A7-Beam 2) was subjected to higher damage strains of 90 ε_y, 60 ε_y, and 60 ε_y for damage cycles 1, 2, and 3 respectively. The restraining stress of 0.50 M_p was held constant for all three repair cycles. A maximum temperature of 1200 °F was enforced for both A7 beams.

The first A36 beam (A36-Beam 1) was subjected to a damage strain (ε_d) of 30 ε_y for all three damage cycles. Varying restraining moments of 0.25 M_p, 0.50 M_p, and 0.25 M_p were applied for repair cycles 1, 2, and 3, respectively. The maximum heating temperature applied while repairing was strictly enforced to be 1200 °F. The experimental results of Task III indicated that subjecting the A36 steel to overheated temperatures benefited its fracture toughness results substantially. The mean fracture toughness of the damaged-repaired specimens heated to 1400 °F was approximately 330-415% of the undamaged toughness. The mean fracture toughness of the damaged-repaired specimens heated to 1600 °F was approximately 250-390% of the undamaged toughness. However, the recommendations limited the overheating temperature to 1400 °F to prevent surface pitting and excessive distortions. Therefore, the second A36 beam (A36-Beam 2) was subjected to three damage-heat straightening repair cycles with maximum heating temperatures of 1400 °F. The damage strains and restraining moments for each cycle of A36-Beam 2 were identical to those for A36-Beam 1. Thus, the only difference between the two beams is the heating temperature.

The experimental results of Task III indicated that A588 steel is an extremely resilient material with good fracture toughness after even five cycles of damage-heat straightening repairs. The restraining stress (σ_r) was found to have the most significant impact on the resulting fracture toughness of damage-repaired A588 steel. Lower fracture toughness values resulted from specimens repaired with a higher restraining stress of 0.50 σ_y. This comparison was consistent for specimens subjected to all three damage strains of 20 ε_y, 40 ε_y, and 60 ε_y. Other damage-repair parameters, namely the damage strain (ε_d), and the number of damage-repairs (N_r) did not have a direct or clear impact on the fracture toughness results. Hence, both A588 beams (A588-Beam 1 and A588-Beam 2) were subjected to damage strains of 40 ε_y, 20 ε_y, and 20 ε_y, for cycles 1, 2, and 3, respectively. A588-Beam 1 was subjected to a restraining moment of 0.25 M_p for all three repair cycles and A588-Beam 2 was subjected to a restraining moment of 0.50 M_p for all three repair cycles. A maximum heating temperature of 1200 °F was enforced for both A588 beams.

7.3 BEAM SPECIMEN DESIGN

7.3.1 A7 Experimental Beam Specimens

The A7 beam specimens were fabricated from one of the two decommissioned W24x76 A7 steel beams provided by the Michigan Department of Transportation (MDOT). The condition of the beam as received by the researchers was shown in Figure 4.14. The W24x76 steel beam has a depth of 23.9 in., a

base width of 8.99 in., and flange and width thicknesses of 0.68 in. and 0.44 in., respectively. The cross-section of the W24x76 steel beam is shown in Figure 7.1(a). The length of the A7 steel beam after removal of the end conditions was 23 ft. 3 in. A strip of 18 in. was removed from one end of the beam due to a significant denting of one of the flanges. A 3 ft. strip was removed from the center of the beam to obtain material coupons for testing to determine the undamaged A7 steel material properties. The two beams specimens were fabricated from either side of the undamaged material testing area as shown in Figure 7.2. The length of each beam specimen is 113.5 in and the center-to-center length between the end supports is 97 in. (8 ft. 1 in.).

Some fabrication of the beam specimens were required to develop the support and loading condition discussed later in Section 7.4. As explained later, the beam specimens were supported by 3 in. diameter steel shafts, passing through them (at the ends) and the support columns to simulate the roller support conditions. Hence, the webs of each beam specimen were coped (14.5 in. close to each end), and 3.0625 in. diameter holes are made in the flanges to allow the steel shafts to pass through the section at each support end. The last 2.25 in. of web from the ends of each beam was not removed to increase the stiffness between the two flanges. A 4 in. diameter hole was fabricated in the center of the web to allow the threaded rod from the loading frame to pass through. Figure 7.1 (b-c) provides the fabrication details for the A7 beam specimens to be tested.

7.3.2 A36 and A588 Experimental Beam Specimens

The experimental test setup (discussed in more detail in Section 7.4) was designed to be capable of damaging and repairing the W24x76 steel beam for all steel grades. Therefore, the dimensions of the built-up A36 and A588 steel sections related similar to that of the W24x76 section. The A36 and A588 steel beams were fabricated from 20 ft. (240 in.) steel plates. The plates used for the flanges were 9 in. wide and 0.75 in. thick. The plates used for the webs were 21 in. wide and 0.50 in. thick. The total depth of the built-up section is 22.5 in. The 3/8 in. fillet welds which connect the beam flanges and web were made using E70XX electrodes. The built-up cross-section is shown in Figure 7.3(a). The webs used for all beams were fabricated from A36 due to the lack of availability and expense of a 21.0 in. wide and 0.5 in. thick A588 plate.

Additionally, two-ft. were removed from each flange and web plates and welded together to form shorter built-up sections. Material samples for determining the undamaged material properties were obtained from these shorter sections. The lengths of the beam specimens are 108 in. The center-to-center length of the beams between the end supports is 97 in. (8ft. 1 in.). Some fabrication of the beam specimens were required to develop the support and loading condition discussed later in Section 7.4. As explained later, the beam specimens were supported by 3 in. diameter steel shafts, passing through them (at the ends) and the support columns to simulate the roller support conditions. The webs of the beam specimens are coped (14 in. at each end), and 3.0625 in. diameter holes are fabricated in the flanges to allow the steel shafts to pass through the section at each end. A 4 in. diameter hole was fabricated in the center of the webs to allow the threaded rod from the loading frame to pass through. Figure 7.3 (b-c) provides the fabrication details for the beam specimens to be tested.

7.4 TEST SETUP DESIGN AND FABRICATION

Two specially designed built-up steel columns provided support reactions to the beam specimens. Each column was fabricated from two C10x20 channel sections, which were welded together using ¼ in. batten plates to form a rectangular section. The built-up columns were welded to each ½ in. thick base plate, which was post-tensioned to the laboratory strong floor with a force of 140 kips. Figure 7.4 shows the details of the column supports. A photograph of the fabricated column is shown in Figure 7.5.

The beam specimens are supported by 3 in. diameter steel shafts, which pass through the flanges of the beam and the webs of the built-up steel column. These shafts pass through slotted holes fabricated in

the webs of the built-up steel column. The dimensions of the slotted hole are 3.0625 x 4.5625 in [see Figure 7.4(b)]. The additional 1.5 in. width of the slotted hole allows the shaft to translate laterally and act as a roller support. The center-to-center distance from the slots of the two columns is 96 in. (8 ft.). Therefore, the 97 in. beam specimens are free to translate 1.25 in. at each support. The ends of the 3 in. steel shafts were threaded so that structural nuts could be used to secure the shafts to the setup as a safety precaution. The column supports and steel shafts were fabricated from A36 steel.

A specially designed loading frame was used to apply the concentrated force at the beam midspan during the damage and heat straightening repair cycles. The loading frame was designed to apply forces in both the upward and downward directions, i.e., the damaging force in the upward direction (pushing up) and the restraining force in the downward direction (pulling down). The forces were applied using a double-acting hydraulic actuator, which was bolted to a bottom beam post-tensioned to the laboratory strong floor with a force of 100 kips. One end of a 2.5 in. high strength threaded rod was threaded into the plunger of the hydraulic actuator. The other end is fixed to a small built-up loading beam using structural plates and nuts. Figures 7.6(a) shows a schematic of the loading frame. Figure 7.6(b) shows a photograph of this part of the setup. The loading beam is a built-up section with two webs designed for a total section modulus of 21.7 in^3. It is used to apply the concentrated damaging and restraining forces to the beam midspan. The damaging (upward) force is applied by the hydraulic actuator pushing the loading beam against the flanges of the W24x76 (or equivalent) beam specimen being tested. Two semi-circular shafts provide bearing contact between the loading beam and the flanges of the specimen being tested. The shafts allow the specimen to rotate freely with respect to the loading beam at the point of contact. Figure 7.7 shows a drawing of the loading condition from the side view. Additional details of the loading beam including elevation and plan views are shown in Figure 7.8(a – b).

The restraining (pulling downward) force during heat straightening is applied using the loading beam and additional attachments. The additional attachments consist of two 4 x 29 x 1 in. steel plates. Each steel plate is connected to the loading beam using two 0.75 in. threaded rods. The steel plates bear against the top of the flanges of the W24x76 (or similar) beam specimen as shown in Figures 7.6 and 7.7. Two semi-circular shafts are used with each steel plate to provide the bearing between the plates and the two flanges of the specimen being tested. The restraining force is applied by the hydraulic jack pulling the loading beam downwards. Thus, the restraining force is applied as two equal concentrated forces acting at a distance of 4.8 in. on either side of the beam midspan. This was the closest the setup could acquire to applying one concentrated force at the midspan. The midspan Vee-heat was applied in between the threaded rods applying the concentrated forces at midspan during repair.

Figures 7.9 and 7.10 show photographs of the completed test setup with the first W24x76 A7 steel beam (A7-Beam 1) in place, ready to be tested. These photographs identify the supporting columns, loading beam, hydraulic actuator, and the beam specimen.

7.5 INSTRUMENTATION AND EXPERIMENTAL PROCEDURE

7.5.1 Instrumentation

This section describes the instrumentation layout used while damaging and heat straightening the beam specimens. Several instruments that are being used include: (a) pressure transducers for measuring loads, (b) displacement transducers for measuring deflections, (c) rotation meters for measuring end rotations, (d) infrared thermometer for measuring surface temperatures, and (e) strain gages to measure longitudinal strains. Additionally, punch mark sets are made on the specimen flanges and the distances between them are measured to further determine the longitudinal strains. All these are described below after defining the terminology used to address the orientations and locations on the beam specimens.

The following terminology (i.e. front and back, left and right, top and bottom) addresses the orientation of the beam specimen. The front of the beam is considered to be the side where the graduate

researcher applies the Vee-heat. Figure 7.9 shows the front of the beam and Figure 7.10 shows the back of the beam. The front of the beam corresponds to Flange B and the back of the beam corresponds to Flange A as shown in Figures 7.9 and 7.10. The left and right sides are distinguished by looking at the setup from the front of the beam. The bottom of the beam is defined where the semi-circular shafts bear against the flanges while damaging. The top of the beam is referred to as the tension side. It is also the region where the Vee-heats are applied.

Pressure Transducers:

Two pressure transducers were used within the hydraulic network. One transducer measured the pressure when the hydraulic actuator pushes upwards (advance mode) and the specimen is being damaged. The force acting on the beam was computed as the measured pressure multiplied by the cylinder area in advance mode specified by the manufacturer (21.63 in^2) and verified (calibrated) by the MSU researcher. The second transducer measured the pressure when the hydraulic actuator pulls downwards (retract mode) and the specimen is being heat straightened. The restraining force acting on the beam was computed as the measured pressure multiplied by the cylinder area in retract mode specified by the manufacturer (13.54 in^2) and verified (calibrated) by the MSU researcher.

Longitudinal Strain Gages

Six strain gages are used to measure the longitudinal strains in the beam specimens during the damage cycles. These strain gages are located at the midspan cross-section of the beam specimen, which also coincides with the location of the damaging force. Three strain gages are bonded to each flange of the steel beam at the midspan section. On each flange, one strain gage is bonded at the top, one strain gage is bonded 3.0 in. (b_f / 3) from the top, and one strain gage is bonded 1.5 in. (b_f / 6) from the bottom. The strain gage orientation is shown in Figure 7.11. The strain gages at the top of the flanges are used to monitor the magnitude of the damage strain (ε_d) during the first damage cycle of each beam specimen. The bottom strain gages are located 1.5 in. from the bottom of the flange to avoid distortion effects due to stress concentrations at the point of loading. The intermediate strain gage (3.0 in. from the top) along with the top and bottom gages establishes a linear strain distribution over the cross-section. These strain gages help to estimate longitudinal strains over the cross-section.

Rotation meters

The end rotations of the beam specimen are measured using four rotation meters, where two rotation meters are placed on either flange and at each end of the beam specimen. These rotation meters are located approximately 6 in. from the support (rotation) points. For example, Figure 7.12 shows the location of a rotation meter with respect to the rotationally free end support for the specimen. These four rotation meters are used to monitor the magnitude and symmetry of the beam end rotations during the damage and heat straightening repair cycles. Since curvatures within the end 6 in. is very small, the difference in actual end rotation and the measured values are almost negligible. The MSU researchers initially intended to use two additional rotation meters to measure the relative rotation of the midspan plastic hinge during the damage and heat straightening repair cycles (refer to Figure 7.9). This would provide a better estimate of the magnitude of repair during each heating cycle. However, problems occurred with the rotation meters becoming too hot during the repair cycles regardless of various insulation techniques attempted.

Displacement transducers

Displacement transducers were used to measure the deflections of the beam specimen during damage and repair cycles. Deflections were measured at the beam midspan and at the quarter points along the length of the beam, which are located 2 ft. from the end supports.

- The midspan deflection was measured using two 12 in. stroke displacement transducers that were placed on either side (front and back) of the beam at midspan. The jig used to connect the

displacement transducers to the beam midspan of the beam is shown in Figure 7.13. The transducers were tied to small steel brackets clamped to the loading beam while damaging [Figure 7.13(a)] and to the bottom of flanges while repairing [Figure 7.13(b)].

- The quarter point deflections were measured using two 6 in. stroke displacement transducers that were placed on either side (right and left) of the beam midspan. The location of these displacement transducers in respect to the test setup are shown in Figures 7.14 and 7.15.
- Thus, a total of four displacement transducers were used. They provided deflection measurements at midspan and quarter points during the various damage and repair cycles.
- The displacement transducers also serve as guides for establishing the completion of heat straightening repair. For multiple damage cycles, they determine the magnitude of damage (explained in Section 7.5.2).

Infrared Temperature Thermometer:

An infrared thermometer was used to measure the time-temperature response of the heated steel beam specimen. This non-contact thermometer was placed perpendicular and away from the heating surface. Figure 7.16 shows a picture of the infrared thermometer away from the heating surface.

Digital caliper and punch marks

The digital caliper was used to measure average longitudinal strains at various locations along the length of the beam. The method is performed for each point by: (1) making punch marks in the beam specimen, (2) measure the original length between punch marks, (3) measure the length between punch marks after damage or repair, and (4) calculate the approximate strain as change in length divided by original length. A total of 20 punch mark sets were made on the flanges of the beam specimens. Ten punch mark sets were made on each of the two flanges of the beam specimens. These included punch mark sets at the midspan (both at the top and bottom of each flange), and at the top of Vee heats R1, R3, R5, L1, L3, and L5, which are explained further in Section 7.5.3.

7.5.2 Experimental Damage Procedure

To subject the beam specimen to the damage magnitude, the hydraulic actuators are set to advance mode. This lifts the loading frame and subjects the beam specimen to bending stresses. Hydraulic oil is pumped out of a 20-series electric pump into the bottom of the hydraulic core actuators. The area of the bottom piston within the hydraulic jack as specified by the manufacturer is 20.63 in^2. With the pressure known, the force acting on the beam is computed using Equation 7.1. This equation was verified (calibrated) earlier by the MSU research team.

$$P_i \text{ (kips)} = \text{pressure (psi)} * 20.63 \text{ (in}^2\text{)} / 1000 \qquad (7.1)$$

The damage of the beam specimen during the first damage cycle was monitored using longitudinal strain gages attached to the top of each flange as shown in Figure 7.11. The load was increased slowly until the strain readings from the top of each flange averaged the required damage strain. The required magnitude of damage strain ε_d was determined from using the measured yield strain ε_y of the undamaged steel as summarized later in Section 7.6.7.1. The researchers planned on using similar longitudinal strain gages for subsequent damage cycles. However, the repaired beam flanges developed small out-of-plane distortions, which resulted in poor strain gage readings. Hence, the subsequent damage cycles after the first one were controlled using the midspan displacement and verified using the quarter displacements and end rotations. The midspan deflections, quarter-span deflections, and the end rotations during the first damage cycle were noted carefully. Subsequent damage cycles were completed when the instruments changed in magnitude with respect to the required amount as interpreted using the measurements from the first damage cycle.

7.5.3 Experimental Repair Procedure

Application of an external restraining stress

Heat straightening repair cycles were conducted by applying an external restraining moment (M_r) of 0. 25 M_p or 0.50 M_p. M_p is the plastic moment capacity of the section about the minor axis of bending. M_p is calculated using Equations 7.2, 7.3, and 7.4 for A7, A36, and A588, respectively, where Z_y is the minor-axis plastic section modulus and σ_y is the measured yield strength of the material. The values of in Equations 7.2, 7.3, and 7.4 for σ_y were determined from uniaxial tension tests conducted on the undamaged material summarized in Section 7.6.1.1.

$$M_p = Z_y \text{ x } \sigma_y = 28.6 \text{ x } 36.6 = 1058.2 \text{ kip-in} \quad \text{(A7)} \tag{7.2}$$

$$M_p = Z_y \text{ x } \sigma_y = 31.7 \text{ x } 46.0 = 1458.2 \text{ kip-in} \quad \text{(A36)} \tag{7.3}$$

$$M_p = Z_y \text{ x } \sigma_y = 31.7 \text{ x } 58.5 = 1854.5 \text{ kip-in} \quad \text{(A588)} \tag{7.4}$$

In applying an external restraining force, hydraulic oil was pumped out of a 20-series electric pump into the top of the hydraulic core actuators. The actuator pulls down on the loading frame. The half-circular shafts contact the flange at points approximately 4.8 in. from the beam center (refer to Figures 7.6 and 7.7). The area of the bottom piston within the hydraulic jack is 13.54 in^2. With the pressure known, the force in the actuator was computed in Equation 7.5. This equation was verified (calibrated) by the MSU research team.

$$\text{P (kips)} = \text{pressure (psi)} * 13.54 \text{ (in}^2\text{)} / 1000 \tag{7.5}$$

The maximum moment applied to the beam was computed assuming that one concentrated force was applied at midspan. The moment at midspan was computed as:

$$M = \frac{PL}{4} \tag{7.6}$$

As presented later, Vee heats were also applied at locations away from midspan. The moment at each of the Vee heat locations was computed using the load *P*. The load required to subject the beam to the level of restraining moment at the center of the Vee heat being heated was applied.

Application of Vee heats along length of the beam

Heating cycles were performed using 5/8 in. diameter oxy-acetylene heating torches. Two researchers used two oxy-acetylene torches and applied Vee heats to both flanges of the beam test specimens. The temperature at the surface of the steel was monitored using an ST80 infrared temperature gun as introduced in Section 4.7.2. Heat-straightening was practiced while maintaining the surface temperature between 1100 ºF and 1200 ºF with the exception of A36-Beam 2 which was practiced to overheating of approximately 1400 ºF. Initially, a spot heat is applied to the apex of the Vee until the desired temperature is reached. The torch is moved in a serpentine path from the apex to the edge of the flange to apply the Vee heat.

Figure 7.17 shows the locations of multiple, overlapping Vee heats used to straighten the damaged beam specimens. These Vee heats are within the center 40 in. length of the beam specimen subjected to plastic strains. The nomenclature used to identify the individual Vee heats is also shown in the figure: the Vee heat located at midspan is identified as C; the Vee heats left of the midspan are L1, L2, L3, L4, and L5, respectively; and the Vee heats right of the midspan are R1, R2, R3, R4, and R5, respectively. In some cases, the researcher also applied Vee heats outside to L6, R6, L7, and R7 if needed. This nomenclature is the same for Vee heats located on either flange (front or back) of the beam specimen, i.e., L1 on the front flange is directly opposite to L1 on the back flange. The Vee heat locations and emphasis (repetitions) of each was aided using a plastic damage region analysis which is described later in Section 7.7.2. Some important details of the Vee heating are indicated below:

- Heat straightening was conducted by heating the same Vee on both flanges simultaneously. Therefore, two persons are heating directly across from each other, and are required to conduct a heating cycle on the damaged specimen.
- The depth and width of each Vee are equal to 4.5 in, which corresponds to a Vee angle of about 53°. These Vee heats are geometrically similar to those used by the Statewide Bridge Crew (SBC). The observations and discussions in Task II (Chapter 3) indicated that the SBC uses half-depth Vees with a width of 5.0 in, which typically results in a Vee angle of about 50°.
- As indicated in Figure 7.17, Vee heats could not be applied close to the restraining load application points, i.e., the points of contact between the steel plates and flanges while heat straightening.

Significant Data Collection during Experimental Investigations

The researchers kept a well organized table of the instrument history for each beam specimen. An example is provided in Table 7.2, which shows the history of the four rotation meters and the four displacement transducers. For the rotation meters, F_L represents Rotation_Front_Left, etc. In Table 7.2, "Contact" represents the point when the setup begins to load the beam. Due to gaps in the test setup, the "Contact" was recorded when the load reached 1 kip, for consistency. The "full damage" represents the amount of movement at the maximum damage load which was recorded such that multiple damage cycles could be completed when the amount of displacements and rotations are equivalent to the first damage cycle. The "plastic damage" represents the amount the researchers have to repair. This table represents the complete damage-repair history of A7-Beam 1.

7.6 MATERIAL TESTING PROCEDURES

7.6.1 Undamaged Material Testing Procedures and Results

This section summarizes the material testing conducted on undamaged steels. These results are compared to the results obtained from the damaged-repaired experimental beam specimens. The material tests included: (a) uniaxial tension tests, (b) fracture toughness tests, (c) hardness tests, and (d) microstructure inspection. As mentioned previously, the A7 steel beam was a W24 x76 and the A588 and A36 steel beam were built up-sections. Samples were taken out of the flanges of the A7 beam and from the plates used for the flanges of the built-up sections.

The original length of the W24x76 A7 steel beam was 23 ft. 3 in. A 3 ft. strip was removed from the beam at the center. Undamaged material testing was conducted by taking samples from this strip. The two beam specimens were fabricated from either side of the undamaged material testing area as shown in Figure 7.2. The plates used for the built-up A36 and A588 steel sections were 20 ft. long. 2 ft. strips were removed from the center of the plates. Undamaged material testing was conducted by taking samples from these strips. The two experiment beams specimens were fabricated from either sides of the undamaged material testing area.

Due to possible variations in the material properties, each side of each flange segment was specified as 1A, 2A, 1B, or 2B. The nomenclature was later altered to TA, BA, TB, and BB where "TA" would represent the top of Flange A (Vee heated side of the back flange). As mentioned previously, when placed in the test setup, the back of the beam refers to Flange A and the front of the beam refers to Flange B. Variability in material properties was evaluated by comparing the results of the uniaxial tension tests and charpy v-notch fracture toughness conducted on samples taken from flange segments TA, BA, TB, and BB.

7.6.1.1 Uniaxial Tension Tests on Undamaged Steel Plates

Four uniaxial tension test coupons were fabricated from the flange segments TA, BA, TB, and BB (one per segment for each steel type). The material coupons were removed within 1 in. of the edge of the flanges as shown in Figure 7.18. The tension coupons were flat bar-type specimens with standard ASTM dimensions as shown in Figure 7.19. These coupons were tested according to ASTM E8 standard.

The resulting uniaxial tension stress-strain (σ–ε) curves for the undamaged A7 steel are shown in Figure 7.20. The corresponding material properties as described in Section 4.9.1(yield stress, elastic modulus, etc.) are summarized in Table 7.3. Table 7.3 and Figure 7.20 indicate that the variability in flange segment (TA, BA, TB, and BB) material properties is insignificant. Table 7.3 also provides the average material properties of all four coupons which will be used for comparisons to the results from damage-repaired steel.

The resulting uniaxial tension σ–ε curves for undamaged A36 steel are shown in Figure 7.21. The corresponding material properties are summarized in Table 7.4. Table 7.4 also provides the average structural properties from each plate (A or B) and also the overall average structural properties. The results of the two material coupons fabricated from each plate (i.e., 1A and 2A or 1B and 2B) related extremely well to each other. Therefore, each test was considered to be validated and further tests were not required. Flange A has a higher yield strength and tensile strength as compared to Flange B. Flange B exhibited a slight increase in ductility. These discrepancies between the two flange plates were considered for the comparisons to experimental results of damage-repaired A36 steel. As explained later, tension coupons were fabricated only from Flange A of the damaged-repaired steel beam specimens. Hence, only the undamaged tension test results of Flange A are required for further comparisons. The overall average structural properties were only used for determining the required damage strain (ε_d) and for applying the external restraining moment (M_r).

The resulting uniaxial tension σ–ε curves for the undamaged A588 steel are shown in Figure 7.22. The corresponding material properties are summarized in Table 7.5. Table 7.5 also provides the average structural properties from each plate (A or B) and also the overall average structural properties. The ultimate stress of flange segment BA was slightly higher (1 ksi) than the ultimate stress of other flange segments. Other than this slight discrepancy, Table 7.5 and Figure 7.22 indicate that the variability in flange segment (TA, BA, TB, and BB) material properties is insignificant. Therefore, the average values of all structural properties will be used for comparisons to damaged-repaired specimens.

7.6.1.2 Charpy Impact Fracture Toughness Tests on Undamaged Steel

Charpy specimens were fabricated from the four flange segments of each undamaged steel type. Five (A36 and A588) or six (A7) mid-thickness charpy specimens were fabricated from each of the flange segments 1A, 2A, 1B, or 2B with the grain orientation shown in Figure 7.22. As shown in Figure 7.22, all specimens were originally located within 3.00 in. from the flange edges. The results of the fracture toughness tests on undamaged A7 steel are summarized in Table 7.6.

Student's t-test analysis was conducted to evaluate the statistical difference between the A7 fracture toughness results from: (a) flange segments BA and TA; (b) flange segments TB and BB; (c) Flange A and Flange B. As mentioned previously in Section 4.9.2, the t-test evaluates the statistical difference between two data sets using their respective means, standard deviations, and sample set sizes. The results from the t-test include the t-value and the corresponding probability of null hypothesis, where the null hypothesis implies that the data sets are statistically similar. Tables 7.7 to 7.9 provide Student's t-tests which compare the results of fracture toughness data sets. Table 7.7 compares the results from segments BA and TA. Table 7.8 compares the results from segments TB and BB. Table 7.9 compares the results from Flange A and Flange B. Statistical similarity exists within each flange (probability that data sets are

statistically similar = 72%) for Flange A and 0.54 for Flange B). Significant statistical difference exists between the results obtained from Flange A and Flange B (probability that data sets are statistically similar = 2%). Higher values with less variation, as evident from the 95% high and low confidence intervals, is found in the results of Flange B. Table 7.10 provides the mean values, standard deviations, values for the high and low limits of the 95% confidence intervals, median values, and absolute average variation from the median for each flange (A or B). As explained later, charpy specimens were fabricated only from Flange B of the damaged-repaired specimens. Hence, only the undamaged results of Flange B will further be used for comparisons.

For the A36 and A588 undamaged fracture toughness results, Student's t-tests were only conducted to evaluate the statistical difference between the two flanges (A and B) and not between the individual results within each flange (i.e. T and B). Discrepancies within the same flange were further assumed to be insignificant.

The results of the fracture toughness tests on undamaged A36 are provided in Table 7.11. Overall, the fracture toughness results of both A36 steel plates are quite low. Statistical difference again exists between the results obtained from Flange A and Flange B. Higher values with more variation, as evident from the 95% confidence intervals, are found in the results of Flange B. Table 7.12 provides the statistical properties computed for each flange (A or B). Table 7.13 provides the results of a Student's t-test that compares the fracture toughness values obtained from Flange A and Flange B. The results of Student's t-test indicate that the statistical difference between the flanges is not as significant (probability that data sets are statistically similar = 17%) as for the A7 specimens. The statistical difference is significant enough such that the charpy impact results from each flange will still be treated separately for comparing to damage-repaired specimens.

The results of the fracture toughness tests on undamaged A588 are provided in Table 7.14. Statistical difference again exists between the results obtained from Flange A and Flange B. This result was surprising since the rest of the material properties related extremely well. Higher values with more variation, as evident from the 95% confidence intervals, are found in the results of Flange A. Table 7.15 provides the statistical properties computed for each flange (A or B). Table 7.16 provides the results of a Student's t-test that compares the fracture toughness values obtained from Flange A and Flange B. The result of Student's t-test for the A588 charpy data is very similar to the A36 result (probability that data sets are statistically similar = 10%). The statistical difference is significant enough such that the charpy impact results from each flange will still be treated separately for comparing to damage-repaired specimens.

7.6.1.3 Rockwell Hardness and Microstructure Investigations

The procedures for conducting Rockwell Hardness tests and also investigating the microstructure of steel were introduced in Sections 4.9.3 and 4.9.4, respectively. The procedures did not alter in between Task III and Task IV. One specimen from each flange for each steel type was prepared as specified by ASTM E3 standard. The charpy specimens used were taken from flange segments 2A and 2B and are labeled 2 in Figure 7.19. This specimen is the second outermost specimen with respect to the end of the plate. Rockwell hardness tests were conducted according to ASTM E18. Four hardness tests were conducted on each charpy specimen and the average value was considered to represent the overall hardness of the undamaged flange plates. The results of the Rockwell Hardness tests are shown later in Chapter 8 with the corresponding damaged-repaired A7, A36, and A588 specimens in Table 8.8. Table 8.8 also provides comparisons between the approximate ultimate strengths as estimated by ASTM A370 to the actual ultimate strengths. The results from Flange B will be used for normalized comparisons to the results from the damaged-repaired specimens.

In comparing the two A7 flange plates, the hardness of Flange B is higher than the hardness of Flange A. In comparing the two A36 flange plates, the hardness of Flange B is slightly lower with less statistical

variation than Flange A. The two A588 plates compare considerably well to each other. The ASTM approximate tensile strengths are somewhat low for A7 and A36 and compare favorably well with the actual tensile strengths for A588.

The grain sizes were determined using the general line intercept procedure in ASTM E112 standard. Most microstructure pictures were taken at 480X for each steel type. An exception was for Flange A of A7 which was taken at 240X. The resulting microstructures on undamaged A7, A36, and A588 steel specimens are shown in Figure 7.23. The resulting grain sizes and percentages of pearlite grains are shown with the experimental results of damage-repaired specimens in Table 8.9. As discussed in Section 4.9.4, a more fine-grained microstructure is generally stronger and tougher than a more coarse-grained microstructure. There is a slight increase on the surface hardness and a slight decrease on the ductility. A microstructure that is more pearlitic is harder, stronger, and more brittle. However, only significant and consistent changes in the percent pearlite would be further analyzed as the amount is related to the location taken for the picture as discussed in Section 2.4.3. The results are provided in Table 8.8 for completeness.

In comparing the two A7 flanges, the grain size of Flange B was smaller than the grain size of Flange A. A higher percentage of pearlite was also noticed for Flange B in Figure 7.23(b) and Table 8.8. In comparing the two A36 flange plates, a higher amount of pearlite was found in Flange A which is likely related to the higher strength and less ductility of Flange A. The two A588 plates have very similar microstructures. This relates well to the similarities of other material properties.

7.6.2 Damage-Repaired Material Testing Procedure

This section describes the material specimens and testing for damaged-repaired beam specimens. Charpy v-notch specimens were removed from the front flange (Flange B) and uniaxial tension coupons were removed from the back flange (Flange A) for each damaged-repaired beam specimen.

Three uniaxial tension specimens were removed from Flange A of each beam specimen. The dimensions of the uniaxial tension coupons were given in Figure 7.19. All three were removed from Vee heated region (*C*) at midspan. The MSU machinist was instructed to remove all three specimens as close to the edge of the flange as possible within a maximum distance of 2.5 in. The location of the uniaxial tension coupons in the top half of the flange is shown in Figure 7.24. The nomenclature used for each uniaxial tension coupon is also shown in Figure 7.24, where X represents the outermost coupon, Y represents the center coupon, and Z represents the innermost coupon. The reduced sections of all three uniaxial tension coupons lie within the center Vee heat.

The tests conducted on the charpy specimens included fracture toughness tests, Rockwell hardness tests, and microstructure investigations. The charpy specimens were removed from the three Vee heats (i.e. *C*, *L1*, and *R1*) located at the midspan of each beam. The charpy specimens were removed in three columns of four specimens with the notches located along the centerline of each of the three Vee heat locations (i.e. *C*, *L1*, and *R1*). The charpy specimens were removed within a distance of 2.25 in. (b_f/ 4) of the flange edge. The location of the fracture toughness specimens with respect to the top half of the flanges where the Vee heats are applied are shown in Figure 7.25. Figure 7.25 shows that the v-notches open towards to top of the flange similar to the undamaged specimens. The nomenclature used for each specimen is indicated in Figure 7.25. Rockwell hardness tests and microstructure investigations were conducted on charpy Specimen C-2. This specimen is the second outermost specimen in respect to the end of the plate and is located directly at midspan. The undamaged charpy specimen used was also the second outermost specimen in respect to the edge of the flange.

7.7 ANALYTTICAL FIBER-BASED MODEL OF BEAM SPECIMENS

The beam specimen is damaged by a concentrated force acting at midspan. This causes a linear moment gradient along the length of the beam and maximum moment at midspan. As the concentrated force increases, yielding occurs at the midspan and then spreads along the length of the beam. As the material undergoes strain hardening, yielding or plasticity spreads further along the length of the beam. A significant portion of the beam length undergoes plasticity before the target damage strain (ε_d) is achieved at the midspan section. The damaged beam will be repaired by heat straightening, where Vee heats must be applied in the regions of the beam subjected to plastic strains during damage. The region of the beam subjected to plastic strains during damage can be calculated as follows:

- The maximum force (P) required to achieve the damage strain (ε_d) at the midspan section is obtained experimentally from the damage cycle.
- The moment at any location along the length of the beam is equal to $P\ x\ /2$, where x is the distance from the support. Maximum moment at midspan is equal to $P\ L/4$
- Inelastic strains or yielding will occur when the moment $P\ x\ /2$ exceeds the yield moment for the section M_y, which can be calculated as $S_x\ \sigma_y$.
- Therefore, plastic strains will occur in the beam after a distance x from the supports, Where, $x = S_x\ \sigma_y\ 2\ /\ P$

This method provides an estimate of the beam region subjected to yielding (or plastic strains), but it does not provide any information regarding the magnitude and distribution of plastic strains with the damage region. Therefore, a more advanced analysis tool (section fiber analysis) was used to determine the magnitude and distribution of plastic strains within the damage region.

7.7.1 Fiber Models of the Beam Specimens

Fiber models of the beams specimens subjected to weak axis damage were developed using MATLAB version 6.5. In the fiber model, the steel cross-section is discretized into a number of steel web and flange fibers as illustrated in Figure 7.26. Each fiber has an area (A_f), distance from the neutral axis (y_f) measured from the centroid of the section, and an implemented uniaxial stress-strain (σ - ε) curve. The fiber σ-ε responses are integrated over the cross section to obtain the section force-deformation (moment-curvature) response. The amount of fibers used to discretize the cross-section and the accuracy of the σ-ε relationship govern the accuracy of the fiber based model. In the fiber based model, 100 fibers were used to discretize each flange and 20 fibers were used to discretize the web.

The fiber model is initiated assuming a range of varying curvature (ϕ) at midspan and a linear strain distribution as shown in Figure 7.27(a). The average strain in each fiber (ε_f) is computed as the curvature multiplied by the distance from the neutral axis y_f [see Figure 7.27(b)]. The average stress in each fiber (σ_f) is computed using the σ-ε relationship derived from uniaxial tension tests conducted on the undamaged material as in Figure 7.27(c). The material σ-ε curve is idealized into three separate regions; elastic, yield plateau, and strain hardening as shown in Figure 7.28 for the undamaged A7 material. If the strain in the fiber was computed to be less than the yield strain (ε_y), the averaged stress in the fiber was computed using Equation 7.7. If the strain was computed to be greater than εy but less than the strain at the offset of strain hardening ε_{sh}, then the stress in the fiber was identified as σ_y.

$$\sigma_f = \varepsilon_f \text{ x E} \tag{7.7}$$

Fifth-order trend line equations were determined using Microsoft Excel 2003 to predict the stress as a function of the strain in the strain-hardening region, which is shown for undamaged A7 in Figure 7.29. If the strain in the fiber was computed to be higher than ε_{sh}, then the average stress in the fiber is computed

using this fifth order equation or similar for the strain hardening of the A36 and A588 uniaxial σ-ε relationships.

The force contribution of each fiber (F_f) is computed by multiplying the average stress (σ_f) and the area of each fiber (A_f). The moment induced to the cross-section is computed as a sum of the each force multiplied by the distance from the centroidal axis (y_f) as in Equations 7.8 and 7.9. Varying the curvature develops a moment-curvature response of the section which is shown for the W24x76 A7 beam specimen in Figure 7.30. Figure 7.30 also shows the moment curvature relationship assuming an elastic-perfectly plastic σ-ε relationship as usually assumed by AISC for comparisons.

$$F_f = \sigma_f \text{ x } A_f \tag{7.8}$$

$$M = \sum F_f \, x \, y_f \tag{7.9}$$

7.7.2 Plastic Damage Region and Magnitudes

The maximum moment required to achieve the damage strains (ε_d) for each beam was determined using the fiber models. A linear moment distribution is assumed to each support, where the moment at the support is zero. Using an interpolation scheme of the moment-curvature response of the section, the curvature along the length of the beam is calculated. In the fiber analysis using MATLAB, the curvature was computed using interpolation at 1001 points from the support to midspan. The strain in each fiber along the length of the beam is computed as a multiplication of the curvature obtained from interpolation and the distance from the centroidal axis (y_f). The stress in each fiber along the length of the beam is computed using the uniaxial σ-ε relationship as described in Section 7.7.1. The plastic strain is computed in each fiber using Equation 7.10.

$$\varepsilon_{plastic} = \varepsilon - \frac{\sigma}{E} \tag{7.10}$$

Figure 7.31 shows the magnitude and distribution of maximum plastic strains at the top of the flanges of the A7 steel W24x76 beam specimen. The plastic strain distributions are shown for three levels of damage, i.e., when the midspan damage strain ε_d reaches: (a) 30 ε_y, (b) 60 ε_y , and (c) 90 ε_y.

Figure 7.32 shows the magnitude and distribution of maximum plastic strains at the top of the flanges of the A36 steel built-up beam specimen. The plastic strain distribution is shown only for a midspan maximum strain of 30 ε_y since it was the only ε_d for A36 beam specimens. For the A36 beam, the σ-ε relationships of both flanges were taken into consideration. However, the discrepancies in the resulting plastic strain distributions were negligible. The web was assumed to have the σ-ε relationship of Flange B. Figure 7.33 shows the magnitude and distribution of maximum plastic strains at the top of the flanges of the A588 built-up beam specimen. The plastic strain distributions are shown for both damage strain levels, i.e., when the midspan damage strain (ε_d) reaches: (a) 20 ε_y and (b) 40 ε_y. The web was assumed to have the σ-ε relationship as Flange B of the A36 material. As shown in Figures 7.31 and 7.33, larger damage strains results in greater magnitudes and distribution of plastic strains along the length of the beam. Figures 7.31 and 7.33 clearly indicate the need for several Vee heats within the region of the beam subjected to plastic strains.

Figures 7.34, 7.35, and 7.36 show the magnitudes of plastic strains along half the width (tension strains) of the flange at the center of each Vee-heat location for the A7 beams for maximum damage strains of 30 ε_y, 60 ε_y, and 90 ε_y, respectively. The plastic strains for a symmetric Vee-heat location on the opposite side of centerline (i.e. L1 in relation to R1) would be the equivalent. Figure 7.37 show the magnitudes of plastic strains along half the width (tension strains) of the flange at the center of each Vee-heat location for the A36 beams with a maximum damage strain of 30 ε_y. Figures 7.38 and 7.39 show the

plastic strains induced along half the width (tension strains) of the flange at the center of each Vee-heat location for the A588 beams for damage strain of 20 ε_y and 40 ε_y, respectively.

7.7.3 Residual and Restraining Stress Computations

The fiber-based model was further used to compute the induced residual stresses along the length of the beam after damage. The induced residual stresses are significant for determining the actual restraining stress induced to the locations of the removal of each charpy and tensile specimen. In the fiber-based model, the stress in each fiber of the cross-section along the length of beam at the maximum damage strain was computed. The beam unloads elastically assuming Hooke's Law. The unloading stress in each fiber is computed using Equation 7.11; where M is the moment at a point along the length of the beam, c is the distance from the neutral axis of the cross section, and I_y represents the moment of inertia of the cross section about the weak axis.

$$\sigma_{unload} = \frac{Mc}{I_y} \tag{7.11}$$

The induced residual stresses are computed as the damage stress minus the unloading stresses. An example is shown in Figure 7.40 [*1*]. Figure 7.40(a) gives the stress-strain profile of a steel plate subjected to pure bending as shown in Figure 7.40(b). As the plate is bent so that the stresses in the section exceed the elastic capacity, then the curves *AO* and *OA'* would represent the compressive and tensile stresses along the height of the member. Assuming the material follows Hooke's law, it will follow the unloading stress distribution represented by the lines *BO* and *OB'* given by Equation 7.11. Note that the moment required to bend the beam as represented by the stress-distribution *AOA'* is equal to the moment represented by *BOB'* when assuming linear-elastic bending behavior. The resulting residual stresses are found by subtracting the unloading stress-distribution from the bending stress. The final residual stress distribution is shown in Figure 7.40(b) represented by the curve *COC'*.

Residual stresses were computed along the cross-section at every fiber along the length of each experimental beam specimen. This includes 100 fibers along the 9 in. width of the flange at 1001 points from the support to midspan. The residual stresses along the center of the Vee heat locations (i.e., C, R1, L1, L2, R2, etc) were arranged and plotted. The fiber analysis was further verified at a distance of 2 ft. from the support end, which did not undergo plasticity. The residual stresses in the cross section were computed to be zero.

Prior to repairing the beam specimens, they are subjected to an external restraining moment (M_r) of either 0.25 M_p or 0.50 M_p. The actual restraining stress at each fiber along the cross-section is computed as the addition of the elastic reloading stress and the induced residual stresses after damage and unloading. The elastic reloading stress is computed using Equation 7.11 with compressive stresses at the top and tensile stresses at the bottom.

For beam specimens subjected to restraining moments of 0.50 M_p, the restraining stresses in some fibers were computed higher than the yield stress (σ_y). For restraining stresses computed higher than σ_y, the restraining strains were required in order to use the implemented σ-ε relationship of the material. The residual strains were assumed to be equal to the residual stresses divided by the elastic modulus. The additional reloading strains were assumed to be equal to the elastic reloading stresses divided by the elastic modulus. The restraining strains in the fibers were computed as the addition of the residual strains and the reloading strains. All strain values computed higher than the yield strain (ε_y) were found to be less than ε_{sh}. Therefore, no restraining stresses were computed higher than σ_y.

A few examples of the damage-repair stress history are provided in Figures 7.41 to 7.43. The results along the center Vee heat (*C*) of the A36 beam subjected to a damage strain of 30 ε_y at the extreme tension fiber and an external restraining moment of 0.25 M_p are shown in Figure 7.41. The damage

stresses, unloading stresses, residual stresses, reloading stresses, and final restraining stresses are all shown in Figure 7.41. The restraining stresses at the ends of the beam specimen are as high as 40.8 ksi, which corresponds to approximately 88.7 % of the yield stress. The results along the cross-section of the furthest Vee heat (*R5*) for the same beam specimen are shown in Figure 7.42. The stress results away from the center of the beam are not as significant. The results along the center Vee heat (*C*) of the A7 beam subjected to a damage strain of 90 ε_y at the extreme tension fiber and an external restraining moment of 0.50 M_p (first damage-repair cycle of A7-Beam 2) is shown in Figure 7.43. The restraining stresses at the ends of the specimen are equal to the yield stress (36.25 ksi).

The restraining moment of 0.50 M_p subjects the beam specimens to significantly high restraining stresses. The results of the fiber analysis indicate that the steel is being cold worked at the edges before applying heat.

7.7.4 Damage Strain-Restraining Stress History of Each Material Coupon

This section provides a summary of the analytical damage strain (ε_d) and restraining stress (σ_r) subjected to each charpy and tensile coupon. The ε_d and σ_r were computed at the center of each coupon using analytical fiber analysis as described in Sections 7.7.2 and 7.7.3, respectively. For multiple damage-repair cycles, the values are nominal, since residual stresses after repair were not taken into consideration.

Charpy specimens 1, 2, 3, and 4 (for L1, C, and R1) were assumed to be at a distance from the edge of the flange of 0.322 in., 0.841 in., 1.360 in., and 1.879 in., respectively. These distances assume 1/8 in. gaps from the flange end and between each charpy specimen. The results of fiber analysis for the ε_d and σ_r history of each charpy specimen are provided for each damage-repair cycle of all beam specimens in Table 7.17.

Uniaxial tensile coupons X, Y, and Z were assumed to be at a distance of 0.4375 in., 1.2500 in., and 2.0625 in. from the flange end, respectively. These distances assume 1/16 in. gaps from the flange end and in between each coupon. The results of fiber analysis are provided for each damage-repair cycle of all beam specimens in Table 7.18.

In Tables 7.17 and 7.18, the damage strains (ε_d) are given as a ratio to the yield strain (ε_y). The damage strains include the elastic strains before unloading. The restraining stresses (σ_r) are provided as a percentage of the yield stress (σ_y).

7.7.5 Validation of Fiber Based Model with Experimental Data

Figures 7.31-7.39 of Section 7.7.2 were used as guidance to the researchers in how much emphasis (repetition) should be applied to each Vee heat location within the plastic damage region. The curvature and plastic strain distributions along the length could not be experimentally measured. In order to validate the plastic strain distributions, the fiber model was enhanced using MATLAB version 6.3 to compute the load-strain (P-ε), the load-rotation (P-θ), and the load-displacement (P-Δ) behavior of the beam specimens. The load, strain at the extreme tension fiber, end rotations, quarter displacements, and the center displacement were all measured during the experiments using instruments described in Section 7.5.1.

In the fiber analyses, the range of curvature was specified and the moment at every curvature increment was computed as described in Section 7.7.1. The strain at the extreme tension fiber was computed using Equation 7.12:

$$\varepsilon = \phi \; x \; \frac{b_f}{2} \tag{7.12}$$

As mentioned in Section 7.7.2, the load is applied at midspan and a linear moment distribution is assumed to the end support. The load required to cause this moment distribution was computed using Equation 7.13:

$$P = \frac{4M}{L} \tag{7.13}$$

Figure 7.44 shows a comparison between the P-ε behaviors of the first damage cycle of A7-Beam 1 to the results of the fiber analysis. The experimental P-ε behavior compares favorable well with the analytical results.

The curvature along the length of the beam can be expressed by some function of the beam length $\phi(x)$. In the fiber analysis, the curvature at 1001 points was found from the beam midspan to the support. A numerical integration of the curvature-length $\phi(x)$ function can be used to find the rotation at any point along the length of the beam. The change in rotation within any length along the length of the beam is computed using Equation 7.14 where the variable C is a constant:

$$\theta(x) = \int \phi(x)dx + C \tag{7.14}$$

Within a finite length, the change in rotation is represented by the area along that strip underneath the $\phi(x)$ function. In the fiber analysis, the change in rotation within a finite length was found using a trapezoidal rule using two points of curvature at both ends of the finite length; taking the average of the two points and multiplying the average by the finite length. An illustration of the trapezoidal rule is shown in Figure 7.45 where h represents the finite length. The change in rotation within length h can be computed using Equation 7.15.

$$\Delta\theta_h = \frac{\phi_1 + \phi_2}{2} x\ h \tag{7.15}$$

The change in rotation along the length of the beam was added to the previous to find the full change rotation at every length increment. With the given loading and boundary conditions, it is known that the rotation is decreasing and is zero at midspan. The constant C is therefore computed as the value for the full change in rotation computed at midspan. The vector which forms for each point for the full change in rotation along the length is subtracted from this value. This process is repeated for each value of implemented curvature at midspan to develop the P-θ response at any point along the beam length.

The vertical displacement of each point is found by numerically integrating the rotation function in a similar fashion. The displacement at any point along the length of the beam is computed using Equation 7.16 where the variable C is a constant:

$$\Delta(x) = \int \theta(x)dx + C \tag{7.16}$$

With the given loading and boundary conditions, it is known that the constant C is equal to the end displacement which is zero. In the fiber analysis, the change in displacement within each length increment was found using Riemann's integration rule; taking each point of rotation and multiplying it by the finite length. An illustration of implementing Riemann's rule is shown in Figure 7.46 where h represents the finite length. Figure 7.45 in comparison to Figure 7.46 indicates that Riemann's rule is not as accurate as the trapezoidal rule. However, Riemann's rule was determined to work as sufficiently as the trapezoidal rule because enough increments along the beam length were used (each finite area under the curve was computed within a length of 0.0485 in). The changes in displacements are added to the previous to compute the full change in displacement at each point. This process is repeated for each value of implemented curvature at midspan to develop the P-Δ response at any point along the beam.

Figure 7.47 provides comparisons between the P-Δ relationships derived from fiber analysis and the experimental behavior of A7-Beam 1 (damage cycle 1). The comparisons include the displacement at the center of the beam as well as the displacement at the quarter point (at L/4 from the support). The analytical and experimental results compare well to each other. The right quarter point displacement indicates a better comparison than the center displacement. The experimental stiffness of the center displacement is not as steep as the stiffness of the fiber analysis. This behavior is due to the small indentions which occur in the steel at the point of contact. The analytical elastic P-Δ compares well with equations from beam theory. Figure 7.48 provides a comparison of the P-θ relationships derived from fiber analysis and from the experimental behavior of A7-Beam 1. The P-θ relationships compare extremely well to each other.

Figure 7.49 provides comparisons between the P-Δ relationships derived from the fiber analysis and the experimental behavior of A7-Beam 2 (damage cycle 1). The results include the displacements at the center of the beam as well as at the quarter point (at L/4 from the support). The analytical and experimental results compare extremely well at low values of displacement and favorably well as the displacements increase. The discrepancies at higher displacements are likely due to the implemented σ–ε for the web. The web was assumed to have the same σ–ε behavior as the flange since undamaged material coupons were not removed from the web. The web fibers yielded in the fiber analysis at higher displacements. Figure 7.50 shows a comparison of the P-θ derived from the fiber analysis and the experimental behavior of A7-Beam 2. The P-θ relationships compare better than the P-Δ relationships but discrepancies still exist at higher values of rotation. Since the known A7 experimental behavior compares well with analytical predictions, it is assumed that the analytical plastic strain distribution along the length of the beam is a good approximation of the actual being induced to the beam specimens.

Figure 7.51 provides comparisons between the P-Δ relationships derived from the fiber analysis and the experimental behavior of A36-Beam 1 (damage cycle 1). For the A36 beam, the σ–ε relationships of both flanges were considered. The web was assumed to have the σ–ε relationship of Flange B. The results include the displacement found at the center of the beam as well as the displacement at the quarter point (at L/4 from the support). The analytical and experimental results compare favorably well to each other. Again, the experimental elastic stiffness is likely found to be lower due to indentions that form at the contact points. Figure 7.52 provides a comparison of the P-θ behaviors derived from fiber analysis and that of A36-Beam 1. The P-θ relationship once again compares better than the P-Δ relationships.

Since the known A36 experimental behavior compares well with analytical approximations, it can be assumed that the analytical plastic strain distribution along the length of the beam is a good approximation of the actual being induced in the beam specimens.

Figure 7.53 provides comparisons between the P-Δ relationships derived from the fiber analysis and the experimental behavior of A588-Beam 1 (damage cycle 1). The web was assumed to have a stress-strain relationship as A36-Flange B. The analytical and experimental results compare favorably well to each other but not as well as in the A36 and A7 cases. The analytical stiffness was matched against equations from beam theory in the elastic region and was determined to be accurate. Again, the experimental stiffness at the center is likely found to be lower due to indentions that form at the contact points. The reason for discrepancies of the elastic stiffness at the quarter point is unknown. Figure 7.54 provides a comparison of the P-θ behaviors of the fiber analysis and that from the experimental behavior of A588-Beam 1. The P-θ relationships once again compare better than the P-Δ relationships.

Although the experimental and analytical results do not compare as well for A588, the analytical plastic strain distribution along the length of the beam is likely a good approximation of the actual values being induced to the beam specimens.

7.8 REFERENCE

1. Almen, J. O., and Black , P. H., *Residual Stresses and Fatigue in Metals*, McGraw Hill Book Company, Inc., New York, 1964.

Table 7.1
Experimental test matrix for large-scale beam specimens

Specimen Name	*Cycle Number*	*Damage Strain (ε_d)*	*Approx. Plastic Displacement (in)*	*Restraining Moment (M_r)*	*Maximum Temperature (T_{max})*
A7-Beam 1	1	30 ε_y	2.2	0.25 M_p	1200 ºF
	2	30 ε_y	2.2	0.50 M_p	
	3	30 ε_y	2.2	0.25 M_p	
A7-Beam 2	1	90 ε_y	8.5	0.50 M_p	1200 ºF
	2	60 ε_y	5.5	0.50 M_p	
	3	60 ε_y	5.5	0.50 M_p	
A36-Beam 1	1	30 ε_y	3.1	0.25 M_p	1200 ºF
	2	30 ε_y	3.1	0.50 M_p	
	3	30 ε_y	3.1	0.25 M_p	
A36-Beam 2	1	30 ε_y	3.1	0.25 M_p	1400 ºF
	2	30 ε_y	3.1	0.50 M_p	
	3	30 ε_y	3.1	0.25 M_p	
A588-Beam 1	1	40 ε_y	4.9	0.25 M_p	1200 ºF
	2	20 ε_y	2.1	0.25 M_p	
	3	20 ε_y	2.1	0.25 M_p	
A588-Beam 2	1	40 ε_y	4.9	0.50 M_p	1200 ºF
	2	20 ε_y	2.1	0.50 M_p	
	3	20 ε_y	2.1	0.50 M_p	

Table 7.2
Instrument history during the experimental investigations of A7-Beam 1

	Rot. 1	Rot. 2	Rot. 3	Rot. 4	LVDT	LVDT	LVDT	LVDT
	F_L	B_L	B_R	F_R	6 Left	6 Right	12 Fron	12 Back
Damage 1								
Contact of Damage 1	1.4111	1.3029	-0.6336	1.9574	1.8330	0.5560	0.3114	0.6452
Peak of Damage 1	-2.8070	-1.4818	2.3953	6.2668	3.8055	2.5260	3.7714	4.1006
End of Damage 1	-2.0342	-1.2545	2.1355	5.4771	3.3314	2.0933	2.6215	2.7836
Full Damage	-4.2180	-2.7847	3.0289	4.3094	1.9725	1.9700	3.4600	3.4554
Plastic Damage	-3.4452	-2.5574	2.7691	3.5197	1.4984	1.5373	2.3101	2.1384
Repair 1								
Start of Repair 1	-2.0342	-1.2545	2.1355	5.4771	3.3314	2.0933	5.2978	3.3525
End of Repair 1	1.4080	-	-	2.0085	1.8847	0.5086	2.5876	0.6331
Repair	3.4422	-	-	-3.4686	-1.4467	-1.5847	-2.7103	-2.7194
Damage 2								
Contact of Damage 2	1.3961	-2.0708	4.4942	1.9940	2.0037	0.6282	0.8398	3.1811
Peak of Damage 2	-2.3583	1.6206	0.7016	5.8066	3.6440	2.2952	3.5324	5.8786
End of Damage 2	-1.4688	0.7402	1.6088	4.9086	3.1120	1.7888	2.8325	5.1426
Full Damage	-3.7544	3.6915	-3.7926	3.8126	1.6404	1.6671	2.6926	2.6974
Plastic Damage	-2.8649	2.8110	-2.8854	2.9146	1.1083	1.1607	1.9926	1.9614
Repair 2								
Start of Repair 2	-1.4688	0.7402	1.6088	4.9086	3.1069	1.7786	4.4850	6.7212
End of Repair 2	1.3971	-2.0605	4.4790	1.9650	1.8220	0.4975	2.3587	4.4152
Repair	2.8659	-2.8006	2.8702	-2.9436	-1.2849	-1.2811	-2.1263	-2.3060
Damage 3								
Contact of Damage3	1.3971	-2.0605	4.4790	1.9650	1.8220	0.4975	0.8430	2.8560
Peak of Damage 3	-2.3981	1.4269	0.8782	5.7333	3.2496	2.2763	3.5277	5.5915
End of Damage 3	-1.5007	0.4814	1.7874	4.7710	2.7363	1.7632	2.8323	4.8749
Full Damage	-3.7952	3.4874	-3.6008	3.7683	1.4276	1.7787	2.6847	2.7356
Plastic Damage	-2.8978	2.5419	-2.6916	2.8060	0.9143	1.2657	1.9893	2.0189
Repair 3								
Start of Repair 3	-1.4290	0.5232	1.8685	4.7831	2.6910	1.7261	4.2971	6.3577
End of Repair 3	1.3482	-2.0446	4.4350	1.8649	1.6761	0.4739	2.1602	4.5338
Repair	2.7771	-2.5677	2.5665	-2.9183	-1.0149	-1.2522	-2.1368	-1.8239

Table 7.3
Structural properties of undamaged A7 steel

Specimen	BA	TA	BB	TB	Average
Upper σ_y (ksi)	37.8	36.7	37	37.2	37.2
Lower σ_y (ksi)	35.4	36	36.3	35.5	35.8
Plateau σ_y (ksi)	36.7	36.5	36.5	36.6	36.6
E (ksi)	30220	31086	30520	30193	30505
ε_y	0.00121	0.00117	0.00120	0.00121	0.00120
σ_t (ksi)	61	61.7	61.3	61.6	61.4
ε_u	0.233	0.216	0.234	0.211	0.224
ε_u / ε_y	191.9	184	195.7	174.1	186.4
% Elongation	41.97	42.84	41.67	41.38	41.96
% Reduction	62.69	62.56	62.5	62.27	62.51
$30\ \varepsilon_y$	0.036	0.035	0.036	0.036	0.036
$60\ \varepsilon_y$	0.073	0.07	0.072	0.073	0.072
$90\ \varepsilon_y$	0.109	0.106	0.108	0.109	0.108

Table 7.4
Structural properties of undamaged A36 steel

	BA	TA	Avg A	BB	TB	Avg B	Average
Upper σ_y (ksi)	48.7	48.6	48.7	46.7	46.5	46.6	47.6
Lower σ_y (ksi)	45.5	46.7	46.1	44.3	44.1	44.2	45.2
Plateau σ_y (ksi)	46.6	46.9	46.8	45.1	45.3	45.2	46.0
E (ksi)	29554	31541	30547	31499	30886	31193	30870
ε_y	0.00158	0.00149	0.00153	0.00143	0.00147	0.00145	0.00149
σ_u (ksi)	75.1	75.1	75.1	71.6	71.6	71.6	73.4
ε_u	0.191	0.191	0.191	0.197	0.193	0.195	0.193
ε_u / ε_y	121.13	128.45	124.79	137.59	131.59	134.59	129.69
% Elongation	36.94	36.77	36.85	38.85	39.26	39.06	37.95
% Reduction	60.72	58.56	59.64	62.02	61.72	61.87	60.75
$30\ \varepsilon y$	0.0473	0.0446	0.0460	0.0430	0.0440	0.0435	0.0447

Table 7.5
Structural properties of undamaged A588 steel

	BA	TA	Avg A	BB	TB	Avg B	Average
Upper σ_y (ksi)	59.4	60.0	59.7	60.2	60.5	60.4	60.0
Lower σ_y (ksi)	58.1	58.2	58.2	57.1	57.7	57.4	57.8
Plateau σ_y (ksi)	59.0	58.5	58.8	58.3	58.0	58.2	58.5
E (ksi)	30208	29837	30022	29280	30453	29867	29945
ε_y	0.00195	0.00196	0.00196	0.00199	0.00190	0.00195	0.00195
σ_u (ksi)	85.4	84.3	84.9	84.3	84.1	84.2	84.5
ε_u	0.144	0.144	0.144	0.143	0.143	0.143	0.144
ε_u / ε_y	73.73	73.44	73.59	71.82	75.08	73.45	73.52
% Elongation	36.17	35.16	35.66	34.74	35.62	35.18	35.42
% Reduction	69.96	68.79	69.37	69.41	69.09	69.25	69.31
20 εy	0.0391	0.0392	0.0391	0.0398	0.0381	0.0390	0.0390
40 εy	0.0781	0.0784	0.0783	0.0796	0.0762	0.0779	0.0781

Table 7.6
Fracture toughness results of undamaged A7 steel

Specimen	BA	TA	BB	TB
1	73	61	73	67
2	78	82	86	72
3	58	55	75	60
4	52	28	50	90
5	27	40	66	67
6	44	42	84	48
Mean	55.3	51.33	72.33	67.33
Std. Dev.	18.8	19.01	13.19	13.88

Table 7.7
Student's t-test results comparing the means of data sets in Table 7.6 (BA and TA)

t-test to establish the statistical difference between the fracture toughness of A7 charpy specimens from BA and TA
Results of unpaired t-test (see Section 4.9.2):
t=0.366
Std. deviation=18.9
Degrees of freedom=10
Probability of null hypothesis (the data sets are statistically similar) = 0.72

Table 7.8
Student's t-test results comparing the means of data sets in Table 7.6 (BB and TB)

t-test to establish the statistical difference between the fracture toughness of A7 charpy specimens from BB and TB
Results of unpaired t-test (see Section 4.9.2):
t=0.64
Std. deviation=13.5
Degrees of freedom=10
Probability of null hypothesis (the data sets are statistically similar) = 0.54

Table 7.9
Student's t-test results comparing the means of data sets in Table 7.6 (Flange A and Flange B)

t-test to establish the statistical difference between the fracture toughness of A7 charpy specimens from Flange A and Flange B
Results of unpaired t-test (see Section 4.9.2):
t=2.55
Std. deviation=15.9
Degrees of freedom=22
Probability of null hypothesis (the data sets are statistically similar) = 0.018

Table 7.10
Statistical values of undamaged A7 fracture toughness of both flanges

Statistical Property	Flange A	Flange B
Mean	53.3	69.8
Std. Dev.	18.2	13.2
95% High	64.88	78.2
95% Low	41.79	61.47
Median	53.5	69.5
Average Absolute From Median	14.5	10.2

Table 7.11
Fracture toughness results of undamaged A36 steel

Specimen	BA	TA	BB	TB
1	41	51	75	62
2	46	47	60	44
3	38	35	36	38
4	41	40	48	39
5	44	35	35	45
Mean	42	41.6	50.8	45.6
Std. Dev.	2.76	6.44	15.14	8.64

Table 7.12
Statistical values of undamaged A36 fracture toughness of both flanges

Statistical Property	Flange A	Flange B
Mean	41.8	48.2
Std. Dev.	5.22	13.3
95% High	45.54	57.7
95% Low	38.06	38.7
Median	41.0	44.5
Average Absolute From Median	4.0	13.3

Table 7.13
Student's t-test results comparing the means of data sets in Table 7.12 (Flange A and Flange B)

t-test to establish the statistical difference between the fracture toughness of A36 charpy specimens from Plate A and Plate B
Results of unpaired t-test (see Section 4.9.2):
t=1.42
Std. deviation= 10.1
Degrees of freedom=18
Probability of null hypothesis (the data sets are statistically similar) = 0.17

Table 7.14
Fracture toughness results of undamaged A588 steel

Specimen	1A	2A	1B	2B
1	96	99	85	99
2	125	99	94	96
3	100	100	95	87
4	110	107	84	106
5	101	90	110	101
Mean	106.4	99.0	93.6	97.8
Std. Dev	11.59	6.04	10.45	7.05

Table 7.15
Statistical values of undamaged A588 fracture toughness of both flanges

Statistical Property	Flange A	Flange B
Mean	103	95.7
Std. Dev.	9.55	101.9
95% High	109.5	89.48
95% Low	95.87	8.69
Median	100.0	95.5
Average Absolute From Median	5.9	6.7

Table 7.16
Student's t-test results comparing the means of data sets in Table 7.15 (Flange A and Flange B)

t-test to establish the statistical difference between the fracture toughness of A588 charpy specimens from Plate A and Plate B
Results of unpaired t-test (see Section 4.9.2):
t=1.71
Std. deviation= 9.13
Degrees of freedom=18
Probability of null hypothesis (the data sets are statistically similar) = 0.10

Table 7.17
Nominal damage strain-restraining stress of each uniaxial tension coupon using fiber analysis

	Damage-Repair 1		*Damage-Repair 2*		*Damage-Repair 3*	
Specimen	$\varepsilon_d / \varepsilon_y$	σ_r / σ_y	$\varepsilon_d / \varepsilon_y$	σ_r / σ_y	$\varepsilon_d / \varepsilon_y$	σ_r / σ_y
A7-Beam 1						
X	26.9	77.9	26.9	100.0	26.9	77.9
Y	21.6	46.4	21.6	78.6	21.6	46.4
Z	15.7	16.6	15.7	41.1	15.7	16.6
A7-Beam 2						
X	80.8	100.0	53.9	100.0	53.9	100.0
Y	64.9	73.8	43.2	82.0	43.2	82.0
Z	48.9	20.5	32.6	33.0	32.6	33.0
A36-Beam 1 and A36-Beam 2						
X	26.9	77.3	26.9	100.0	26.9	77.3
Y	21.6	44.1	21.6	74.8	21.6	44.1
Z	16.3	12.8	16.3	35.4	16.3	12.8
A588-Beam 1						
X	36.3	80.2	18.2	74.2	18.2	74.2
Y	29.1	40.2	14.6	39.3	14.6	39.3
Z	21.9	2.0	11.0	5.8	11.0	5.8
A588-Beam 2						
X	36.3	100.0	18.2	100.0	18.2	100.0
Y	29.1	67.9	14.6	67.8	14.6	67.8
Z	21.9	22.9	11.0	27.3	11.0	27.3

Table 7.18
Nominal damage strain-restraining stress of each charpy specimen using fiber analysis

	Damage-Repair 1				*Damage-Repair 2*				*Damage-Repair 3*			
	C		*L1 or R1*		*C*		*L1 or R1*		*C*		*L1 or R1*	
Specimen	$\varepsilon_d / \varepsilon_y$	σ_r / σ_y	$\varepsilon_d / \varepsilon_y$	σ_r / σ_y	$\varepsilon_d / \varepsilon_y$	σ_r / σ_y	$\varepsilon_d / \varepsilon_y$	σ_r / σ_y	$\varepsilon_d / \varepsilon_y$	σ_r / σ_y	$\varepsilon_d / \varepsilon_y$	σ_r / σ_y
A7-Beam1												
1	27.5	81.4	22.7	80.8	27.5	100.0	22.7	100.0	27.5	81.4	22.7	80.8
2	24.0	60.2	19.8	60.4	24.0	95.8	19.8	96.0	24.0	60.2	19.8	60.4
3	20.4	39.7	16.8	40.5	20.4	70.1	16.8	71.0	20.4	39.7	16.8	40.5
4	17.5	23.1	14.4	24.4	17.5	49.3	14.4	50.6	17.5	23.1	14.4	24.4
A7-Beam2												
1	82.6	100.0	64.1	100.0	55.1	100.0	44.9	100.0	55.1	100.0	44.9	100.0
2	72.0	96.3	55.8	94.1	48.0	100.0	39.1	100.0	48.0	100.0	39.1	100.0
3	61.3	62.8	47.5	62.7	40.9	71.8	33.3	72.0	40.9	71.8	33.3	72.0
4	52.4	35.9	40.6	37.8	34.9	47.2	28.5	48.7	34.9	47.2	28.5	48.7
A36-Beam1 and A36-Beam 2												
1	27.5	81.1	22.7	79.6	27.5	100.0	22.4	100.0	27.5	81.1	22.7	79.6
2	24.0	58.6	19.8	58.2	24.0	93.1	19.5	92.7	24.0	58.6	19.8	58.2
3	20.4	36.9	16.8	37.5	20.4	65.9	16.6	66.5	20.4	36.9	16.8	37.5
4	17.5	19.5	14.4	20.8	17.5	43.9	14.2	45.2	17.5	19.5	14.4	20.8
A588-Beam1												
1	37.1	84.7	26.4	81.2	18.6	78.1	14.2	76.1	18.6	78.1	14.2	76.1
2	32.3	57.8	23.0	56.1	16.2	54.6	12.4	53.7	16.2	54.6	12.4	53.7
3	27.5	31.5	19.6	31.5	13.8	31.7	10.5	31.8	13.8	31.7	10.5	31.8
4	23.5	10.3	16.7	11.8	11.8	13.1	9.0	13.8	11.8	13.1	9.0	13.8
A588-Beam2												
1	37.1	100.0	26.4	100.0	18.6	100.0	14.2	100.0	18.6	100.0	14.2	100.0
2	32.3	88.6	23.0	86.8	16.2	86.3	12.4	85.4	16.2	86.3	12.4	85.4
3	27.5	57.7	19.6	57.7	13.8	58.6	10.5	58.7	13.8	58.6	10.5	58.7
4	23.5	32.7	16.7	34.1	11.8	36.1	9.0	36.8	11.8	36.1	9.0	36.8

a) Cross-Section

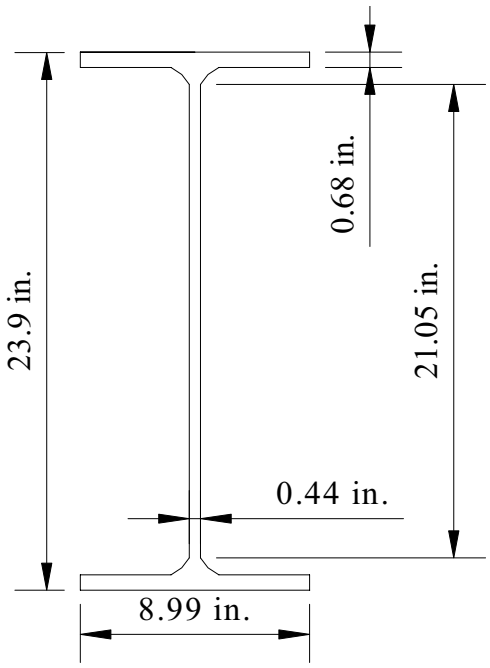

b) Plan View

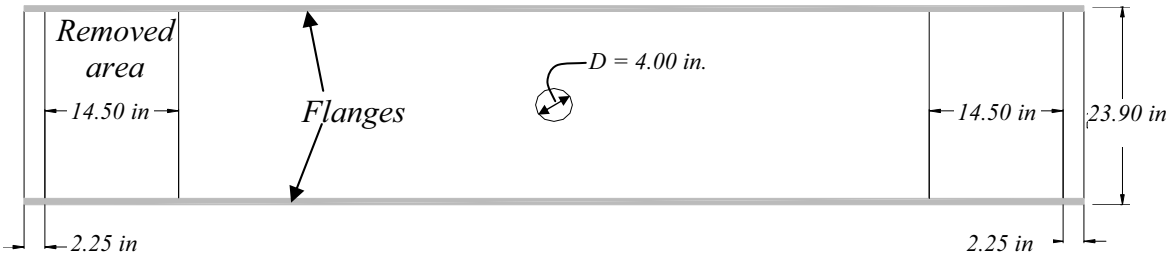

c) Elevation View

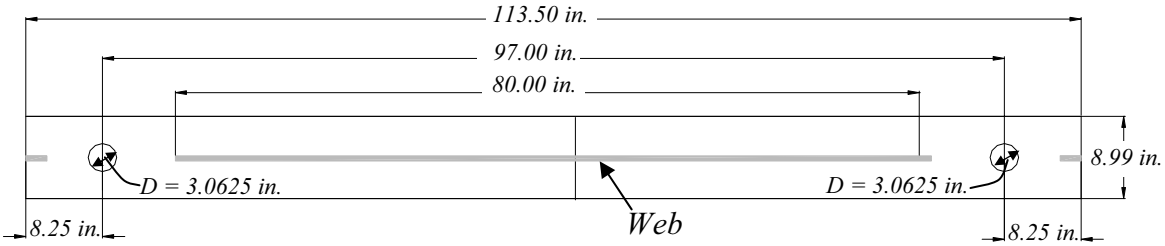

Figure 7.1
Details of the A7 experimental beam specimens

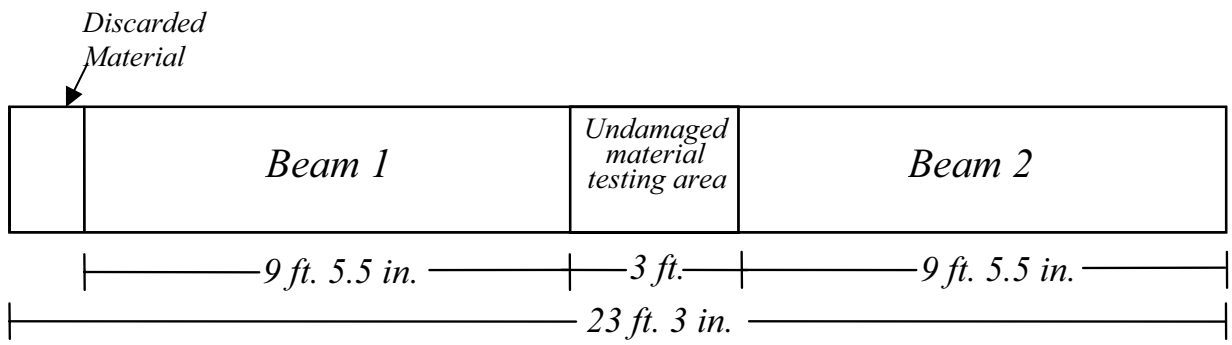

Figure 7.2
Fabrication of A7 beam used for large scale testing

a) Cross-Section

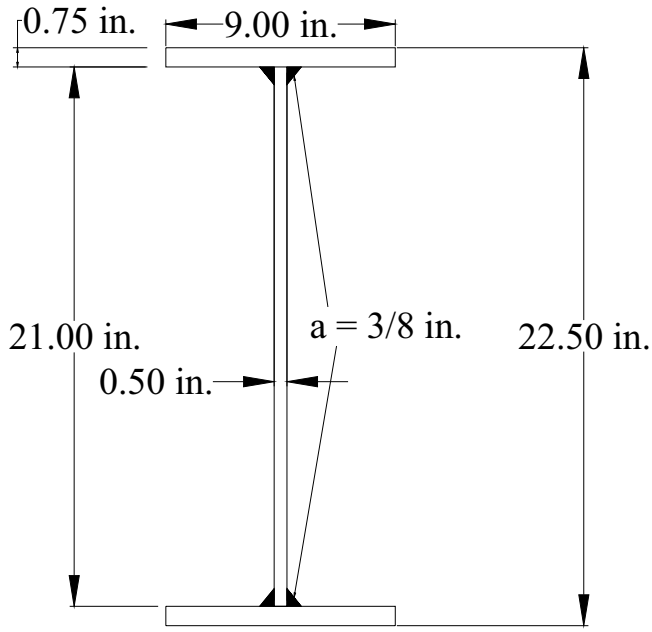

b) Plan View

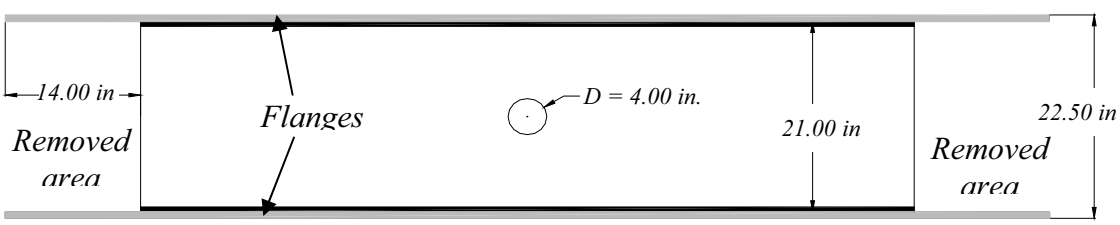

c) Elevation View

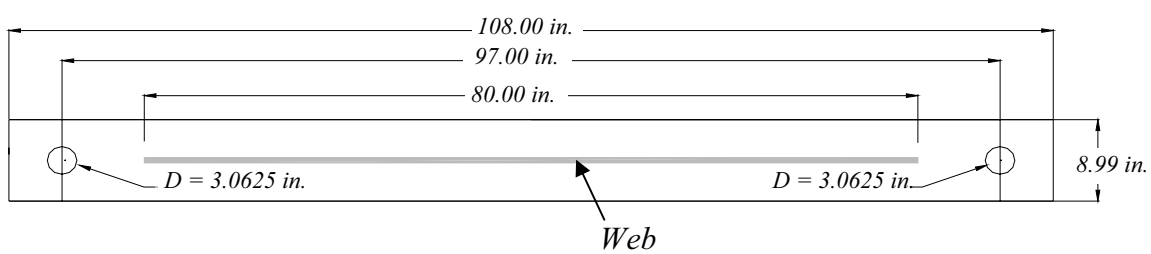

Figure 7.3
Details of the A36 and A588 experimental beam specimen

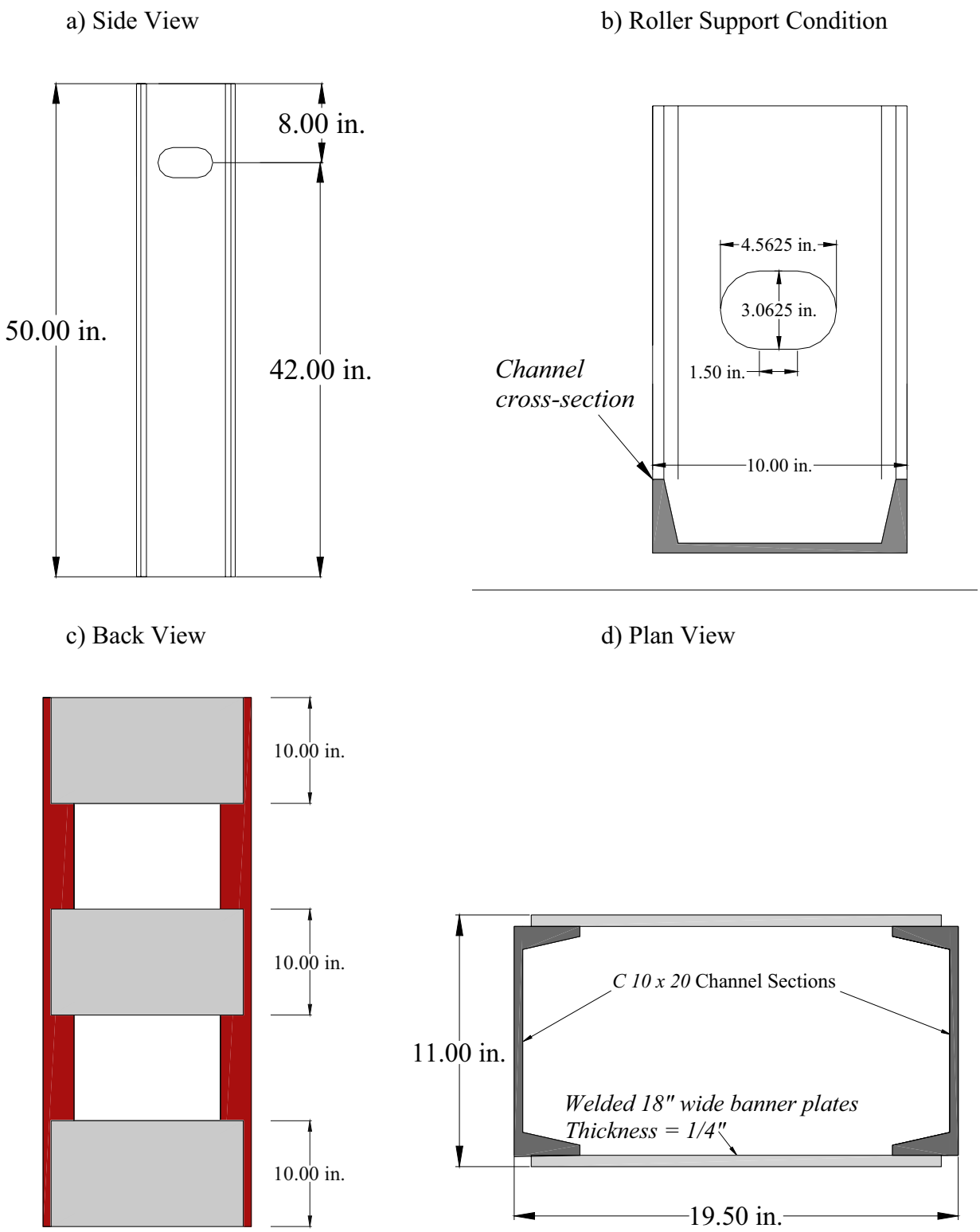

Figure 7.4
Details of the roller support columns

Figure 7.5
Photograph of the roller support column

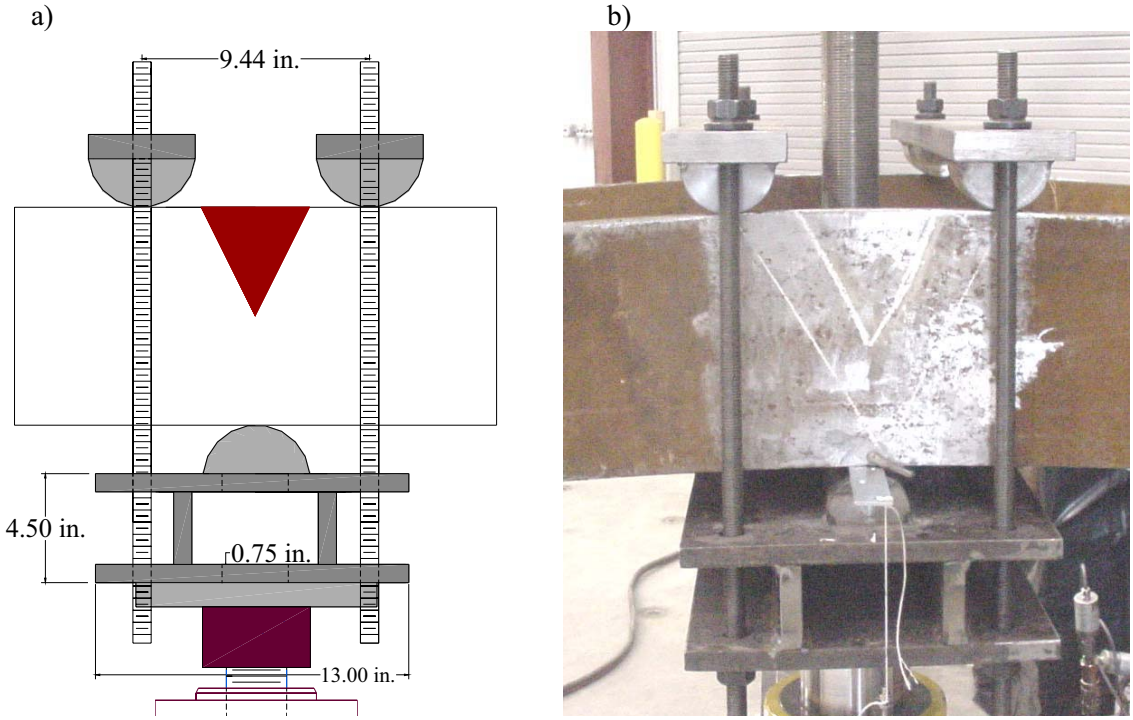

Figure 7.6
Schematic (a) and photograph (b) of the loading frame at beam midspan

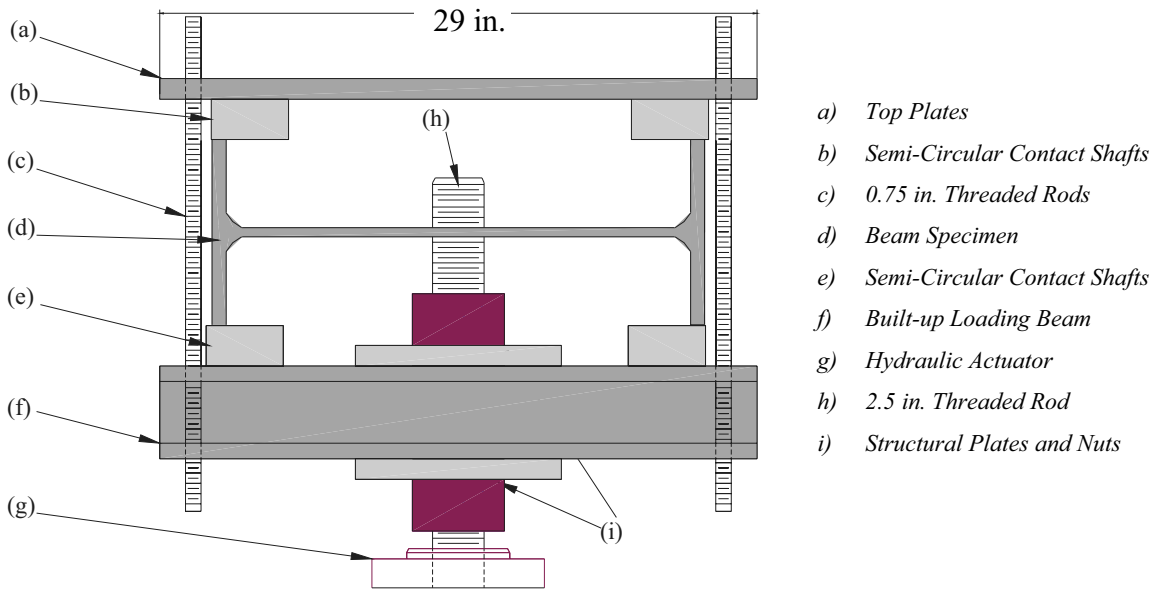

Figure 7.7
Schematic side view of the loading setup

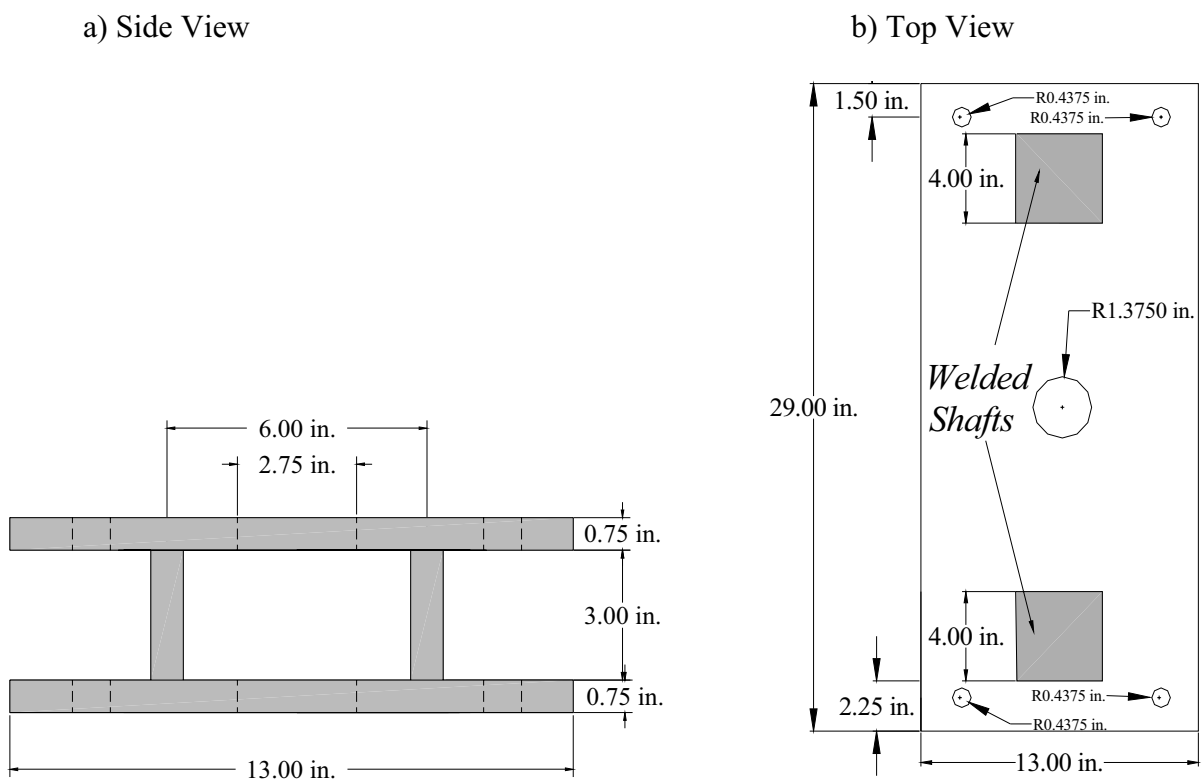

Figure 7.8
Details of the built-up loading beam

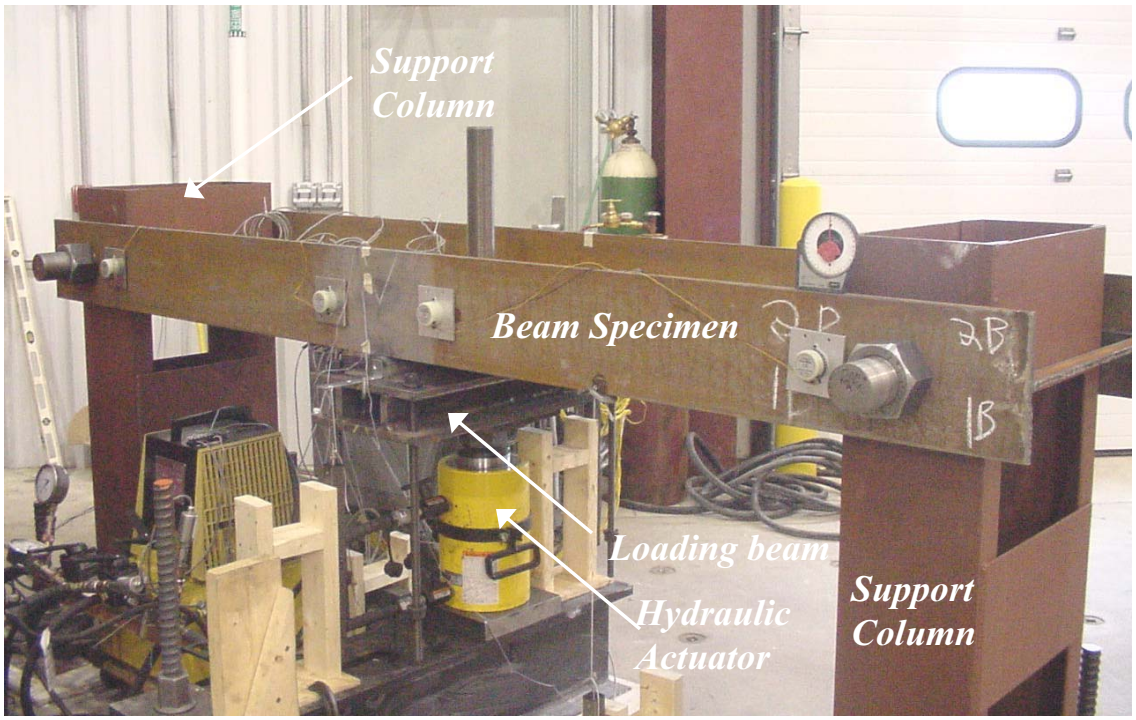

Figure 7.9
Photograph of the front side of the test setup

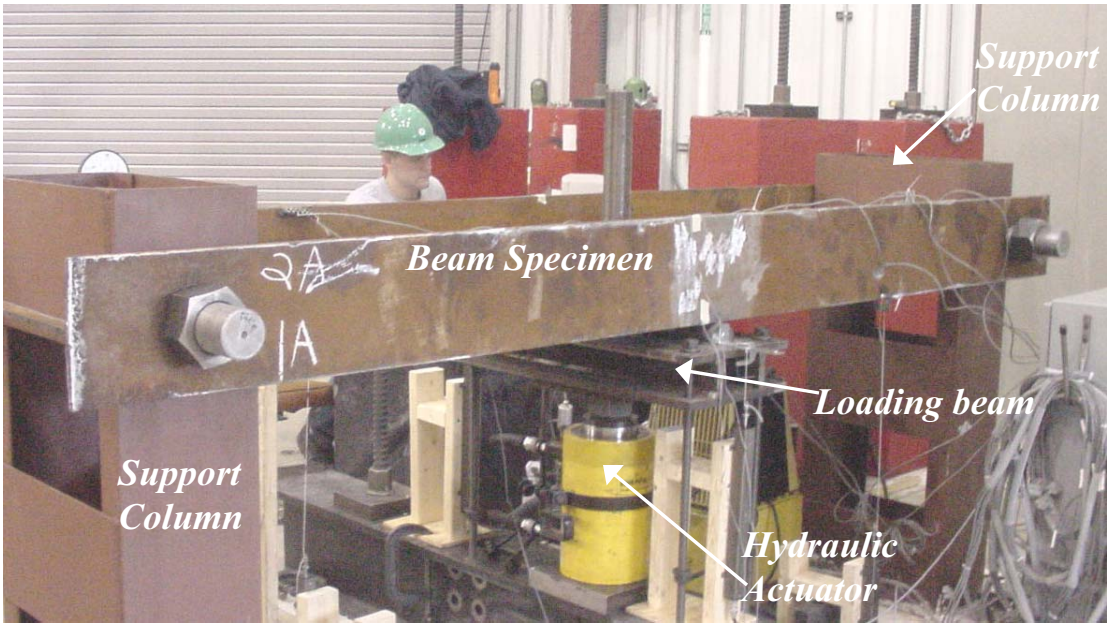

Figure 7.10
Photograph of the back side of the test setup

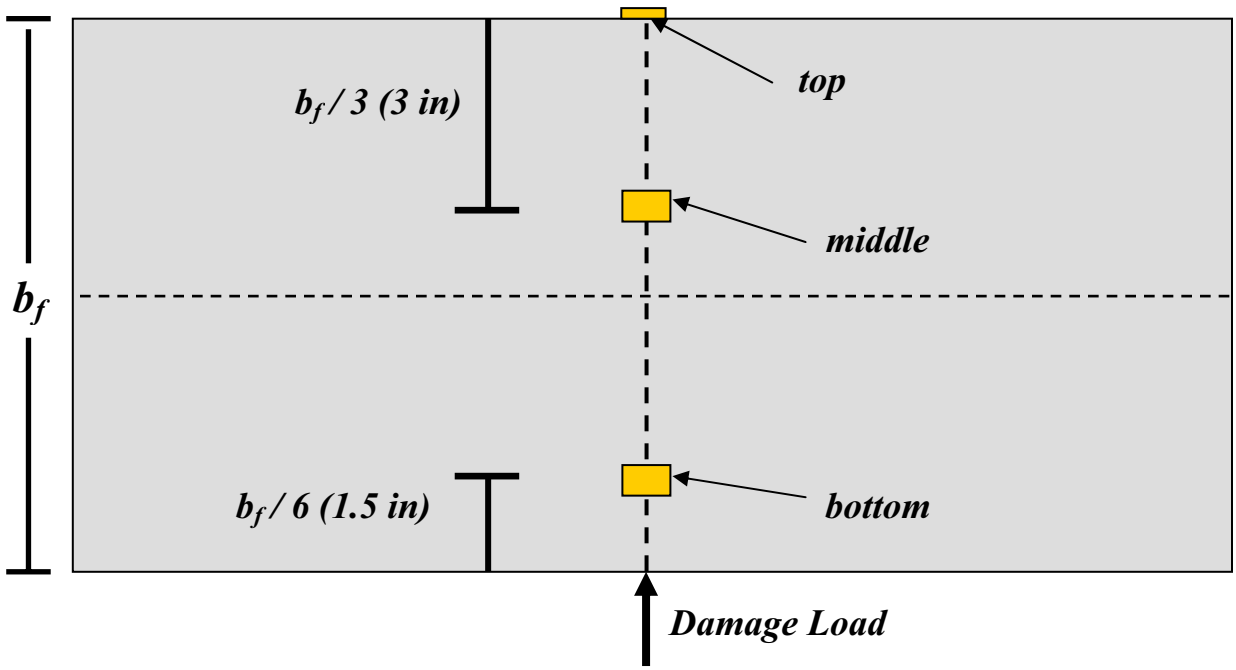

Figure 7.11
Location of longitudinal strain gages attached to both flanges at midspan

Figure 7.12
Location of rotation meter in respect to roller support

a) During Damage

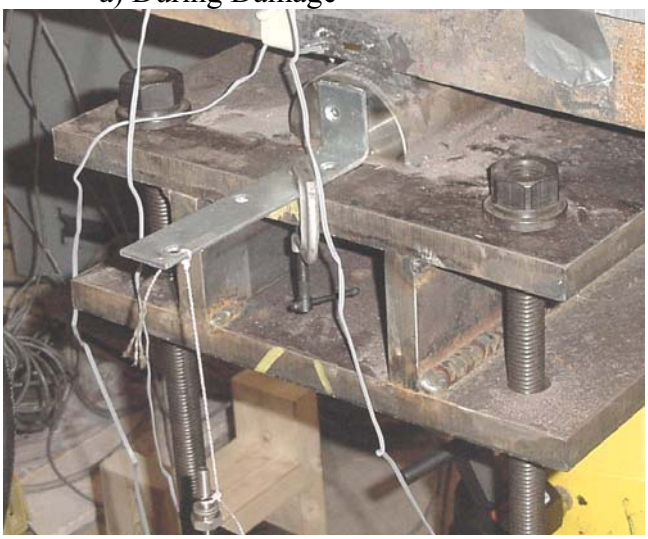

b) During Repair

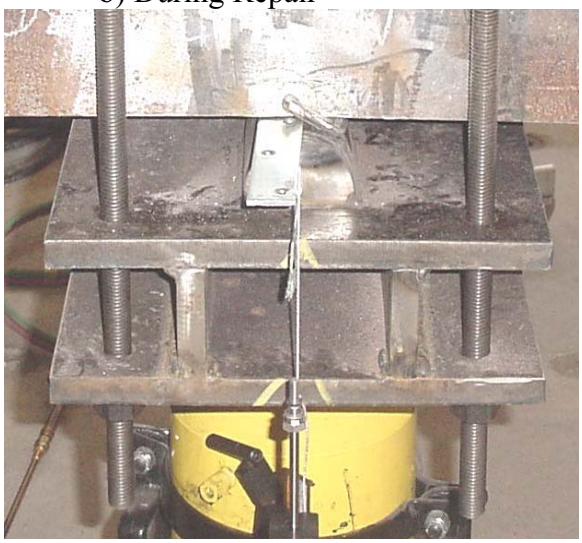

Figure 7.13
Location of displacement transducers (12 in. stroke) located at beam midspan

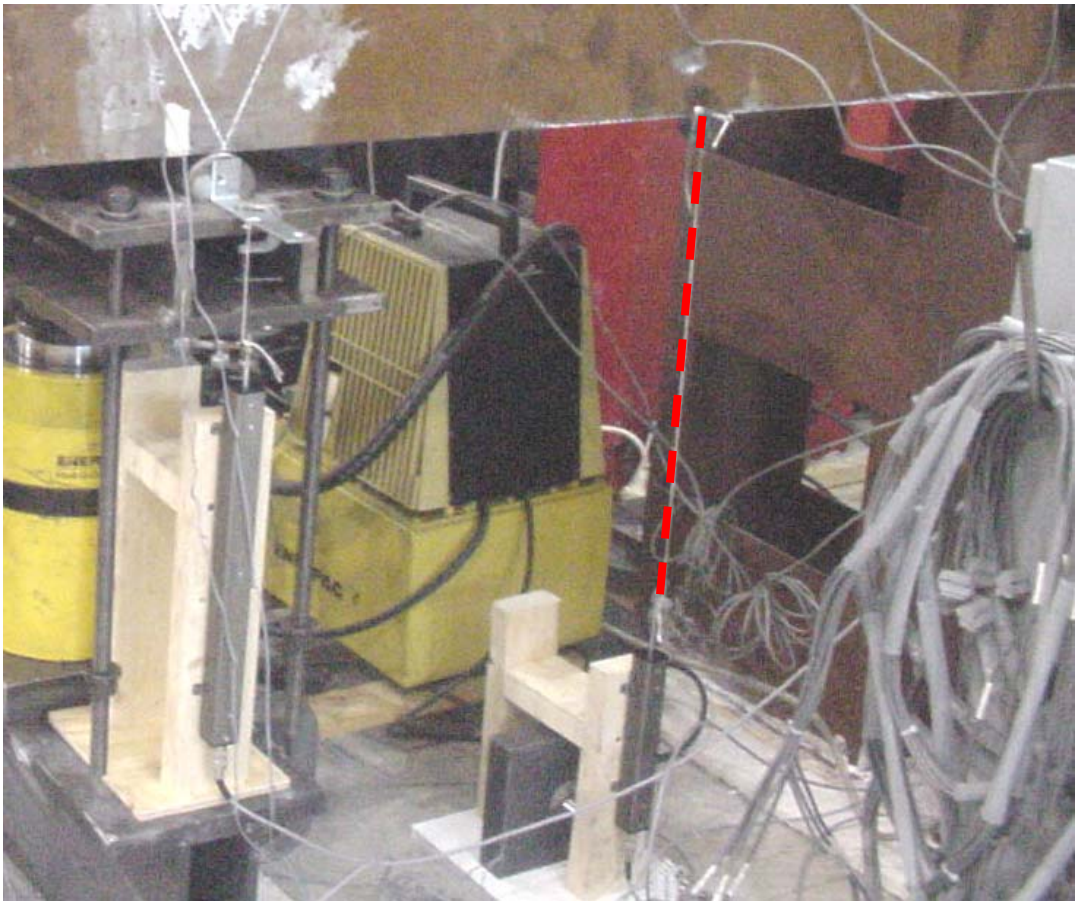

Figure 7.14
Location of displacement transducer (6 in. stroke) at left quarter point

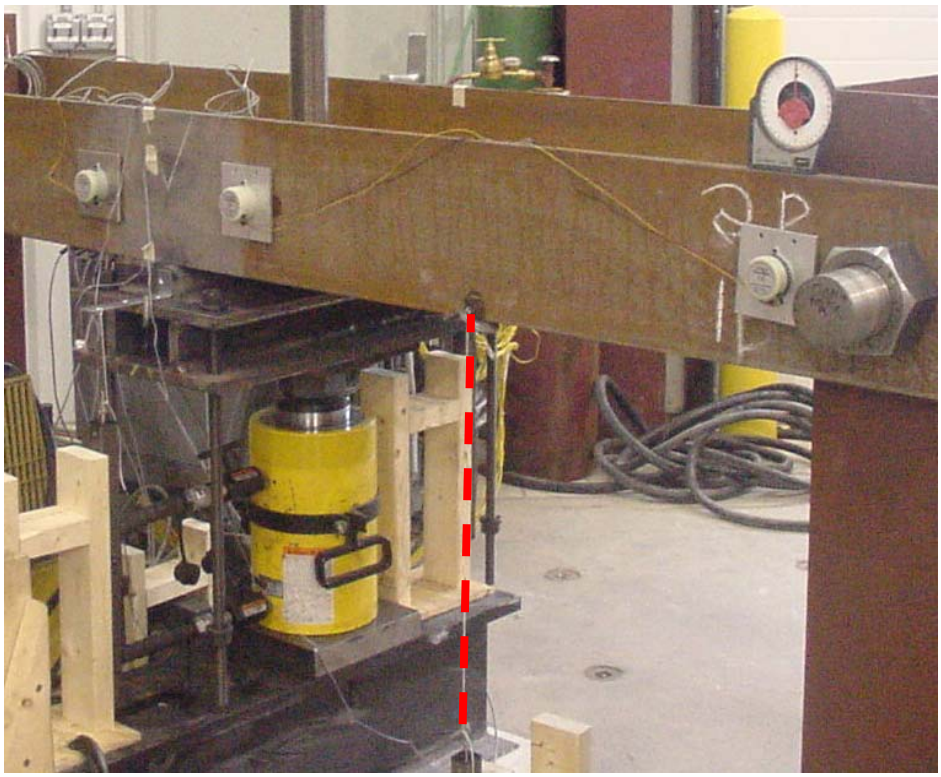

Figure 7.15
Location of displacement transducer (6 in. stroke) at right quarter point

Figure 7.16
Location of infrared thermometer in respect to test setup

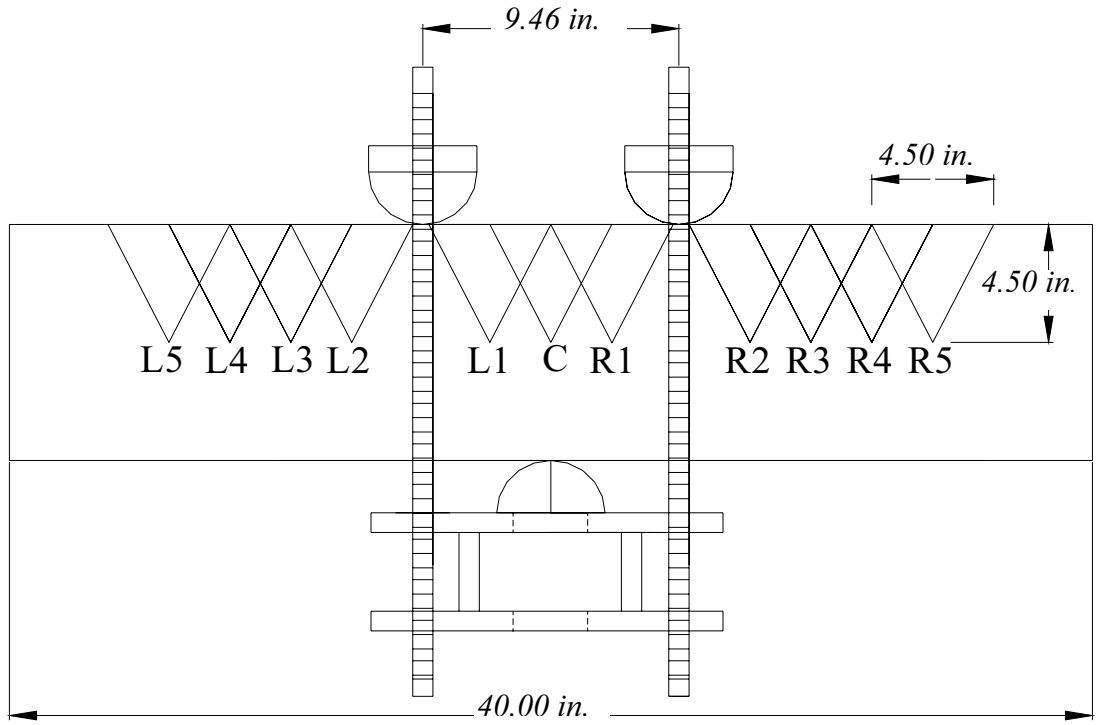

Figure 7.17
Front side view of Vee heat locations and nomenclature

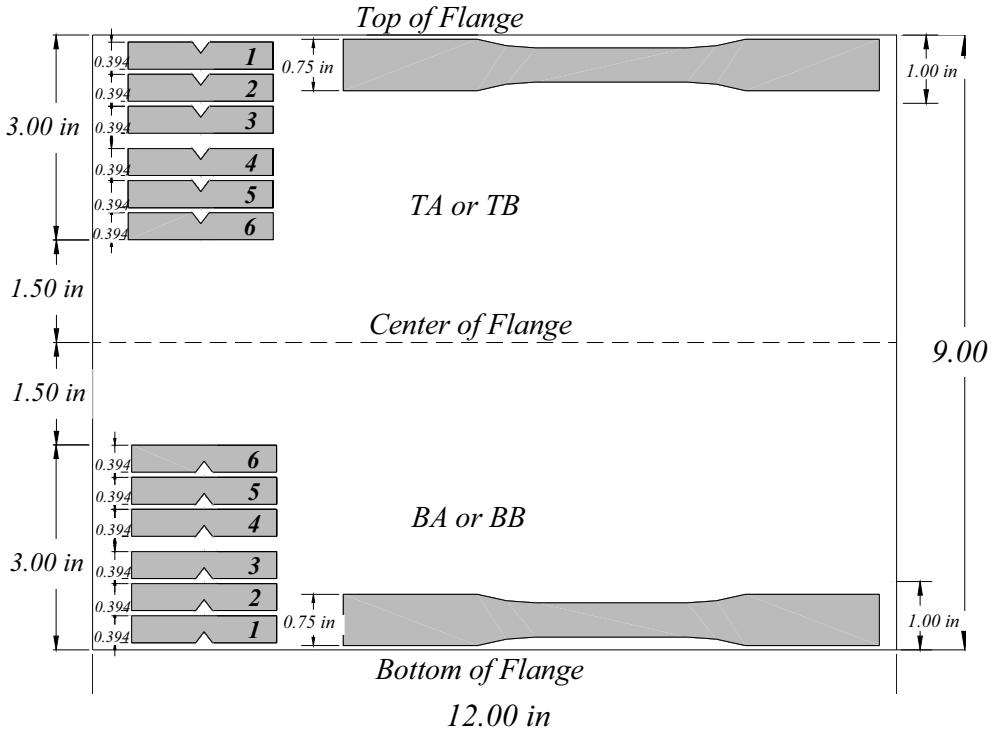

Figure 7.18
Location and nomenclature of undamaged material testing coupons

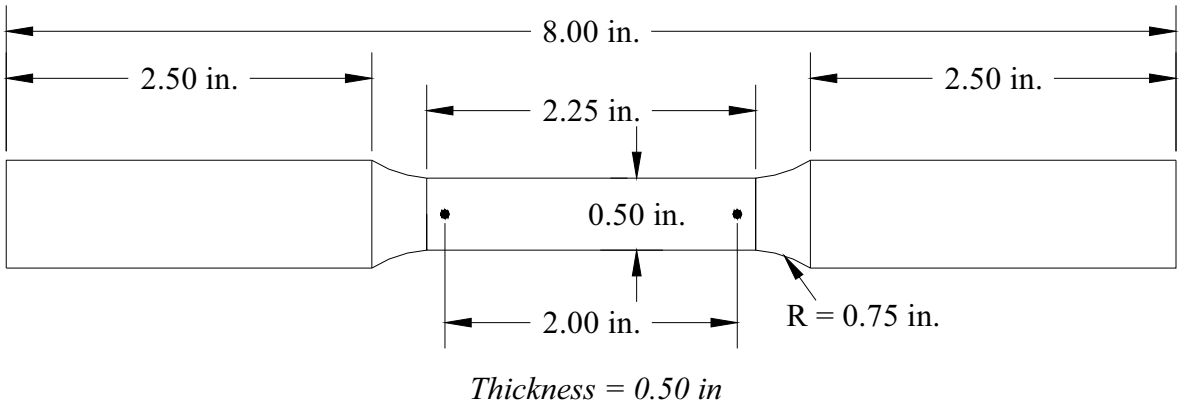

Figure 7.19
Uniaxial tension coupon fabricated from the flanges of beam specimens

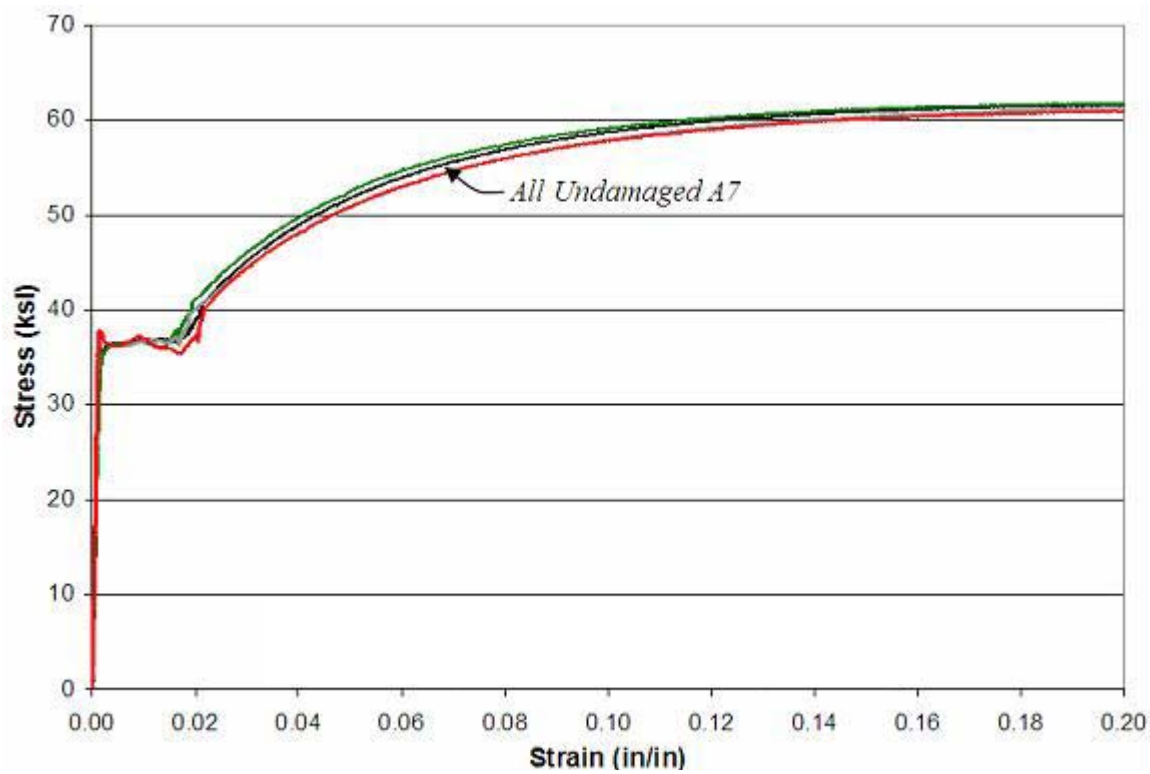

Figure 7.20
Stress-strain relationships of undamaged A7 steel

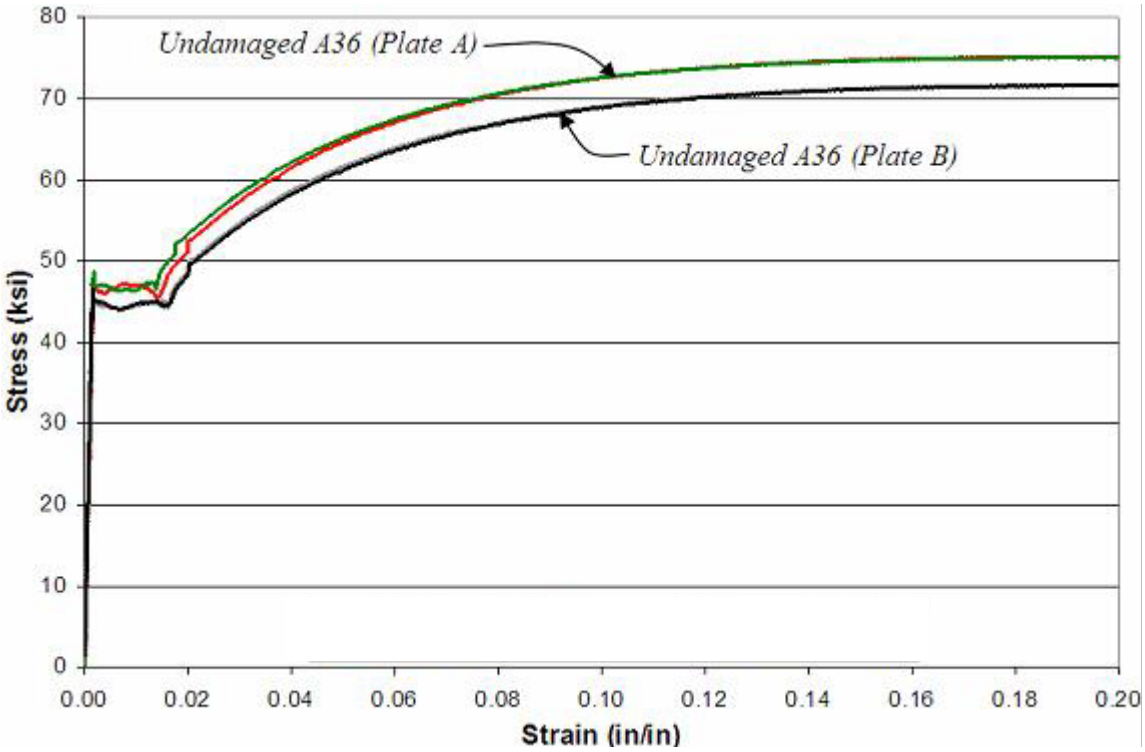

Figure 7.21
Stress-strain relationships of undamaged A36 steel

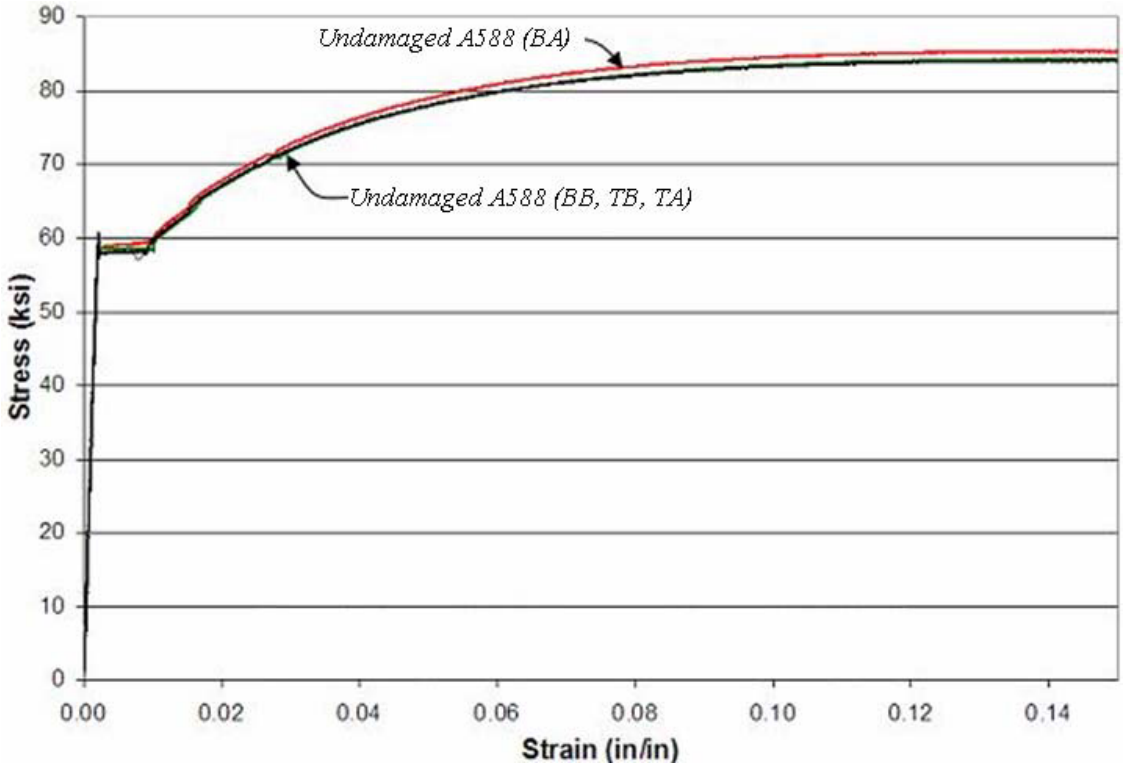

Figure 7.22
Stress-strain relationships of undamaged A588 steel

a) Undamaged A7-Flange A

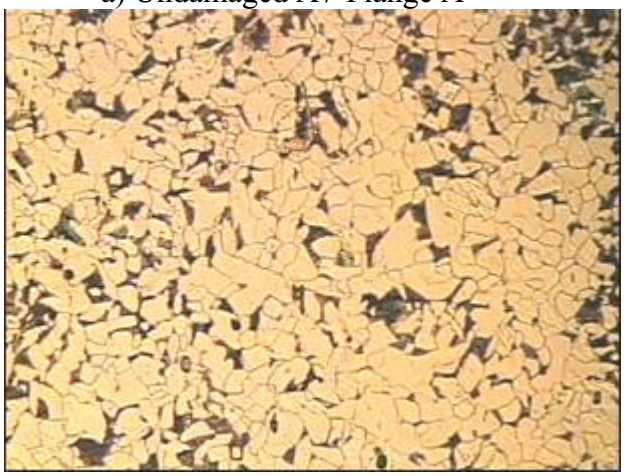

b) Undamaged A7-Flange B

c) Undamaged A36-Flange A

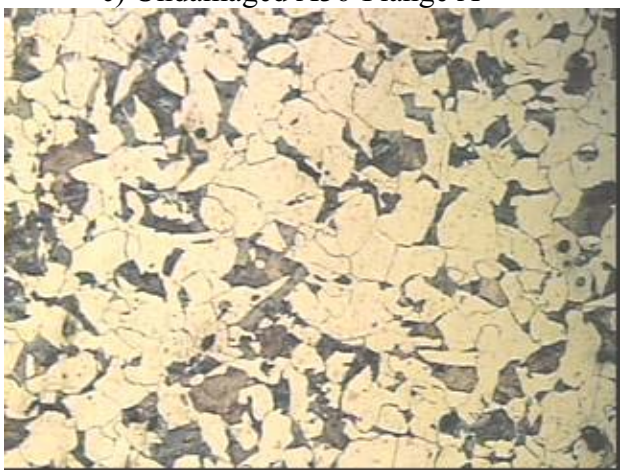

d) Undamaged A36-Flange B

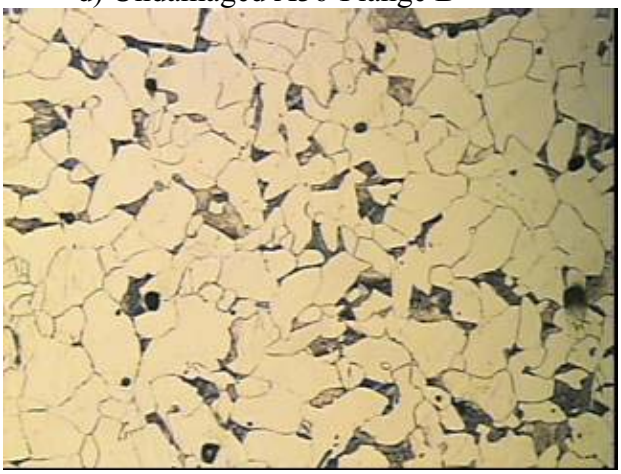

e) Undamaged A588-Flange A

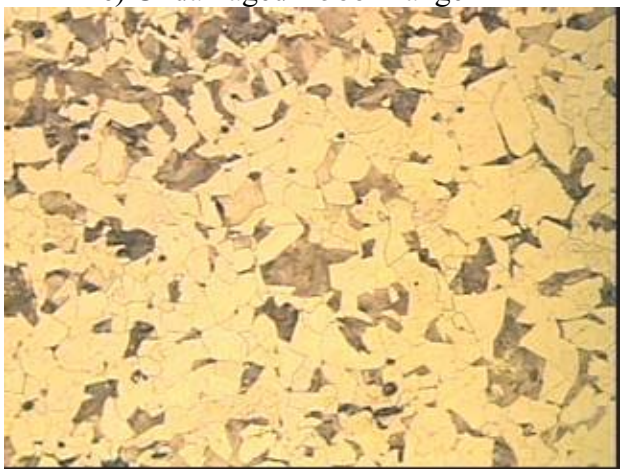

f) Undamaged A588-Flange B

Figure 7.23
Microstructure of undamaged A7, A36, and A588 steel

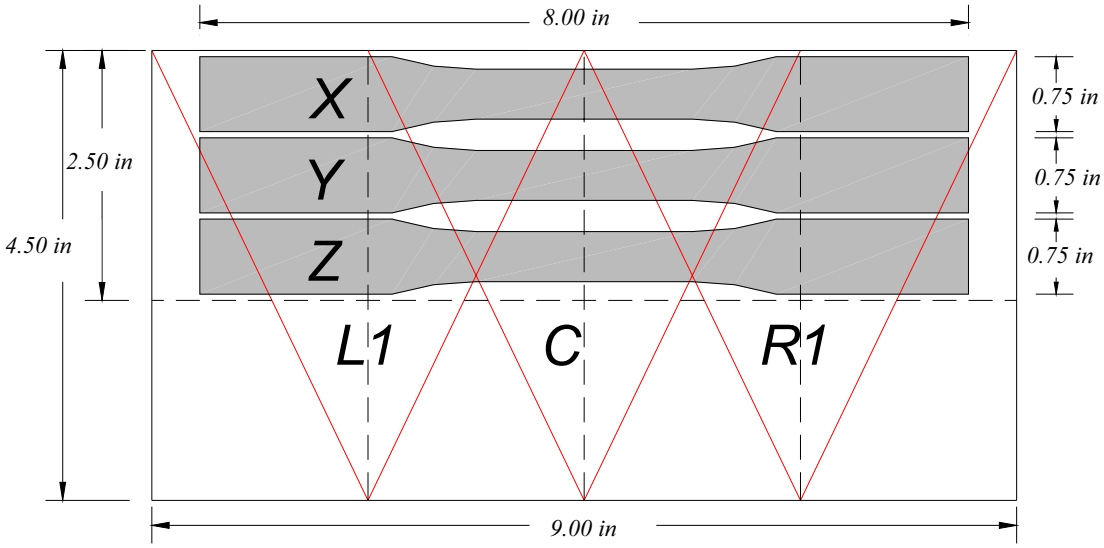

Figure 7.24
Nomenclature and location of damaged-repaired uniaxial tension coupons

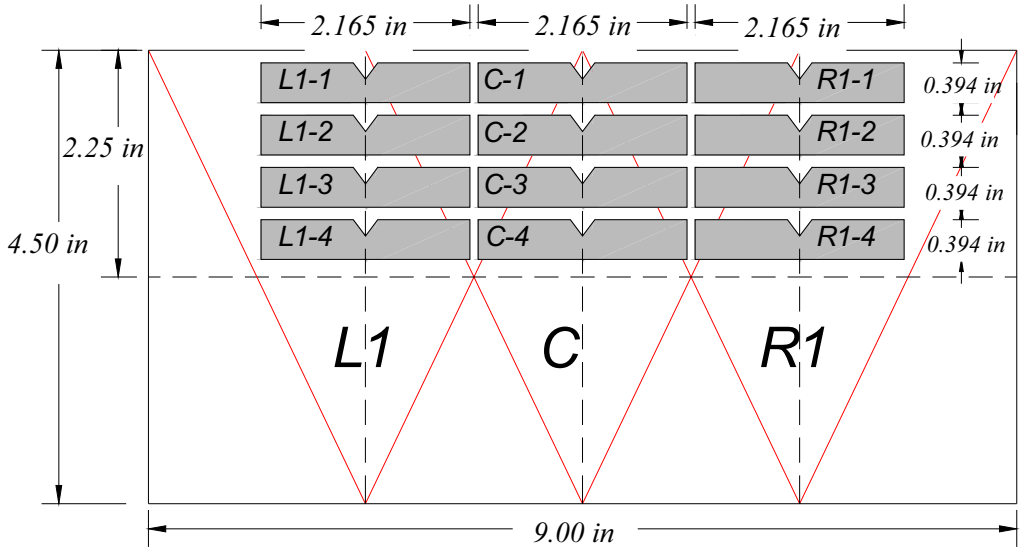

Figure 7.25
Nomenclature and location of damaged-repaired fracture toughness specimens

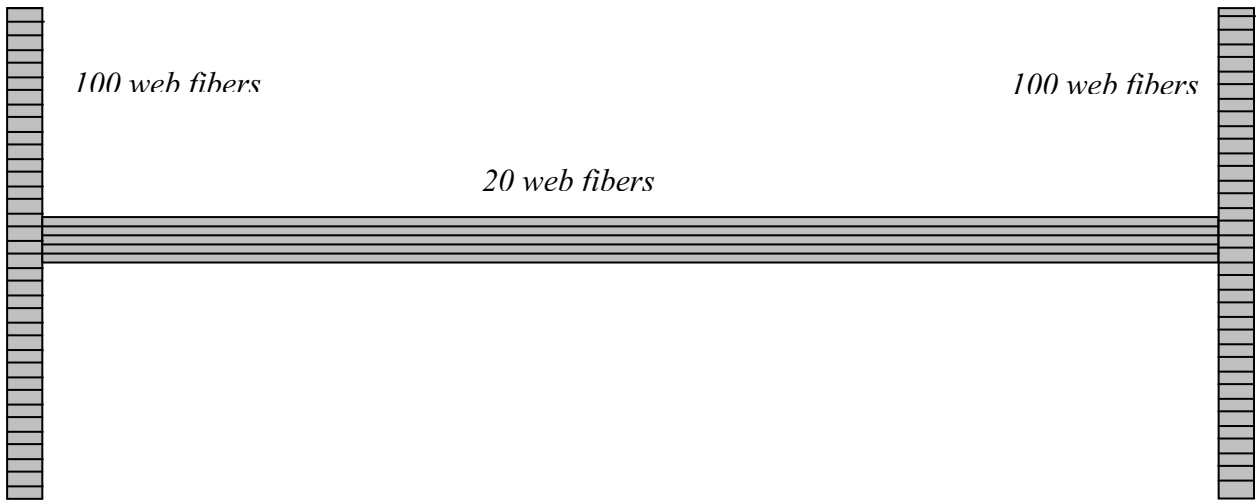

Figure 7.26
Discretization of steel flange and web fibers

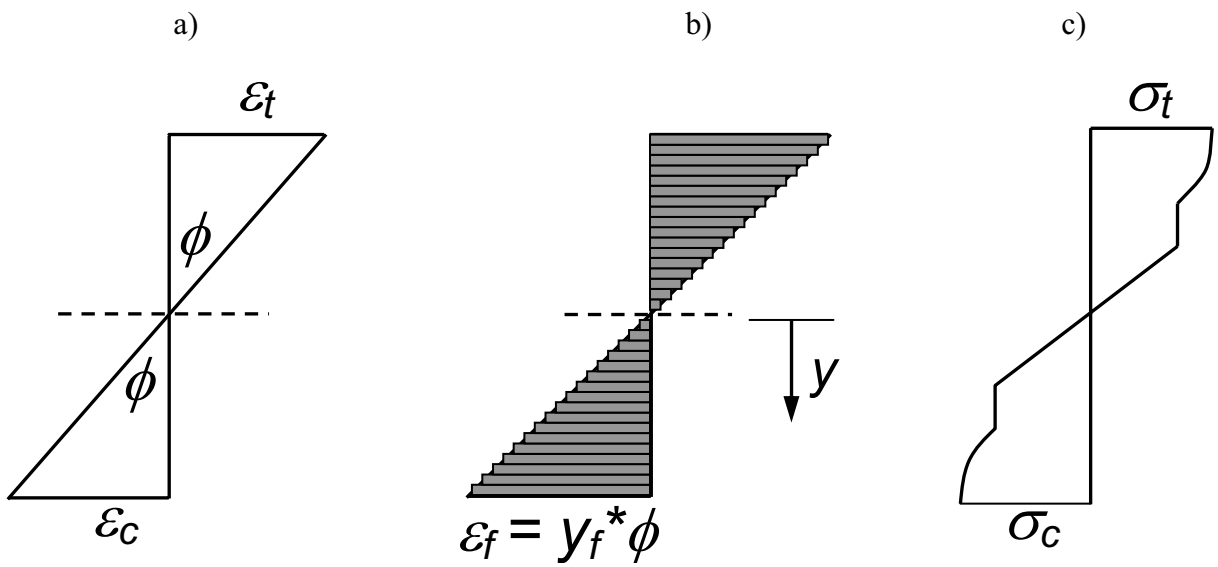

Figure 7.27
Illustration of computing the stress in each fiber

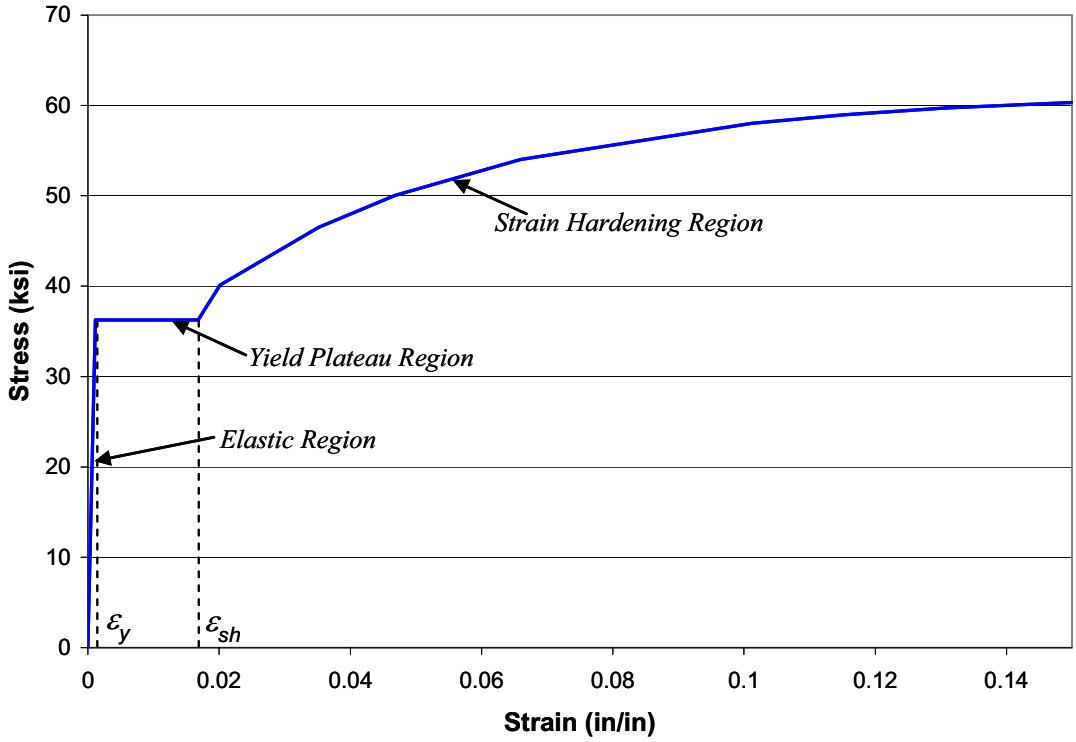

Figure 7.28
Idealized stress-strain relationship of undamaged A7 steel

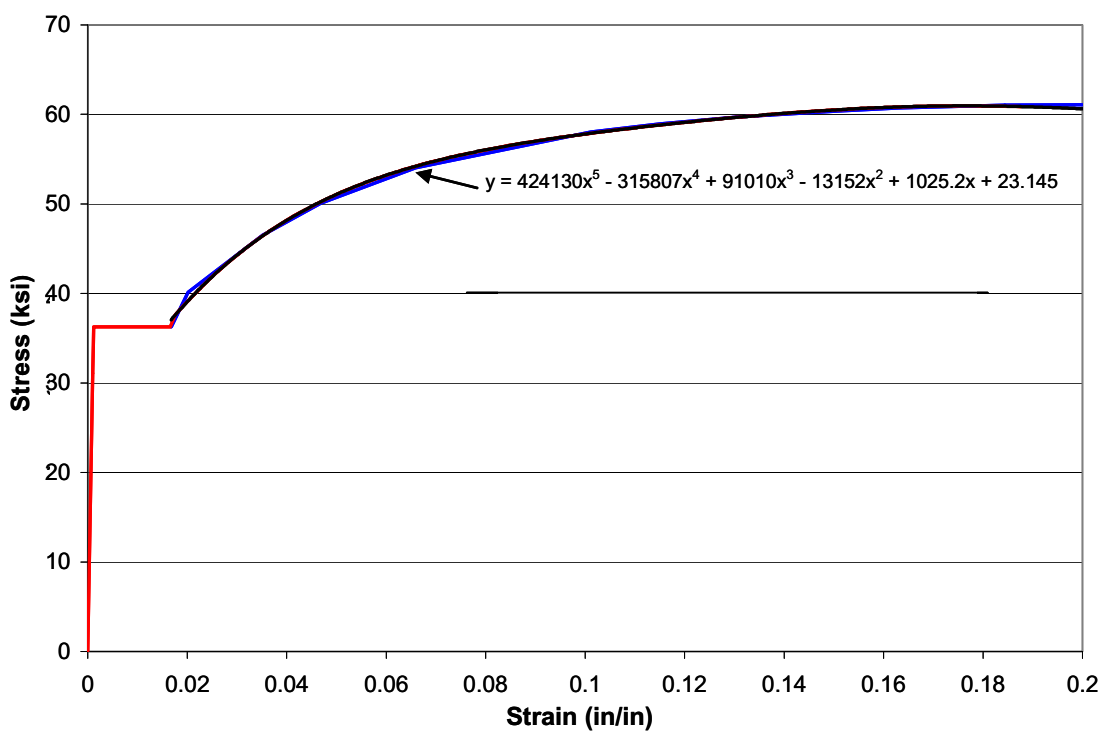

Figure 7.29
Fifth order equation computed by Excel for the strain hardening of A7 steel

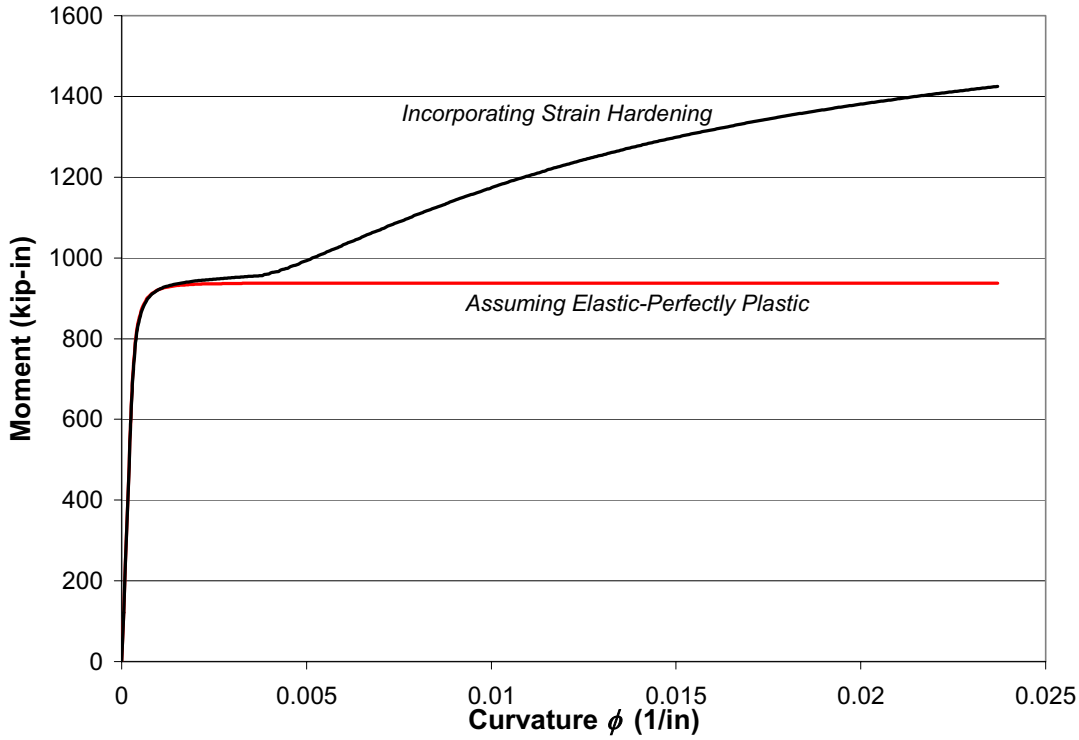

Figure 7.30
Moment-curvature relationship for W24 x76 A7 beam subjected to weak axis bending

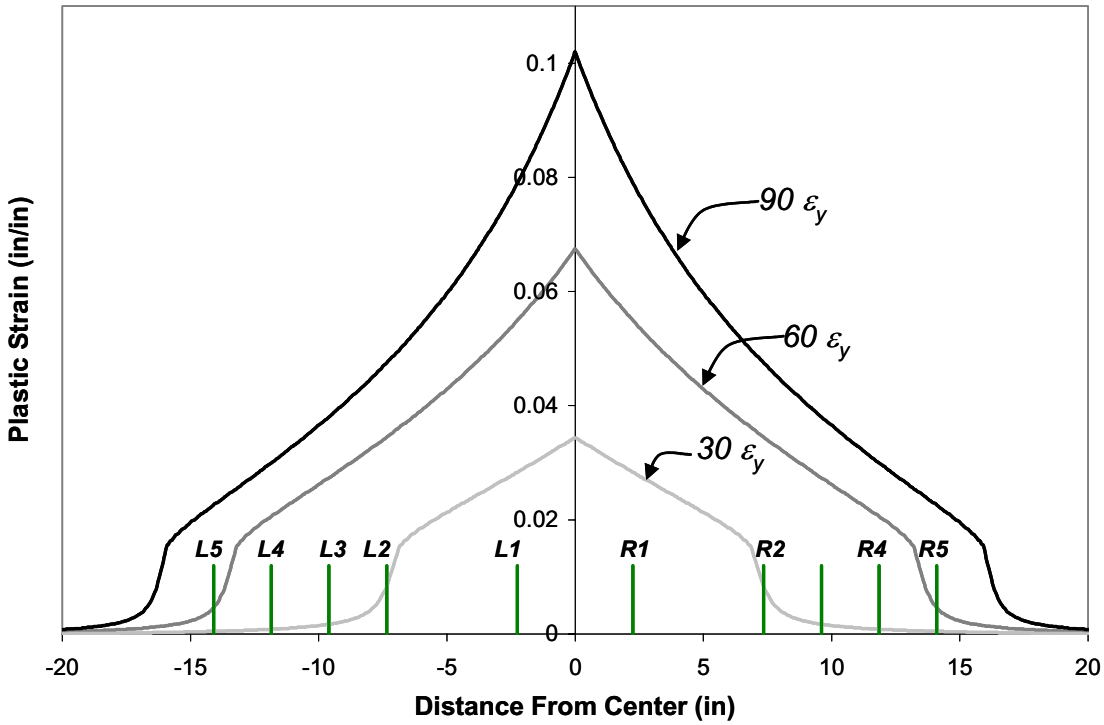

Figure 7.31
Plastic strain distribution along the top of A7 beam specimens

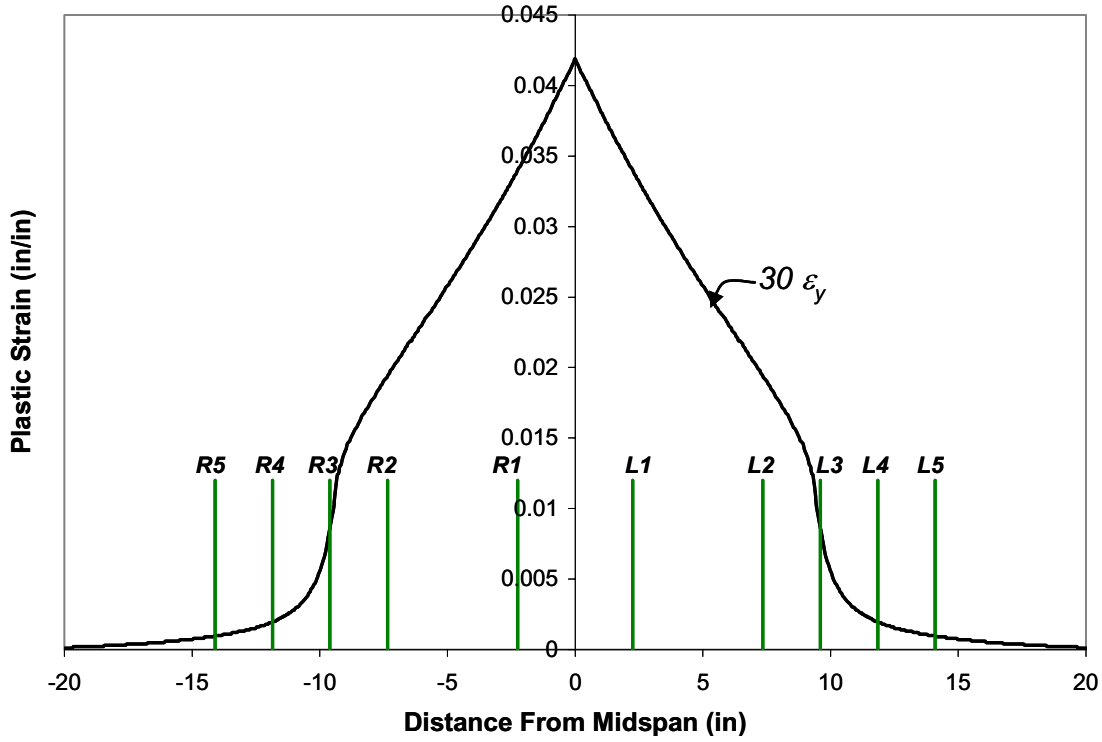

Figure 7.32
Plastic strain distribution along the top of A36 beam specimens

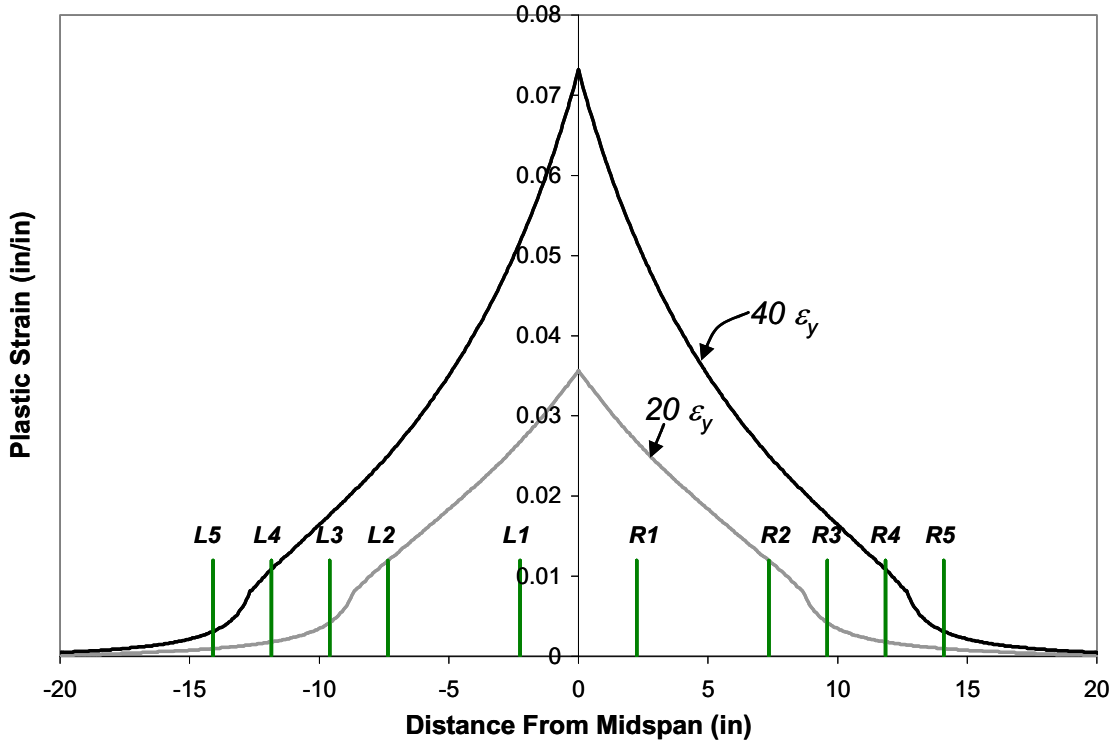

Figure 7.33
Plastic strain distribution along the top of A588 beam specimens

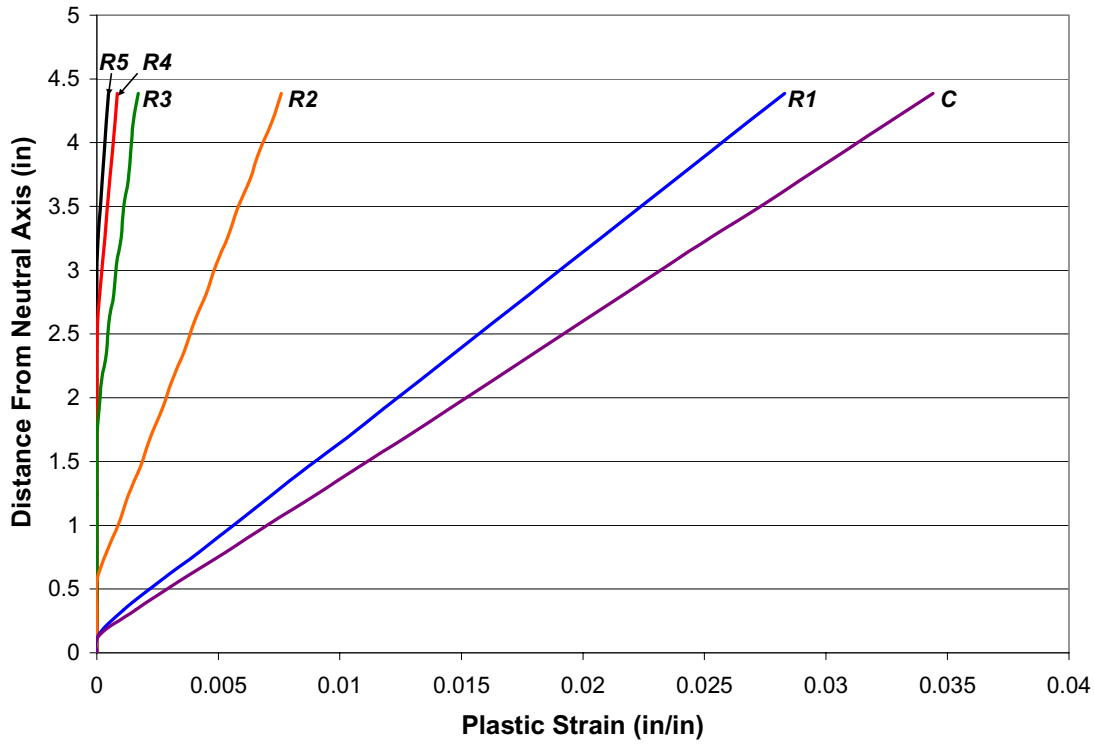

Figure 7.34
Plastic strain distribution along half the depth of A7 beams damaged to 30 ε_y

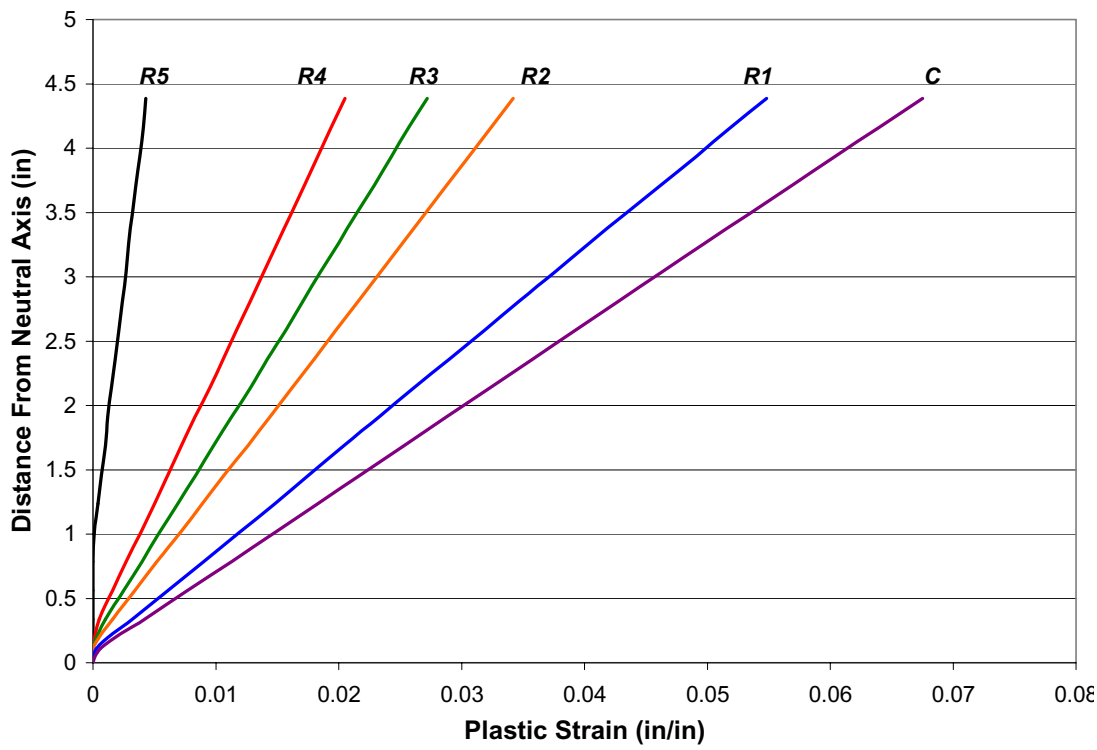

Figure 7.35
Plastic strain distribution along half the depth of A7 beams damaged to 60 ε_y

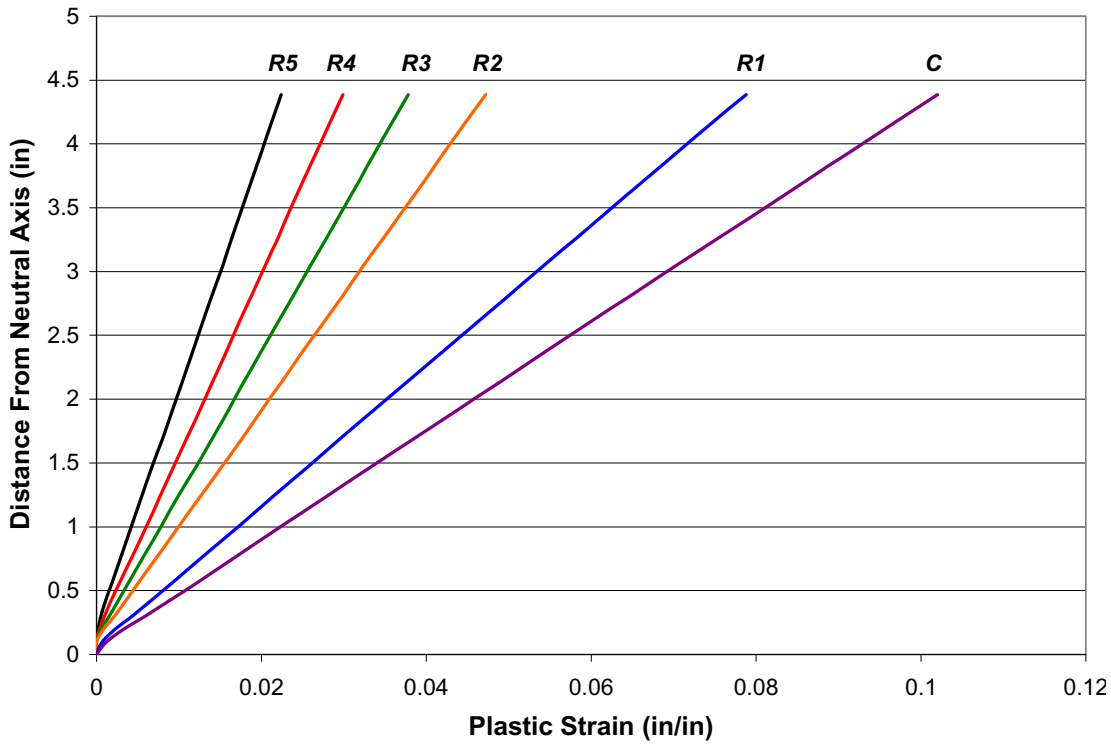

Figure 7.36
Plastic strain distribution along half the depth of A7 beams damaged to 90 ε_y

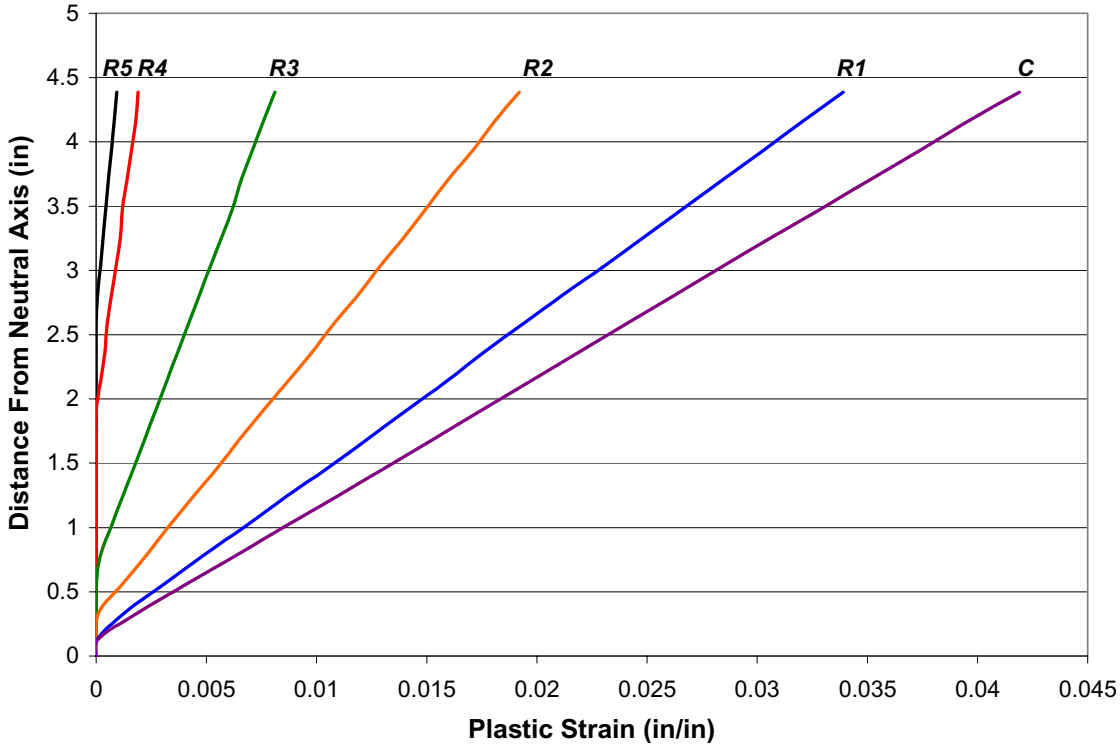

Figure 7.37
Plastic strain distribution along half the depth of A36 beams damaged to 30 ε_y

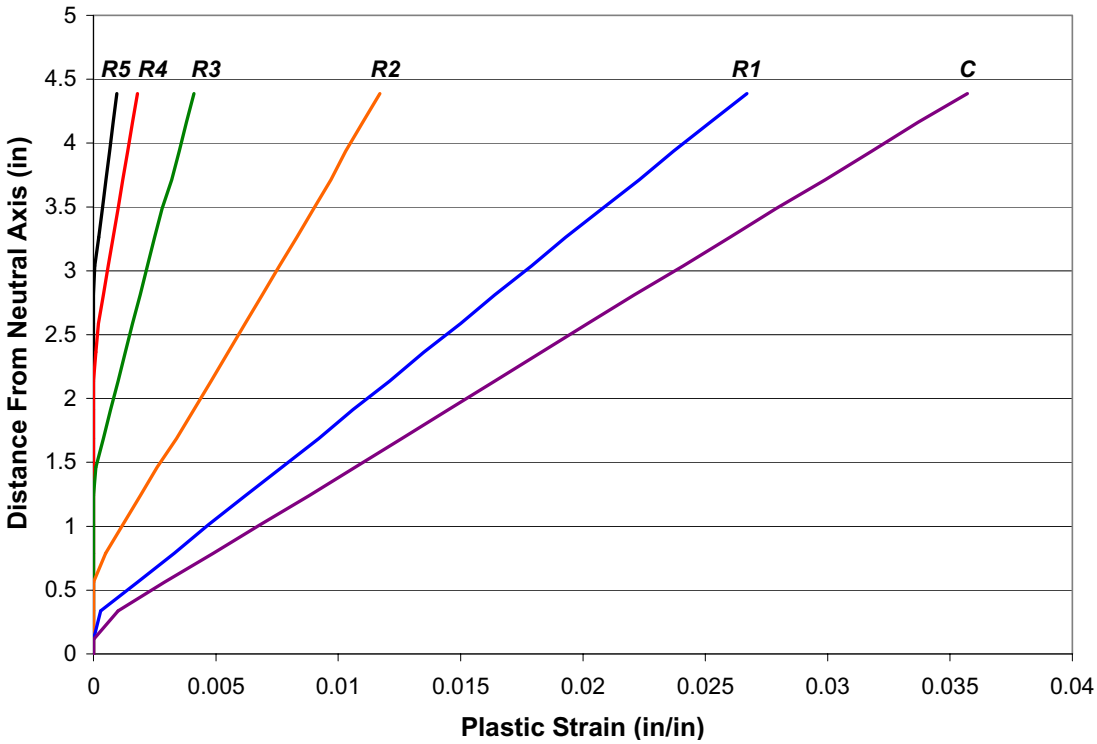

Figure 7.38
Plastic strain distribution along half the depth of A588 beams damaged to 20 ε_y

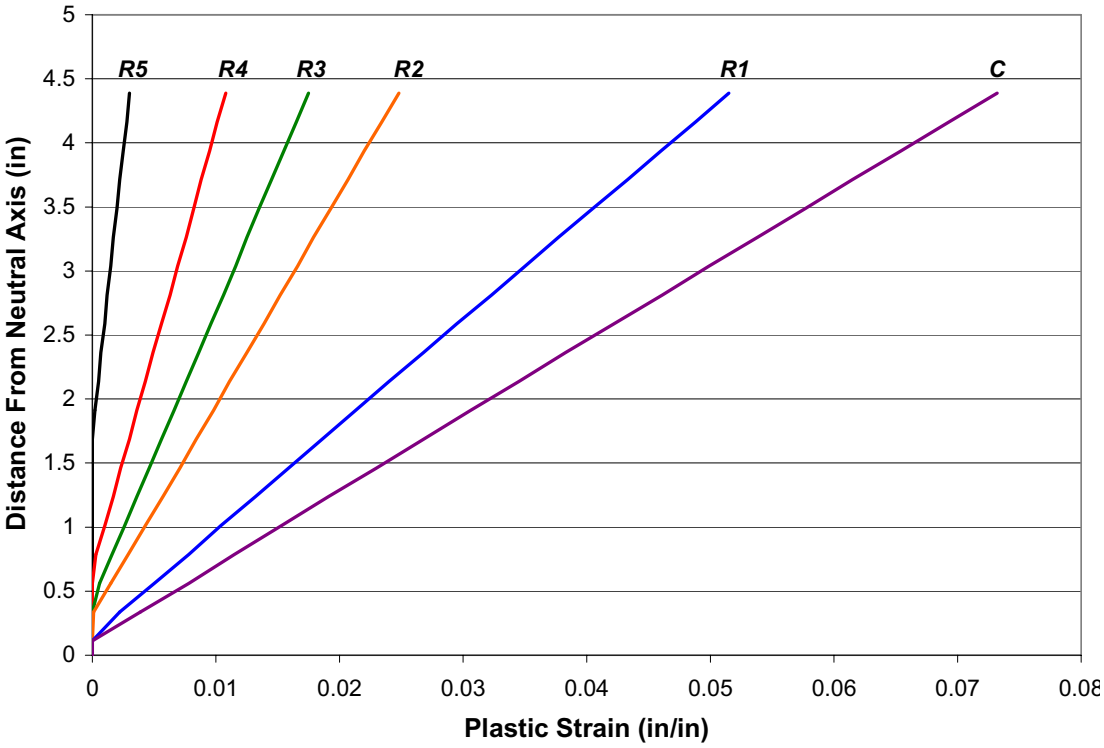

Figure 7.39
Plastic strain distribution along half the depth of A588 beams damaged to 40 ε_y

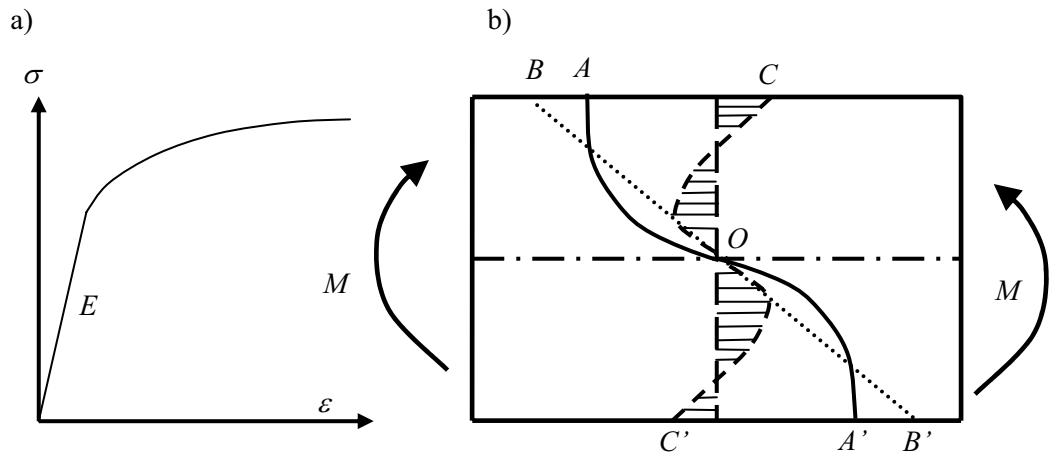

Figure 7.40
Induced residual stresses in a steel beam subjected to bending [*1*]

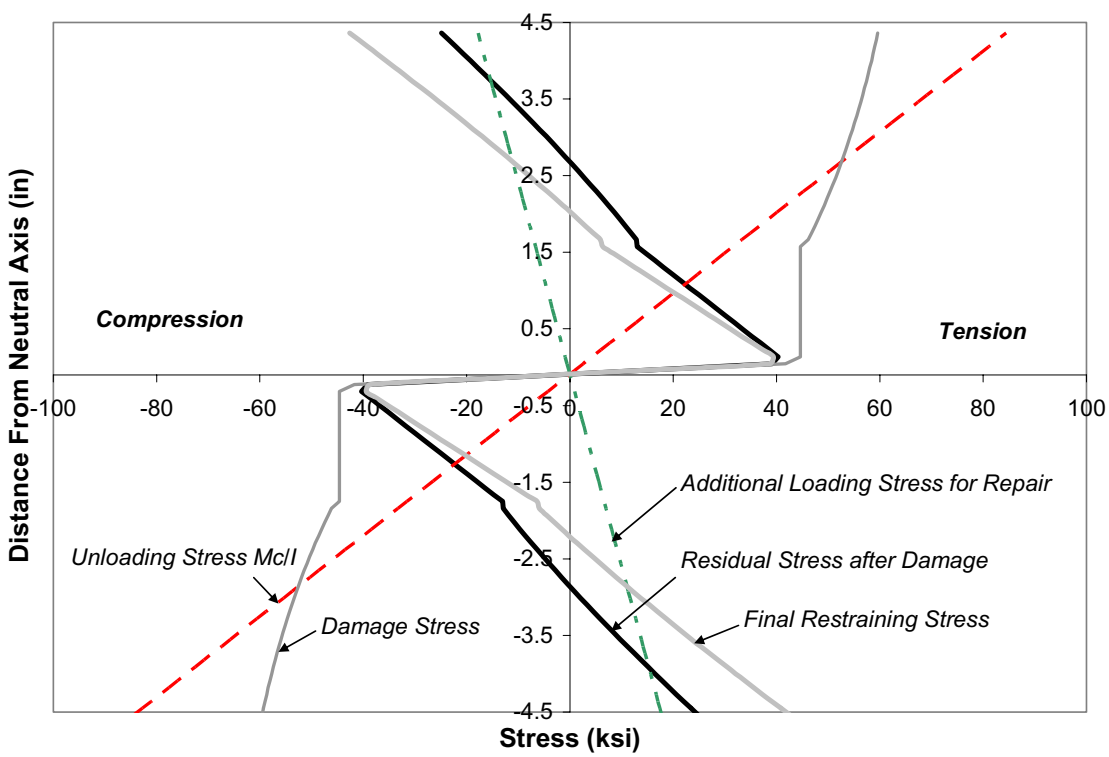

Figure 7.41
Damage-repair stress history of A36-Beam 1 (30 ε_y max) along the center Vee heat (*C*)

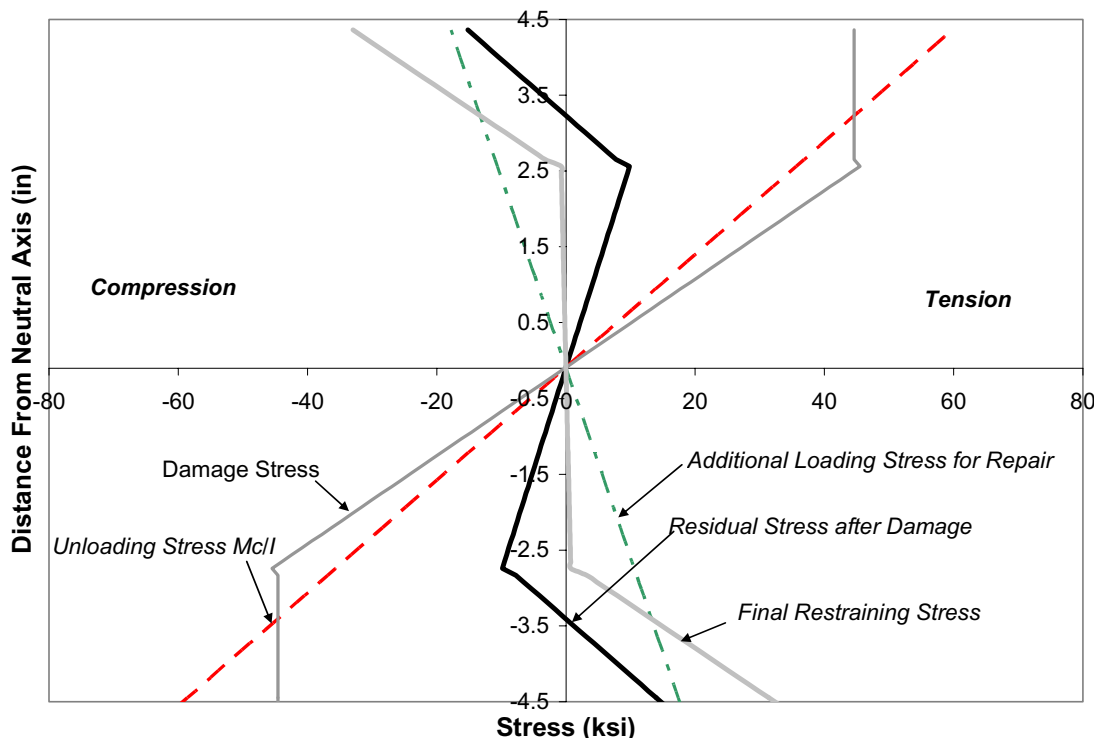

Figure 7.42
Damage-repair stress history of A36-Beam 1 along the furthest Vee heat from center (*R5*)

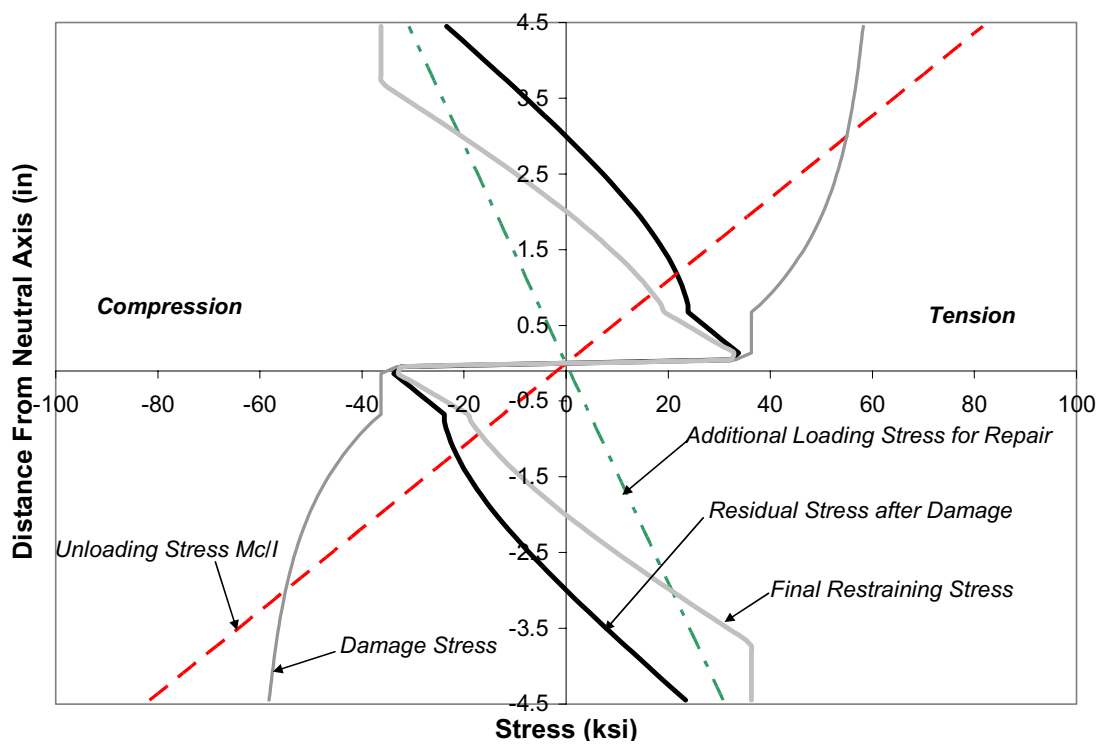

Figure 7.43
Damage-repair stress history of A7-Beam 2 (90 ε_y max) along the center Vee heat (*C*)

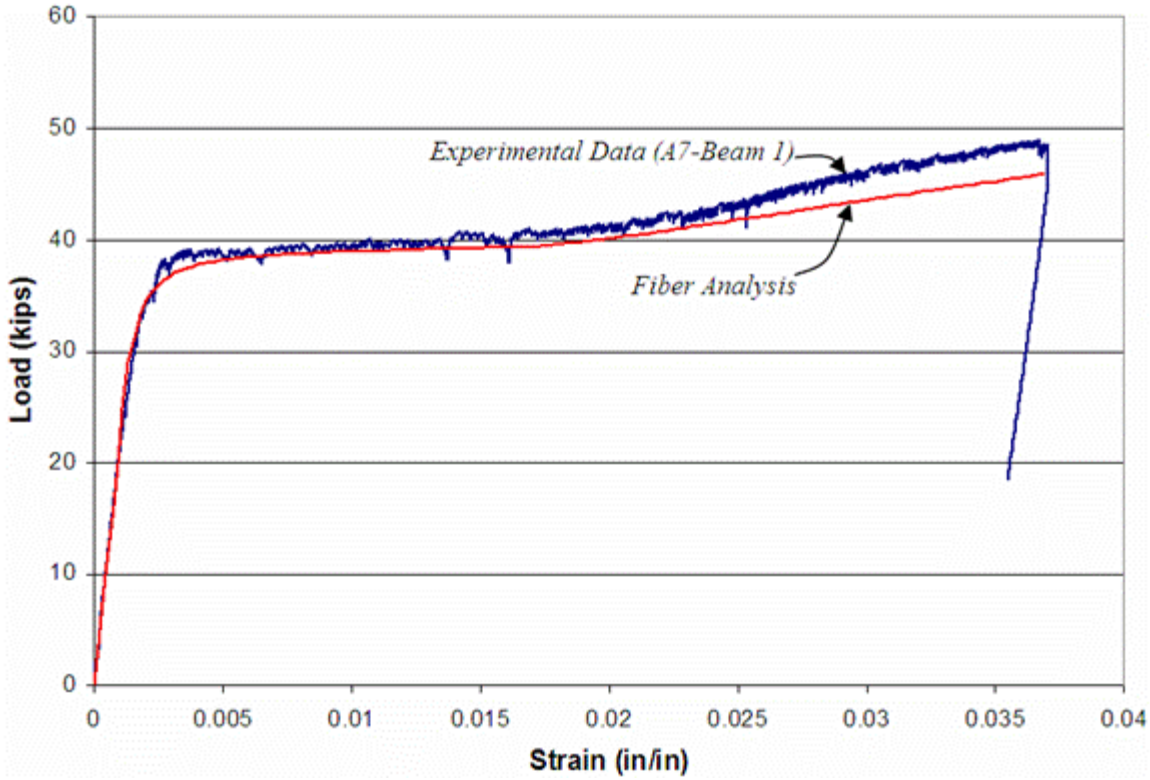

Figure 7.44
Load-strain comparisons between fiber analysis and experimental results (A7-Beam 1)

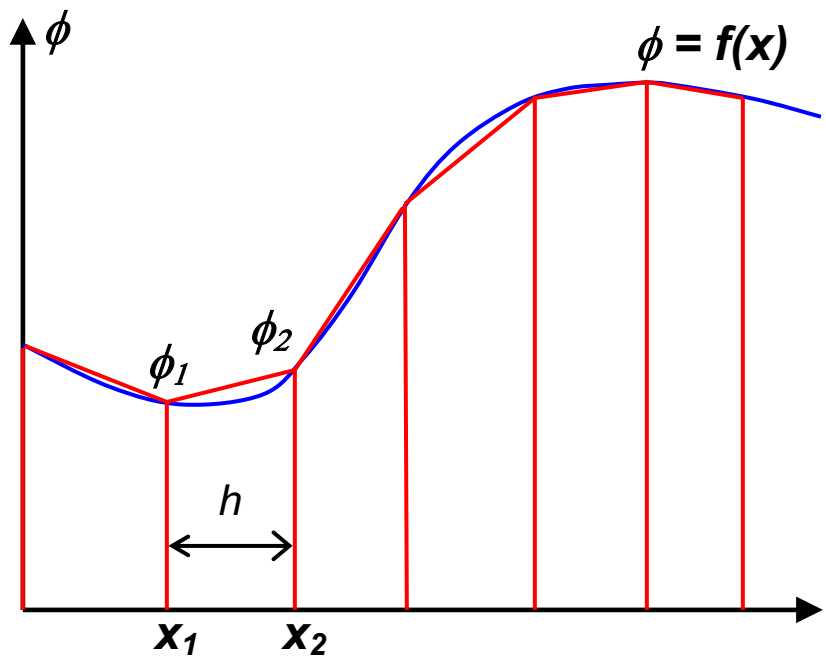

Figure 7.45
Illustration of trapezoidal rule of integration used to compute rotations

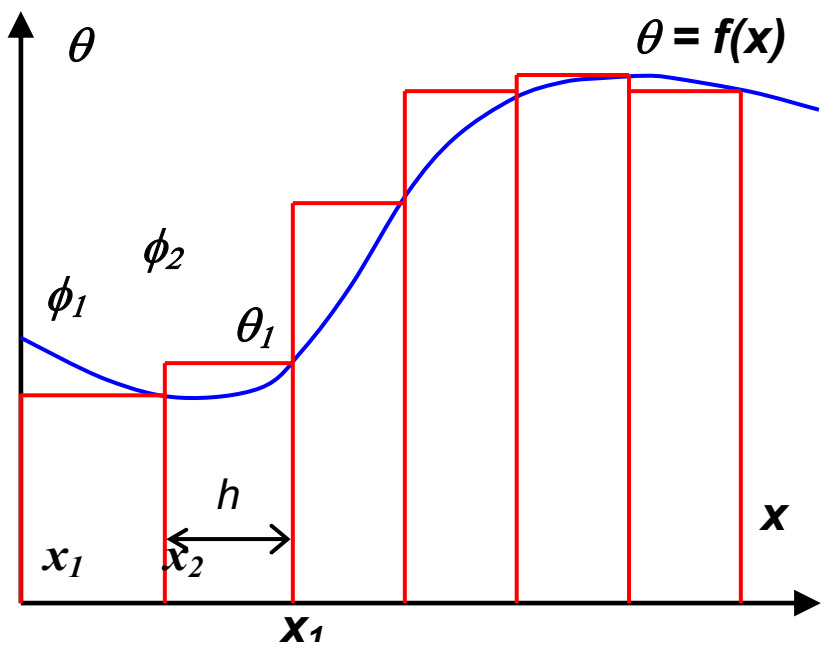

Figure 7.46
Illustration of Rieman's rule of integration used to compute displacements

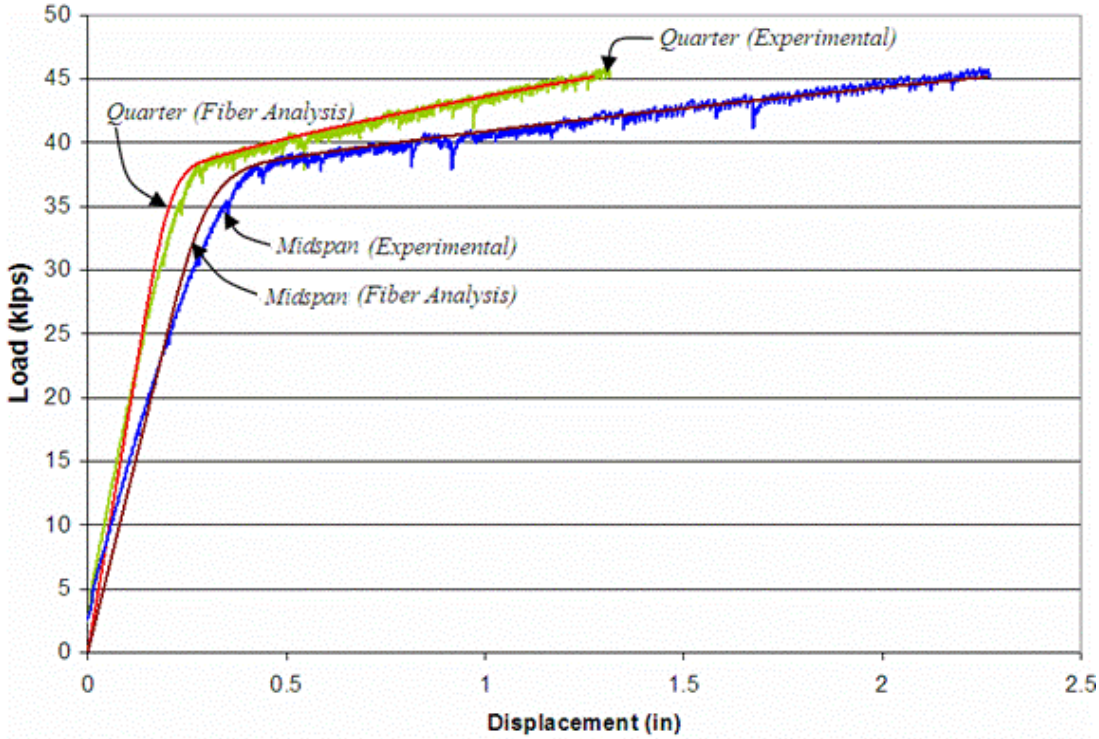

Figure 7.47
Load-displacement comparisons between fiber analysis and experimental data (A7-Beam 1)

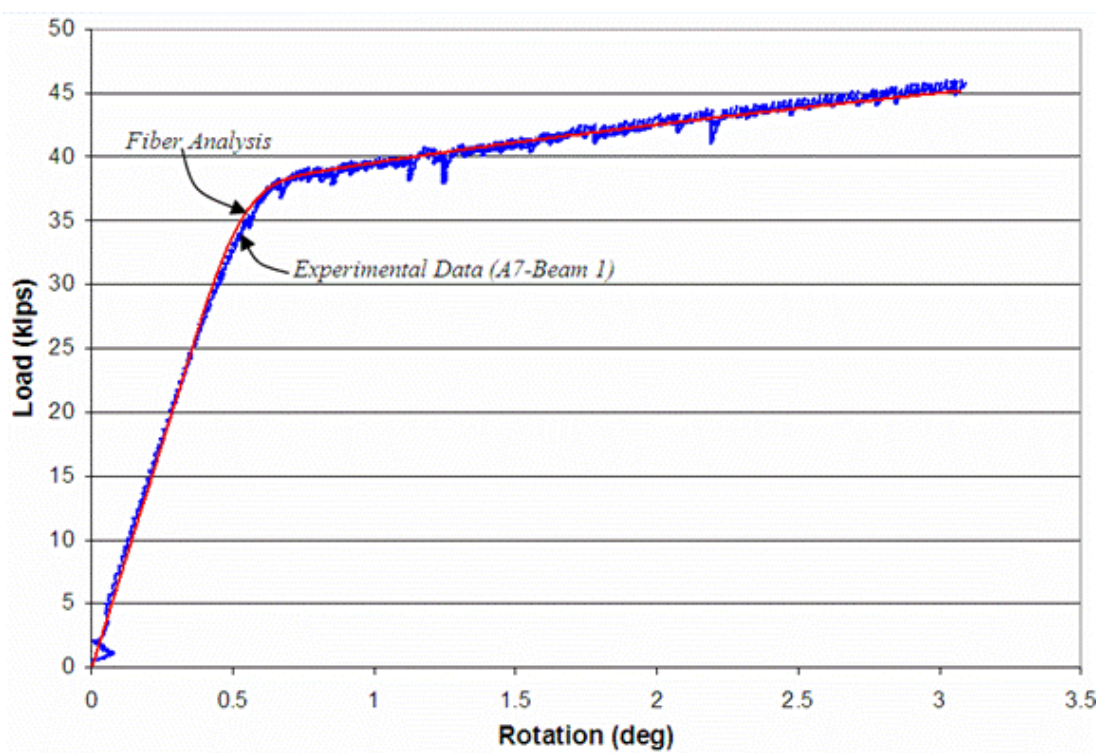

Figure 7.48
Load-rotation comparisons between fiber analysis and experimental data (A7-Beam 1)

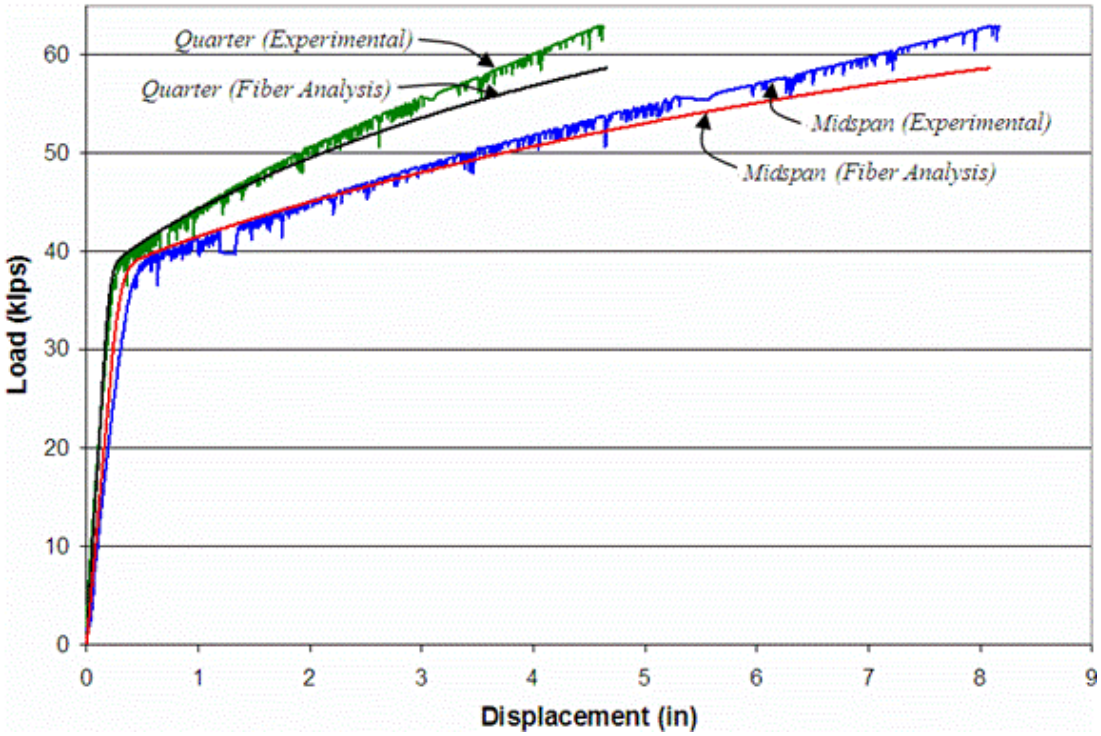

Figure 7.49
Load-displacement comparisons between fiber analysis and experimental data (A7-Beam 2)

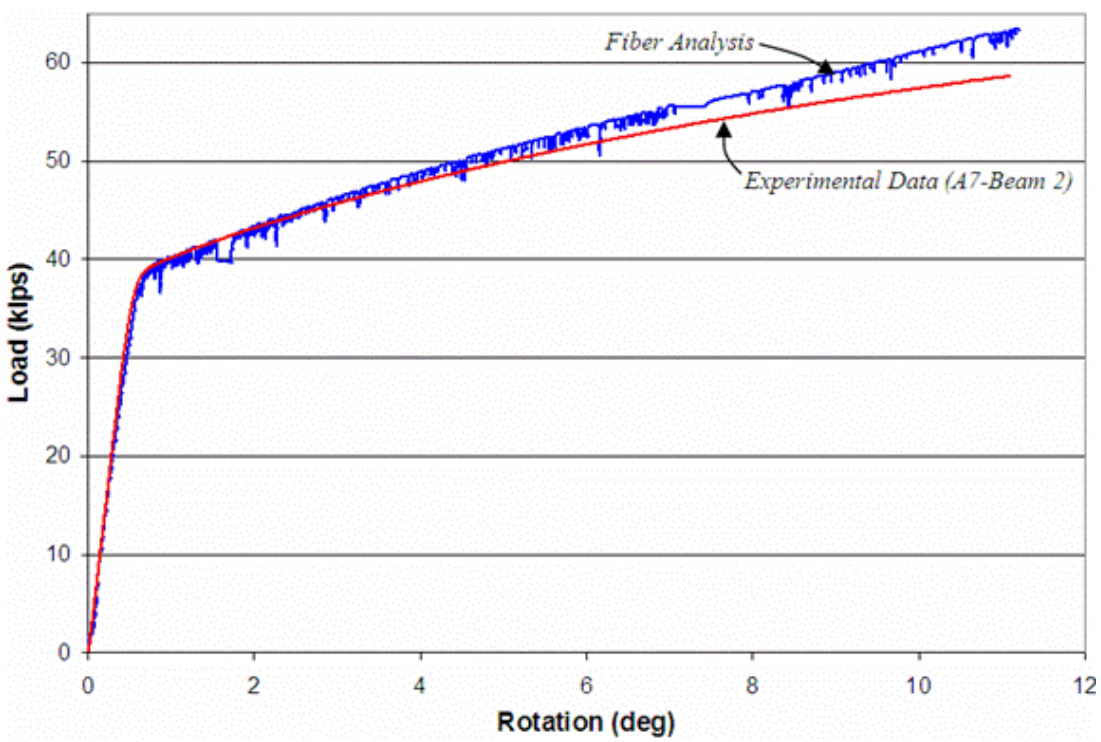

Figure 7.50
Load-rotation comparisons between fiber analysis and experimental data (A7-Beam 2)

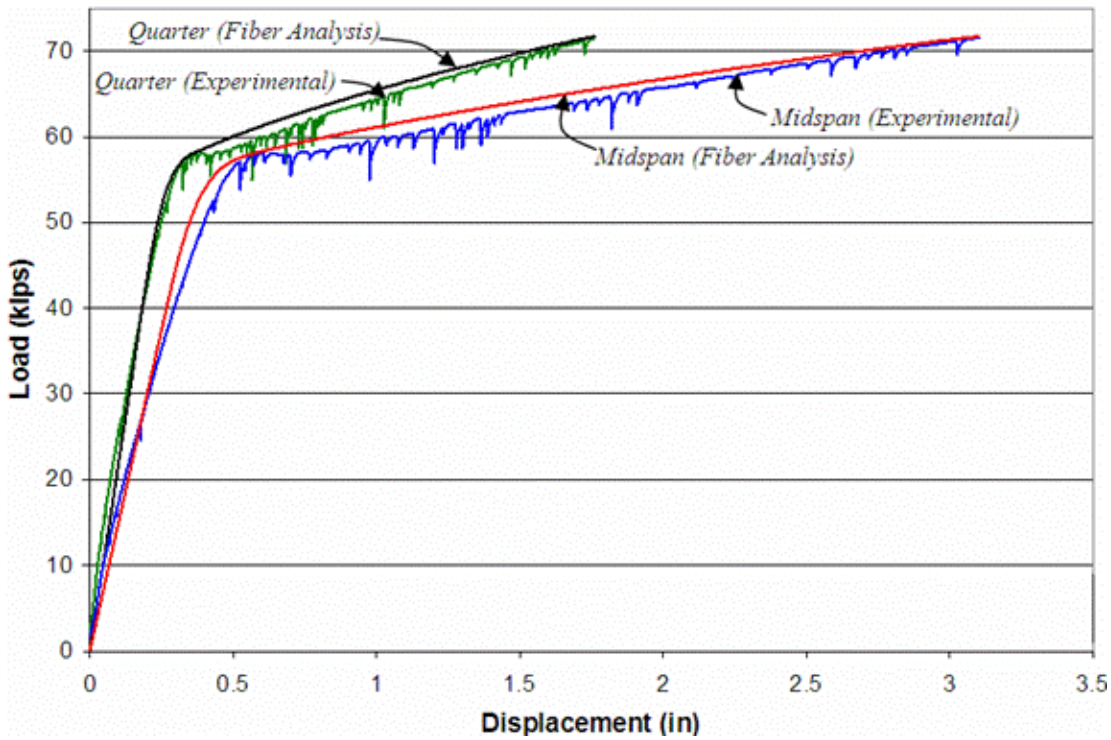

Figure 7.51
Load-displacement comparisons between fiber analysis and experimental data (A36-Beam 1)

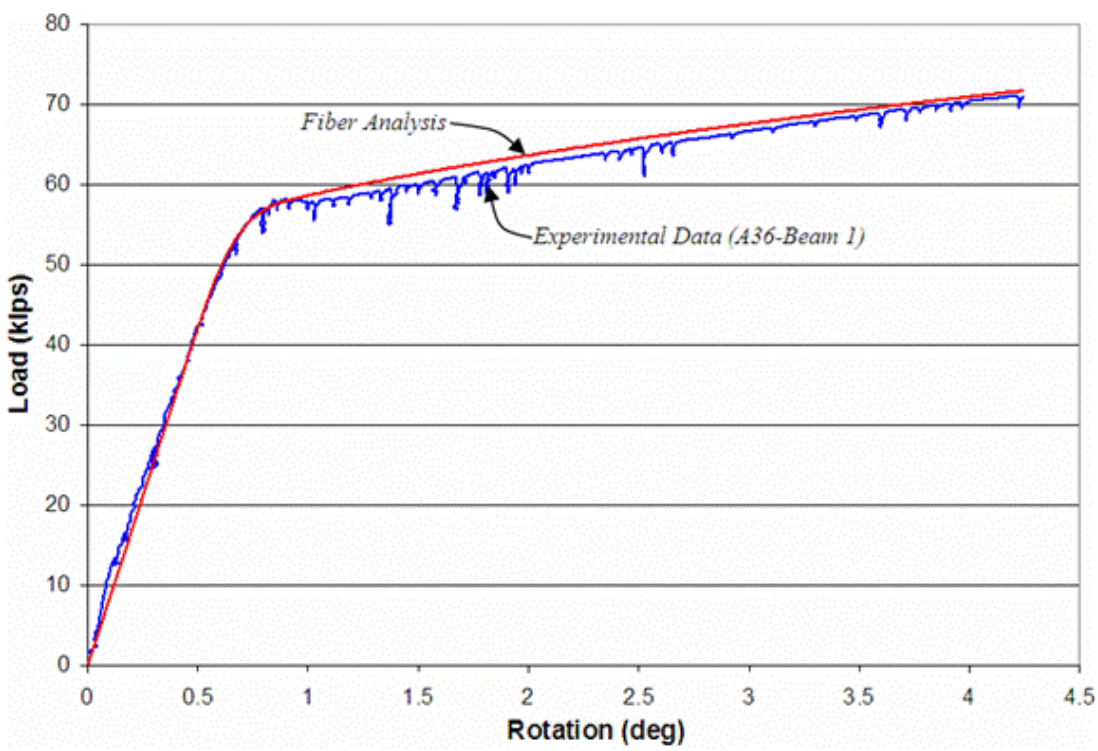

Figure 7.52
Load-rotation comparisons between fiber analysis and experimental data (A36-Beam 1)

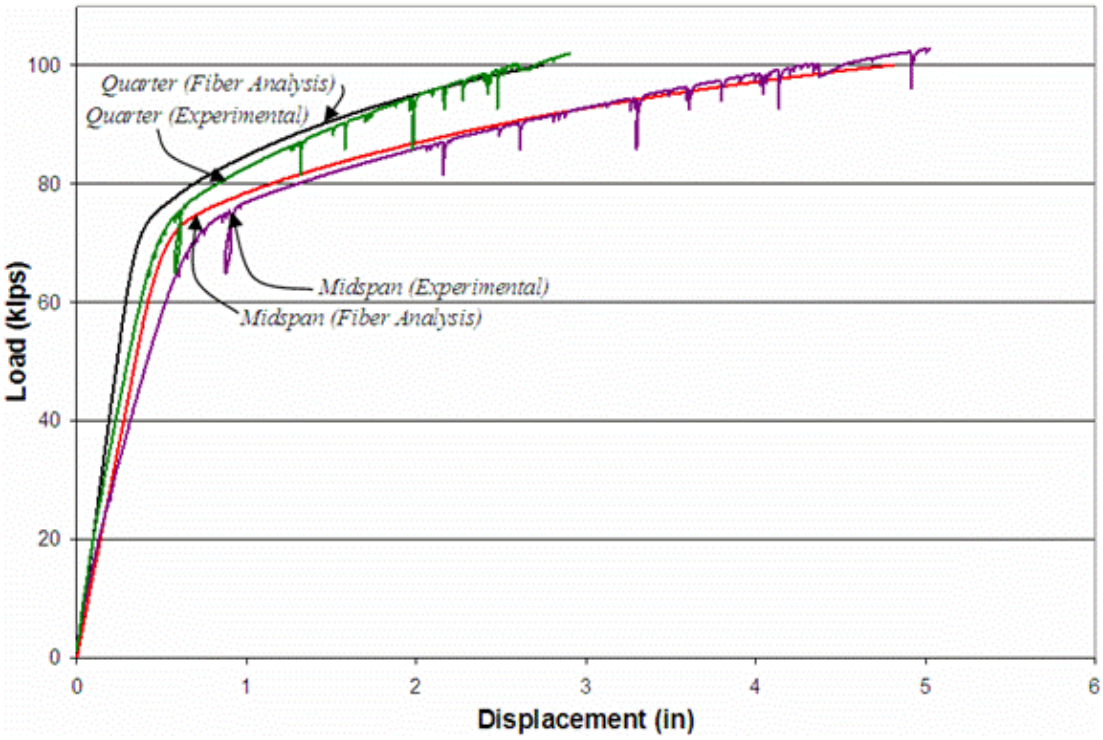

Figure 7.53
Load-displacement comparisons between fiber analysis and experimental data (A588-Beam 1)

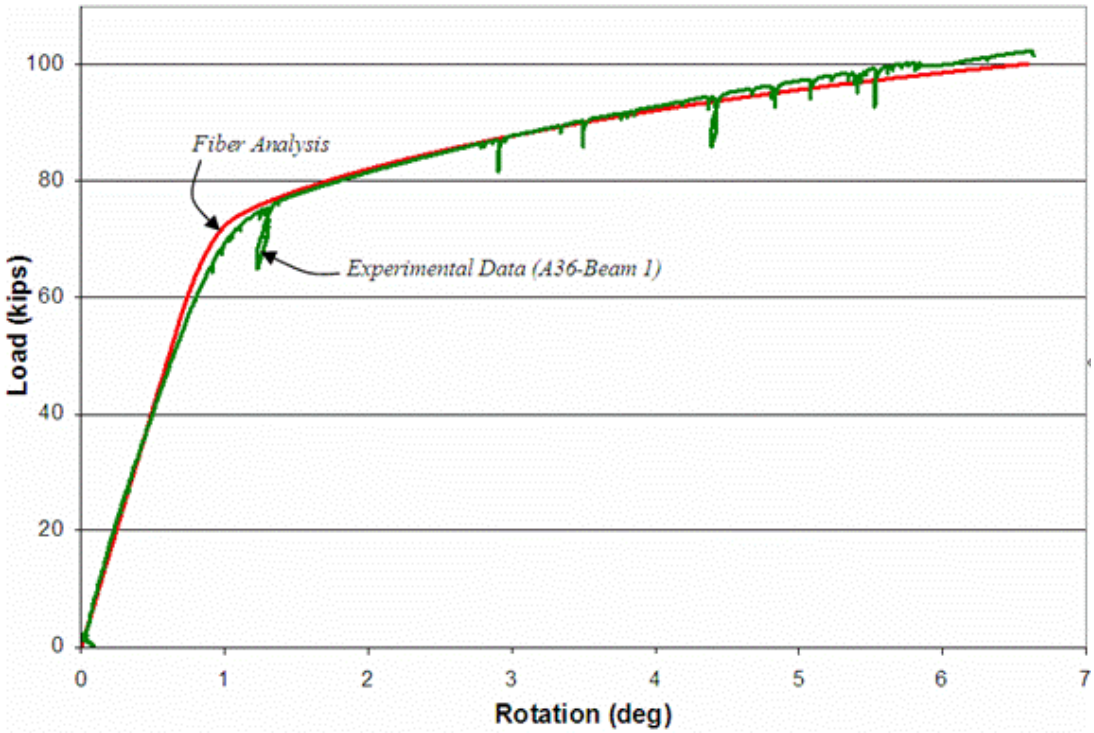

Figure 7.54
Load-rotation comparisons between fiber analysis and experimental data (A588-Beam 1)

[Intentionally Blank Page]

8 EXPERIMENTAL BEHAVIOR AND RESULTS FROM LARGE-SCALE BEAMS

8.1 EXPERIMENTAL DAMAGE-REPAIR HISTORY

Six large-scale beam specimens were tested by subjecting them to multiple damage-heat straightening repair cycles. These beams specimens and the damage and heat straightening repair parameters were presented in Table 7.1. The following sections, 8.1.1, 8.1.2, 8.1.3, 8.1.4, 8.1.5, and 8.1.6, summarize the damage and heat straightening repairs conducted on A7-Beam 1, A7-Beam 2, A36-Beam 1, A36-Beam 2, A588-Beam 1, and A588-Beam 2, respectively. Each sub-section summarizes the three damage cycles and the three repair cycles of the corresponding beam. For example, Section 8.1.1.1 summarizes all three damage cycles conducted on A7-Beam 1 and Section 8.1.1.2 summarizes all three repair cycles conducted on A7-Beam 1

The experimental behavior of the beam specimens during the damage cycles is presented and discussed using the data provided by the instrumentation (see Section 7.5.1). As mentioned previously, the longitudinal strain gages worked well during the first damage cycle only. Hence, the load-strain P-ε behavior during the first damage cycle and the load-midspan deflection P-Δ and the load-end rotation P-θ during all three damage cycles are shown. These comparisons indicate the change in strength and stiffness of the beam after the previous damage-repair event. Photographs of the beam specimens before and after the first damage cycle are provided. Other significant information noted during the experimental damage cycles is provided.

The behavior of the beam specimens during the repair cycles is presented using some of the data provided by the instrumentation (see Section 7.5.2). At least one figure which shows the pressure in the hydraulic jack, the temperature at the surface of the Vee heated steel, and the deflections measured by the displacement transducers is provided for each steel type. The final condition of the damaged-repaired beam specimens are also shown and discussed. Finally, the number of Vee heats required to repair each damage cycle is also reported. A frequency chart showing the total number of times each Vee was heated is also shown for the beam specimens. All three repair cycles are combined in the development of these frequency charts.

8.1.1 A7-Beam 1

8.1.1.1 Damage cycles

Longitudinal strain gages were used to monitor the longitudinal strains during the first damage cycle of A7-Beam 1. These strain gages were located slightly differently than the layout mentioned in Section 7.5.1:

- Two strain gages were bonded to the top of the front and back flanges as in Figure 7.11 (one each).
- Two strain gages were bonded close to the bottom of the front and back flanges (one each). These gages were too close to the bearing contact with the concentrated force, which causes localized multiaxial strains. These strain gages did not provide useful data, and were moved further away from the contact point for future beam specimens.
- One strain gage was bonded 3 in. from the top of the front flange as in Figure 7.11. This is referred to as the “Front_Middle” strain gage.
- One strain gage was bonded 1 in. below the top of the front flange. This strain gage provided redundant measurements for the first damage cycle and is referred to as the “Front Top_2” strain gage.

The beam specimen was damaged by monotonically increasing the concentrated force. The damage was monitored using the longitudinal strain gages. The test was considered complete when the average value of front top and back top strain gages reached 30 ε_y (0.036 in/in). The complete strain gage data for the first damage cycle is shown in Figure 8.1. Figure 8.2 shows the initial loading slopes of the strain gage readings during the first damage cycle. This figure clearly indicates that the placing strain gages directly at the bottom results in unreliable readings. Figure 8.3 shows photographs of the beam specimen before (a) and after (a) the first damage cycle.

For the second and third damage cycles, four strain gages were attached to the beam. Two gages were bonded to the top of the front and back flanges (see Figure 7.11), and two strain gages were bonded 1.5 in. from the bottom of the front and back flanges (see Figure 7.11). The initial intent was to use the front and back top strain gages to control the level of damage during the second damage cycle. However, the flanges had undergone out-of-plane distortions after the first damage-repair cycle. As a result, the front and back top strain gage data were unreliable as shown in Figure 8.4.

The researchers reviewed the results of the first damage cycle and conducted subsequent damage cycles in displacement control. The plastic displacement after the first cycle of damage was found to be 2.7 in. Therefore, the beam was damaged to a displacement of 2.7 in. in the second damage cycle. The amount of elastic recovery had been underestimated, and the final damage displacement for the second damage cycle was slightly lower than the damage displacement for the first damage cycle. The beam specimen was also subjected to a midspan displacement of 2.7 in. during the third damage cycle. The front and back top strain gages were moved 2 in. below the top to avoid poor measurements due to flange curvature. This approach also did not work well.

Figure 8.5 shows the P-Δ relationships for all three damage cycles. As shown in Figure 8.5, the load required for a higher beam displacement is significantly higher for subsequent damage cycles. However, the load required to cause a low displacement is reduced. Figure 8.6 shows the P-θ relationships for all three damage cycles.

8.1.1.2 Repair Cycles

Repair cycles 1, 2, and 3 were conducted by applying external forces causing restraining moments (M_r) of 0.25 M_p, 0.50 M_p, and 0.25 M_p at the midspan, respectively. The first repair cycle was initially conducted using simultaneous Vee heats applied at the center (C) Vee of the front and back beam flanges. This process progressed well until the heated area began distorting out-of-plane. The researchers conducted the plastic strain distribution analysis presented in Section 7.7.2, and applied further heats strategically to other Vees (R1, L1, R2, and L2, etc.) besides the center (C) one.

The second and third repair cycles for A7-Beam 1 progressed smoothly. The resistance of the beam to heat straightening increased after several heats probably due to the build up of residual stresses in the cross-section. However, the displacements and rotations required to straighten the beam were achieved successfully. Twenty-six Vee heats were required to complete the first repair cycle, i.e., repair the damage caused by the first damage cycle. Fourteen Vee heats were required to repair the second damage cycle, and thirty-eight Vee heats were required to repair the third damage cycle. The frequency chart indicating the amount of Vee heats applied to each location is shown in Figure 8.7.

- Figure 8.8 shows the data from second repair cycle. This figure includes: (a) the displacements from the four displacement transducers in inches, (b) the pressure in the hydraulic jacks in ksi, and (c) the temperature of the steel in F, which is divided by 1000 (i.e. 1.0 on the graph corresponds to 1000 °F) for clarity.
- Figure 8.9 shows the same data for the first four heats of the third repair cycle. This figure indicates that approximately 0.1 in. midspan deflection was achieved for each Vee heat at a restraining moment of 0.25 M_p. It also shows that as the temperature of the steel increases, the load slightly increases and

as the material expands. As more heating cycles were applied during repair cycle 3, the load increased more considerably and less movement was achieved during each heating cycle. The beam resisted the repair more as the repair progressed.

- Figures 8.10 and 8.11 show the condition of the beam specimen after three damage-repair cycles. Figure 8.10 shows the full beam and Figure 8.11 shows the out-of-plane distortion that remained in the front and back flanges.

For the first repair of A7-Beam 1, the first six Vee heats were all applied directly to the center Vee heat (*C*). For the majority of repair cycles on all beam specimens, the location of the Vee heat was altered immediately after the first or second Vee heat was applied to the center (*C*). An additional analysis was conducted using the first six heats of the first repair cycle to study the load and displacement behavior of the beam for multiple Vee heats applied to the same location. Previous research investigations have indicated that the amount of displacement achieved reduces for multiple Vee heats applied to the same location. This behavior was also noticed during the experimental investigations of this research project.

Also observed during the experimental investigations was a significant increase in the load while subjecting the beam to several heating cycles to the same location. The chart used to conduct this analysis is shown in Figure 8.12. The center displacement is shown in inches and the load is given in kips and is divided by 20 to be seen on the same plot. The target load was approximately 11 kips. The dashed line in Figure 8.12 shows that approximately equal loads were applied to the beam before heating each cycle. The dashed line indicates that higher loads occurred for additional heating cycles due to the beam resisting the downward movement. The increase in loads while heating the beam was not caused by the researcher applying an initial higher load.

In this analysis, the increase in load was measured from the point when the Vee heat started to the maximum load achieved as the material expanded. The load increase is illustrated using an example in Figure 8.13. The amount of displacement achieved during each heating cycle was measured between the points where loads were applied as illustrated in Figure 8.13. This was the most logical place to estimate the amount of movement achieved during each heating cycle as the beam was subjected to equivalent loads. Since the beam was not reloaded after the sixth heating cycle, the amount of displacement achieved during the sixth heating cycle was unknown using this procedure. The results of this displacement analysis are provided in Table 8.1. Table 8.1 indicates that the load increases for subsequent Vee heats to the same location. The amount of displacement achieved during each heating cycle decreased for subsequent heating cycles with the exception of Heat 3 as opposed to Heat 4. After reviewing the results in Table 8.1, it appears as if a higher amount of movement was achieved during Heat 4 than expected. This analysis was also conducted during the first repair cycle of A588-Beam 2, which is discussed in Section 8.1.6.2.

8.1.2 A7-Beam 2

8.1.2.1 Damage Cycles

For the first damage cycle of A7-Beam 2, the strain gage layout as described in Section 7.5.1 was used (see Figure 7.11). Two strain gages were attached to the top of either flange, two were attached 3.0 in. ($b_f/3$) from the top, and two were attached 1.5 in. ($b_f/6$) from the bottom. The beam specimen was loaded to achieve an average strain of 90 ε_y (0.108 in/in) in the extreme tension fiber as indicated by the front and back top strain gages. This required a total midspan deflection of approximately 8.5 in. However, the hydraulic jack pushing the beam upwards had a stroke of only 6 in. Therefore, the beam had to be unloaded, the loading setup readjusted, and the beam re-loaded to achieve the required damage strain and deflection level.

Towards the end of the first damage cycle, the bottom of front flange (close to the contact point with the applied force) buckled inwards towards the web of the section. This local buckling progressed very slowly and was not observed visually until close to the end of the damage cycle. Figure 8.14 shows the *P-ε* data for the first damage cycle. Due to buckling, the strain gage at the bottom of the front flange began to debond. Figure 8.15 shows the beam specimen before and after the first damage cycle.

Damage cycles 2 and 3 were conducted even more cautiously than the first damage cycle due to the condition of the bottom of the front flange. Both these damage cycles were conducted in displacement control, because the front and back top strain gage data had become unreliable due to the flange curvature from heating. The target displacement for the 60 ε_y damage strain cycles had been noted in the previous 90 ε_y damage cycle. These target displacements were used carefully by the researchers to control the damage during the second and third cycles.

- During the second damage cycle, all the displacements and end rotations compared favorably with the corresponding values noted from the first damage cycle when ε_d=60 ε_y. Therefore, the midspan displacement transducers (12 in. stroke) were used to control the damage cycle.
- During the third damage cycle, the midspan displacement transducers did not compare favorably with noted values or with each other. However, the quarter length (6 in. stroke) displacement transducers and the end rotations compared favorably with each other and the noted values. Therefore, the third damage cycle was controlled using the end rotation and quarter length displacement measurements.

Figure 8.16 compares the load-displacement relationships for the three damage cycles. The figure includes data from one 6 in. stroke displacement transducer at quarter length and one 12 in. stroke displacement transducer at midspan. Figure 8.17 shows and compares the front flange end rotations for all three damage cycles. Figures 8.16 and 8.17 indicate that the bending strength of the beam increases after one damage-repair cycle and then increases slightly after the second damage-repair cycle.

While conducting the second and third damage cycles, the bottom of the front flange continued buckling inwards. However, all three damage-repair cycles were completed successfully. The condition of the bottom of the front flange after all three damage cycles is shown in Figure 8.18.

8.1.2.2 Repair Cycles

All three repair cycles of A7-Beam 2 were conducted by applying an external restraining moment (M_r) of $0.50\ M_p$. The first repair cycle took 4 days and a total of seventy-five Vee heats on both sides in order to complete. The second and third repair cycles took 3 days and approximately sixty Vee heats each to complete. The frequency distribution of the total number of Vee heats with respect to location is shown in Figure 8.19.

The Vee heats were strategically applied along the length of the beam. Strip heats were also applied to the bottom of the front flange in order to straighten out the buckled flange. This was crucial to aid in re-damaging the beam during the second and third damage cycles. Strip heats were also applied to the web of the beam since the plastic strain analysis of Section 7.7.2 indicated plastic strains were being induced in the web. This did not benefit the researchers as much as expected. Since the researchers intended on taking material coupons from the flanges, the web was left with slight curvature after experimental investigations. Figure 8.20 shows the locations of the web strip heats.

During the third repair cycle, the torch used to apply Vee heats to the back flange of the beam was replaced since it was behaving poorly. The new torch provided more heat flux to the specimen and it seemed that the researcher might have overheated the back flange occasionally. The overheating temperatures were less than 1350 °F. However, once this was noticed, future heats were applied more carefully to restrict the maximum temperature to 1200 °F.

- Figures 8.21 to 8.23 show the final condition of the beam specimen (A7-Beam 2) after three damage-repair cycles.
- Figure 8.21 shows the full beam span from the front side.
- Figure 8.22 shows the final condition of the center of the front (a) and back (b) flanges. The red spots seen in Figure 8.21(b) are induced from a lack of acetylene supply from the torch and not from overheating.
- Figure 8.23 shows the lateral displacement of the front (a) and back (b) flanges.

After completing the third damage-repair cycle, the researcher attempted more strip heats to repair the local buckling at the bottom of the front flange. However, during the first strip heat itself; the flange fractured (tore) slightly at the crest of the local buckling. This can be seen clearly in Figure 8.24. The researcher halted and left the flange bottom as it was.

Heat straightening the beam specimen caused the flanges to curve slightly outwards. While the exact reason for this curving is not known, it is speculated that slight unavoidable eccentricities of loading and heating with respect to the mid thickness of the flange caused it. The beam specimen was removed from the test setup and line heats were applied along 5 in. lines of the top k-region in order to straighten the flanges longitudinally. An illustration of line heats applied to the inside of the flanges at the k-region is shown in Figure 8.25. The next heating cycle involved applying 5 in. line heats to the k-regions in between the line heats from the previous cycle.

An external restraining force was provided by using a large clamp with a nominal pressure of 4.88 kips and pulling the two flanges together as shown in Figure 8.25. The level of restraining force was limited to the researcher's ability to twist the clamp, which could not be measured. After applying several line heats, the flanges moved approximately 0.75 in. towards each other at midspan. This procedure was also used as an aid for other beam specimens (i.e. A7-Beam 1, A588-Beam 1, and A588-Beam 2) but not as much as for A7-Beam 2.

The damage-repair of A7-Beam 2 did not proceed efficiently. A number of problems had to be addressed and the repair focused only on the vertical displacement of the beam specimen. The restraining force caused unintentional out-of-plane distortions of the flanges. It would seem that the amount of damage subjected to this test specimen was too high for the researchers to control with the test setup capabilities. The researchers therefore decided it beneficial to limit the magnitude of damage induced to further A36 and A588 beam specimens.

8.1.3 A36-Beam1

8.1.3.1 Damage Cycles

In all three damage cycles, A36-Beam 1 was loaded to achieve the required displacement to cause an average strain of 30 ε_y (0.045 in/in) in the extreme tension fiber as indicated by the front and back top strain gages. The strain gage layout as described in Section 7.5.1 (see Figure 7.11) was used for the first damage cycle. Two strain gages were attached to the top of either flange, two were attached 3.0 in. ($b_f / 3$) from the top, and two were attached 1.5 in. ($b_f / 6$) from the bottom. The strain gage data from the first damage cycle is provided in Figure 8.26. The condition of A36-Beam 1 before (a) and after (b) the first damage cycle is provided in Figure 8.27.

Damage cycles 2 and 3 were conducted much more smoothly than the multiple damage cycles conducted on the A7 beam specimens. In general, all rotation meters and displacement transducers related well to each other when comparing what was observed during the first damage cycle. Figure 8.28

compares the P-Δ behavior of all three damage cycles of A36-Beam 1. The quarter displacements are not shown for clarity. Figure 8.29 compares the P-θ behavior of all three damage cycles of A36-Beam 1.

As shown in Figures 8.28 and 8.29, the initial bending stiffness of the beam was affected after the first damage-repair event. Also distinguished in Figures 8.28 and 8.29 is that the bending strength of the beam increases for higher displacements after each damage-repair event. These behaviors are likely due to built-up residual stresses along the flange plates and not as substantially due to significant material property changes (i.e. σ-ε relationships). However, the A36 material is becoming a little stronger after damage-repairs, which was verified after the material testing results of Section 8.2.2.1. Since the onset of nonlinearity happens at a substantially lower load, the induced residual stresses must be quite significant.

8.1.3.2 Repair Cycles

Repair cycles 1, 2, and 3 of A36-Beam 1 were conducted by applying external forces corresponding to restraining moments (M_r) of 0.25 M_p, 0.50 M_p, and 0.25 M_p, respectively. The first repair cycle took 2 days and thirty-nine Vee heats on both sides in order to complete. The second repair cycle took less than 1 day and sixteen Vee heats to complete. The third repair cycle took 2.5 days and fifty Vee heats to complete. The frequency distribution of the total number of Vee heats with respect to location is shown in Figure 8.30. All three repair cycles progressed well. Some out-of-plane distortions were noticed in the flanges. The final condition of the beam specimen was much better than the final condition of the A7 beam specimens.

- Figures 8.31 and 8.32 show the final condition of the beam specimen (A36-Beam 1) after three damage-repair cycles.
- Figure 8.31 shows the full beam span from the front side.
- Figure 8.32 shows the out-of-plane curvature of the flanges.

8.1.4 A36-Beam2

8.1.4.1 Damage Cycles

A36-Beam 2 was subjected to three damage-repair cycles, where each damage cycle corresponded to an average damage strain of 30 ε_y (0.045 in/in). The damage strain in the first cycle was measured using the strain gage layout described in Section 7.5.1 (see Figure 7.11). Two strain gages were attached to the top of either flange, two were attached 3.0 in. ($b_f / 3$) from the top, and two were attached 1.5 in. ($b_f / 6$) from the bottom. One of the bottom strain gages debonded while testing. The strain gage data from the first damage cycle is provided in Figure 8.33. The condition of A36-Beam 2 after the first damage cycle was very similar to that of A36-Beam 1 (refer to Figure 8.27).

Damage cycles 2 and 3 were conducted under displacement control, where the displacement at midspan reached the required magnitude. Figure 8.34 compares the P-Δ behavior of all three damage cycles of A36-Beam 2. The quarter displacements are not shown for clarity. Figure 8.35 compares the P-θ behavior of all three damage cycles of A36-Beam 2. In all three damage cycles of A36-Beam 2, the back flange appeared to displace and rotate slightly more than the front.

As shown in Figures 8.34 and 8.35, the initial stiffness of the beam has been affected after the first damage-repair event similar to that found for A36-Beam 1. This behavior is likely due to built-up residual stresses in the cross section. Figures 8.34 and 8.35 also indicate that the bending strength of the beam increases for higher displacements after each damage-repair event. The increase is very similar to A36-Beam 1 but the load increase in not as significant. The material becomes stronger after damage-repairs, which was verified after the material testing results of Section 8.2.2.1.

8.1.4.2 Repair Cycles

Repair cycles 1, 2, and 3 of A36-Beam 2 were conducted by applying external forces corresponding to restraining moments (M_r) of 0.25 M_p, 0.50 M_p, and 0.25 M_p, respectively. These restraining forces were equal to those used for A36-Beam 1. The difference was that each Vee heat was subjected to a maximum temperature of 1400 °F as opposed to 1200 °F. The color of the Vee at a maximum temperature of 1400 °F is shown in Figure 8.36 (a). Figure 8.36(b) shows the color of a Vee heat on A36-Beam 1 at a maximum temperature of 1200 °F for comparison. Figure 8.37 shows the color of the backside of the front flange at slightly lower temperatures than 1400 °F.

Twenty Vee heats on both flanges were required to complete the first repair cycle. The second repair cycle took nineteen Vee heats to complete. The third repair cycle took twenty-nine Vee heats to complete. Repair cycles on A36-Beam 1 took thirty-nine, sixteen, and fifty Vee heats to complete. The frequency distribution of the total number of Vee heats with respect to location is shown in Figure 8.38.

Figure 8.39 shows the behavior of A36-Beam 2 during the second repair cycle. In Figure 8.39, the center displacement (back side) and quarter displacement (right side) are shown positive as the beam descends in inches. The pressure in the hydraulic jack is shown in ksi. The temperature of the steel is given in degrees Fahrenheit and is divided by 1000 to be seen on the same graph. The temperature in Figure 8.39 was measured at the center Vee (*C*), and it is lower than 1400 ºF for cases where the heat was applied to other Vees.

The displacement behavior of this specimen was found to be quite unique. For the first few heating cycles, the steel material expands and the beam moves up. The beam descends slowly as it cools. For later Vee heats, the beam expanded but continued to ascend as the material cooled. The only downward movement occurred when the load was applied.

Some out-of-plane distortion was noticed in the flanges after the experimental investigations. The condition of the final beam specimen was in better condition than the previous beams specimens and flange straightening was not required for the removal of material coupons from the flanges.

- Figures 8.40 and 8.41 show the final condition of the beam specimen (A36-Beam2) after three damage-repair cycles.
- Figure 8.40 shows the full beam span from the front side.
- Figure 8.41 shows the out-of-plane curvature of the flanges.

8.1.5 A588-Beam1

8.1.5.1 Damage Cycles

In the first damage cycle of A588-Beam 1, the beam specimen was loaded to achieve an average strain of 40 ε_y (0.078 in/in) in the extreme tension fiber as indicated by the front and back top strain gages. For the first damage cycle, the strain gage layout as described in Section 7.5.1 was used (see Figure 7.17). Two strain gages were attached to the top of either flange, two were attached 3.0 in. ($b_f / 3$) from the top, and two were attached 1.5 in. ($b_f / 6$) from the bottom. One of the bottom strain gages debonded while testing. The strain gage data from the first damage cycle is provided in Figure 8.42.

During the first damage cycle, the spread of yielding was seen with the peeling of mill scale at the surface. Figure 8.43 shows a close up of the yielded area. The surface began to look as in Figure 8.43 at locations with a damage strain of approximately 10-15 ε_y or higher. It appears that more yielding is occurring at the bottom of the beam specimen as opposed to the top of the beam specimen. This theory may be contradicted as the bottom of the beam is in compression instead of tension, which may peal the

mill scale at smaller damage strains. The conditions of A588-Beam 1 around 4 ε_y and after the first damage cycle are shown in Figures 8.44(a) and (b), respectively.

Damage cycles 2 and 3 were conducted until the displacement transducers at midspan (front and back) reached the required magnitude of displacement to cause a damage strain of 20 ε_y at the extreme tension fiber. The required magnitude of displacement was found by relating to the first damage cycle of 40 ε_y. The condition of the beam after the third damage cycle corresponding to 20 ε_y is shown in Figure 8.45.

Figure 8.46 compares the P-Δ behavior of all three damage cycles of A588-Beam 1. The quarter displacements are not shown for clarity. Figure 8.47 compares the P-θ behavior of all three damage cycles of A588-Beam 1. As shown in Figures 8.46 and 8.47, the P-Δ and P-θ behaviors of the beam specimen during the second and third damage cycles appear very similar. The stiffness of the beam has been affected after the first damage-repair event. It also appears as if the bending strength of the beam increases slightly for higher displacements after the first damage-repair event. The material testing results on small-scale test specimens (see Section 6.2) have indicated that the strength of A588 steel does not increase significantly after damage-repair cycles. Therefore, both the strength and stiffness changes are likely due to built-up residual stresses along the cross-section and not due to significant material changes (i.e. σ-ε relationships).

8.1.5.2 Repair Cycles

All three repair cycles of A588-Beam 1 were conducted using an external restraining moment (M_r) of 0.25 M_p. The Vee heats were subjected to a maximum temperature of 1200 °F and applied strategically along the length of the plastic damage region, which was determined as described in Section 7.7.2. Since the specimen was subjected to so many heating cycles during the first repair cycle, the out-of-plane curvature of the top flanges became significant. The researcher added Vee heats in between L1 and L2, as well as R1 and R2. These Vee heats were identified as RC and LC, where the nomenclature identified the right and left contact points. The center of these Vee heats was directly at the contact points. The Vee heats were 4.5 in. wide and along half the depth. These are the same dimensions as all other Vee heats applied to the beam specimens. These locations was not heated on the first four beam specimens as the researchers were concerned about the threaded rods becoming too hot as well as localized indentions which may occur significantly at the contact points. However, the researcher sensed that applying these heats might benefit the repair substantially. Applying Vee heats to RC and LC aided the displacement of the beam and did not cause damage to the threaded rods or significant indentions to the top of the flanges. Therefore, these Vee heats were applied during all repairs on both A588 beam specimens.

The first repair cycle took 89 Vee heats on each side to complete. The second repair cycle took 33 Vee heats to complete. The third repair cycle took 40 Vee heats to complete. The frequency distribution of the total number of Vee heats with respect to location is shown in Figure 8.48.

The condition of A588-Beam 1 after three damage-repairs was found to be better than A7-Beam 2 but more out-of-plane curvature was found in the flanges than other A7 or A36 beam specimens. Therefore, the beam flanges were clamped together as shown in Figure 8.25 and strategic line and strip heats were applied within the bent region as shown in Figure 8.49. The researcher applied enough heating cycles to the flanges in order to remove straight material coupons. In order to ensure that the flanges were straight enough, the researcher laid a 0.5 in. wide steel tape, 8 in. long at the center of the flanges. This is the size, along the thickness, of the uniaxial tension coupon.

- Figures 8.50 and 8.51 show the final condition of the beam specimen (A588-Beam 1) after three damage-repair cycles.
- Figure 8.50 shows the full beam span from the front side.

- Figure 8.51 shows the out-of-plane curvature of the flanges before (a-b) and after (c-d) straightening.

8.1.6 A588-Beam 2

8.1.6.1 Damage Cycles

In the first damage cycle of A588-Beam 2, the beam specimen was loaded to achieve an average strain of 40 ε_y (0.078 in/in) in the extreme tension fiber as indicated by the front and back top strain gages. The strain gage layout as described in Section 7.5.1 was used (see Figure 7.11) with additional strain gages. Two strain gages were attached to the top of either flange, two were attached 3.0 in. ($b_f / 3$) from the top, and two were attached 1.5 in. ($b_f / 6$) from the bottom. One of the bottom strain gages debonded while testing. Strain gage data from the first damage cycle is provided in Figure 8.52. The condition of A588-Beam 2 after the first damage cycle was very similar to that of A588-Beam 1 (Refer to Figures 8.43 and 8.44). Mill scale peeled off in the plastic damage region similar to A588-Beam 1 as shown in Figure 8.43.

Four additional strain gages were attached along the top of the front flange. These strain gages were placed along the center lines of Vee heat locations L4, L2, R2, and R4. These measurements were used and compared to validate the analytical plastic strain analysis presented in Section 7.7.2. The load-strain behavior as indicated by all strain gages attached to the top of the front flange is shown in Figure 8.44. As shown in Figure 8.44, plastic strains are clearly being induced at locations away from the beam center. The results of this analysis indicated that more strain was being measured by the strain gages away from midspan than that interpreted from fiber analysis. The maximum average elastic strain from the tops of R2 and L2 was found to be approximately 0.0336 in/in as opposed to the analytical result of 0.0278 in/in. The maximum average elastic strain from the tops of R4 and L4 was found to be approximately 0.0184 in/in as apposed to the analytical results of 0.0131 in/in. Reasons for the discrepancies are unknown.

Damage cycles 2 and 3 were conducted until the displacement transducers at midspan (front and back) reached the required amount of displacement to cause a damage strain of 20 ε_y at the extreme tension fiber. The condition of the beam after the second and third damage cycles was similar to A588-Beam 1 as shown in Figure 8.45.

Figure 8.54 compares the load-midspan deflection behavior of all three damage cycles of A588-Beam 2. Figure 8.55 compares the load-end rotation behavior of all three damage cycles of A588-Beam 2. As shown in Figures 8.54 and 8.55, the P-Δ and P-θ behaviors of the beam specimen during the second and third damage cycles appear very similar. The stiffness of the beam has been affected after the first damage-repair event. It also appears as if the bending strength of the beam increases slightly for higher displacements after the first damage-repair event. The P-Δ and P-θ behaviors of the beam specimen during the second and third damage cycles appear very similar as they did with A588-Beam 1. A comparison between the midspan P-Δ behaviors of A588-Beam 1 and A588-Beam 2 during their respected second and third damage cycles is shown in Figure 8.56. The P-Δ results for multiple damage cycles conducted to both beams are indeed very similar. It appears from this experimental data that applying a higher external restraining stress is having a negligible effect on the strength and stiffness of the A588 beam specimen.

8.1.6.2 Repair Cycles

All three repair cycles of A588-Beam 2 were conducted using an external restraining moment (M_r) of 0.50 M_p. The Vee heats were subjected to a maximum temperature of 1200 °F and applied strategically along the length of the plastic damage region. Additional Vee heats were applied to locations RC and LC as with A588-Beam 1.

The first repair cycle took 47 Vee heats on each side to complete. The second repair cycle took 20 Vee heats to complete. The third repair cycle also took 20 Vee heats to complete (repair cycles 1, 2, and 3 on A588-Beam 1 took 83, 33, and 40 Vee heats to complete, respectively). The frequency distribution of the total number of Vee heats with respect to location is shown in Figure 8.57.

Figure 8.58 shows the behavior of A588-Beam 2 during the second repair cycle. In Figure 8.58, the center displacement (back side) and quarter displacement (right side) are shown positive as the beam descends in inches. The pressure in the hydraulic jack is shown in ksi. The temperature of the steel is given in degrees Fahrenheit and is divided by 1000 to be seen on the same graph. The temperature in Figure 8.58 was measured at the center Vee (*C*), and it is lower than 1200 ºF for cases where the heat was applied to other Vees.

The condition of the final beam specimen was found to be very similar to A588-Beam 1. Therefore, the beam flanges were pulled together using the clamp shown in Figure 8.25. Similar line and strip heating patterns were applied to the bent flanges of A588-Beam 2 as illustrated in Figure 8.49.

- Figures 8.59 and 8.60 show the final condition of the beam specimen (A588-Beam 1) after three damage-repair cycles.
- Figure 8.59 shows the full beam span from the front side.
- Figure 8.60 shows the out-of-plane curvature of the flanges before (a-b) and after (c-d) straightening.

Additional load-displacement analyses were conducted using experimental data of the first repair cycle of A588-Beam 2. This analysis investigated the load increase and displacements achieved for subsequent heating cycles to the same location and was conducted similar to the load-displacement analysis conducted on A7-Beam 1 as discussed in Section 8.1.1.2. For the first repair of A588-Beam 2, the first six Vee heats were all applied directly to the center Vee heat (*C*). The seventh Vee heat was conducted on R1 which required the same amount of load for 0.50 M_p. Figure 8.61 presents the experimental data for the seven heating cycles used to conduct this analysis. Both the front and back center displacements were used and are shown in inches. The load is in kips and divided by 20 to plot on the same chart. The dashed line in Figure 8.61 shows that the researcher applied the same load at the beginning of each heating cycle. The load increased with each heating cycle as the steel expanded. The increase in load was determined as illustrated in Figure 8.13. The displacement achieved during each heating cycle was also determined as illustrated in Figure 8.13. The results of the load increases and displacements achieved during each heating cycle are summarized in Table 8.2. Table 8.2 indicates that the load increases more during subsequent Vee heating of the same location. The amount of displacement achieved decreased for subsequent heating cycles with the exception of the sixth heating cycle which increased with respect to the fifth heating cycle. From the experimental data in Figure 8.61, it appears that this discrepancy probably relates to the amount of time the steel was allowed to cool during the fifth heating cycle.

8.2 DAMAGE-REPAIRED MATERIAL TESTING RESULTS

This section summarizes the standard material tests conducted on material specimens removed from the flanges of the damaged-repaired beam specimens. The procedure for obtaining material specimens from the flanges of the damaged-repaired beam specimens was outlined in Section 7.6.2. Uniaxial tension coupons were removed from the back flange (Flange A) as shown in Figure 7.24. Charpy specimens were removed from the front flange (Flange B) as shown in Figure 7.25. Rockwell Hardness tests and microstructure investigations were conducted on charpy Specimen C-2 that is shown in Figure 7.25. The effects of multiple damage-heat straightening repair cycles were evaluated by developing similar comparison charts shown in Chapter 6 for Task III. The following sections present the results of the material testing and the comparisons with the corresponding undamaged material properties to evaluate the effects of multiple damage-repair cycles.

8.2.1 A7 Beam Specimens

8.2.1.1 Uniaxial Tension Tests

Uniaxial tension tests were conducted according to ASTM E8 on tension coupons from the damaged-repaired A7 steel beams. The flanges of the W24x76 steel beams had a total thickness of 0.64 in. The initial intent was to remove 0.50 in. thick and 8 in. long tensile specimens from the flanges as shown in Figure 7.18. However, due to significant curvature in the repaired flanges, the removal of such coupons was not possible. Only specimens from the position labeled Z in Figure 7.25 could be removed with the full dimensions. This was the case for both A7 beam specimens. Specimens X and Y had reduced grip lengths of 1 in. as opposed to 2 in. The resulting specimens were only 6 in. long instead of 8 in. as shown in Figure 8.62. Additionally, to make all specimens straight, Specimen X from A7-Beam 1 had to be fabricated with a reduced thickness of 0.450 in. and Specimen X from A7-Beam 2 had to be fabricated with a reduced thickness of 0.383 in. These specimens are shown in Figure 8.62.

In order to investigate the impact of the reduced size, one specimen 6 in. long with a thickness of 0.383 in. was fabricated from the undamaged A7 material. The coupon was fabricated from flange segment TA. The results of the structural properties are compared to the average results of the four full size tensile specimens in Table 8.3. The values in Table 8.3 include the yield stress (σ_y), the elastic modulus (E), the yield strain (ε_y), the ultimate stress (σ_t), the strain at ultimate stress (ε_u), the strain ductility ($\varepsilon_u/\varepsilon_y$), the percent elongation, and the percent reduction (area) (refer to Section 4.9). The results in Table 8.3 indicate that there is a slight reduction of only 1% in the elongation of the reduced size specimen. The elastic modulus also differs slightly. The rest of the structural properties compare favorably well to the full size uniaxial tension specimen.

The uniaxial tension stress-strain (σ–ε) relationships from the coupons removed from A7-Beam 1 are shown in Figure 8.63. The σ–ε relationships from the coupons removed from A7-Beam 2 are shown in Figure 8.64. Figures 8.63 and 8.64 also include the σ–ε relationships of the undamaged specimen removed from flange Segment TA with full dimensions for comparisons. The results of the structural properties of both A7 beams are summarized in Table 8.4, which includes the individual results of X, Y, and Z as well as an average of the three of each beam. The damage-repaired steel material properties (σ_y, E, σ_t, and percent elongation) were normalized with respect to the undamaged steel material properties and plotted in Figures 8.65 (a-d).

Figure 8.65(a) shows the normalized yield stress for all damaged-repaired specimens. Figure 8.65(b) shows the normalized elastic modulus for all damaged-repaired specimens. Figure 8.65(c) shows the normalized ultimate stress, and Figure 8.65(d) shows the normalized percent elongation for all damaged-repaired specimens.

The yield stress data in Table 8.4 and Figure 8.65(a) indicate that:

- Damage-repair cycles increase the yield stress of A7 steel to approximately 108-123% of the undamaged steel.
- The yield stress increases more for specimens subjected to lower ε_d. This result is valid when comparing the trends of Specimens X, Y, and Z, as well as those from A7-Beam 1 and A7-Beam 2.

The elastic modulus data in Table 8.4 and Figure 8.65(b) indicate that:

- Damage-repair cycles do not have a significant influence on the elastic modulus of A7 steel. The elastic modulus slightly decreases in most cases but is not less than 93% of the undamaged steel.
- The change in elastic modulus does not have a clear or direct trend with the damage strain (ε_d).

The ultimate stress data in Table 8.4 and Figure 8.65(c) indicate that:

- Damage-repair cycles do not have a significant influence on the ultimate stress of A7 steel. The ultimate strength increases in all cases, but is never greater than 106% of the undamaged steel.
- The magnitude of damage strain (ε_d) appears to have a negligible effect on the ultimate stress. However, the tensile specimen subjected to the lowest ε_d (A7-Beam1-Z) did result with the highest ultimate strength and yield strength.

The percent elongation (ductility) data in Table 8.4 and Figure 8.65(d) indicate that:

- Damage-heat straightening repair reduces the percent elongation (ductility) of A7 steel. This reduction in ductility ranges from approximately 80%-95% of the undamaged material. This margin appears to be within an acceptable range.
- The change in ductility does not have a clear or direct trend with the damage strain (ε_d). It still appears that higher damage strains result in a higher ductility level as Specimens Z in both cases resulted in the lowest values.

8.2.1.2 Charpy Impact Fracture Toughness Tests

The results of the fracture toughness tests on damaged-repaired A7 steel are provided in Table 8.5. Averages were taken both across the width of the flanges (i.e. averages of 1, 2, 3, and 4) and along the flange length (i.e. averages of 1, 2, 3, or 4 for L1, C, and R1). The overall average and standard deviations of all twelve charpy specimens are also provided in Table 8.5. These fracture toughness values were normalized with respect to the average (mean) undamaged fracture toughness of undamaged A7 steel from Plate B only. The results from undamaged Plate B were only used for normalized ratios as Table 7.9 indicated a significant statistical difference between the fracture toughness of Plate A and Plate B (probability that the data sets are statistically similar=2%). The normalized fracture toughness values are also shown in Table 8.5. Figure 8.66 shows the normalized fracture toughness of the charpy specimens from the damaged-repaired beams. Table 8.6 provides the means, standard deviations, 95% confidence intervals for the actual mean, medians, and absolute average deviations from the median for the twelve charpy specimens removed from each beam specimen.

Student's t-test analysis was conducted to evaluate the statistical difference between the undamaged fracture toughness values and the fracture toughness of A7-Beam 1 and A7-Beam 2. As mentioned previously in Section 4.9.2, the t-test evaluates the statistical difference between two data sets using their respective means, standard deviations, and sample set sizes. The results from the t-test include the t-value and the corresponding probability of null hypothesis, where the null hypothesis implies that the data sets are statistically similar. Tables 8.7 and 8.8 compare the fracture toughness of A7-Beam 1 and A7-Beam 2 with the undamaged fracture toughness, respectively. Table 8.7 indicates less than 0.01% probability that

the data sets are statistically similar and Table 8.8 indicates an 86% probability that the data sets are statistically similar.

The results in Tables 8.5 to 8.8 and Figure 8.66 indicate that:

- The fracture toughness of A7-Beam 1 is much lower than the undamaged toughness. The beam has become unusable after three damage-repair cycles.
- The fracture toughness of A7-Beam 2 compares favorably with the undamaged toughness. However, some variability is seen in the results and the toughness of material closer to the flange-web junction (k-region) is lower.
- For both beams, the fracture toughness of the specimens from the center Vee heat (*C*) is lowest. The fracture toughness of specimens closer to the flange-web junction (k-region) is low.
- The results indicate that A7-Beam 2 has comparable fracture toughness with the undamaged material, but significant variation with much lower toughness values are also observed.

8.2.1.3 Rockwell Hardness and Microstructure Investigations

Rockwell hardness tests were conducted on damage-repaired A7 steel according to ASTM E18. Four points were taken on Specimens C-2, identified in Figure 7.24. Table 8.9 summarizes the averaged results of the Rockwell hardness tests and the microstructure investigations. Table 8.9 also provides comparisons between the approximate ultimate strengths as estimated by ASTM A370 to the actual results from Section 8.2.1.1.

Microscopic preparation was conducted using the procedures outlined in Section 7.6.1.3. The resulting microstructures of the two A7 steel beam specimens at 480X are shown in Figure 8.67 (Refer to Figure 7.23 for comparisons to undamaged steel). A clear reduction in the grain size is seen for A7-Beam 2. As discussed in Section 4.9.4, a more fine-grained microstructure is generally stronger and tougher than a more coarse-grained microstructure. There is a slight increase on the surface hardness and a slight decrease on the ductility. A microstructure that is more pearlitic is harder, stronger, and more brittle. However, only significant and consistent changes in the percent pearlite would be further analyzed as the amount is related to the location taken for the picture as discussed in Section 2.4.3. The results are provided in Table 8.9 for completeness.

The average hardness and grain sizes of damaged-repaired steel were normalized with respect to the undamaged steel. Figure 8.68 shows the normalized hardness and grain size results of the damaged-repaired steel.

The results in Table 8.9 and Figure 8.68 indicate that:

- Heat straightening increases the hardness of A7 steel. The increase in hardness was more substantial for A7-Beam 2 as apposed to A7-Beam 1.
- Good correlations do not exist between the trends in the hardness data and the ultimate stress of damaged-repaired A7 steel.
- Damage-repair cycles decrease the grain size of A7 steel. The grain size of A7-Beam 2 was as low as 51% of the undamaged steel grain size.

8.2.2 A36 Beam Specimens

8.2.2.1 Uniaxial Tension Tests

Uniaxial tension tests were conducted according to ASTM E8 on tension coupons from the damaged-repaired A36 steel beams. All the A36 tension coupons were fabricated with the dimensions shown in Figure 7.18. Figures 8.68 and 8.69 show the uniaxial stress-strain (σ–ε) relationships of tension coupons from A36-Beam 1 and A36-Beam 2, respectively. Figures 8.69 and 8.70 also include the σ–ε relationships of the undamaged specimen removed from flange Segment TA for comparisons. The structural properties of the damaged-repaired A36 beam specimens are summarized in Table 8.10, which includes the individual results of X, Y, and Z coupons and their average. The damage-repaired steel material properties (σ_y, E, σ_t, and percent elongation) were normalized with respect to the corresponding undamaged steel material properties and plotted in Figures 8.71 (a-d). Figure 8.71(a) shows the normalized yield stress for all damaged-repaired specimens. Figure 8.71(b) shows the normalized elastic modulus for all damaged-repaired specimens. Figure 8.71(c) shows the normalized ultimate stress, and Figure 8.71(d) shows the normalized percent elongation for all damaged-repaired specimens.

The yield stress data in Table 8.10 and Figure 8.71(a) indicate that:

- Damage-repair cycles increased the yield stress of A36-Beam 1 (heated to 1200 °F). The increased yield stress is within 109% of the undamaged yield stress. The results were very consistent for X, Y, and Z.
- Damage-repair cycles significantly yield stress of A36-Beam 2 (heated to 1400 °F). There is move variation and the results range from 111-124% of the undamaged material.

The elastic modulus data in Table 8.10 and Figure 8.71(b) indicate that:

- Damage-repair cycles do not significantly affect the elastic modulus of A36 steel. All results were within 92-103% of the undamaged material.

The ultimate stress data in Table 8.10 and Figure 8.71(c) indicate that:

- Damage-repair cycles do not significantly affect the ultimate stress of A36 steel heated 1200 °F. The values are within 98-100% of the undamaged material.
- The ultimate strength of specimens repaired with overheated temperatures increased slightly (101-107%). The increase was most significant for Specimen X.

The percent elongation (ductility) data in Table 8.10 and Figure 8.71(d) indicate that:

- Damage-heat straightening repairs reduce the percent elongation (ductility) of A36 steel. For specimens subjected to 1200 °F, the reduction in ductility ranges from approximately 86%-94% of the undamaged material. This appears to be within an acceptable range.
- The reductions in the percent elongation from the overheated steel were much more substantial. The reduction was found from 86% to as low as 67% of the undamaged material. The reasons for this reduction are not known.

8.2.2.2 Charpy Impact Fracture Toughness Tests

The results of the fracture toughness tests on damaged-repaired A36 steel are provided in Table 8.11. Averages were taken both across the width of the flanges (i.e. averages of 1, 2, 3, and 4) and along the flange length (i.e. averages of 1, 2, 3, or 4 for L1, C, and R1). The overall average and standard deviations of all twelve charpy specimens are also provided in Table 8.11. These fracture toughness values were normalized with respect to the average (mean) undamaged fracture toughness of undamaged A36 steel

from Plate B only. These fracture toughness values were normalized with respect to the average (mean) undamaged fracture toughness of undamaged A36 steel from Plate B only. The results from undamaged Plate B were used only for normalized ratios as Table 7.13 indicated a slight statistical difference between the fracture toughness of Plate A and Plate B (probability that data sets are statistically similar=17%). The normalized fracture toughness values are also shown in Table 8.11. Figure 8.72 shows the normalized fracture toughness of the charpy specimens from the damaged-repaired beams. Table 8.12 provides the means, standard deviations, 95% confidence intervals for the actual mean, medians, and absolute average deviations from the median for the twelve charpy specimens removed from each beam specimen.

Student's t-test analysis was conducted to evaluate the statistical difference between the undamaged fracture toughness values and the fracture toughness of A36-Beam 1 and A36-Beam 2. As mentioned previously in Section 4.9.2, the t-test evaluates the statistical difference between two data sets using their respective means, standard deviations, and sample set sizes. The results from the t-test include the t-value and the corresponding probability of null hypothesis, where the null hypothesis implies that the data sets are statistically similar. Tables 8.13 and 8.14 compare the fracture toughness of A36-Beam 1 and A36-Beam 2, respectively. Table 8.13 indicates a 47% probability that the data sets are statistically similar and Table 8.14 indicates a 0.5% probability that the data sets are statistically similar.

The data in Tables 8.11 to 8.14 and Figure 8.72 indicates that:

- The overall fracture toughness of A36-Beam 1 is comparable to the undamaged toughness. However, significant variability exists in the toughness of A36-Beam 1. In fact, the toughness of specimens from the center Vee heat (*C*) is much lower than the undamaged toughness.
- With the exception of one value, the fracture toughness of damage-repaired overheated A36 increased. The increase ranges from 101-460% of the undamaged material.
- The fracture toughness results of specimens removed from the center Vee heat (*C*) results in the lowest values. A general trend was noticed that the fracture toughness decreased as the specimens are removed closer to the web (away from the edge of the flange).

8.2.2.3 Rockwell Hardness and Microstructure Investigations

Rockwell hardness tests were conducted on damage-repaired A36 steel according to ASTM E18. Four points were taken on Specimens C-2 identified in Figure 7.24. Table 8.9 summarizes the averaged results of the Rockwell hardness tests and the microstructure investigations. Table 8.9 also provides comparisons between the approximate ultimate strengths as estimated by ASTM A370 to the actual ultimate strengths given in Section 8.2.2.1.

Microscopic preparation was conducted using the procedures outlined in Section 7.6.1.3. The resulting microstructures of the two A36 steel beam specimens at 480X are shown in Figure 8.73 (Refer to Figure 7.23 for comparisons to undamaged steel). The average hardness and grain sizes of damaged-repaired steel were normalized with respect to the undamaged steel from Flange B. Figure 8.74 shows the normalized hardness and grain size results of the damaged-repaired specimens. As discussed in Section 4.9.4, a more fine-grained microstructure is generally stronger and tougher than a more coarse-grained microstructure. There is a slight increase on the surface hardness and a slight decrease on the ductility. A microstructure that is more pearlitic is harder, stronger, and more brittle. However, only significant and consistent changes in the percent pearlite would be further analyzed as the amount is related to the location taken for the picture as discussed in Section 2.4.3. The results are provided in Table 8.9 for completeness.

The results in Table 8.9 and Figure 8.74 indicate that:

- Damage-repair cycles increase the Rockwell hardness of A36 steel heated to a maximum temperature of 1200 °F. The resulting hardness was approximately 110% of the undamaged hardness.

- Damage-repair cycles slightly decrease the Rockwell hardness of overheated A36 steel.
- Poor correlations exist between the hardness data and the ultimate stress of damaged-repaired A36 steel.
- Damage-repair cycles decrease the grain size of A36 steel to either 60% or 73% of the undamaged material. The grain size decreased less when using the overheated temperatures.

8.2.3 A588 Beam Specimens

8.2.3.1 Uniaxial Tension Tests

Uniaxial tension tests were conducted according to ASTM E8 on tension coupons from the damaged-repaired A588 steel beams. All A588 tensile coupons were fabricated with the dimensions shown in Figure 7.18. Figures 8.75 and 8.76 show the uniaxial stress-strain (σ–ε) relationships of tension coupons from A588-Beam 1 and A588-Beam 2, respectively. Figures 8.75 and 8.76 also include the σ–ε relationships of the undamaged specimen removed from flange Segment TA for comparisons. The structural properties of the damaged-repaired A588 beam specimens are summarized in Table 8.15, which includes the individual results of X, Y, and Z coupons and their average. The damage-repaired steel material properties (σ_y, E, σ_t, and percent elongation) were normalized with respect to the corresponding undamaged steel material properties and plotted in Figures 8.77 (a-d). Figure 8.77(a) shows the normalized yield stress for all damaged-repaired specimens. Figure 8.77(b) shows the normalized elastic modulus for all damaged-repaired specimens. Figure 8.77(c) shows the normalized ultimate stress, and Figure 8.77(d) shows the normalized percent elongation for all damaged-repaired specimens.

The yield stress data in Table 8.15 and Figure 8.77(a) indicate that:

- Damage-repair cycles decreased the yield stress of Specimens X and Y from both beam specimens to 89-96% of the undamaged material.
- Damage-repair cycles increased the yield stress of Specimens Z from both beam specimens to approximately 107-108% of the undamaged material.
- Applying a higher external restraining force slightly decreased the yield stress of Specimens X and Y and very slightly increased the yield stress of Specimen Z.

The elastic modulus data in Table 8.15 and Figure 8.71(b) indicate that:

- Damage-repair cycles do not affect the elastic modulus of A588 steel. All results were within a range of 97-102% of the undamaged material.

The ultimate stress data in Table 8.15 and Figure 8.71(c) indicate that:

- Damage-repair cycles decreased the ultimate stress of A588 steel. The results were found within 89-98% of the undamaged material.
- The ultimate stress increased as the specimens were removed closer to the web.
- Applying a higher external restraining force slightly decreased the ultimate stress of Specimens X and Y and very slightly increased the ultimate stress of Specimen Z.

The percent elongation (ductility) data in Table 8.15 and Figure 8.71(d) indicate that:

- Damage-repair cycles increased the percent elongation of the outmost (X) specimen and decreased the percent elongation of the middle (Y) and innermost (Z) specimens.
- The percent elongation decreased as the specimens were removed closer to the web.

- Applying a higher external restraining moment had an insignificant effect on the resulting ductility. A higher restraining stress decreased the ductility of the outermost (X) specimen slightly and increased the ductility of the middle (Y) and innermost (Z) specimens.

8.2.3.2 Charpy V-notch Fracture Toughness Tests

The results of the fracture toughness tests on damaged-repaired A588 steel are provided in Table 8.16. Averages were taken both across the width of the flanges (i.e. averages of 1, 2, 3, and 4) and along the flange length (i.e. averages of 1, 2, 3, or 4 for L1, C, and R1). The overall average and standard deviations of all twelve charpy specimens are also provided in Table 8.16. These fracture toughness values were normalized with respect to the average (mean) undamaged fracture toughness of undamaged A588 steel from Plate B only. The results from undamaged Plate B were only used for normalized ratios as Table 7.16 indicated a slight statistical difference between the fracture toughness of Plate A and Plate B (probability that data sets are statistically similar=10%). The normalized fracture toughness values are also shown in Table 8.16. Figure 8.78 shows the normalized fracture toughness of the charpy specimens from the damaged-repaired beams. Table 8.17 provides the means, standard deviations, 95% confidence intervals for the actual mean, medians, and absolute average deviations from the median for the twelve charpy specimens removed from each beam specimen.

Student's t-test analysis was conducted to evaluate the statistical difference between the undamaged fracture toughness values and the fracture toughness of A588-Beam 1 and A588-Beam 2. As mentioned previously in Section 4.9.2, the t-test evaluates the statistical difference between two data sets using their respective means, standard deviations, and sample set sizes. The results from the t-test include the t-value and the corresponding probability of null hypothesis, where the null hypothesis implies that the data sets are statistically similar. Tables 8.18 and 8.19 compare the fracture toughness of A588-Beam 1 and A588-Beam 2, respectively. Table 8.18 indicates less than 0.01% probability that the data sets are statistically similar) and Table 8.19 indicates a 0.35% probability that the data sets are statistically similar.

The data in Tables 8.16 to 8.19 and Figure 8.78 indicates that:

- Damage-repair cycles increased the fracture toughness of A588 steel significantly.
- Charpy Specimen C-4 from A588-Beam 2 was the only one found to have lower fracture toughness than the mean undamaged value.
- Fracture toughness decreased as the charpy specimens were closer to the flange-web junction (k-area region). In each row, Specimen 1 had higher fracture toughness than Specimen 2, Specimen 2 had higher fracture toughness than Specimen 3, and Specimen 3 had higher fracture toughness than Specimen 4. All three charpy specimens removed across the beam specimens (i.e. 1's, 2's, 3's, and 4's) related very well to each other.
- From A588-Beam 1, Specimens 1, 2, and 3 (including L, C, and R) were found to be exceptionally high with values ranging from 263-308% of the undamaged mean. Specimen 4 was found to be moderately high with values ranging from 126-147% of the undamaged material.
- From A588-Beam 2, Specimens 1 and 2 (including L, C, and R) were found to be exceptionally high with values ranging from 272-308% of the undamaged mean. Specimens 3 and 4 ranged from 77-136% of the undamaged material.
- Therefore, applying a higher external restraining stress reduces the fracture toughness.

8.2.3.3 Rockwell Hardness and Microstructure Investigations

Rockwell hardness tests were conducted on damage-repaired A588 steel according to ASTM E18. Four points were taken on Specimens C-2, identified in Figure 7.24. Table 8.9 summarizes the averaged

results of the Rockwell hardness tests and the microstructure investigations. Table 8.9 also provides comparisons between the approximate ultimate strengths as estimated by ASTM A370 to the actual ultimate strengths given in Section 8.2.3.1.

Microstructure preparations were conducted using the procedures outlined in Section 7.6.1.3. The resulting microstructures of the two A588 steel beam specimens are shown in Figure 8.79 (Refer to Figure 7.23 for comparisons to undamaged steel). The average hardness and grain sizes of damaged-repaired steel were normalized with respect to the undamaged steel from Flange B. Figure 8.80 shows the normalized hardness and grain size results of the damaged-repaired steel. As discussed in Section 4.9.4, a more fine-grained microstructure is generally stronger and tougher than a more coarse-grained microstructure. There is a slight increase on the surface hardness and a slight decrease on the ductility. A microstructure that is more pearlitic is harder, stronger, and more brittle. However, only significant and consistent changes in the percent pearlite would be further analyzed as the amount is related to the location taken for the picture as discussed in Section 2.4.3. The results are provided in Table 8.9 for completeness.

The results in Table 8.9 and Figure 8.80 indicate that:

- Damage-repair cycles decrease the surface hardness of A588 steel to approximately 95% of the undamaged material.
- For A588, the approximate tensile strengths as estimated by ASTM A370 relate well to the actual tensile strengths for both undamaged and damage-repaired steel. The reduction in hardness is likely linked to the sufficient decrease in tensile strength.
- Applying a higher external restraining force had a negligible effect on the resulting hardness.
- Damage-repair cycles decreased the grain size of A588 steel to either 65% or 70% of the undamaged material.
- Applying a higher external restraining force appears to increase the resulting grain size slightly and decrease the amount of pearlite. However, both of these results may simply be a function of the spot chosen for taking the photographs.

8.2.4 Indirect Verification of Fracture Toughness Results

The MSU researchers further verified the fracture toughness testing procedure and Charpy testing machine by examining the broken charpy specimens. A recommended practice guide has been published by the National Institute of Standards and Technology (*NIST*) entitled "Installing, Maintaining, and Verifying your Charpy Impact Machine" [*3*]. Examining the broken charpy specimens is an indirect verification procedure and there are seven possible defects listed in the *NIST* practice guide for performing an indirect verification:

1. Worn Anvils
2. Off center specimen
3. Off center strike
4. Uneven anvil marks
5. Chipped anvil marks
6. Bent Pendulum
7. Damaged anvils

Case 2 is the only defect caused by mishandling of the charpy specimen prior to impact and examines the placement of the specimen and its contact with the anvils. An off-center specimen is misaligned as the striker does not contact the center (directly opposite of the v-notch) at the time of impact. An off-center specimen can be detected by placing the specimens together as shown schematically in Figure 8.81 [*3*].

Off-center specimens can be the resultant of worn centering tongs, careless testing procedures, or the use of cooling fluid too viscous at the test temperature.

Other defects (Case 1, Cases 3-7) are caused by imperfections in the Charpy impact testing machine. It is likely that if imperfections existed in the Charpy testing machine, they would be present towards the end of testing. The damage-repaired charpy specimens from beam specimens were tested after all tests on damaged-repaired small scale specimens as well as undamaged specimens. Therefore, all broken charpy specimens from damaged-repaired beam specimens were further analyzed for the possibilities of imperfections in the testing machine. Each possible imperfection was considered when evaluating each Charpy specimen and was recorded as shown for A36-Beam 2 in Table 8.20. The broken charpy specimens and fracture toughness values from A36-Beam 2 are provided in Figure 8.82.

Table 8.20 and Figure 8.82 indicate that Charpy specimen R-3 has slight misalignment. However, the fracture toughness does not appear to be an outlier as it is between the fracture toughness of Specimens R-2 and R-4. This relationship is expected from other fracture toughness testing of beam specimens. The description of specimens tested with worn anvils is seen in Specimens R-1, R-2, and C-1. However, this defect is unlikely, as it would be noticed in for other specimens as well.

Similar tables were developed for the other beam specimens. The MSU researchers concluded that specimen C-2 from A36-Beam 1 might be a possible outlier since it value was 68 ft-lb and C-1, C-3, and C-4 had fracture toughness values of 16 ft-lb, 16 ft-lb, and 11 ft-lb, respectively. However, after investigating the broken specimen, the test appeared to be conducted accordingly. Some charpy specimens were not broken into two pieces due to high ductility and fracture toughness. An example is shown for A588-Beam 2 in Figure 8.83. For specimens that did not fracture into two pieces, the researchers used their best judgment in estimating possible off-centered specimens.

The researchers found no defects from the broken charpy specimens from A36-Beam 1, A588-Beam 1, and A7-Beam 1. For A588-Beam 2, Specimen C-1 appeared to have slight misalignment, and Specimen R-3 showed signs of chipped anvils (see Figure 8.83). From A7-Beam 2, Specimens L-1 and L-2 indicated slight misalignment. None of these charpy specimens appears to be outliers in the data.

Since the broken Charpy specimens from beam specimens indicated that the Charpy impact machine was functioning adequately, further examinations were not required on charpy specimens from all small-scale specimens. However, some were chosen after examining the data and identifying outliers. Outlier specimens were chosen from significant variation of the three specimens in series (i.e. 1, 2, 3 or 4, 5, 6). The specimens chosen were from A36-30-70-3, A36-30-70-5, A36-60-50-3, A36-60-50-5, A36-90-25-3, A588-60-25-3, A588-60-50-2, A7-60-25-3-2, and A36-90-50-3-1600. All six broken Charpy specimens from each of these damaged-repaired specimens were examined and verified.

Most of the specimens questioned as outliers from the small-scale results had lower fracture toughness values than others. A slight and insignificant amount of defects could be identified in the examination of these specimens. In general, a specimen with lower fracture toughness will have less visible gouge marks and a shinier and flatter fracture surface as shown in Figure 8.84(a-c). Figure 8.84(a-c) shows Specimens 4, 5, and 6, from A36-30-70-3. The fracture toughness results were 17 ft-lb, 61 ft-lb, and 64 ft-lb respectively.

Of all specimens examined, only the results from Specimens 1, 2, and 3 of A36-30-70-5 appear questionable. The fracture toughness results were 8.5 ft-lb, 49 ft-lb, and 56 ft-lb respectively. The gouge marks on Specimen 1 were really light but appeared to be aligned in respect to each broken side. The gouge marks on Specimens 2 and 3 appeared to be slightly misaligned which could persuade a higher fracture toughness result. Overall, the examination of broken Charpy specimens indicates that good practice was performed in conducting the tests and a valid Charpy impact machine was used.

8.3 COMPARISONS OF RESULTS FROM TASKS III AND IV

As mentioned earlier, the large-scale beams tests of Task IV were designed and conducted to validate some of the major conclusions and recommendations from Task III. This section compares the relevant results from Tasks III and IV for each steel type.

8.3.1 A7 Steel

The results from Task III indicated that smaller damage strains have more detrimental effects on the structural properties of damaged-repaired A7 steel and the total number of damage-repairs must be limited to three (see Section 6.4.4). Therefore, the large-scale A7-Beam 1 was tested to evaluate the effects of smaller damage strain (ε_d=30 ε_y) and three damage-repair cycles on the structural properties. Large-scale A7-Beam 2 was tested to compare the effects of larger damage strains (60 ε_y, 90 ε_y) and three damage-repair cycles on the structural properties. The results for A7 steel from Tasks III and IV compare as follows:

- The basic structural properties (yield stress, elastic modulus, and ultimate stress) of damaged-repaired A7 steel are usually comparable to the corresponding undamaged material properties. The Task III results for elastic modulus and yield stress were not completely reliable due to the curvature of some tension coupons, which developed during the damage-repair process. The Task IV results indicate that the yield stress increased for both A7-Beam 1 and A7-Beam 2, but the increase was greater for the A7-Beam-1 subjected to the smaller damage strain.
- The percent elongation (ductility) of A7 steel decreases after three damage-repair cycles. Task III results indicate percent elongation values within 75-80% of the undamaged percent elongation after three damage-repair cycles. However, the Task IV results indicate higher elongation values within 80-95% of the undamaged percent elongation after three damage-repair cycles.
- The fracture toughness of A7 steel subjected to the smaller damage strain of 30 ε_y decreases after three damage-repair cycles. Task III results indicate that the fracture toughness reduces to approximately 50% of the undamaged fracture toughness. However, Task IV results indicate an even more drastic reduction in the fracture toughness to approximately 25% of the undamaged toughness.
- Task III results indicate that the fracture toughness of A7 steel subjected to the higher damage strains of 60 or 90 ε_y is dependent on the restraining stress σ_r; higher σ_r (0.40 σ_y) results in lower fracture toughness (approx. 50-75% of the undamaged toughness) and lower σ_r (0.25 σ_y) results in fracture toughness comparable to the undamaged toughness. The Task IV results for A7-Beam 2 indicate that the mean fracture toughness of A7 steel after three damage-repair cycles (ε_d = 90ε_y or 60ε_y and M_r=0.50 M_p or 0.25 M_p) is approximately equal to the undamaged toughness. However, there is significant variability in the fracture toughness with material location. The average fracture toughness in the center Vee heat (*C*) was 56% of the undamaged toughness with some values as low as 10-20% of the undamaged toughness.

The results for A7 steel from Tasks III and IV compare favorably. Based on the fracture toughness results of Tasks III and IV, it is recommended that A7 steel beams should not be subjected to more than three damage-heat straightening repair cycles. Smaller damage strains are more detrimental to A7 steel as compared to larger damage strains.

8.3.2 A36 Steel

The results from Task III indicate that smaller damage strains have more detrimental effects on the structural properties of damaged-repaired A36 steel and the total number of damage-repairs must be limited to three (see Section 6.2.4). The Task III results also indicate that overheating the steel to 1400 ºF during repair results in improved structural properties and fracture toughness after three damage-repair cycles. Hence, the large-scale A36-Beam 1 was tested to evaluate the effects of smaller damage strain (ε_d=30 ε_y) and three damage-repair cycles on the structural properties. A36-Beam 2 was tested to evaluate the effects of overheating to 1400 ºF on the structural properties, while maintaining the other damage and repair parameters (ε_d, σ_r, and N_r) the same as A36-Beam 1. The results for A36 steel from Tasks III and IV compare as follows:

- The basic material properties (yield stress, elastic modulus, and ultimate stress) of damaged-repaired A36 steel are comparable to the corresponding undamaged material properties. Damage-repair cycles increase the yield stress of A36 steel. Overheating the steel to 1400 ºF increases the yield stress more significantly. Damage-repair cycles at 1200 ºF or 1400 ºF have a small influence on the elastic modulus and ultimate stress of A36 steel.
- The percent elongation (ductility) of A36 steel decreases after three damage-repair cycles. Task III results indicate percent elongation values within 75-80% of the undamaged percent elongation after three damage-repair cycles at 30 ε_y. However, the A36-Beam 1 results from Task IV indicate higher percent elongation values within 85-95% of the undamaged percent elongation after three damage-repair cycles at 30 ε_y and heating up to 1200 ºF. The results from A36-Beam 2 indicate that overheating the steel during repair reduces the percent elongation values significantly to 67-87% of the undamaged percent elongation.
- The fracture toughness of A36 steel subjected to the smaller damage strain of 30 ε_y decreases after three damage-repair cycles. Task III results indicate that the mean fracture toughness reduces to approximately 25-50% of the undamaged fracture toughness. The A36-Beam 1 results from Task IV indicate that the overall mean fracture toughness is 90% of the undamaged fracture toughness. However, the fracture toughness varies significantly with the location of the charpy specimens and the values range from 25-150% of the undamaged toughness. For example, the mean fracture toughness in the center Vee is only 62% of the undamaged toughness with three out of four values close to 30% of the undamaged toughness.
- Task III results indicate that the mean fracture toughness of A36 steel overheated to 1400 ºF during repair is approximately 330-415% of the undamaged fracture toughness. The Task III studies were performed for higher damage strains of 60 or 90 ε_y; there were no studies involving overheating and damage strains of 30 ε_y. The A36-Beam 2 results indicate that the overall mean fracture toughness is 245% of the undamaged toughness. The fracture toughness varies with the location of the charpy specimens and the values range from 101-460% of the undamaged toughness with one outlier at 40%.

The results for A36 steel from Tasks III and IV compare favorably. Based on the fracture toughness results of Tasks III and IV, it is recommended that A36 steel beams should not be subjected to more than three damage-heat straightening repair cycles. Overheating the A36 steel during damage-repair improves its material properties and fracture toughness significantly.

8.3.3 A588 Steel

The results from Task III indicate that A588 steel is extremely resilient. It can undergo several damage-repair cycles without impacting the structural properties and fracture toughness adversely. Task III results also indicate that restraining stress during repair is an important parameter. Higher restraining stresses reduce the fracture toughness of the damaged-repaired A588 steel but never below 50% of the undamaged fracture toughness. The large-scale A588 steel beams in Task IV were subjected to three damage-repair cycles with damage strains of 40 and 20 ε_y combined. A588-Beam 1 was repaired using a lower restraining moment of 0.25 M_p. A588-Beam 2 was repaired using the higher restraining moment of 0.50 M_p to evaluate the effects of restraining stresses. The results for A588 steel from Tasks III and IV compare as follows:

- The basic structural properties (yield stress, elastic modulus, and ultimate stress) of damaged-repaired A588 steel are comparable to the corresponding undamaged material properties. Results from Task III indicate yield stresses within 95-110% and ultimate stresses within 94-104% of the undamaged A588 material. However, results from Task IV indicate smaller yield stresses (approximately 89-96%) and ultimate stresses (approx. 89-98%) than the undamaged A588 material. The reason for this discrepancy is not known. The A588 steels for both Tasks III and IV had similar chemical composition and were ferrite-pearlite steels made without using the quenching and tempering process.
- Task III results indicate that the percent elongation (ductility) of A588 steel decreases after three damage-repair cycles. This reduction in ductility is reasonable with percent elongation values ranging from 74-92% of the undamaged steel. The results from Task IV indicate smaller changes in the percent elongation values (ductility) with damage-repair cycles.
- Task III results indicate that after three damage-repair cycles, the fracture toughness of A588 steel is equal to or greater than the undamaged toughness with values ranging from 75-250% of the undamaged toughness. Increasing the restraining stress reduces the fracture toughness after three damage-repair cycles slightly to values close to 75-100% of the undamaged toughness.
- The results from Task IV indicate that the fracture toughness of A588-Beam 1 repaired with the lower restraining moment is approximately 250% of the undamaged toughness. The toughness varies with the location of the charpy specimens but never reduces below the undamaged toughness. The mean fracture toughness of A588-Beam 2 repaired with the higher restraining moment is approximately 204% of the undamaged fracture toughness (slightly lower than the toughness values for A588-Beam 1). The toughness varies significantly with the location of the charpy specimens with several values close to the undamaged toughness and one value below (approximately 77% of the undamaged toughness).

The results from Tasks III and IV for A588 steel compare favorably. A588 steel is an extremely resilient material that can undergo several (up to five) damage-repair cycles without significant adverse effects on the structural properties including fracture toughness. It is recommended that A588 steel beams can be subjected to several (up to five) damage-heat straightening repair cycles. Lower restraining stresses should be used preferably. However, higher restraining stresses can also be used without impacting the material properties adversely.

8.4 REFERENCE

1. NIST, “Installing, Maintaining, and Verifying your Charpy Impact Machine”, National Institute of Standards and Technology, Special Publication 960-4, Washington, 2000.

Table 8.1
Load increases and displacements during subsequent Vee heats to Location *C (*A7-Beam 1)

Number	Displacement (in)	Load Increase (kips)
Heat 1	0.1674	0.30
Heat 2	0.1560	2.30
Heat 3	0.1459	2.93
Heat 4	0.1531	4.14
Heat 5	0.0756	4.49
Heat 6	-	5.13

Table 8.2
Load increases and displacements during subsequent Vee heats to Location *C* (A588-Beam 2)

	Displacements (in)			
Number	Front	Back	Average	Load Increase (kips)
Heat 1	0.1984	0.2509	0.2247	0.16
Heat 2	0.1843	0.1437	0.164	2.24
Heat 3	0.1408	0.1276	0.1342	2.31
Heat 4	0.1022	0.1327	0.1174	2.85
Heat 5	0.0814	0.0891	0.0853	3.57
Heat 6	0.0906	0.1028	0.0967	4.06

Table 8.3
Comparison of uniaxial tension tests of undamaged A7 with full and reduced dimensions

Property	t=0.500	t=0.383
Upper σ_y *(ksi)*	37.2	37.9
Lower σ_y *(ksi)*	35.8	36.2
Plateau σ_y *(ksi)*	36.6	36.9
E (ksi)	30505	28590
ε_y	0.00120	0.00129
σ_t *(ksi)*	61.4	61.0
ε_u	0.224	0.234
ε_u / ε_y	186.39	181.30
% Elongation	41.96	40.80
% Reduction	62.51	62.00

Table 8.4
Structural properties of damaged-repaired A7 beam specimens

	A7-Beam 1					A7-Beam 2			
	X	**Y**	**Z**	**Avg.**		**X**	**Y**	**Z**	**Avg.**
Upper σ_y *(ksi)*	42.3	43.9	47.5	44.6		39.9	42.9	45.3	42.7
Lower σ_y *(ksi)*	40.8	40.9	45.4	42.4		39.0	41.9	42.9	41.3
Plateau σ_y *(ksi)*	42.3	42.5	45.7	43.5		39.2	42.0	44.0	41.7
E (ksi)	30670	28630	28437	29246		29132	29272	28782	29062
ε_y	0.00138	0.00148	0.00161	0.00149		0.00135	0.00143	0.00153	0.00144
σ_t *(ksi)*	62.3	62.6	65.1	63.3		63.0	62.8	63.2	63.0
ε_u	0.189	0.190	0.168	0.182		0.180	0.217	0.179	0.192
ε_u / ε_y	137.04	127.99	104.54	123.19		133.77	151.24	117.09	134.03
% Elongation	40.20	40.09	33.90	38.07		33.57	39.64	33.55	35.58
% Reduction	60.42	69.08	62.68	64.06		64.62	65.15	63.35	64.37

Table 8.5
Fracture toughness results of damaged-repaired A7 beam specimens

	A7-Beam 1					A7-Beam 2			
	L	**C**	**R**	**Avg**		**L**	**C**	**R**	**Avg**
1	51	9	17.5	25.8		141	74	198	137.7
2	16	5	10	10.3		168	58	62	96.0
3	13	10	9	10.7		72	8	61	47.0
4	8	6.5	8	7.5		9	15	12.5	12.2
Average	22.0	7.6	11.1	**13.6**		97.5	38.8	83.4	**73.2**
Normalized Results									
	A7-Beam 1					**A7-Beam 2**			
	L	**C**	**R**	**Avg**		**L**	**C**	**R**	**Avg**
1	0.734	0.129	0.252	0.372		2.029	1.065	2.849	1.981
2	0.230	0.072	0.144	0.149		2.417	0.835	0.892	1.381
3	0.187	0.144	0.129	0.153		1.036	0.115	0.878	0.676
4	0.115	0.094	0.115	0.108		0.129	0.216	0.180	0.175
Average	0.32	0.11	0.16	**0.20**		1.40	0.56	1.20	**1.05**

Table 8.6
Statistical values of 12 charpy specimens from A7 beam specimens

Statistical Property	A7-Beam 1	A7-Beam 2
Mean	13.6	73.2
Std. Dev.	12.3	64.0
95% High	21.4	113.9
95% Low	5.7	32.5
Median	9.5	61.5
Average Absolute From Median	6.0	46.0

Table 8.7
Student's t-test comparing toughness results of A7-Beam 1 to undamaged A7 (Flange B)

Results of unpaired t-tests:
t=10.8
Std. deviation=12.8
Degrees of freedom=22
Probability of null hypothesis < 0.0001

Table 8.8
Student's t-test comparing toughness results of A7-Beam 2 to undamaged A7 (Flange B)

Results of unpaired t-tests:
t=0.179
Std. deviation=46.2
Degrees of freedom=22
Probability of null hypothesis 0.86

Table 8.9
Rockwell hardness and microstructure results from undamaged and damage-repaired A7steel

Specimen	Hardness		ASTM Approx	Measured Avg.	Grain	
	Avg.	Std. Dev.	Tensile σ_t (ksi)	Tensile σ_t (ksi)	Size (mm)	% Pearlite
Undamaged A7-A	64.1	0.83	55	61.2	0.0293	26.54
Undamaged A7-B	68.9	0.80	59	61.6	0.0249	33.01
A7-Beam 1	73.9	1.12	65	63.3	0.0200	38.74
A7-Beam 2	77.2	0.51	68	63.0	0.0127	25.08
Undamaged A36-A	80.7	0.89	73	75.1	0.0203	35.64
Undamaged A36-B	78.2	0.54	69	73.4	0.0223	23.98
A36-Beam 1	86.3	2.42	83	73.0	0.0134	23.86
A36-Beam 2	83.6	1.81	81	75.5	0.0163	25.21
Undamaged A588-A	87.0	0.39	84	84.9	0.0267	30.07
Undamaged A588-B	86.6	0.38	84	84.5	0.0252	29.70
A588-Beam 1	82.5	0.40	80	79.3	0.0164	24.88
A588-Beam 2	81.6	0.69	77	78.3	0.0176	14.29

Table 8.10
Structural properties of damaged-repaired A36 beam specimens

	A36-Beam 1					A36-Beam 2			
	X	**Y**	**Z**	**Avg.**		**X**	**Y**	**Z**	**Avg.**
Upper σ_y *(ksi)*	50.1	53.9	52.5	52.2		59.4	54.0	56.1	56.5
Lower σ_y *(ksi)*	49.5	48.6	49.7	49.3		56.2	49.9	50.8	52.3
Plateau σ_y *(ksi)*	50.1	50.0	50.2	50.1		56.8	54.0	51.2	54.0
E (ksi)	30435	28495	31669	30200		31711	29610	30037	30453
ε_y	0.00165	0.00175	0.00159	0.00166		0.00179	0.00182	0.00170	0.00177
σ_u *(ksi)*	73.4	72.2	73.4	73.0		78.5	74.2	73.8	75.5
ε_u	0.164	0.189	0.169	0.174		0.149	0.103	0.160	0.137
ε_u / ε_y	99.63	107.71	106.61	104.65		83.19	56.48	93.86	77.84
% Elongation	35.70	34.55	32.60	34.28		32.63	25.36	28.96	28.99
% Reduction	66.01	65.65	63.97	65.21		62.76	62.50	62.15	62.47

Table 8.11
Fracture toughness results of damaged-repaired A36 beam specimens

	A36-Beam 1					A36-Beam 2			
	L	**C**	**R**	**Avg.**		**L**	**C**	**R**	**Avg.**
1	68	16	97	60.3		92	205	180	159.0
2	66	68	37	57.0		112	142	188	147.3
3	17	16	64	32.3		92	55	108	85.0
4	10.5	11	16	12.5		45	18	73	45.3
Average	40.4	27.8	53.5	**40.5**		85.3	105.0	137.3	**109.2**
Normalized Results									
	A36-Beam 1					**A36-Beam 2**			
	L	**C**	**R**	**Avg.**		**L**	**C**	**R**	**Avg.**
1	1.528	0.360	2.180	1.356		2.067	4.607	4.045	3.573
2	1.483	1.528	0.831	1.281		2.517	3.191	4.225	3.311
3	0.382	0.360	1.438	0.727		2.067	1.236	2.427	1.910
4	0.236	0.247	0.360	0.281		1.011	0.404	1.640	1.019
Average	0.91	0.62	1.20	**0.91**		1.92	2.36	3.08	**2.45**

Table 8.12
Statistical values of 12 charpy specimens from A36 beam specimens

Statistical Property	A36-Beam 1	A36-Beam 2
Mean	40.5	109.2
Std. Dev.	30.2	59.4
95% High	59.7	146.9
95% Low	21.3	71.5
Median	27.0	100.0
Average Absolute From Median	26.1	46.7

Table 8.13
Student's t-test comparing toughness results of A36-Beam 1 to undamaged A36 (Flange B)

Results of unpaired t-tests:
t=0.742
Std. deviation=24.1
Degrees of freedom=20
Probability of null hypothesis 0.47

Table 8.14
Student's t-test comparing toughness results of A36-Beam 2 to undamaged A36 (Flange B)

Results of unpaired t-tests:
t=3.17
Std. deviation=44.9
Degrees of freedom=20
Probability of null hypothesis 0.0048

Table 8.15
Structural properties of damaged-repaired A588 beam specimens

	A588-Beam 1					**A588-Beam 2**			
	X	**Y**	**Z**	**Avg.**		**X**	**Y**	**Z**	**Avg.**
Upper σ_y (ksi)	55.8	57.9	63.6	59.1		52.3	58.7	63.6	58.2
Lower σ_y (ksi)	54.8	55.5	61.8	57.4		51.6	53.4	62.5	55.8
Plateau σ_y (ksi)	55.4	56.4	62.9	58.2		52.1	55.1	63.3	56.8
E (ksi)	29928	29809	30287	30008		29262	30527	29571	29787
ε_y	0.00185	0.00189	0.00208	0.00194		0.00178	0.00180	0.00214	0.00191
σ_u (ksi)	76.2	78.3	83.3	79.3		75.3	76.0	83.6	78.3
ε_u	0.175	0.149	0.120	0.148		0.187	0.157	0.119	0.154
ε_u / ε_y	94.54	78.75	57.78	77.02		105.03	86.98	55.59	82.53
% Elongation	36.74	30.04	28.12	31.63		36.28	33.17	28.84	32.77
% Reduction	72.34	69.42	65.81	69.19		73.05	69.36	67.88	70.10

Table 8.16
Fracture toughness results of damaged-repaired A588 beam specimens

	A588-Beam 1					A588-Beam 2			
	L	**C**	**R**	**Avg.**		**L**	**C**	**R**	**Avg.**
1	295	295	295	295.0		295	293	288	292.0
2	294	292	294	293.3		293	275	260	276.0
3	265	252	292	269.7		130	120	106	118.7
4	141	121	130	130.7		104	74	102	93.3
Average	248.8	240.0	252.8	**247.2**		205.5	190.5	189.0	**195.0**
Normalized Results									
	A588-Beam 1					**A588-Beam 2**			
	L	**C**	**R**	**Avg.**		**L**	**C**	**R**	**Avg.**
1	3.083	3.083	3.083	3.083		3.083	3.062	3.009	3.051
2	3.072	3.051	3.072	3.065		3.062	2.874	2.717	2.884
3	2.769	2.633	3.051	2.818		1.358	1.254	1.108	1.240
4	1.473	1.264	1.358	1.365		1.087	0.773	1.066	0.975
Average	2.60	2.51	2.64	**2.58**		2.15	1.99	1.97	**2.04**

Table 8.17
Statistical values of 12 charpy specimens from A588 beam specimens

Statistical Property	A588-Beam 1	A588-Beam 2
Mean	247.0	195.0
Std. Dev.	71.7	94.3
95% High	292.7	245.9
95% Low	201.6	135.1
Median	292.0	195.0
Average Absolute From Median	47.0	89.0

Table 8.18
Student's t-test comparing toughness results of A588-Beam 1 to undamaged A588 (Flange B)

Results of unpaired t-tests:
t=6.61
Std. deviation=53.5
Degrees of freedom=20
Probability of null hypothesis < .0001

Table 8.19
Student's t-test comparing toughness results of A588-Beam 2 to undamaged A588 (Flange B)

Results of unpaired t-tests:
t=3.30
Std. deviation=70.2
Degrees of freedom=20
Probability of null hypothesis 0.0035

Table 8.20
Possible defects indicated in broken Charpy specimens from A36-Beam 2

Specimen	Worn Anvil	Off Center Specimen	Off Center Anvil	Uneven Anvil Marks	Chipped Anvils	Damaged Anvils	Bent Pendulum
R1	possible	ok	ok	ok	ok	ok	ok
R2	possible	ok	ok	ok	ok	ok	ok
R3	ok	slightly	ok	ok	ok	ok	ok
R4	ok	ok	ok	ok	ok	ok	ok
C1	possible	ok	ok	ok	ok	ok	ok
C2	ok	ok	ok	ok	ok	ok	ok
C3	ok	ok	ok	ok	ok	ok	ok
C4	ok	ok	ok	ok	ok	ok	ok
L1	ok	ok	ok	ok	ok	ok	ok
L2	ok	ok	ok	ok	ok	ok	ok
L3	ok	ok	ok	ok	ok	ok	ok
L4	ok	ok	ok	ok	ok	ok	ok

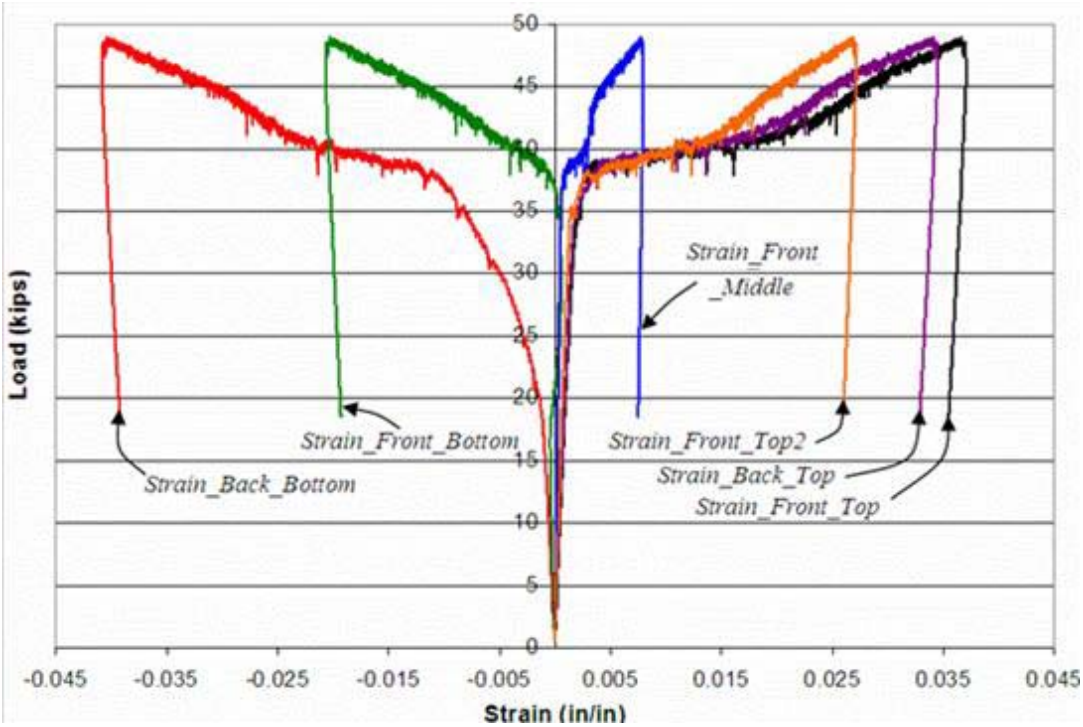

Figure 8.1
Strain gage data during the first damage cycle of A7-Beam 1

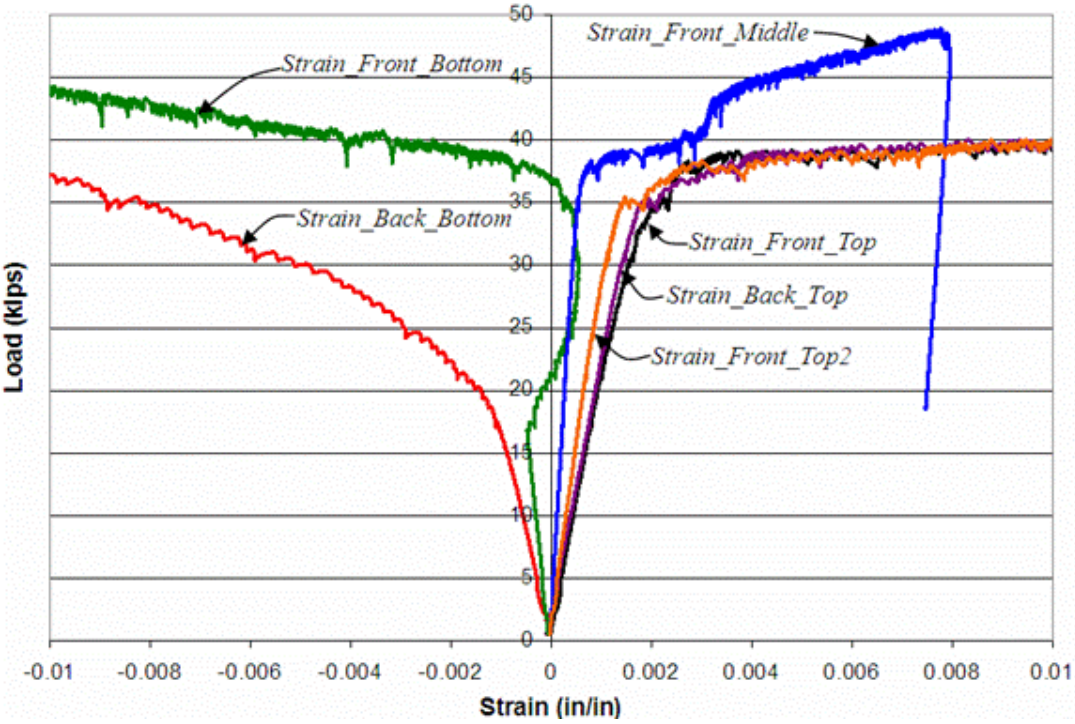

Figure 8.2
Initial strain gage data during the first damage cycle of A7-Beam 1

(a)

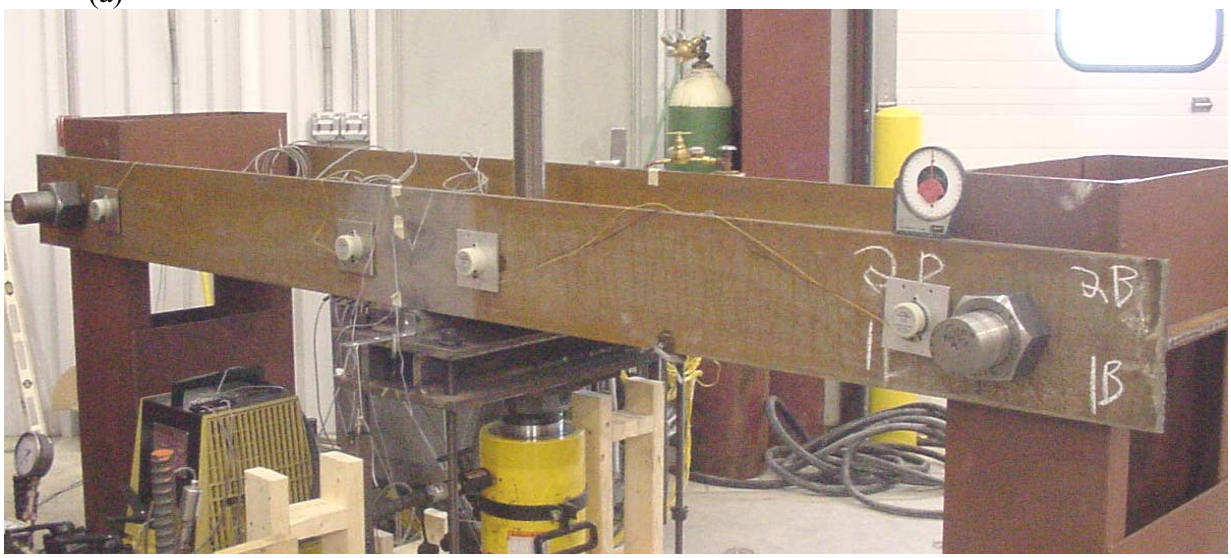

(b)

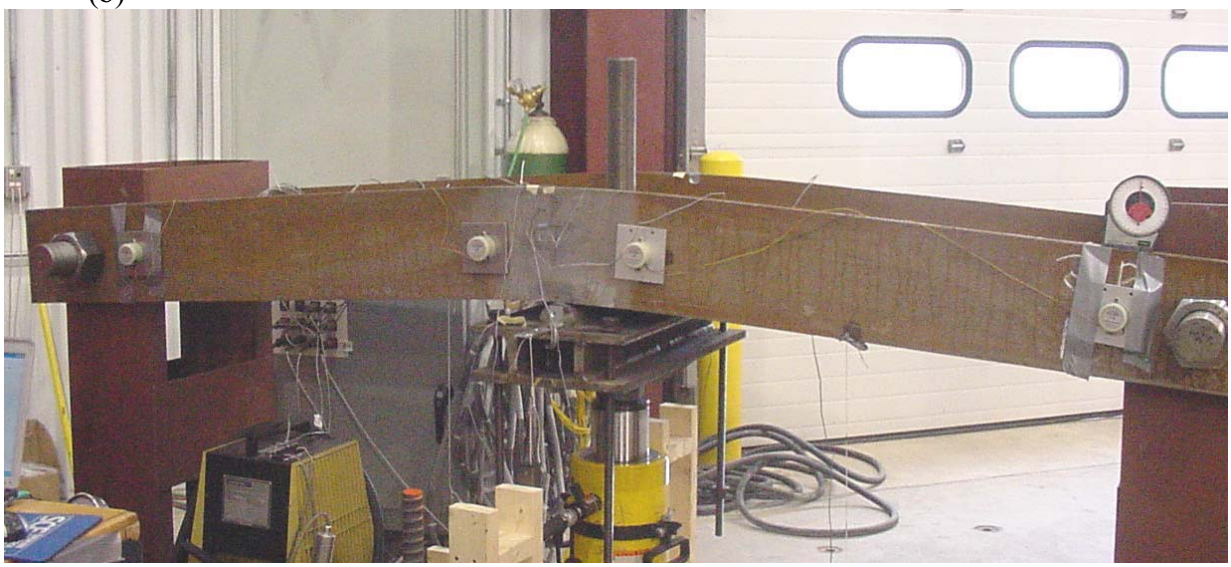

Figure 8.3
Before (a) and after (b) photographs of the first damage cycle of A7-Beam 1

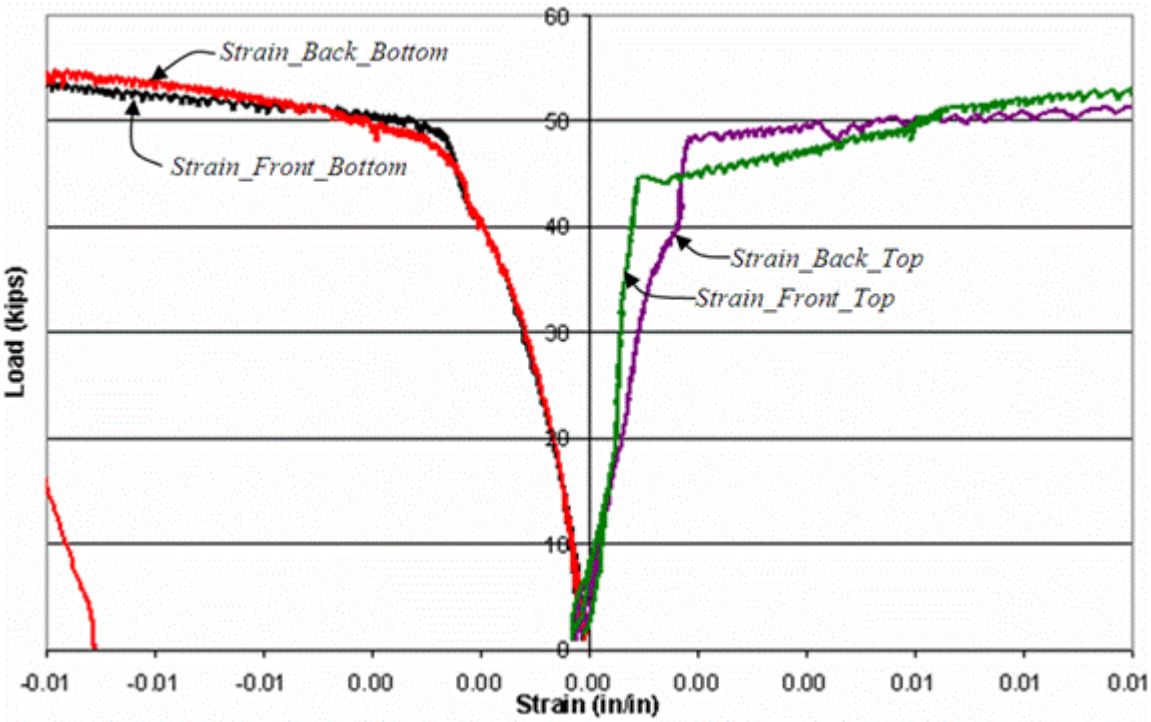

Figure 8.4
Strain gage data during the second damage cycle of A7-Beam 1

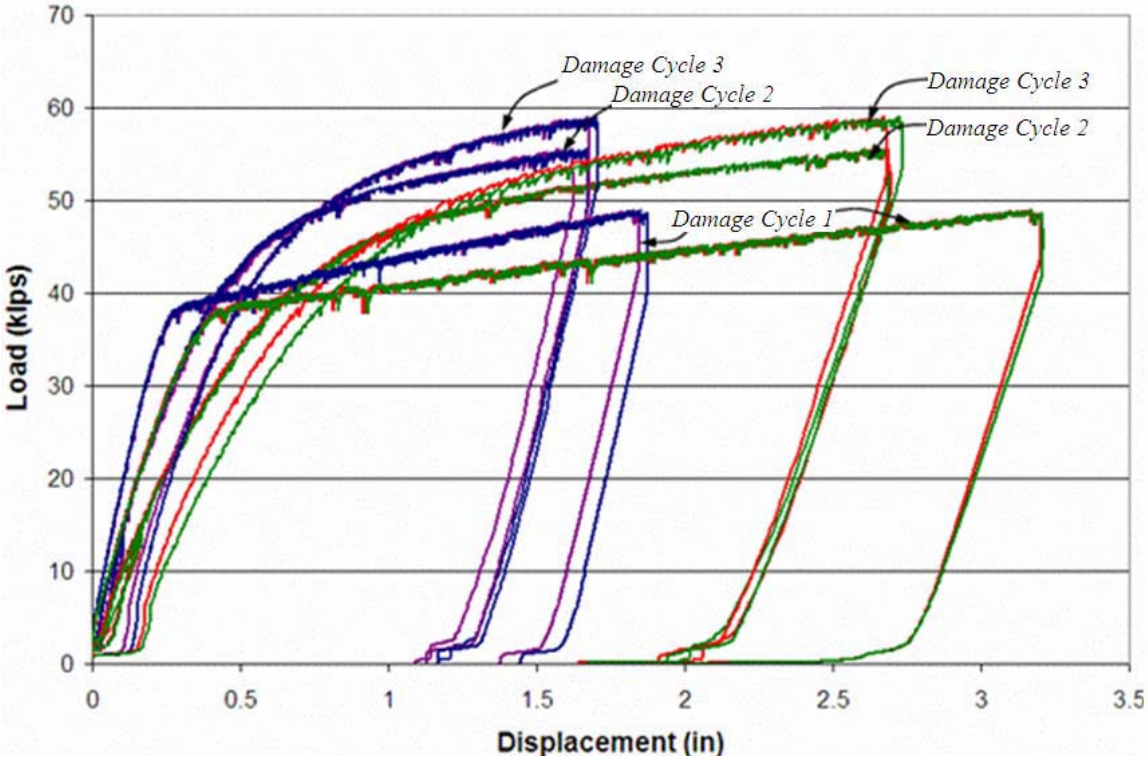

Figure 8.5
Load-displacement behaviors of all three damage cycles of A7-Beam 1

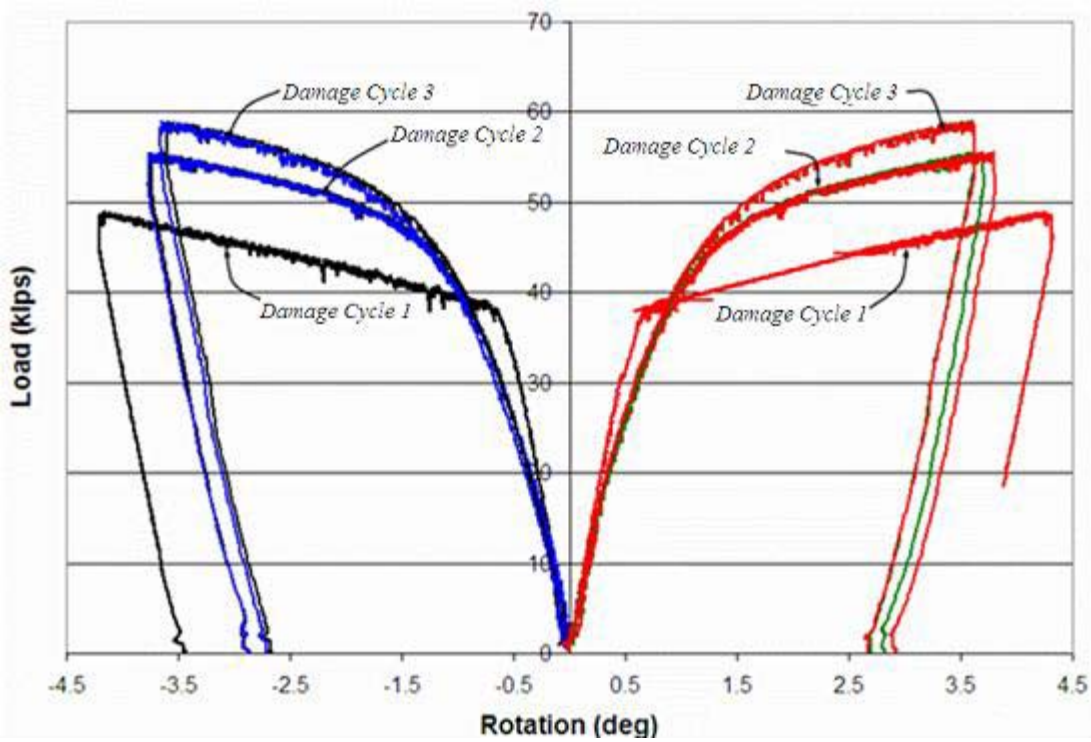

Figure 8.6
Load-rotation behaviors of all three damage cycles of A7-Beam 1

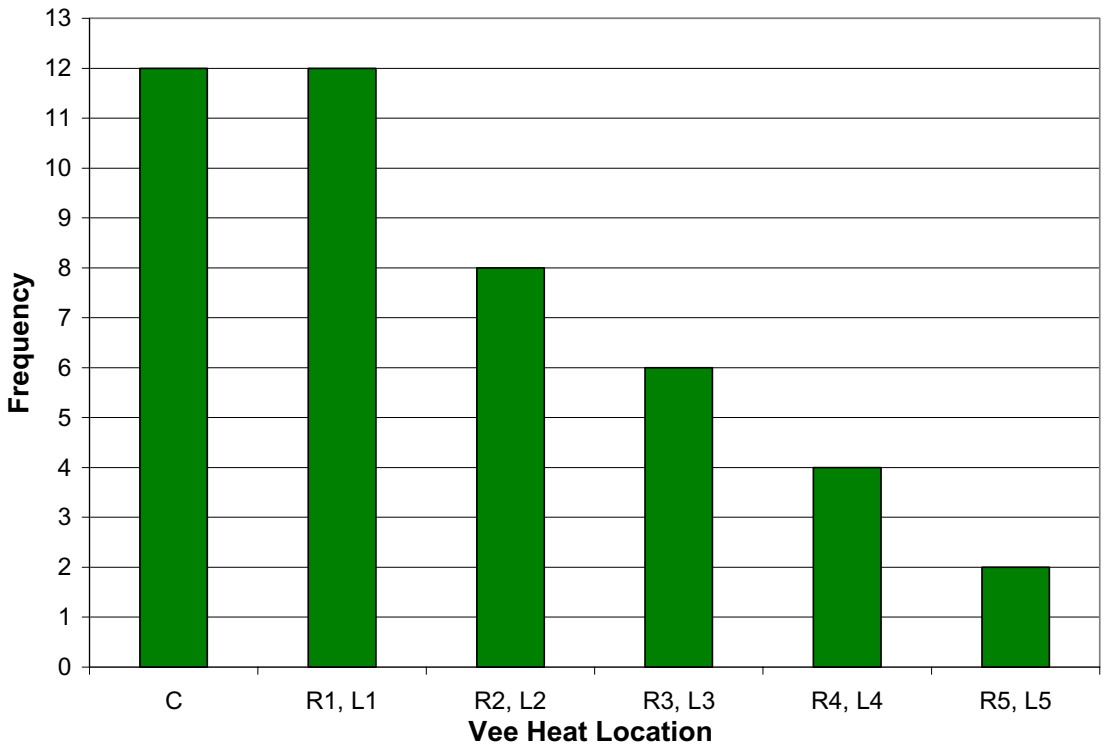

Figure 8.7
Frequency chart of each Vee heat location during three repairs of A7-Beam 1

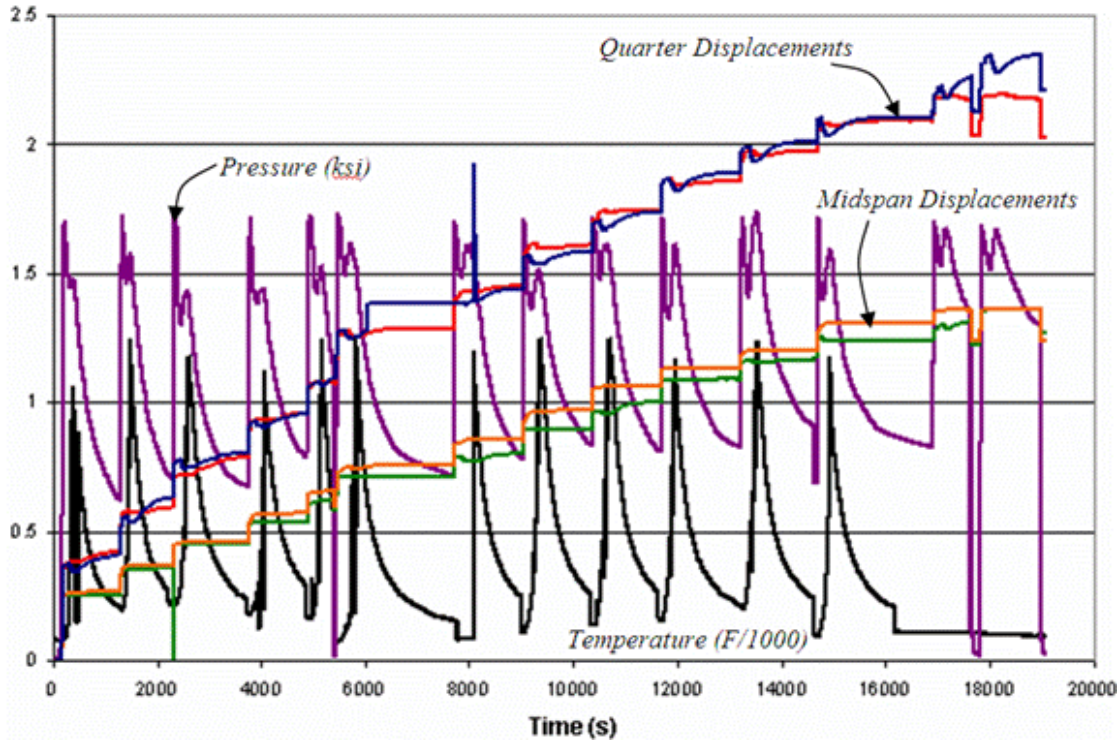

Figure 8.8
Instrument data during the second repair cycle of A7-Beam 1

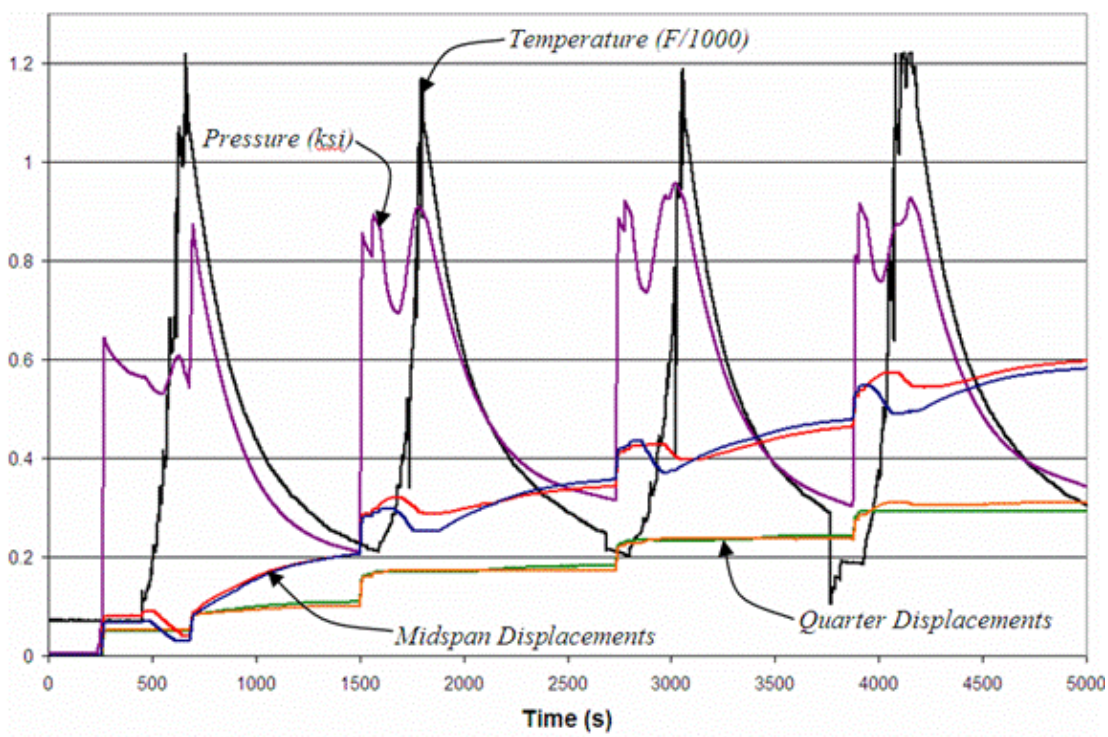

Figure 8.9
Instrument data during the third repair cycle of Beam 1

Figure 8.10
Front view of A7-Beam 1 after experimental investigations

(a) (b)

Figure 8.11
Lateral displacement of front (a) and back (b) flanges after repair cycle 3 of A7-Beam 1

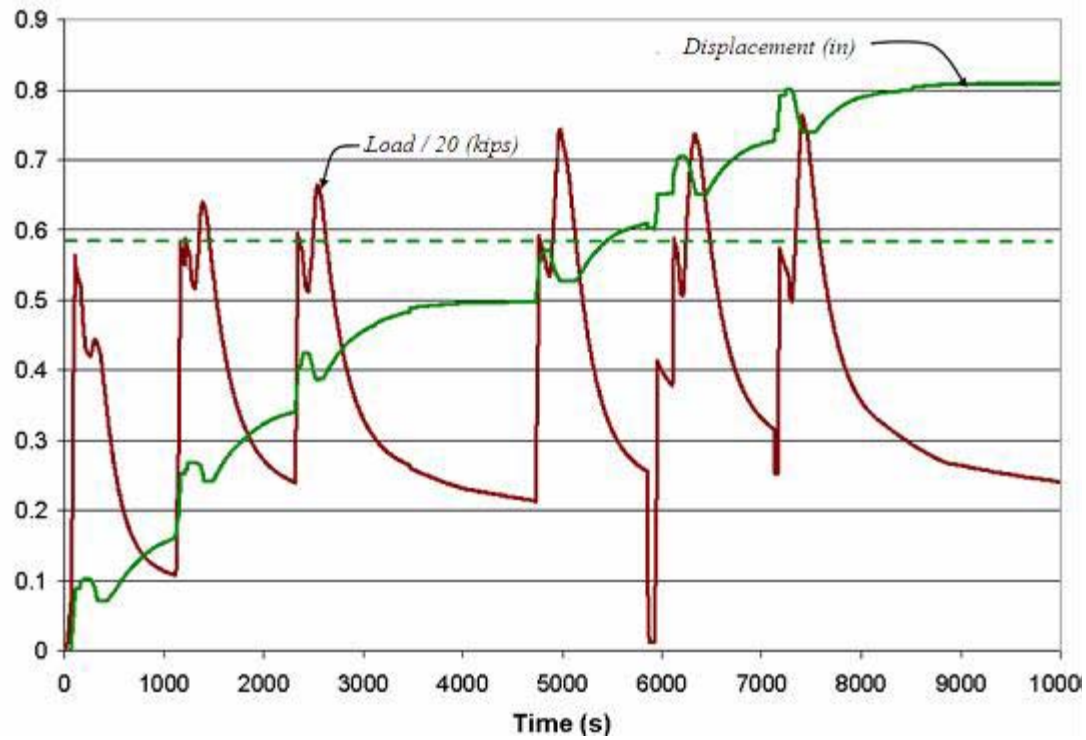

Figure 8.12
Load and displacement data during the first six heating cycles of A7-Beam 1

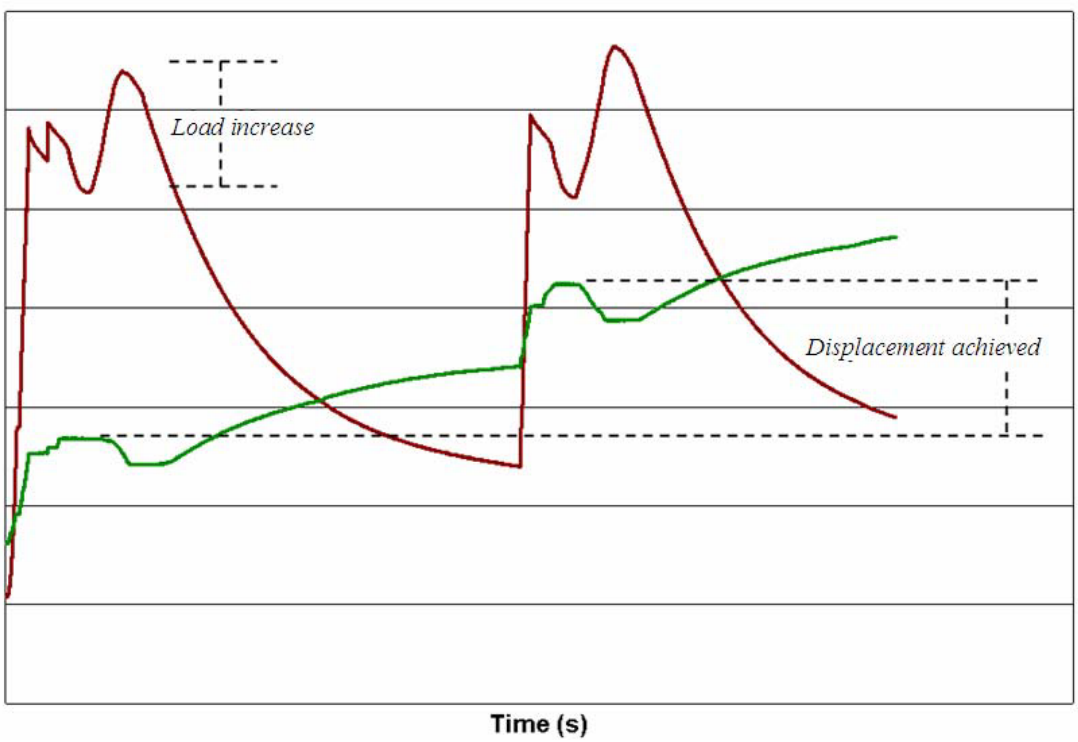

Figure 8.13
Illustration of the load increase and displacements achieved during each heating cycle

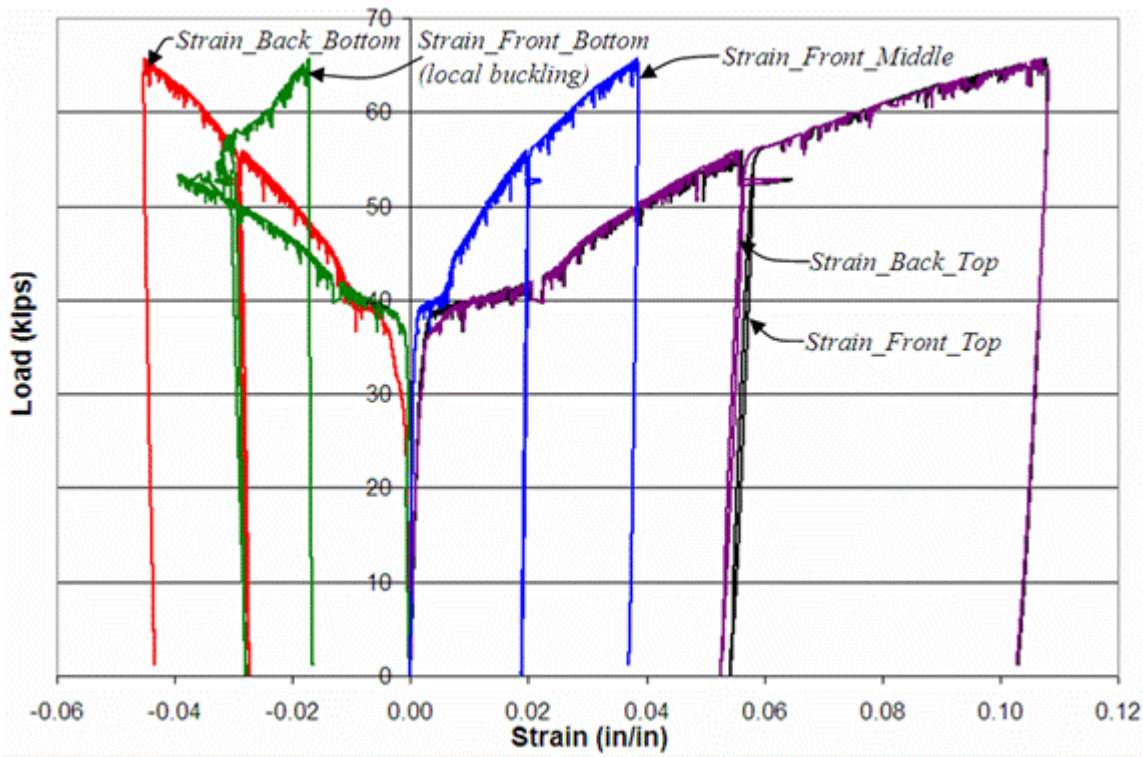

Figure 8.14
Strain gage data during the first damage cycle of A7-Beam 2

(a)

(b)

Figure 8.15
Before (a) and after (b) photographs of the first damage cycle of A7-Beam 2

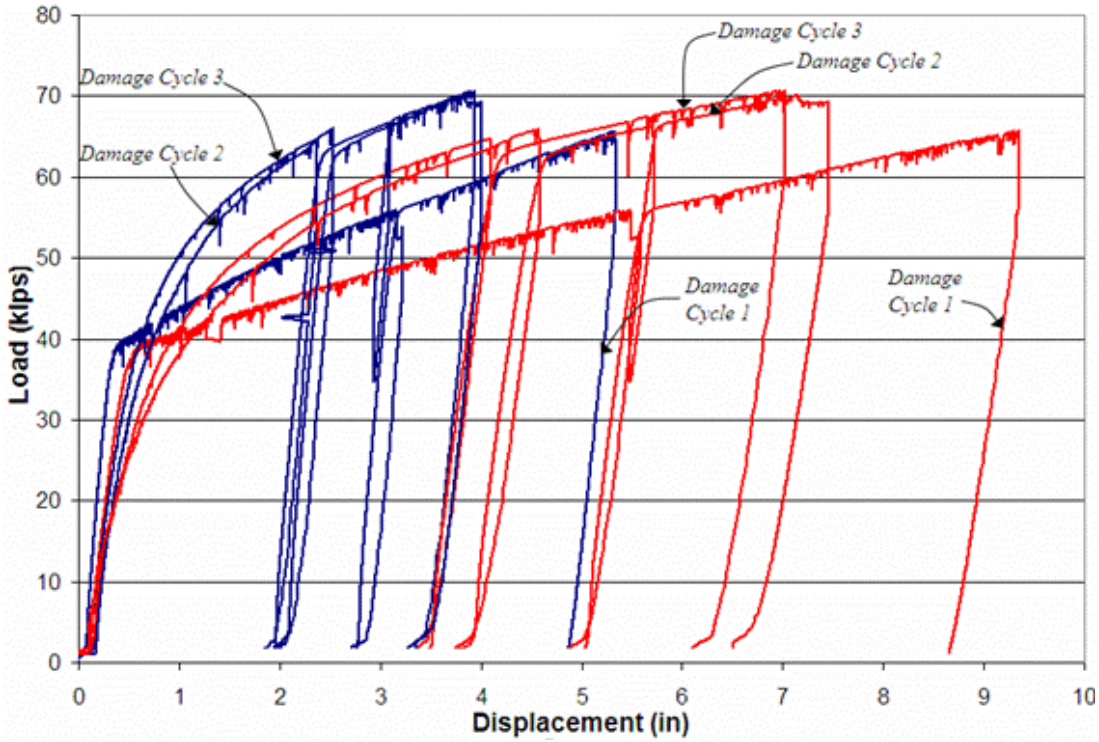

Figure 8.16
Load-displacement behaviors of all three damage cycles of A7-Beam 2

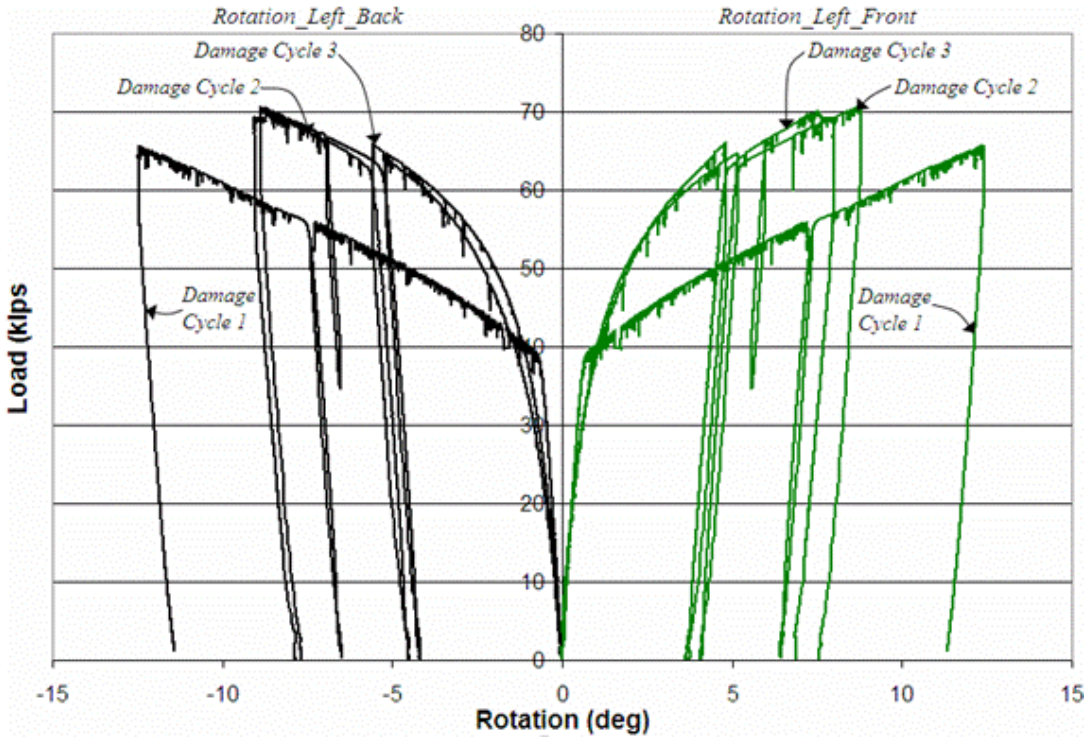

Figure 8.17
Load-rotation behaviors of all three damage cycles of A7-Beam 2

a) Damage Cycle 1 b) Damage Cycle 2 c) Damage Cycle 3

Figure 8.18
Condition of front flange at mid-length after each damage cycle of A7-Beam 2

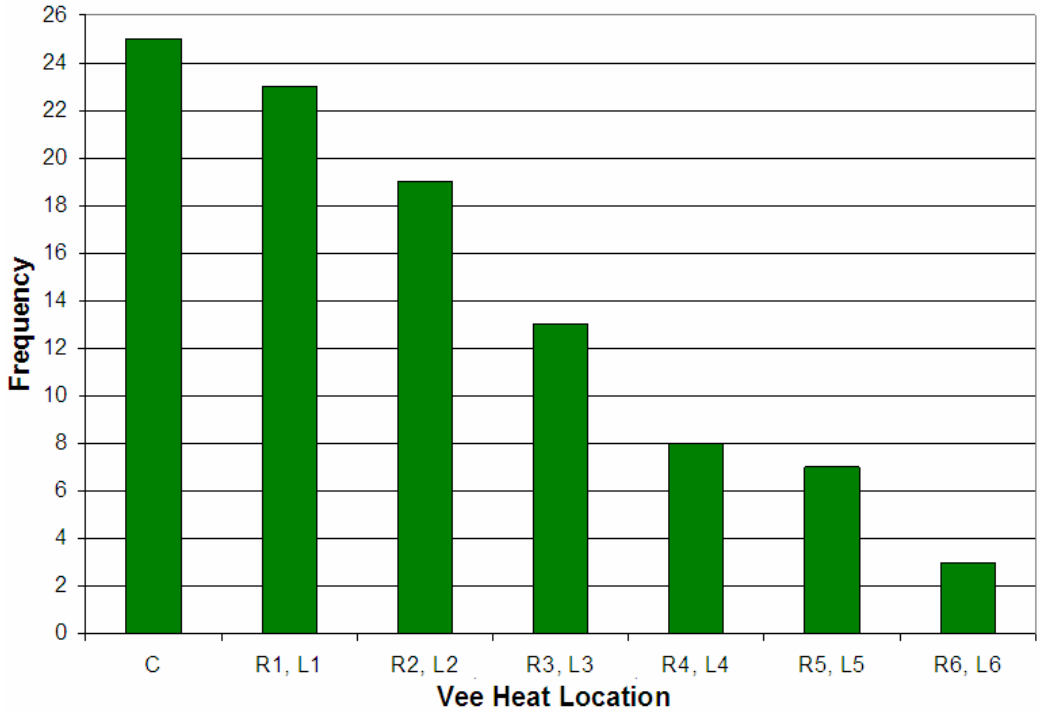

Figure 8.19
Frequency chart of each Vee heat location during three repairs of A7-Beam 2

a) Front side

b) Back side

Figure 8.20
Location of strip heats applied to the web of A7-Beam 2

Figure 8.21
Front view of A7-Beam 2 after experimental investigations

(a) (b)

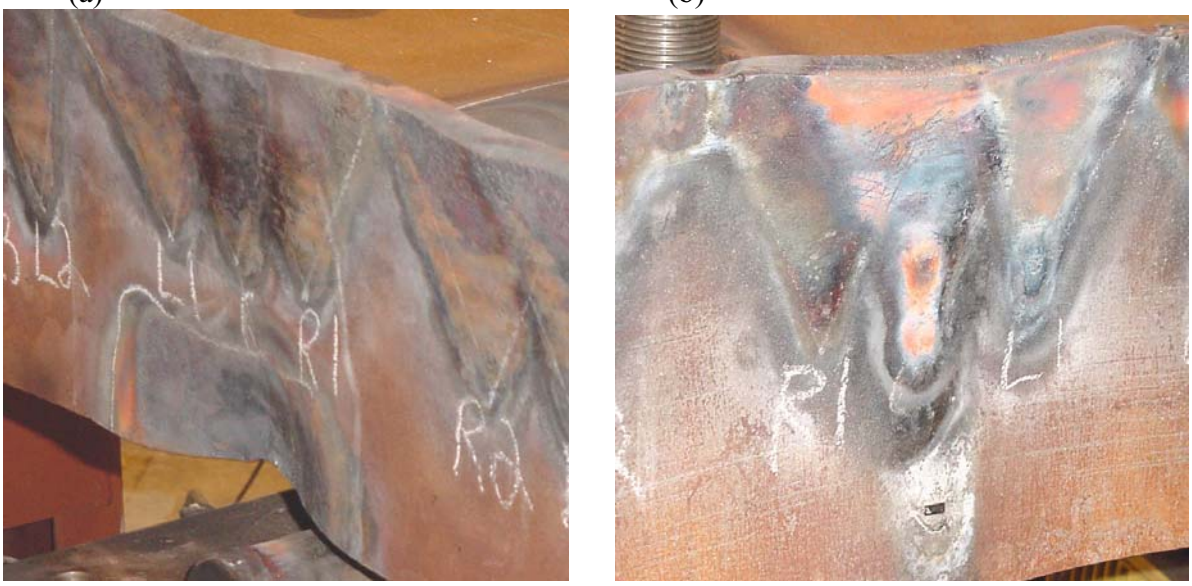

Figure 8.22
Condition of front (a) and back (b) flanges of A7-Beam 2 after repair cycle 3

(a) (b)

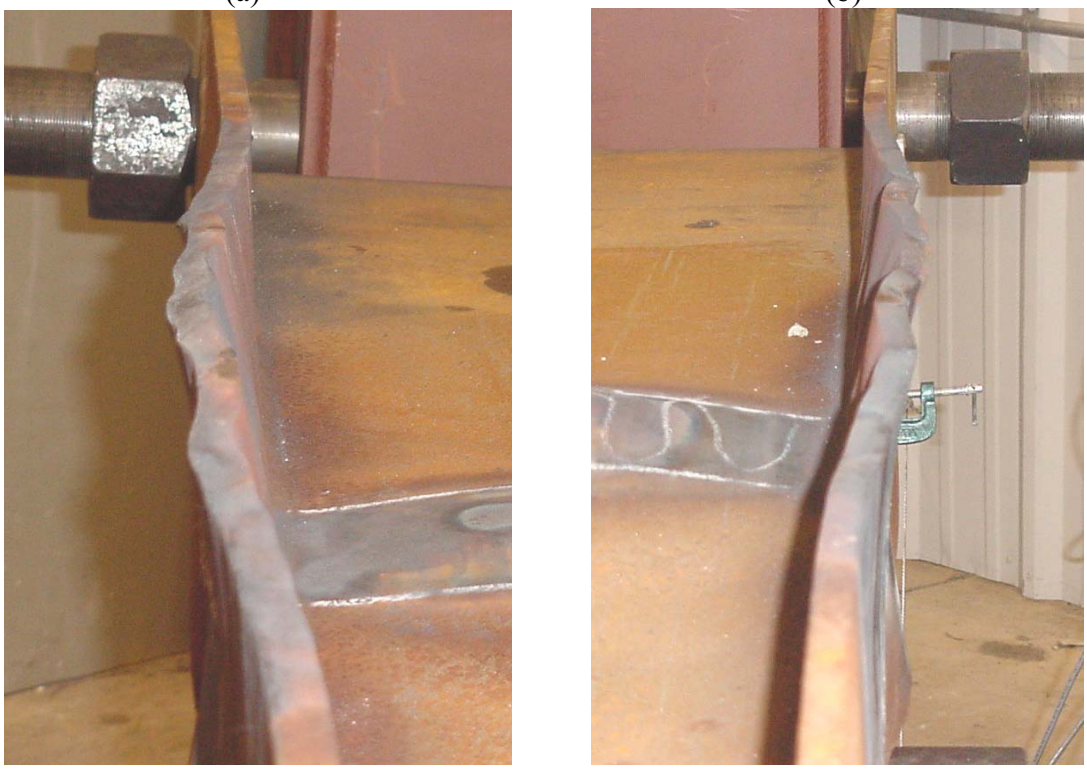

Figure 8.23
Lateral displacement of front (a) and back (b) flanges after repair cycle 3 of A7-Beam 2

Figure 8.24
Fracture of the material at the buckled location of the front flange of A7-Beam 2

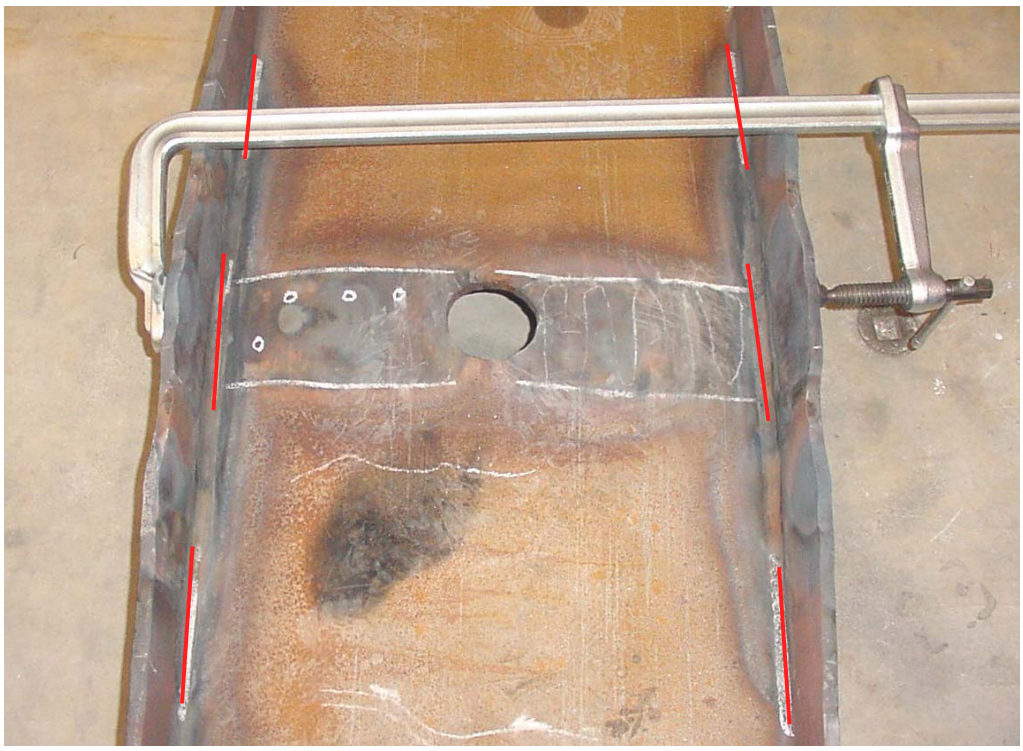

Figure 8.25
Location of line heats applied to straighten flanges (A7-Beam 2)

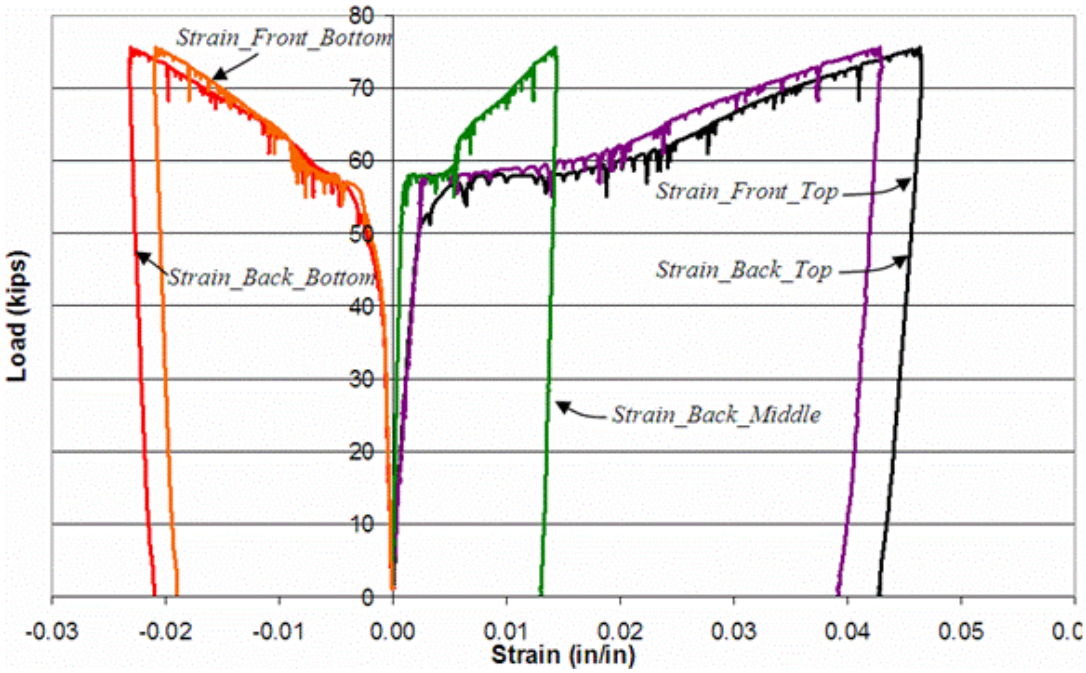

Figure 8.26
Strain gage data during the first damage cycle of A36-Beam 1

(a)

(b)

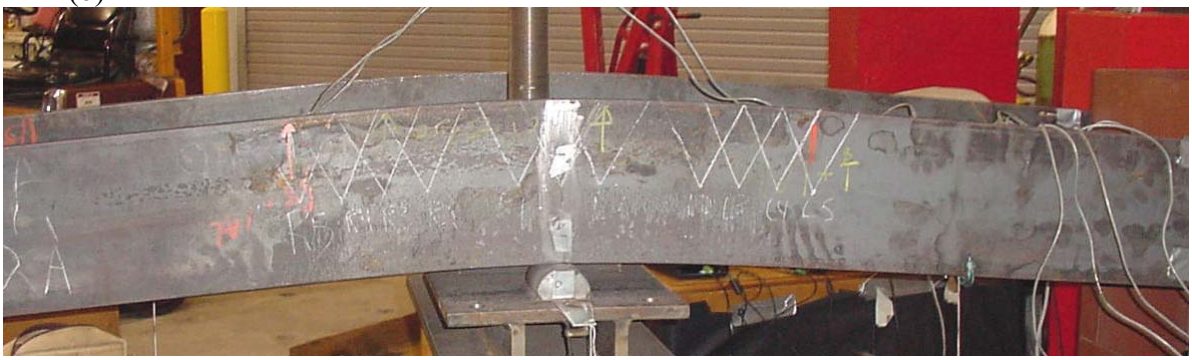

Figure 8.27
Before (a) and after (b) photographs of the first damage cycle of A36-Beam 1

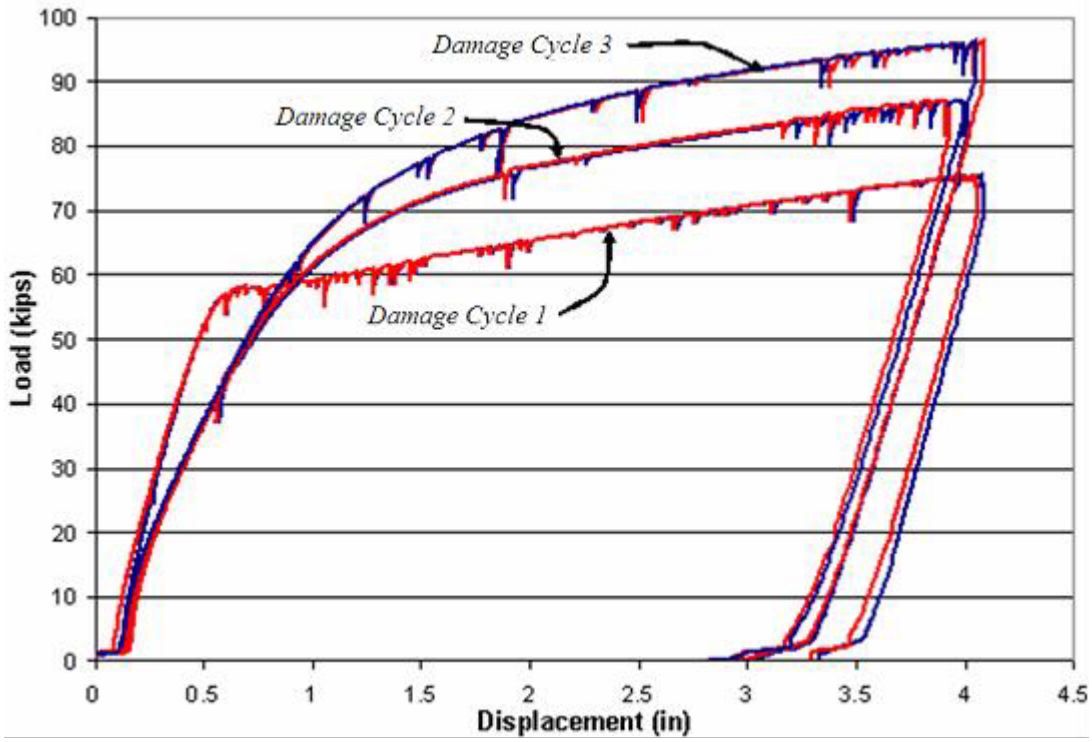

Figure 8.28
Load-displacement behaviors of all three damage cycles of A36-Beam 1

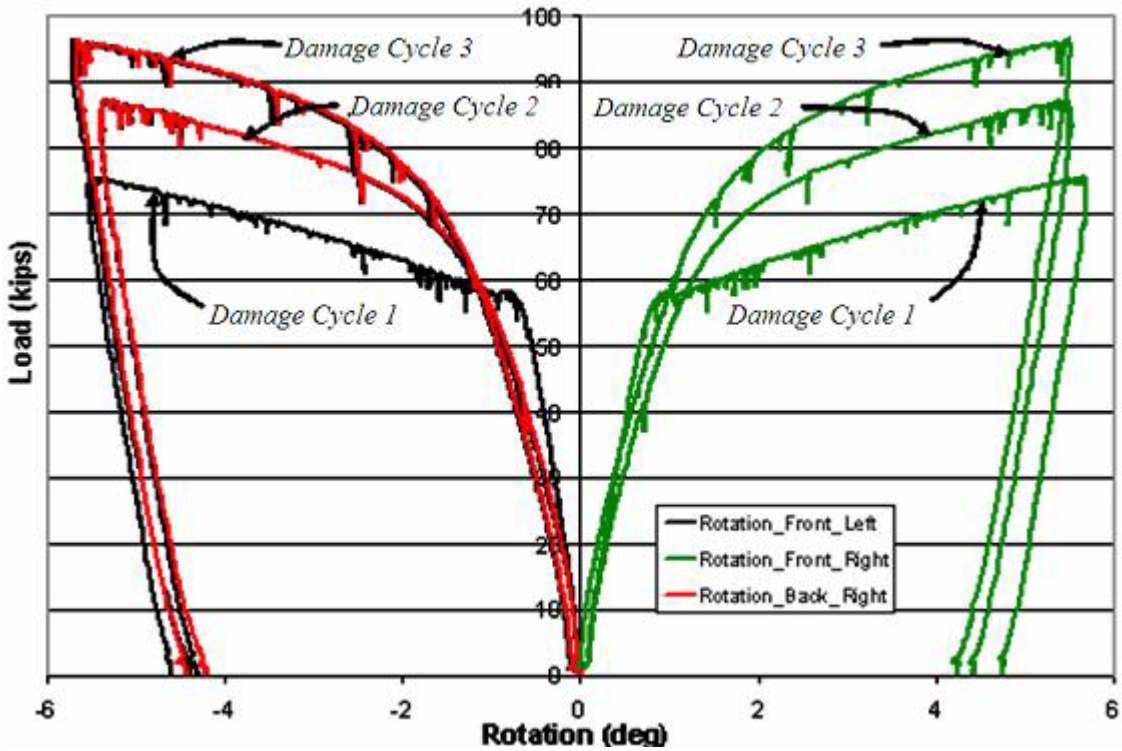

Figure 8.29
Load-rotation behaviors of all three damage cycles of A36-Beam 1

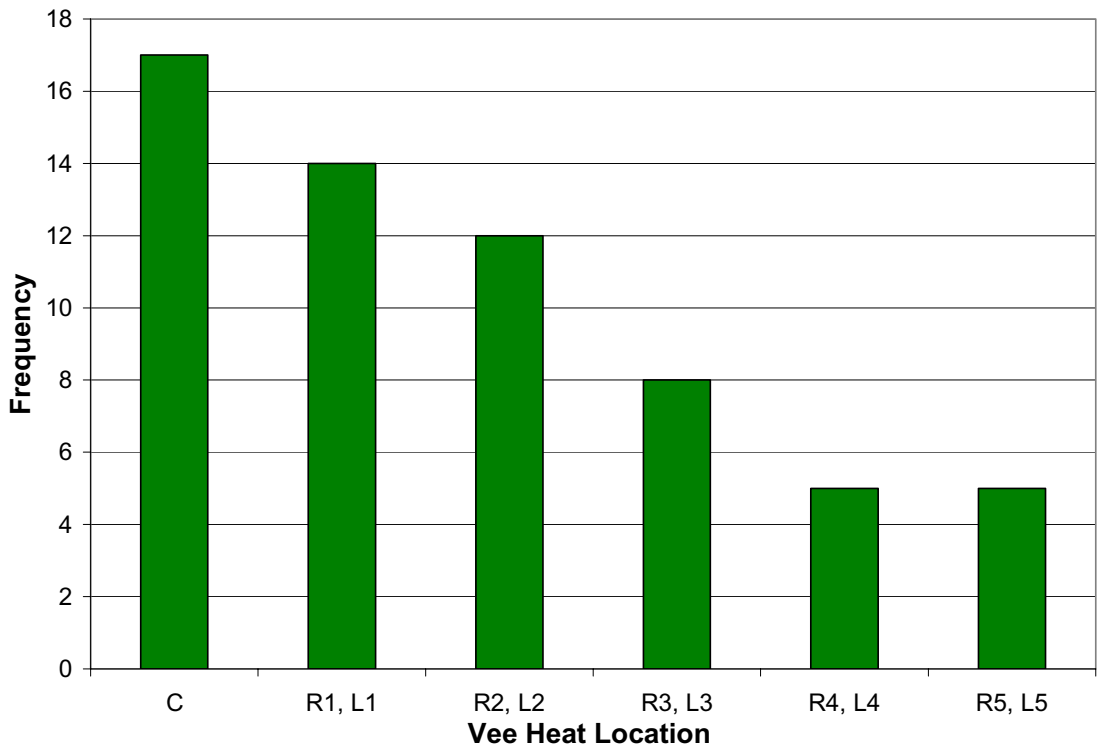

Figure 8.30
Frequency chart of each Vee heat location during three repairs of A36-Beam 1

Figure 8.31
Frontal view of A36-Beam 1 after experimental investigations

Figure 8.32
Lateral displacement of A36-Beam 1 after experimental investigations

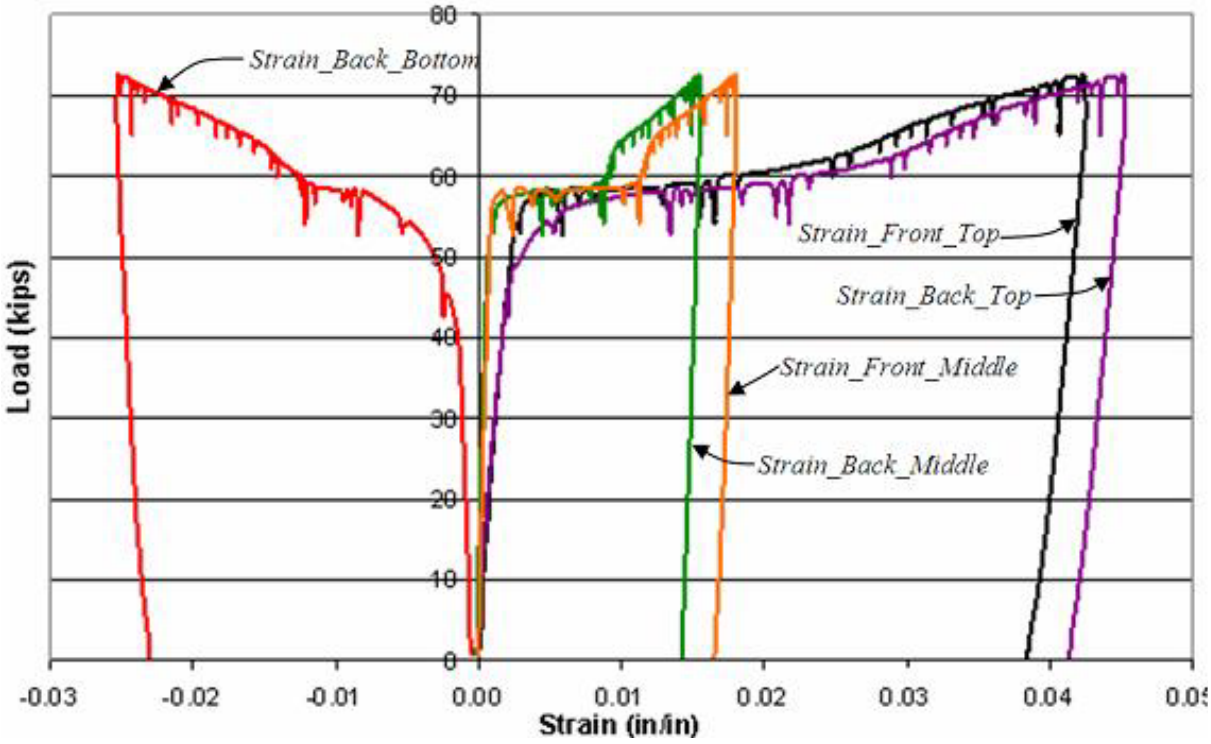

Figure 8.33
Strain gage data during the first damage cycle of A36-Beam 2

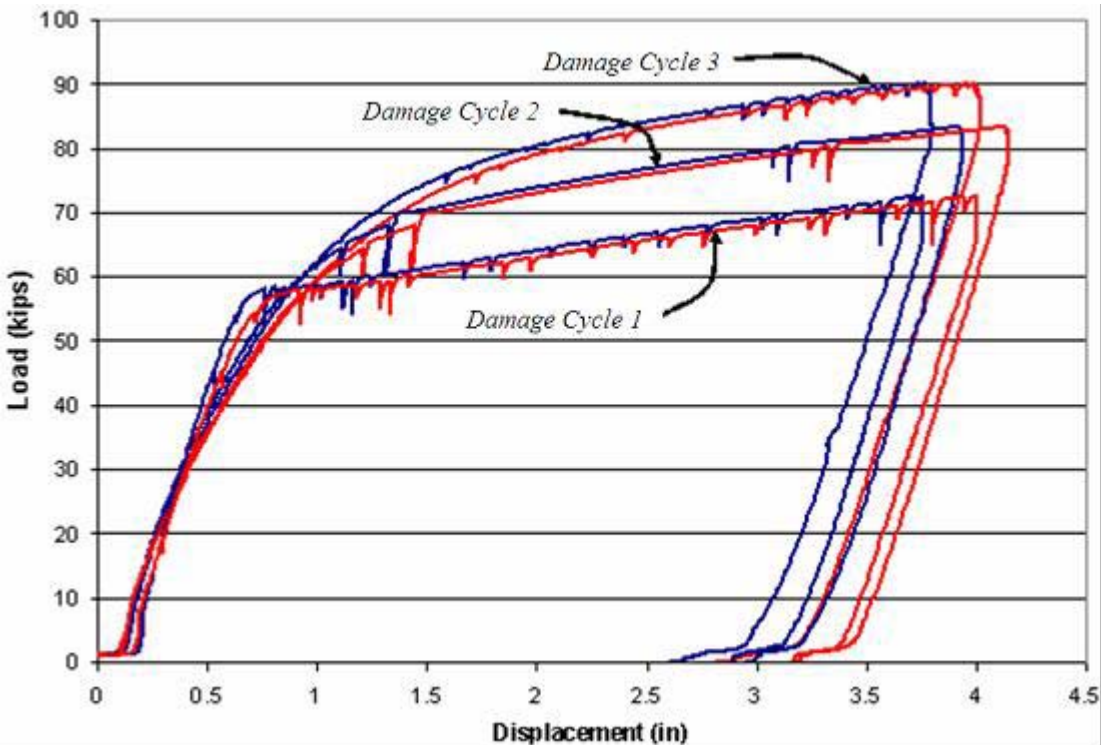

Figure 8.34
Load-displacement behaviors of all three damage cycles of A36-Beam 2

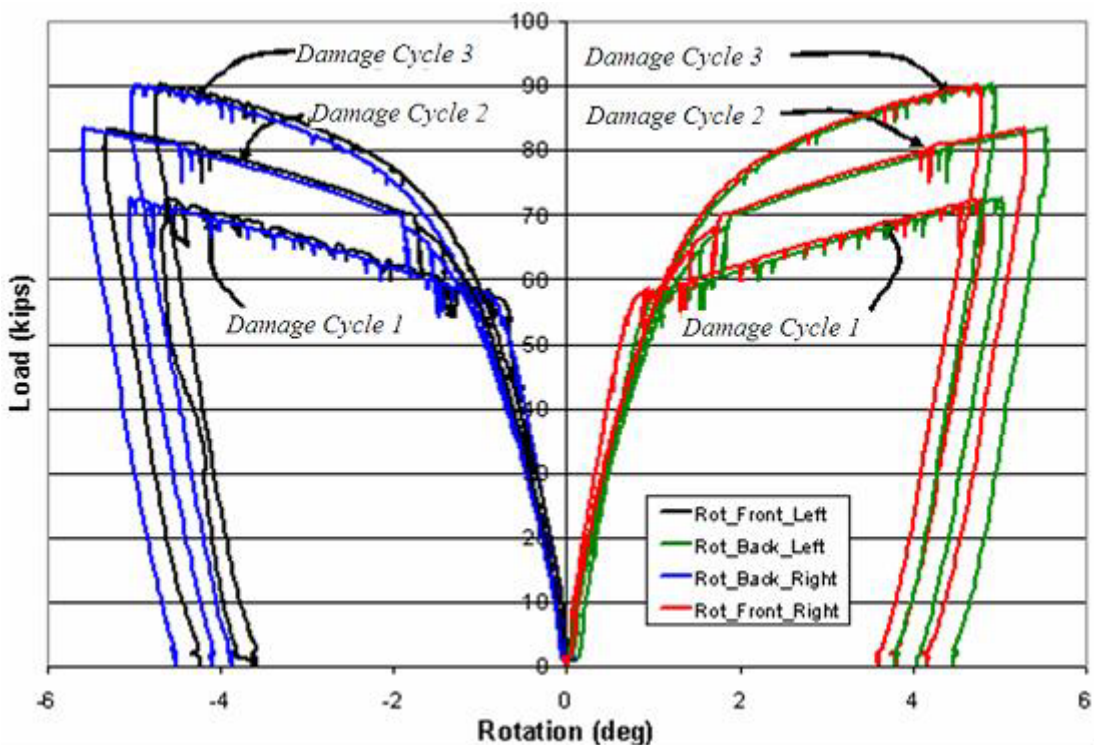

Figure 8.35
Load-rotation behaviors of all three damage cycles on A36-Beam 2

a) 1400 °F (A36-Beam 2)

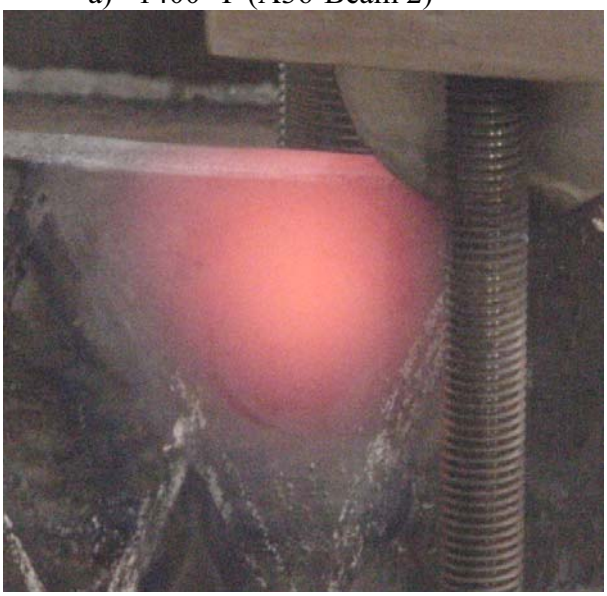

b) 1200 °F (A36-Beam 1)

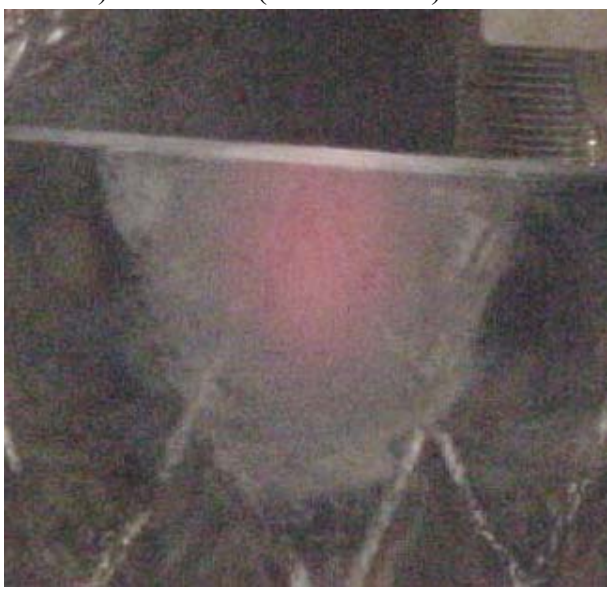

Figure 8.36
Color of A36 steel at maximum heating temperatures

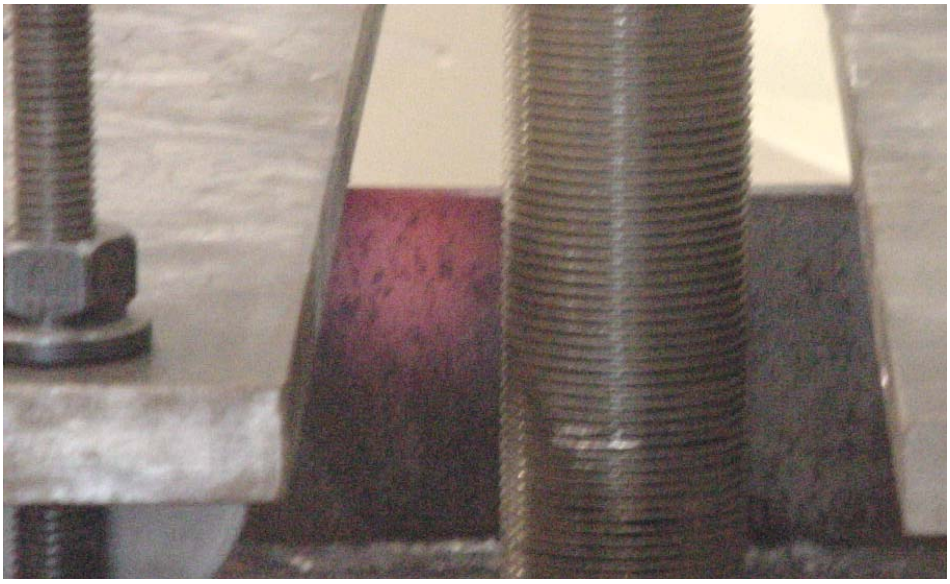

Figure 8.37
Opposite side of Vee heated to a maximum temperature of 1400 °F

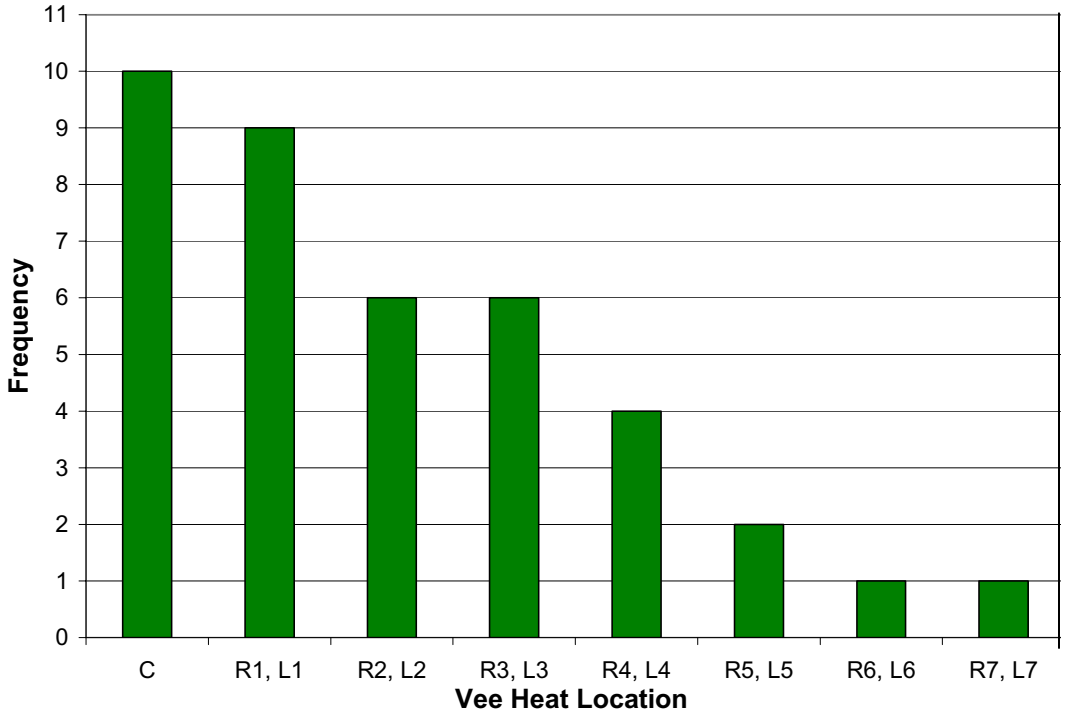

Figure 8.38
Frequency chart of each Vee heat location during three repairs of A36-Beam 2

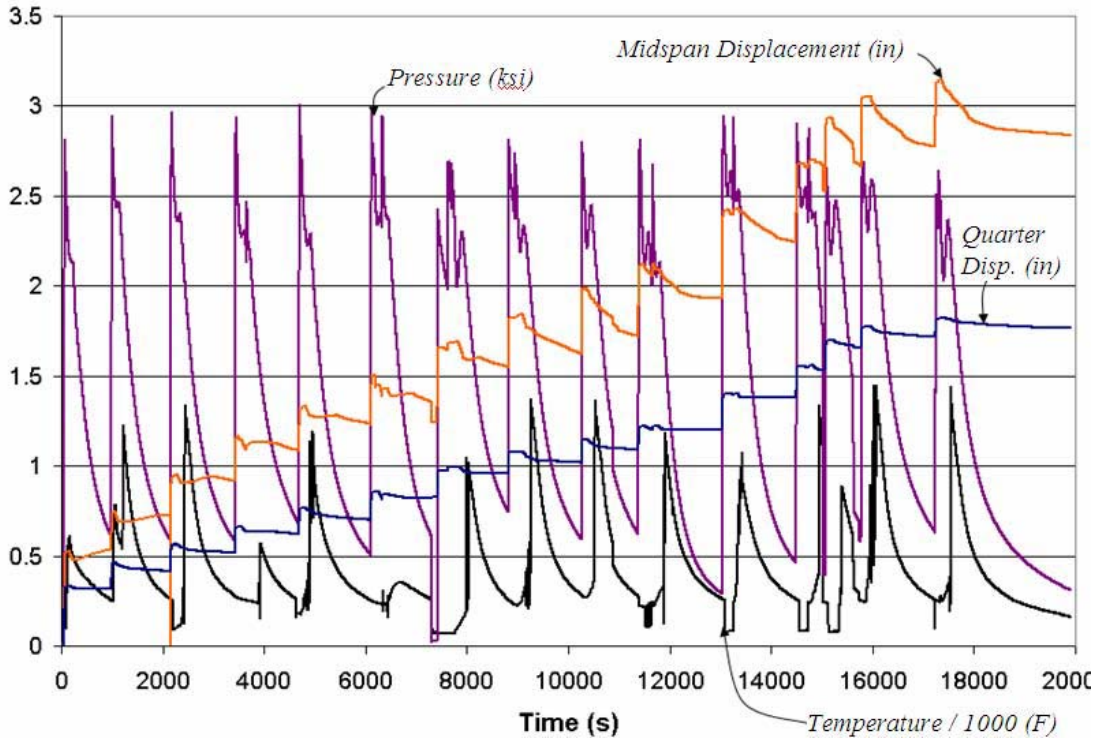

Figure 8.39
Instrument data during the second repair cycle of A36-Beam 2

Figure 8.40
Front view of A36-Beam 2 after experimental investigations

Figure 8.41
Lateral displacement of A36-Beam 2 after experimental investigations

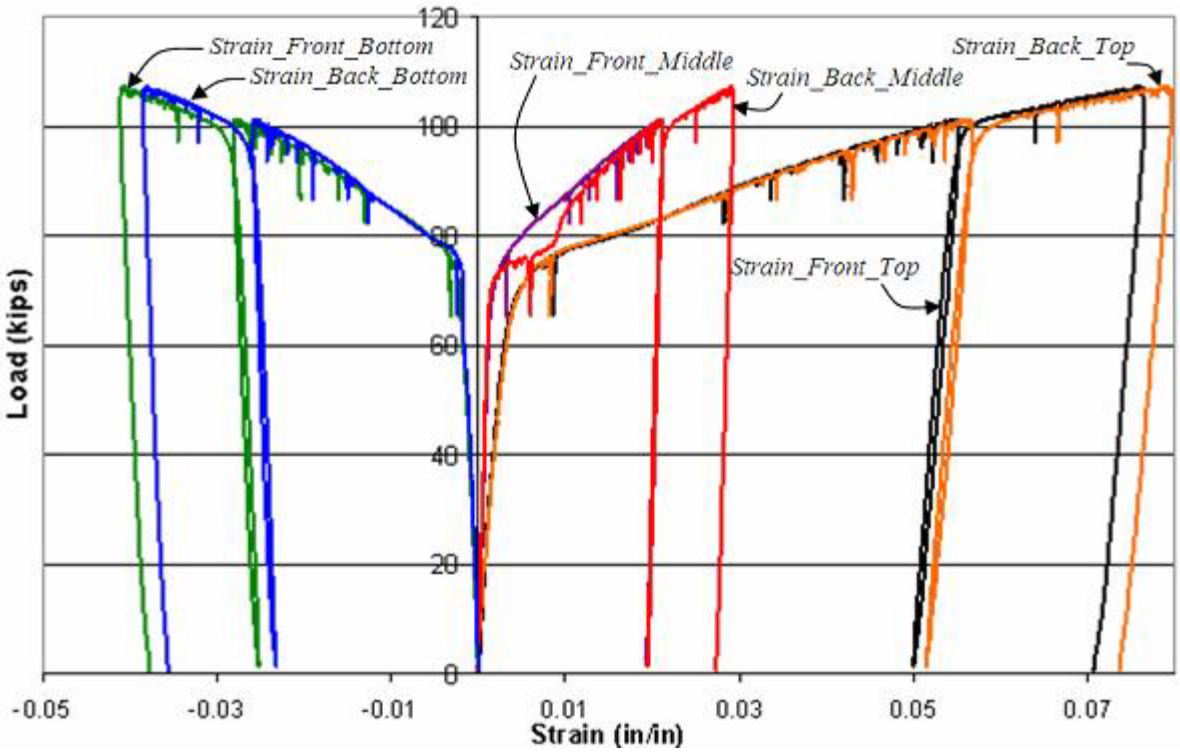

Figure 8.42
Strain gage data during the first damage cycle of A588-Beam 1

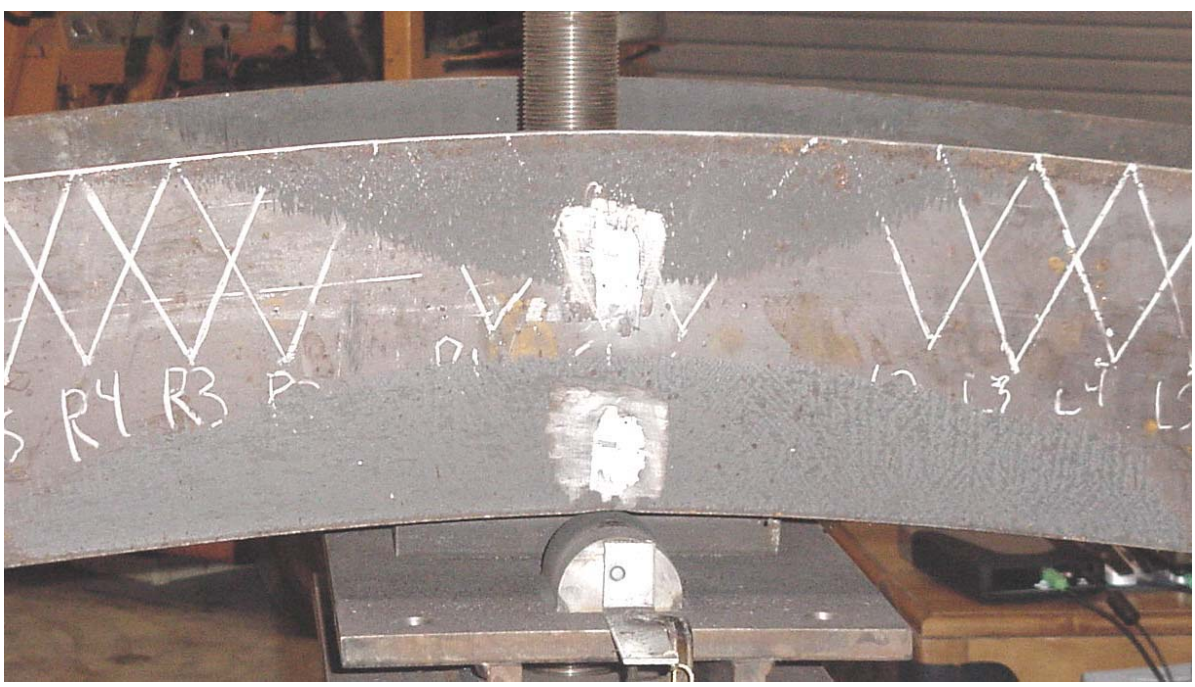

Figure 8.43
Spread of yielding after the first damage cycle of A588-Beam 1

(a)

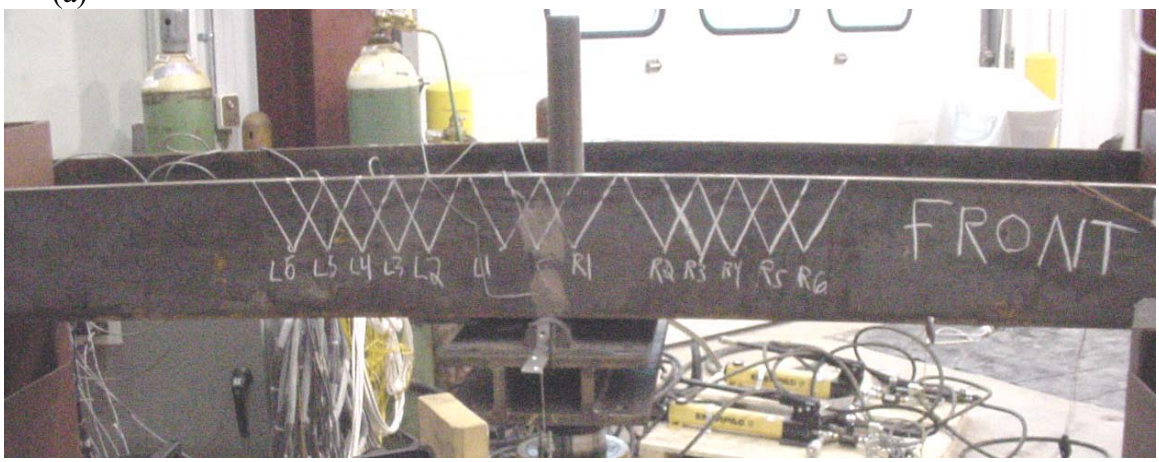

(b)

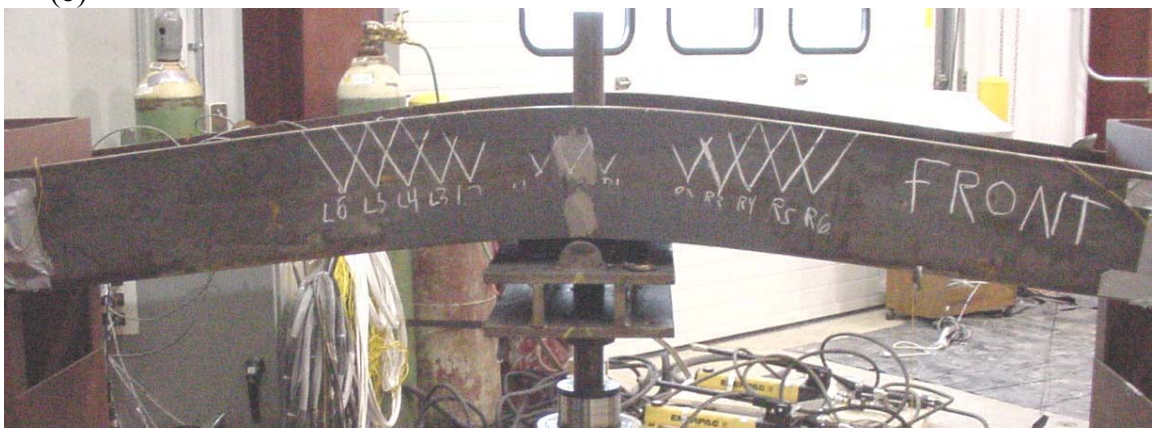

Figure 8.44
Before (a) and after (b) photographs of the first damage cycle of A588-Beam 1

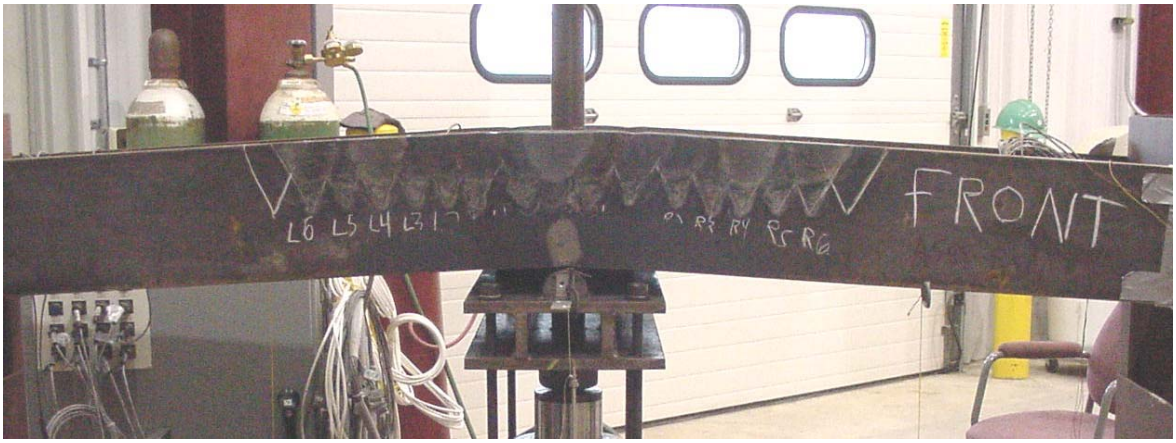

Figure 8.45
Photograph of A588-Beam1 after the third damage cycle

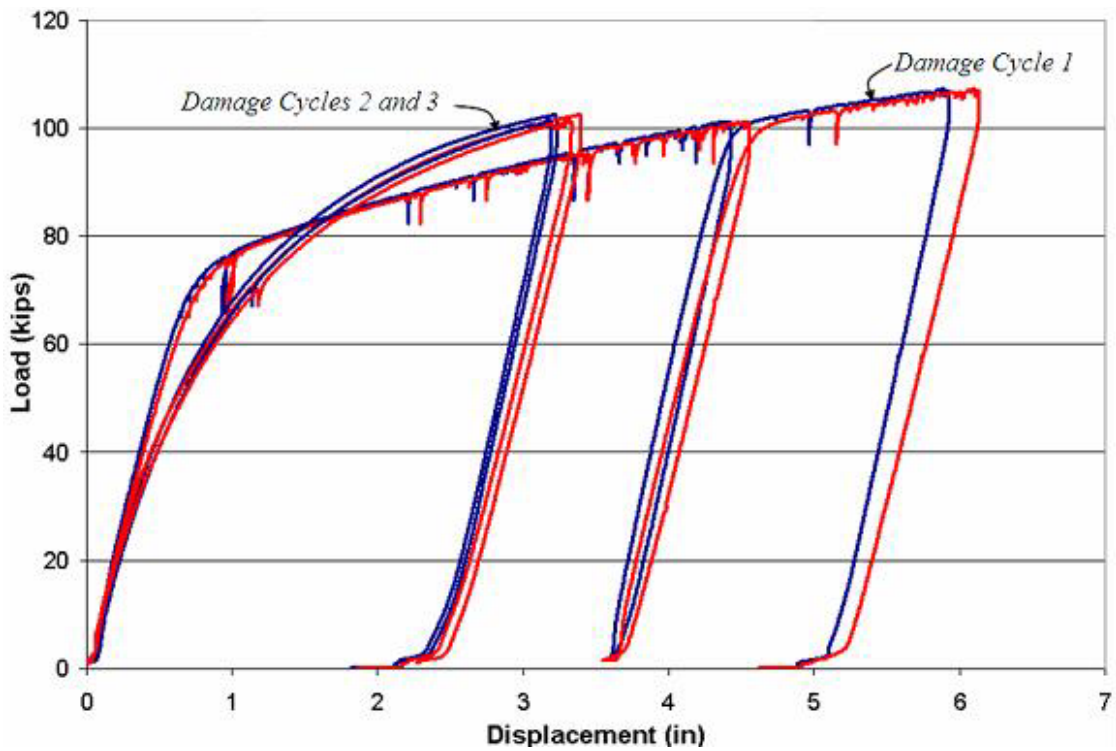

Figure 8.46
Load-displacement behaviors of all three damage cycles of A588-Beam 1

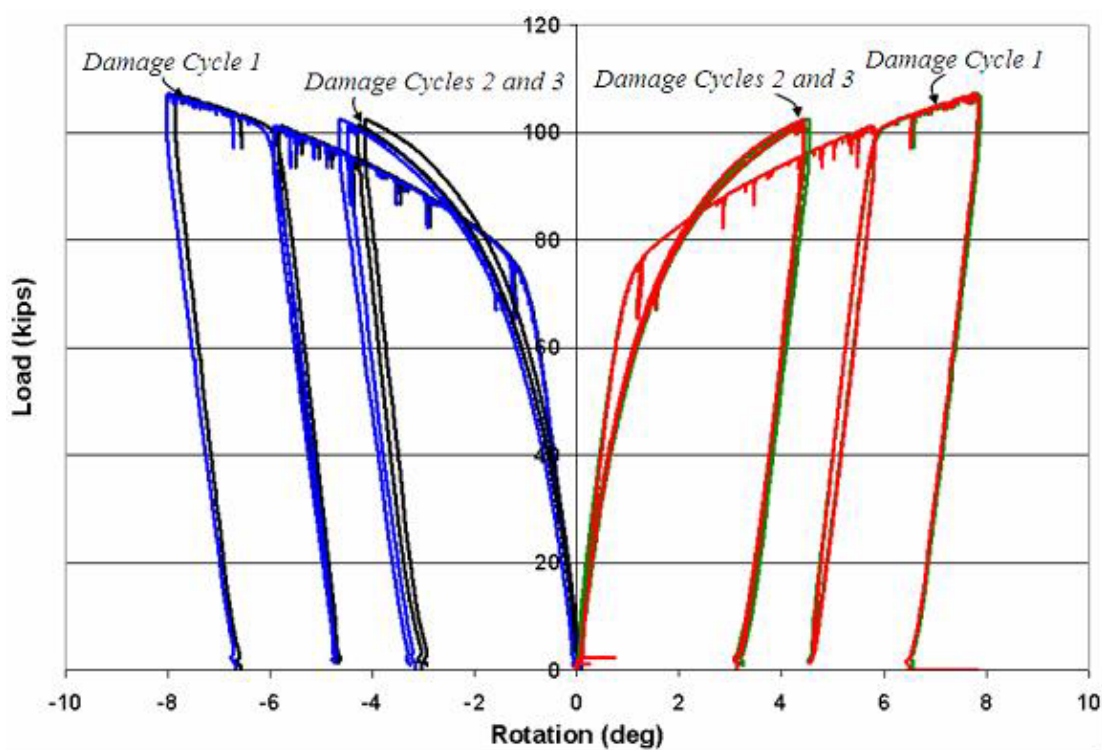

Figure 8.47
Load-rotation behaviors of all three damage cycles of A588-Beam 1

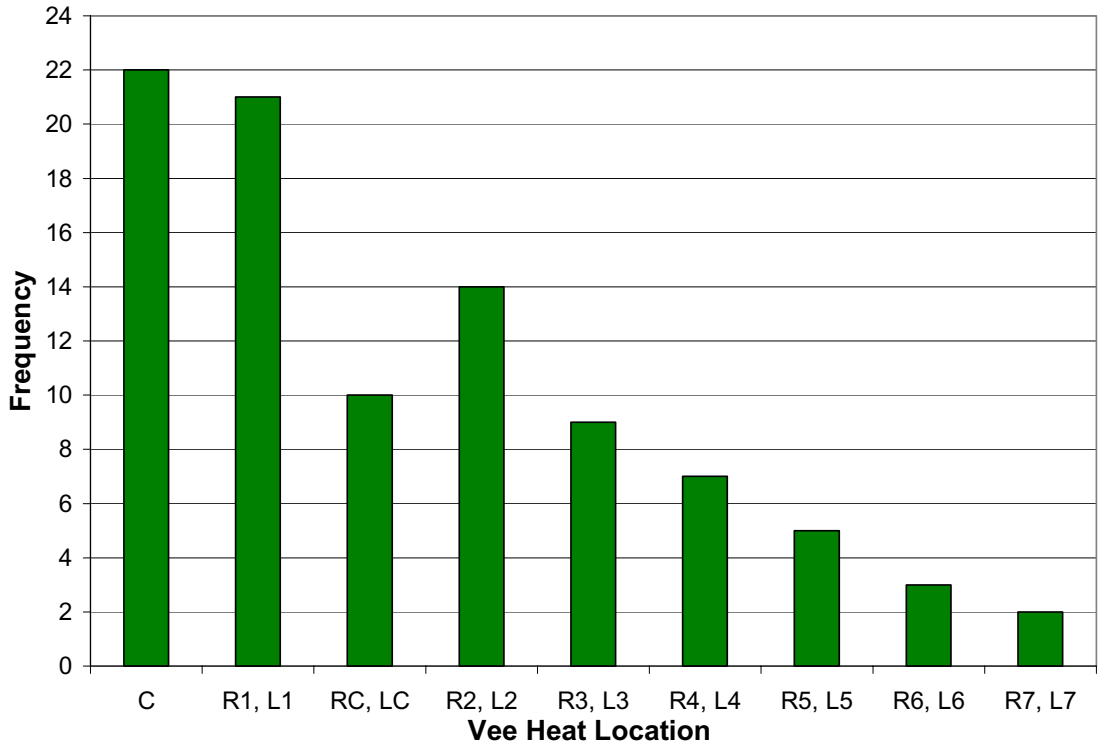

Figure 8.48
Frequency chart of each Vee heat location during three repairs of A588-Beam 1

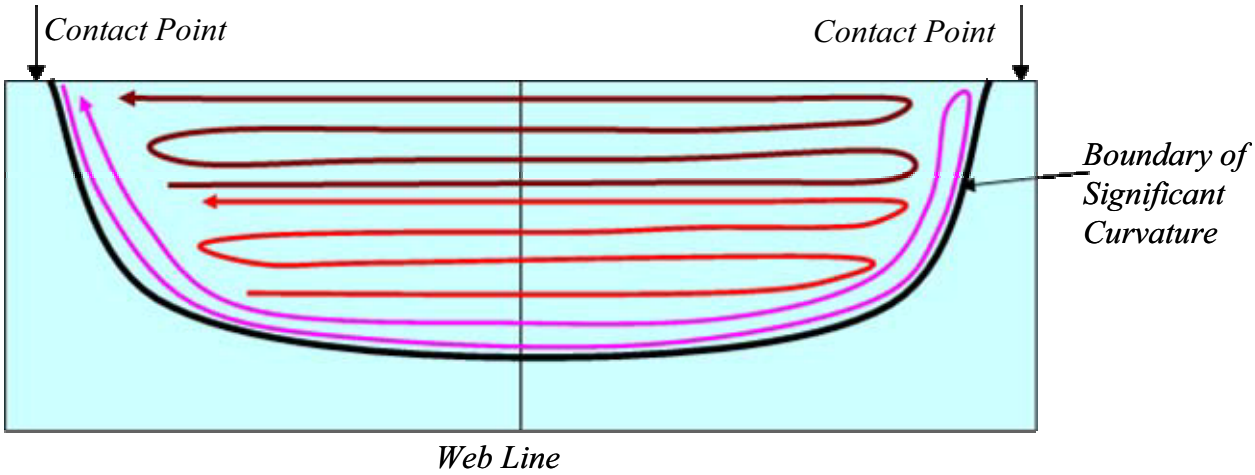

Figure 8.49
Heating patterns used on the inside of flanges to reduce curvature of A588 beams

Figure 8.50
Front view of A588-Beam 1 after experimental investigations

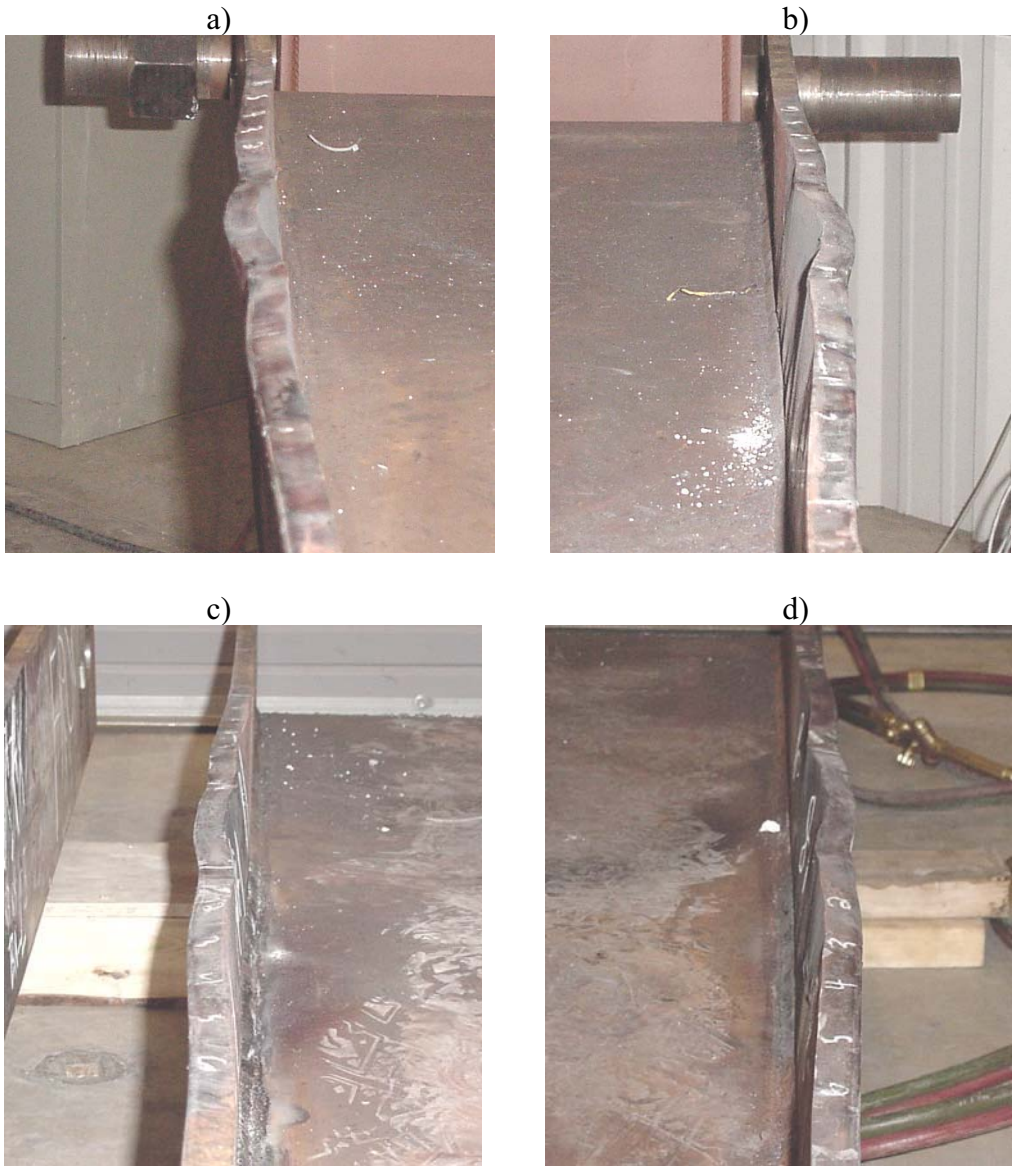

Figure 8.51
Lateral displacement of A588-Beam 1 before (a and b) and after (c and d) straightening

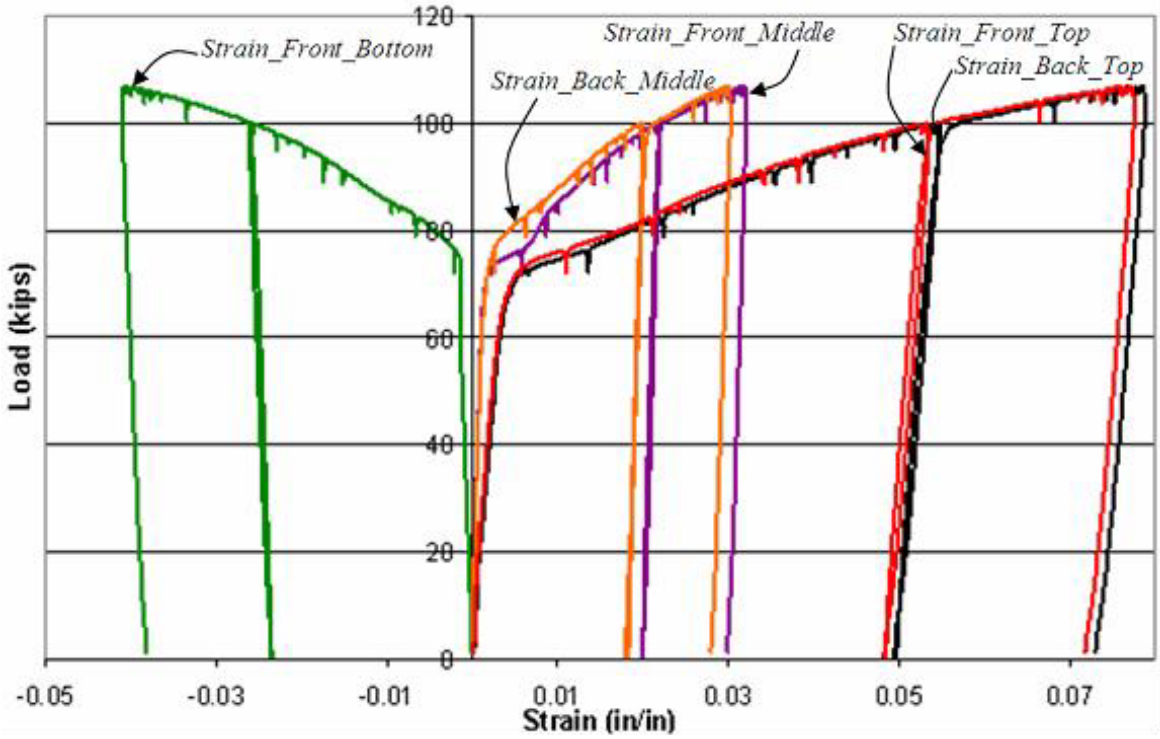

Figure 8.52
Strain gage data during the first damage cycle of A588-Beam 2

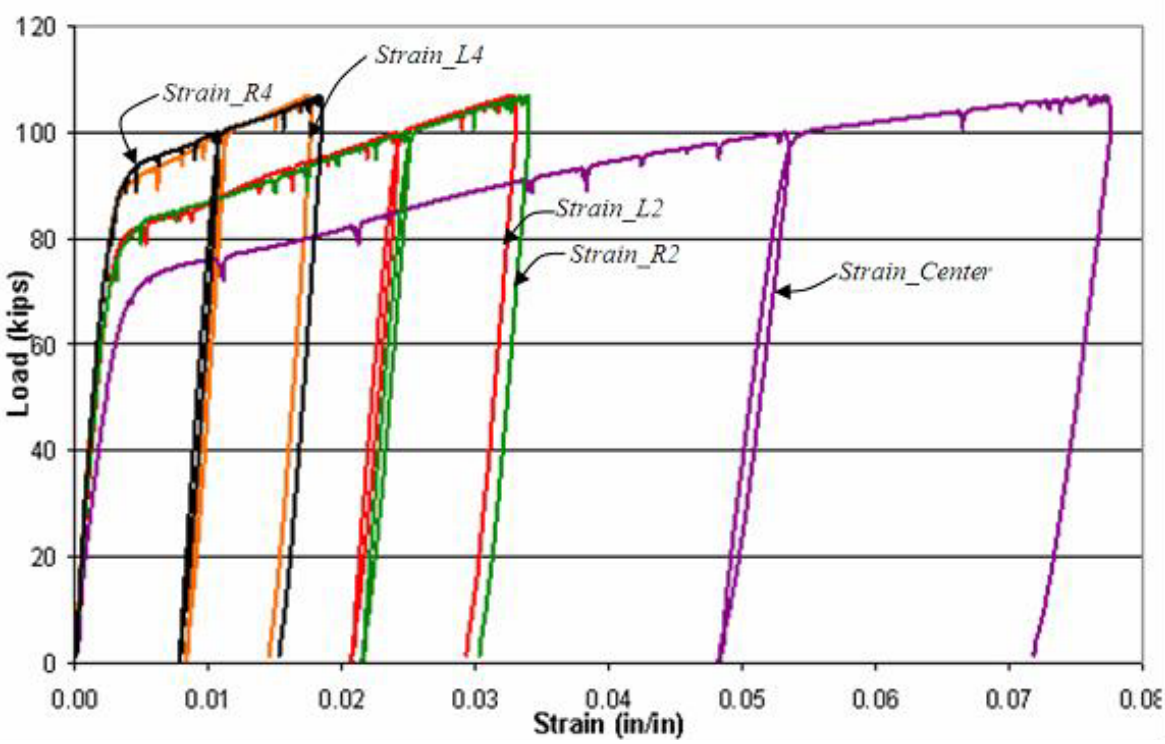

Figure 8.53
Strain gage data at various Vee heat locations during the first damage cycle of A588-Beam 2

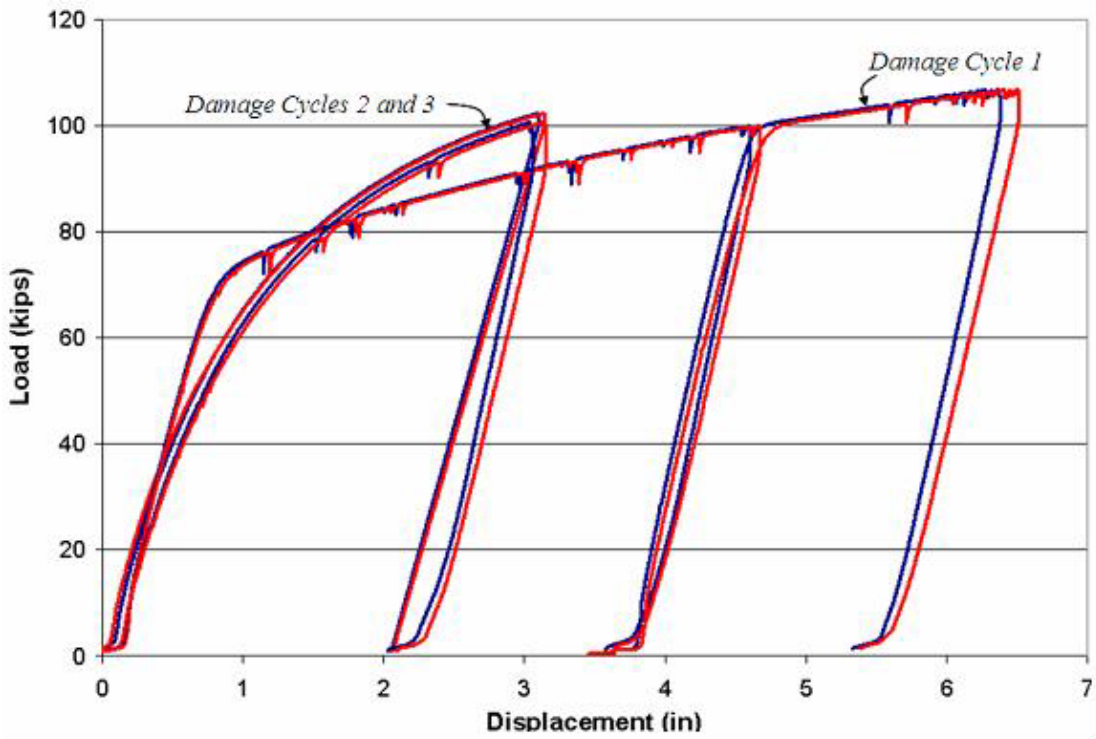

Figure 8.54
Load-displacement behaviors of all three damage cycles of A588-Beam 1

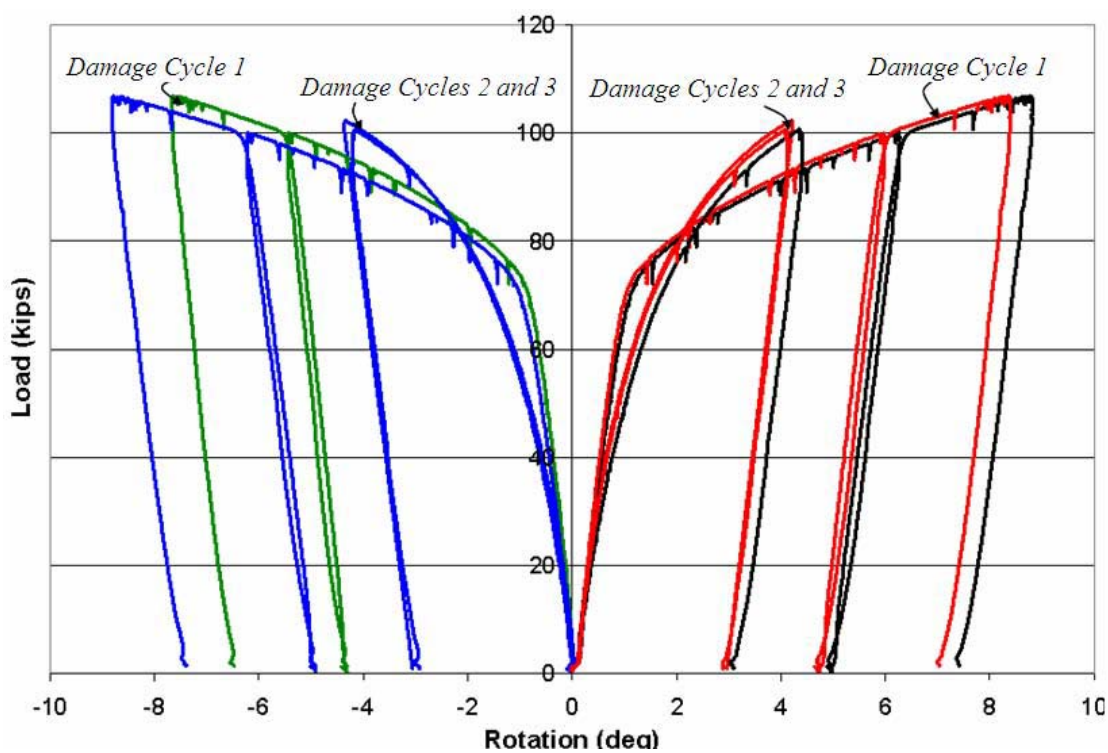

Figure 8.55
Load-displacement behaviors of all three damage cycles of A588-Beam 1

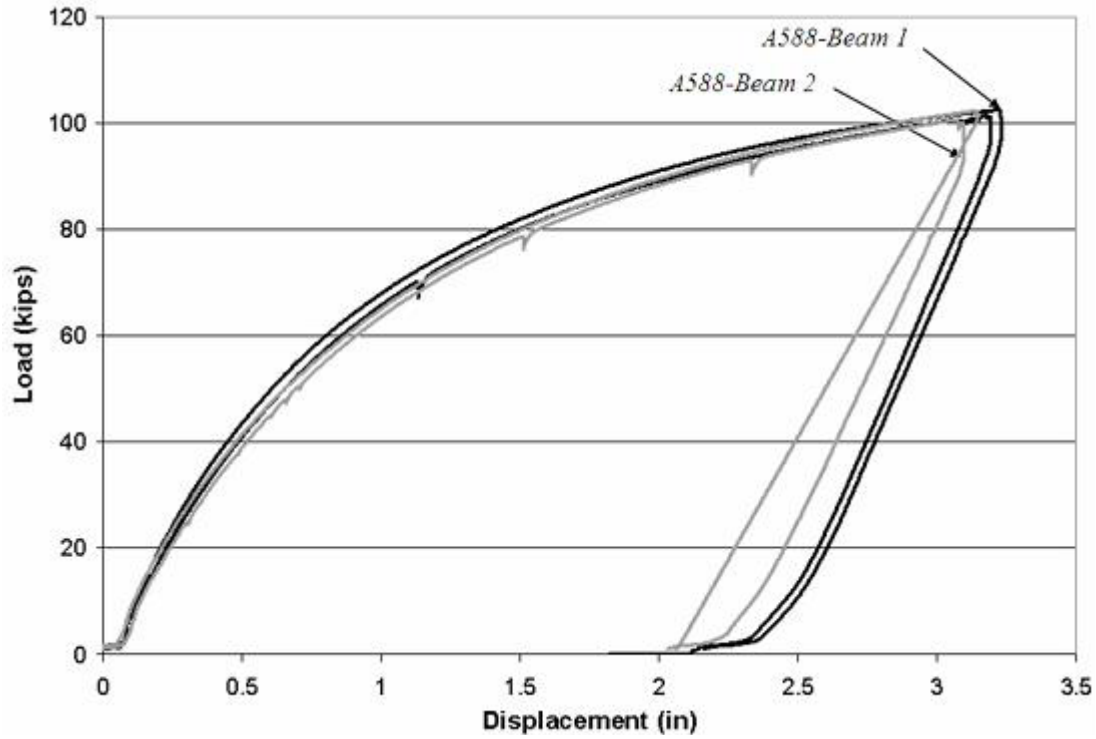

Figure 8.56
Comparison of midspan load-displacement behaviors of A588-Beam 1 and A588-Beam 2 during their respected second and third damage cycles

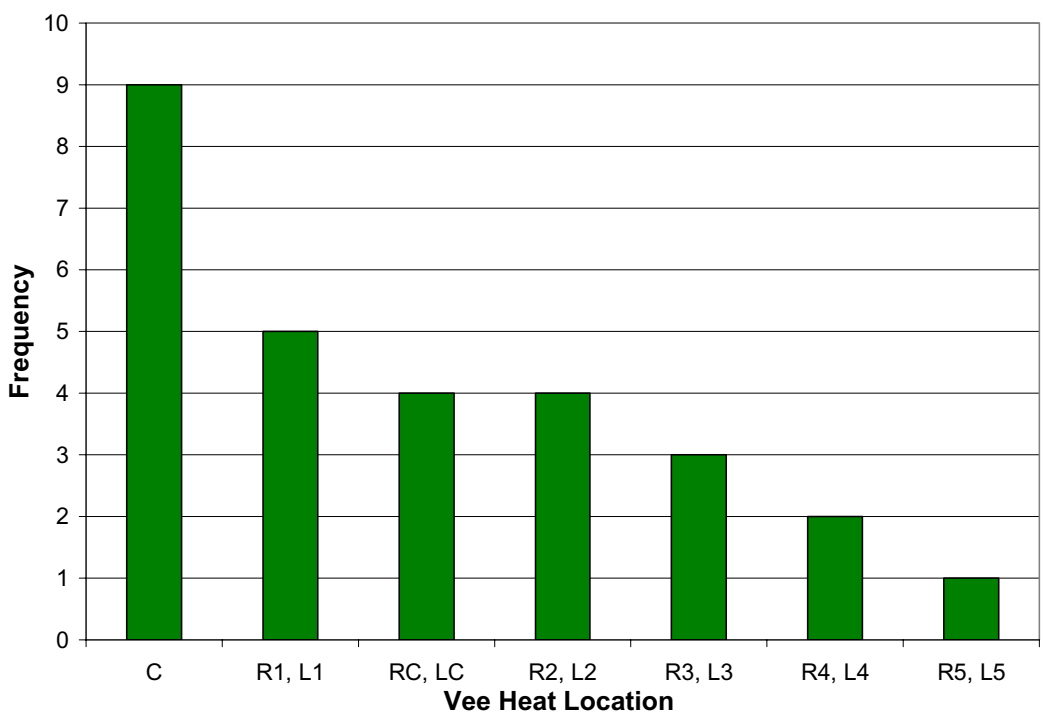

Figure 8.57
Frequency chart of each Vee heat location during three repairs of A588-Beam 2

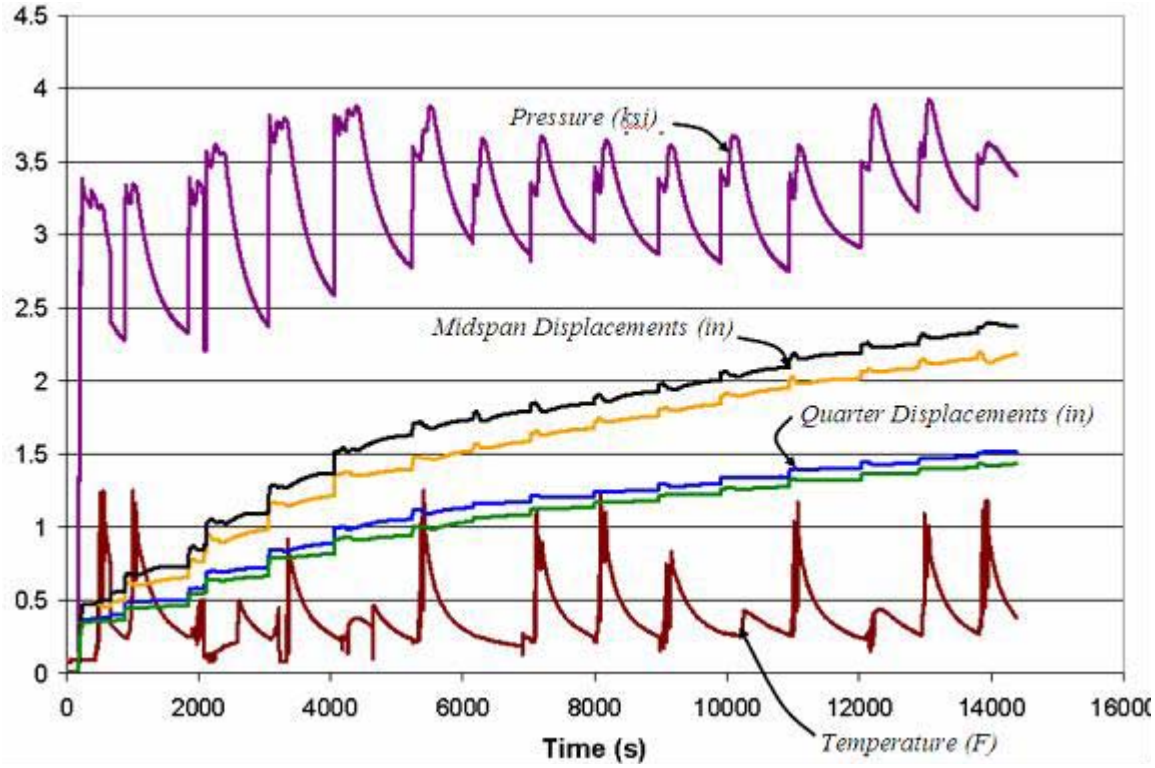

Figure 8.58
Instrument data during the second repair cycle of A588-Beam 2

Figure 8.59
Front view of A588-Beam 2 after three damage-repair cycles

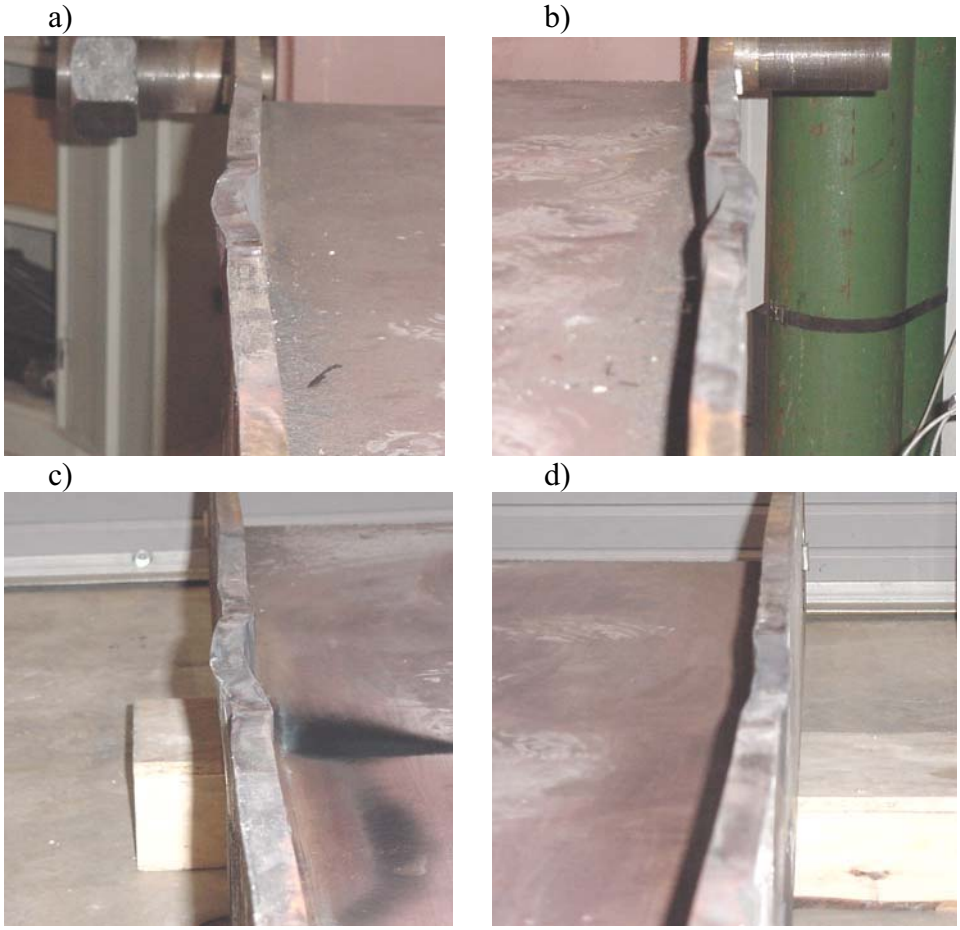

Figure 8.60
Lateral displacement of A588-Beam 2 before (a and b) and after (c and d) straightening

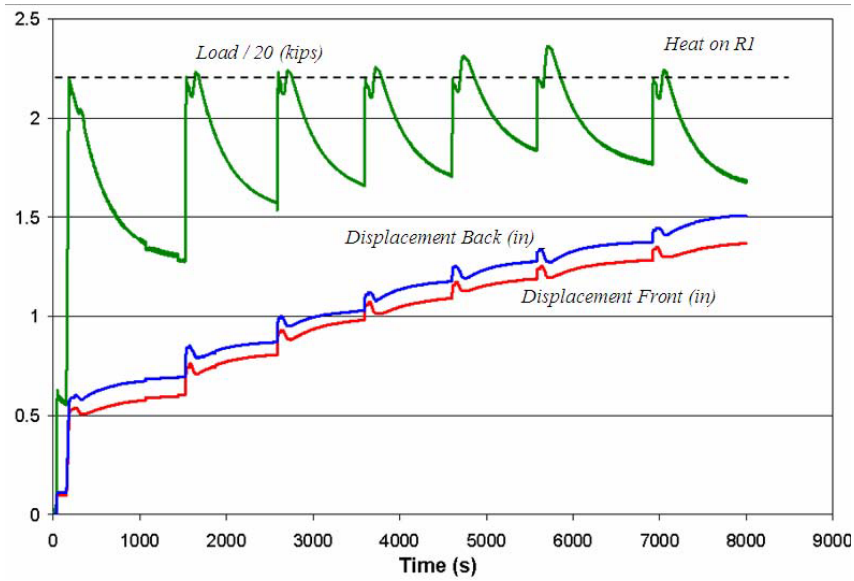

Figure 8.61
Load and displacement data during the first six heating cycles of A7-Beam 1

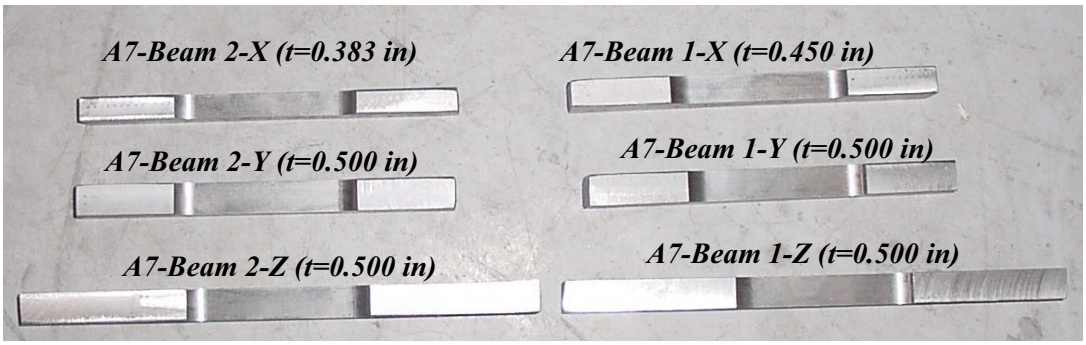

Figure 8.62
Uniaxial tension coupons fabricated from A7 beam specimens

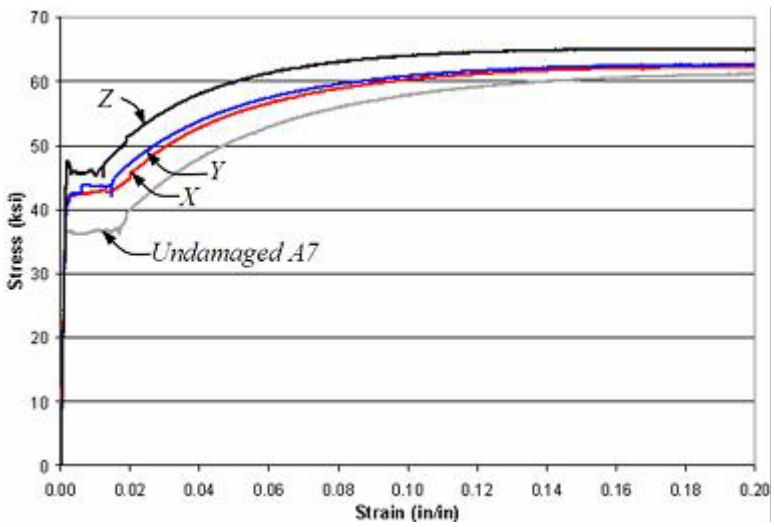

Figure 8.63
Stress-strain behavior of uniaxial tension coupons removed from A7-Beam 1

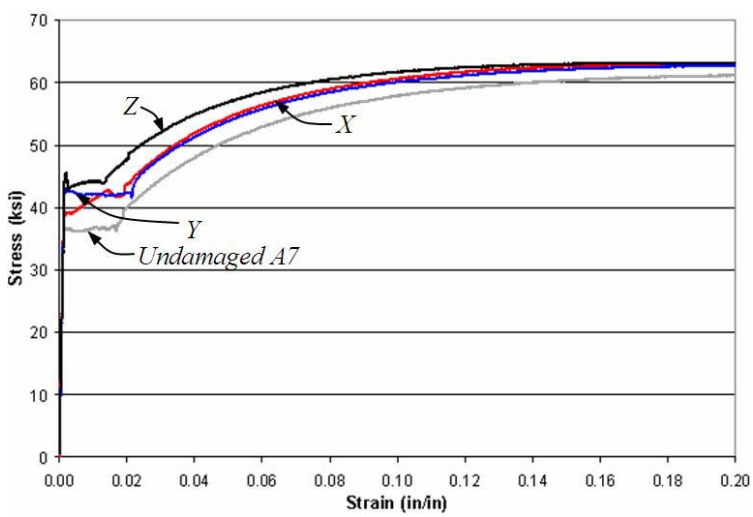

Figure 8.64
Stress-strain behavior of uniaxial tension coupons removed from A7-Beam 2

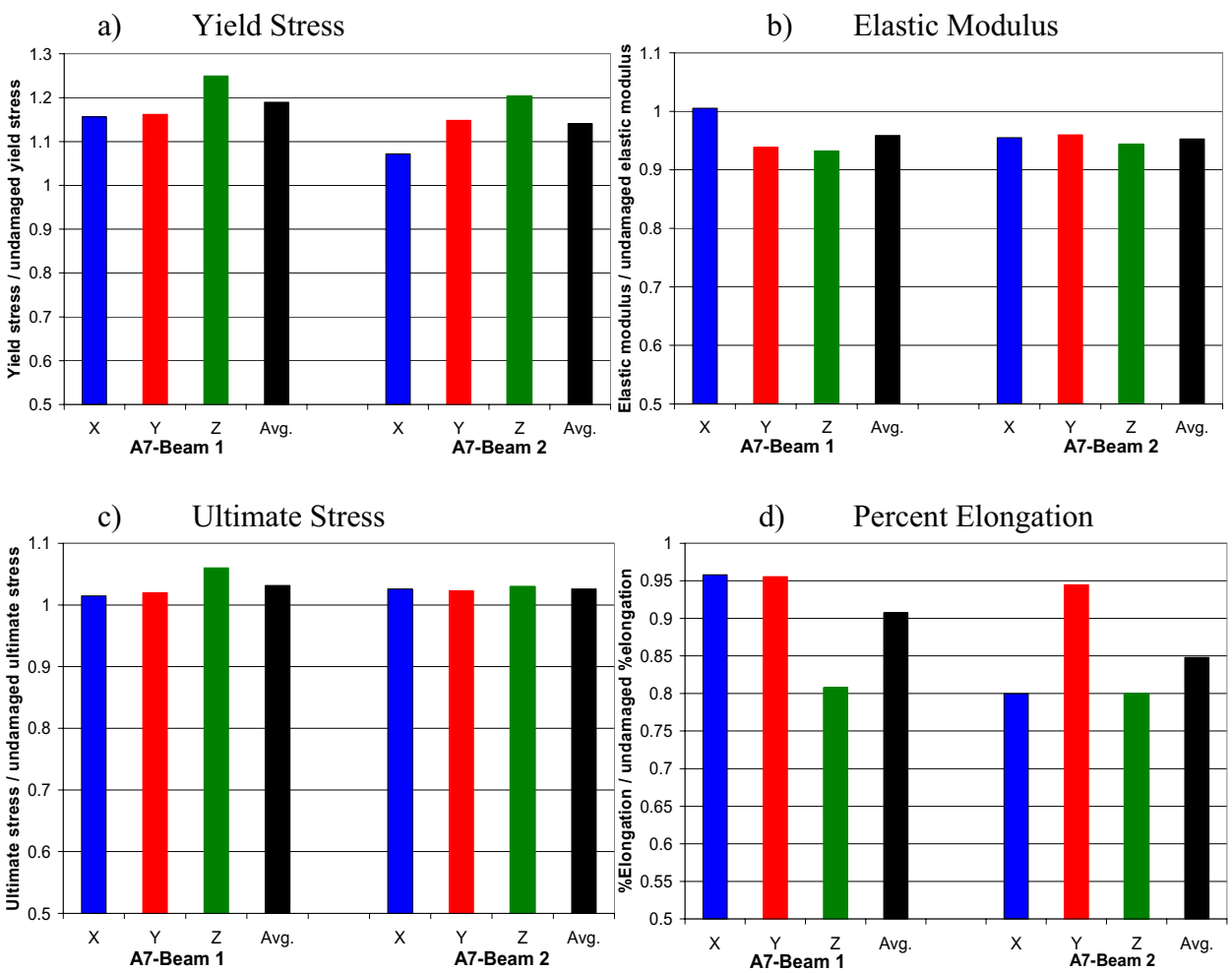

Figure 8.65
Normalized structural properties of damaged-repaired A7 steel

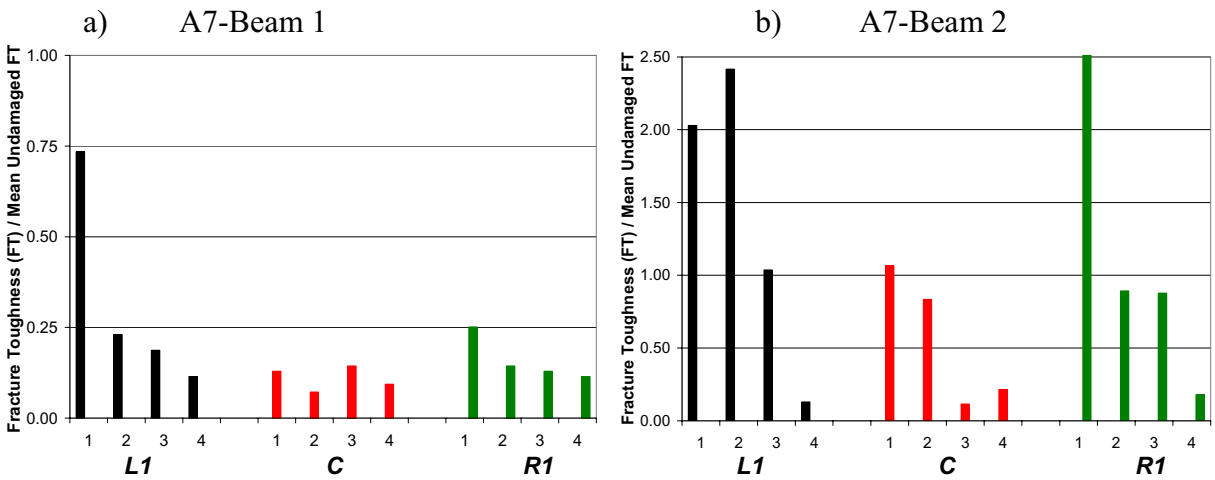

Figure 8.66
Normalized fracture toughness of damaged-repaired A7 steel

a) A7-Beam 1 b) A7-Beam 2

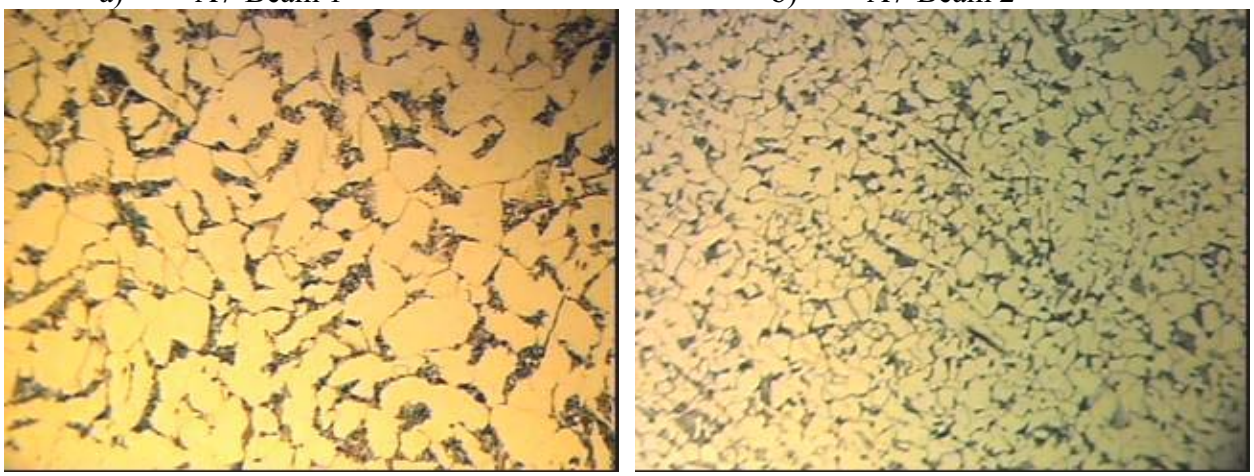

Figure 8.67
Microstructures of the damaged-repaired A7 experimental beam specimens (480X)

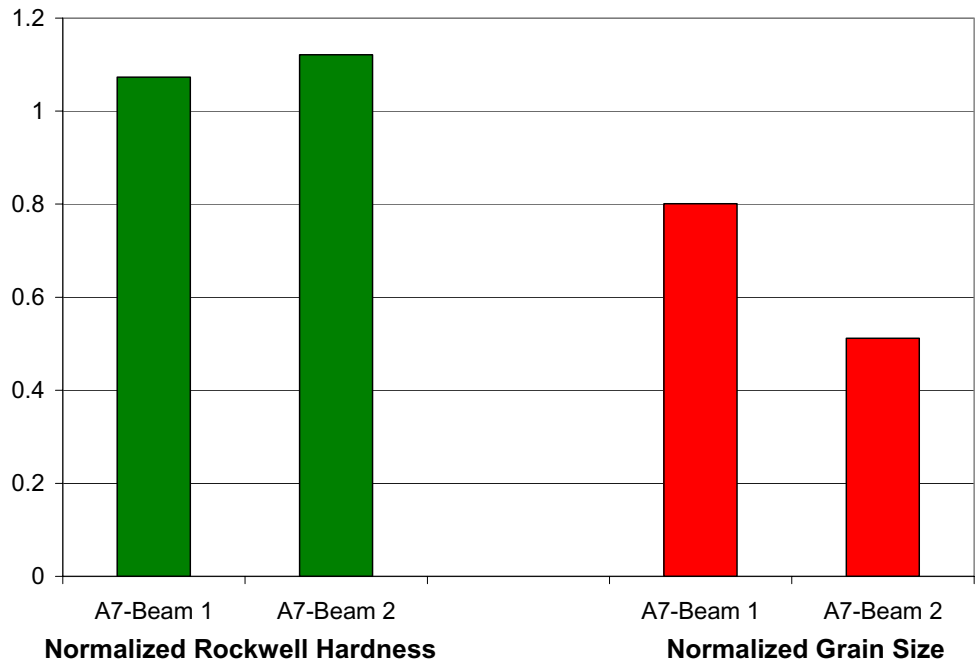

Figure 8.68
Normalized hardness and grain size of damaged-repaired A7 steel

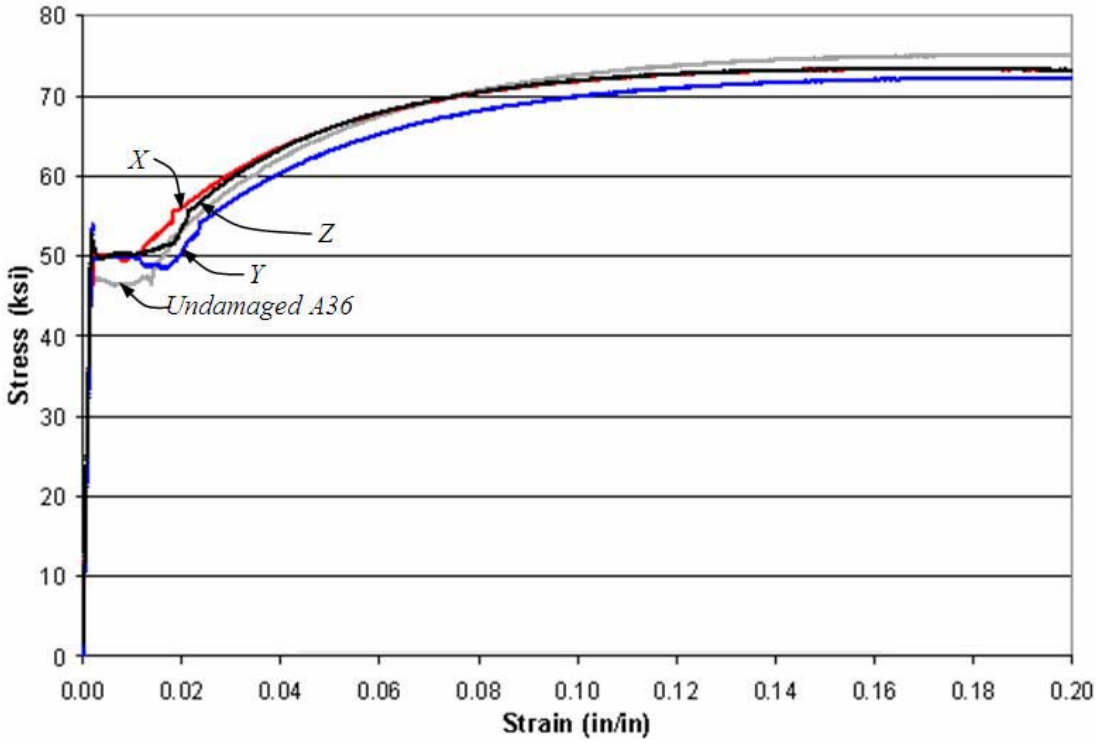

Figure 8.69
Stress-strain behavior of uniaxial tension coupons removed from A36-Beam 1

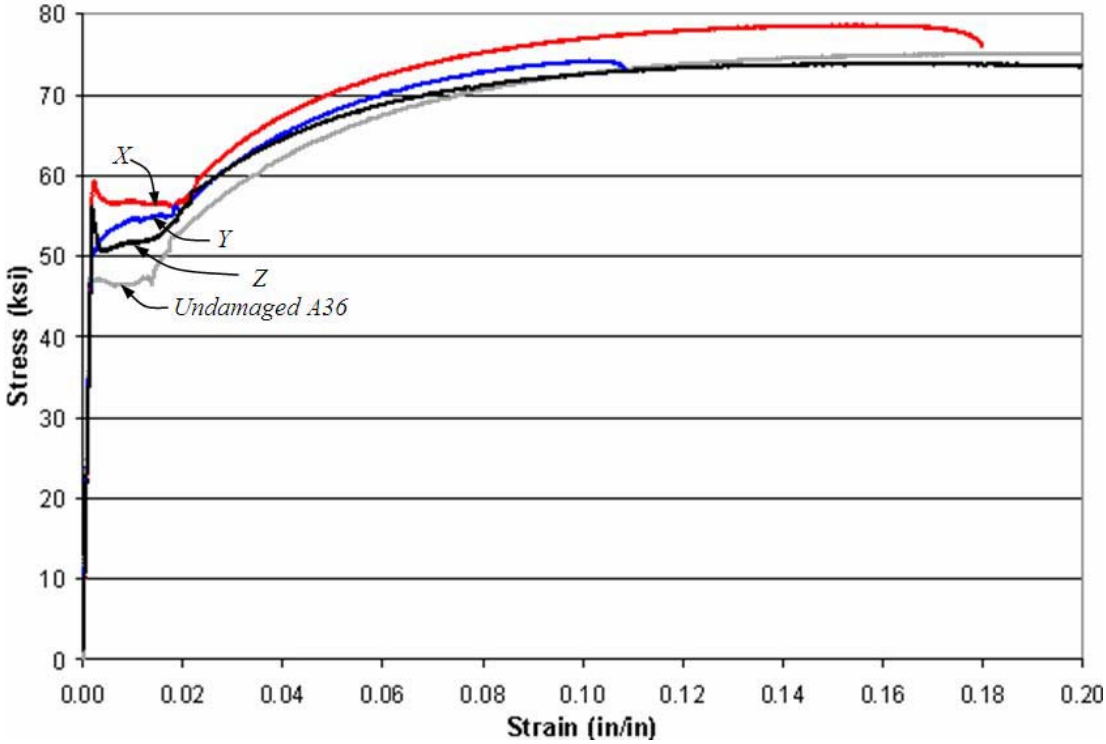

Figure 8.70
Stress-strain behavior of uniaxial tension coupons removed from A36-Beam 2

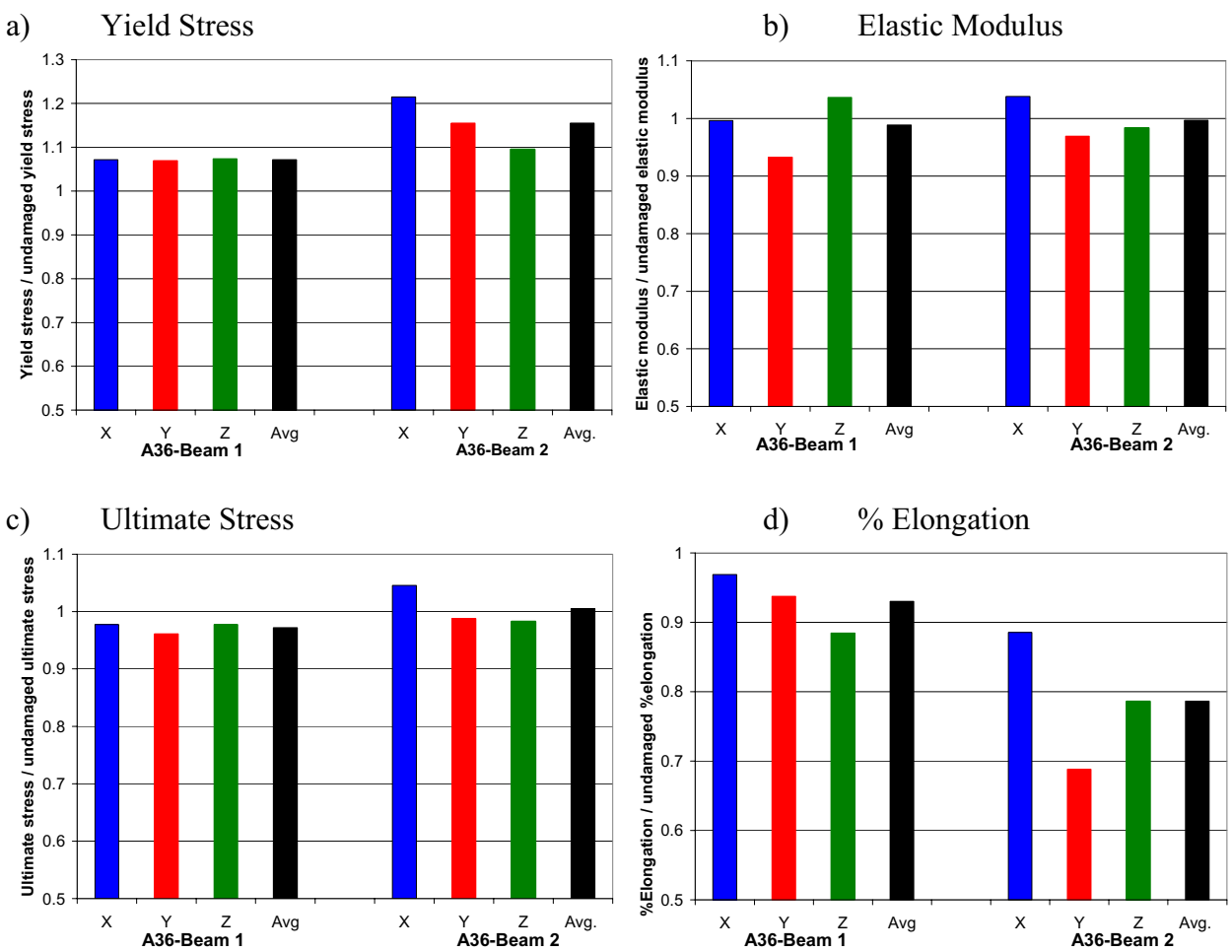

Figure 8.71
Normalized structural properties of damaged-repaired A36 steel

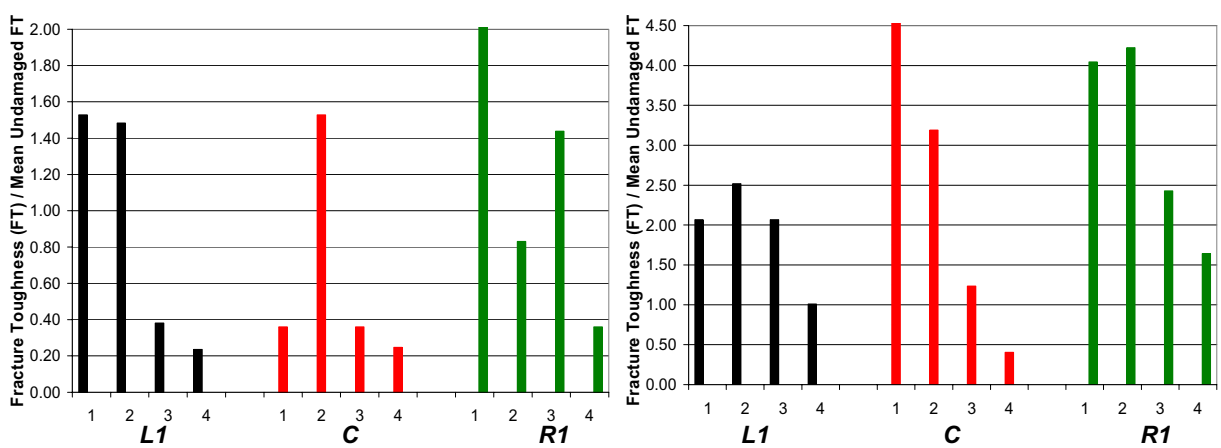

Figure 8.72
Normalized fracture toughness of damaged-repaired A36 steel

a) A36-Beam 1 b) A36-Beam 2

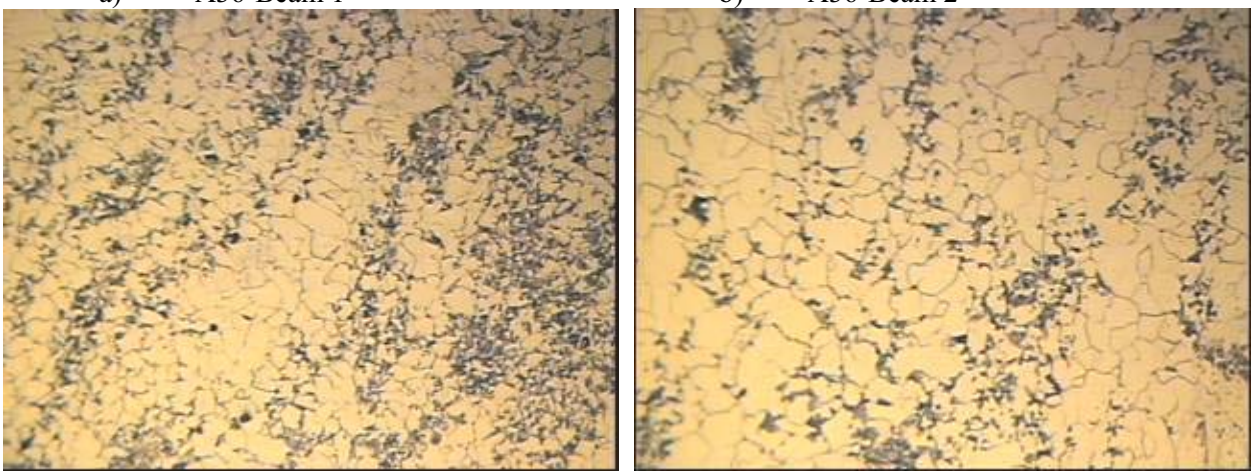

Figure 8.73
Microstructures of the damaged-repaired A36 experimental beam specimens (480X)

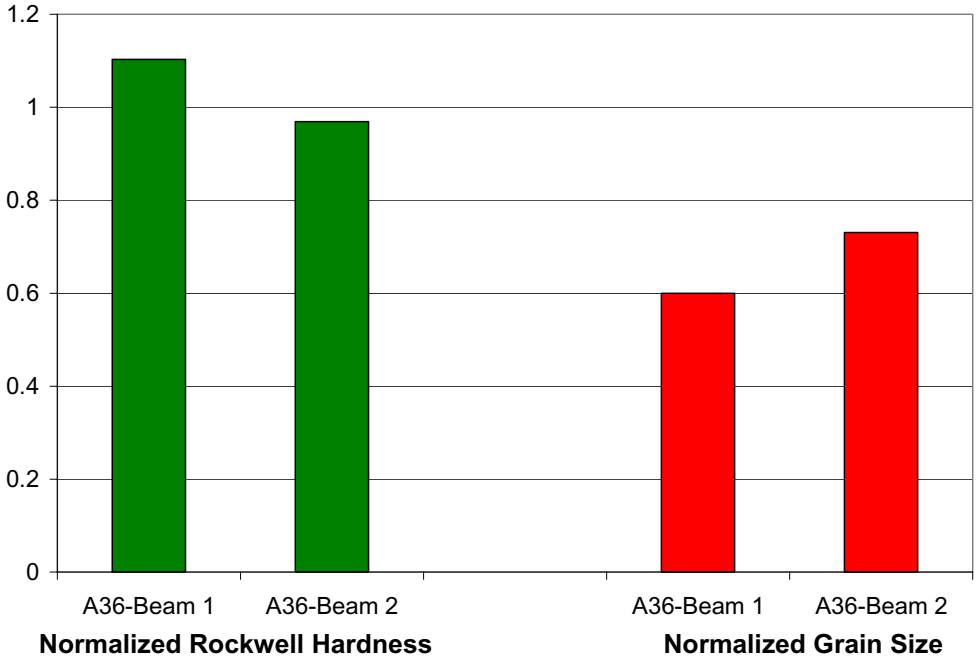

Figure 8.74
Normalized hardness and grain size of damaged-repaired A36 steel

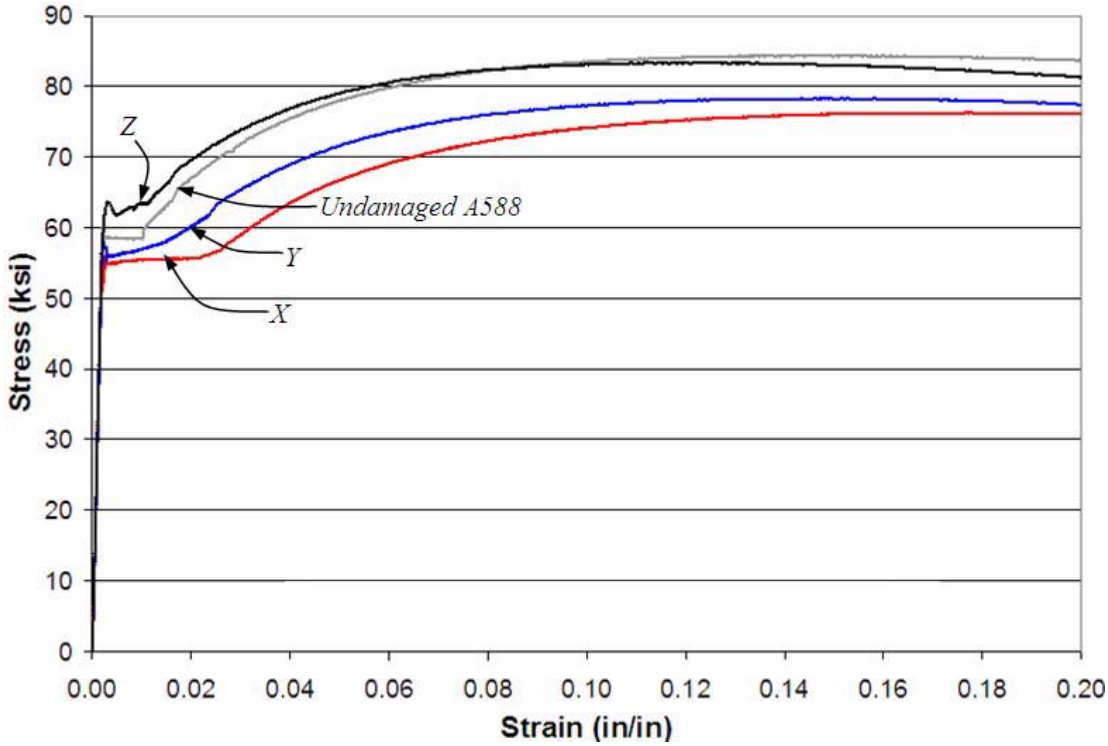

Figure 8.75
Stress-strain behavior of uniaxial tension coupons removed from A588-Beam 1

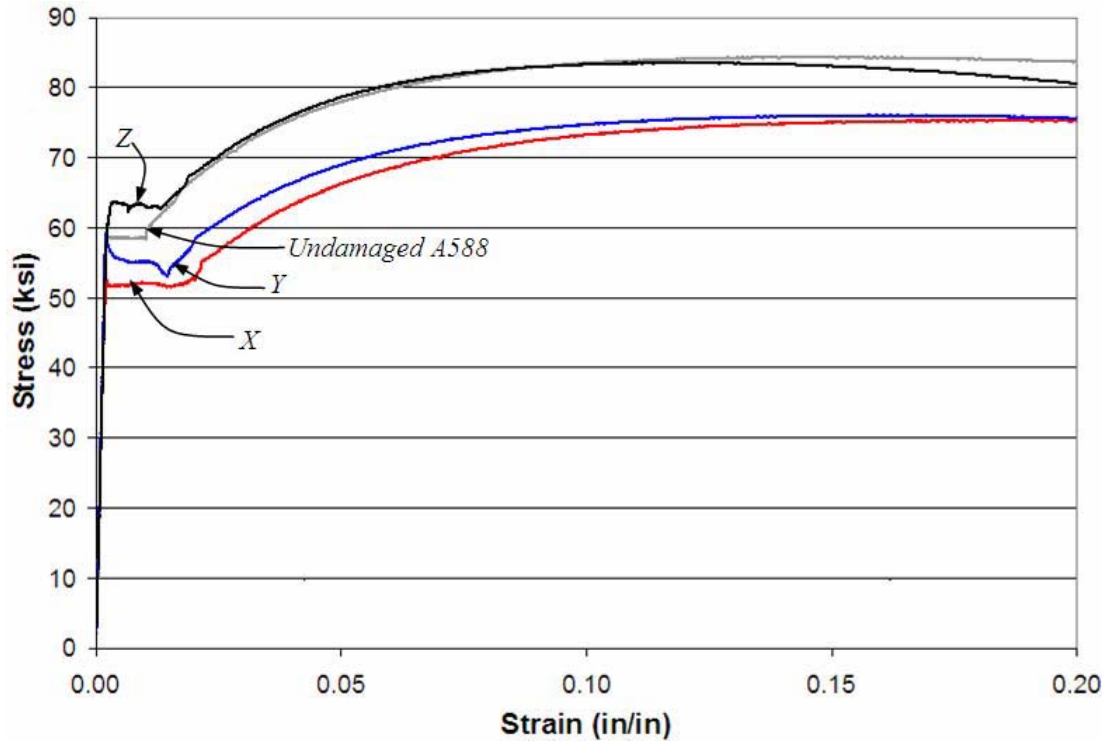

Figure 8.76
Stress-strain behavior of uniaxial tension coupons removed from A588-Beam 2

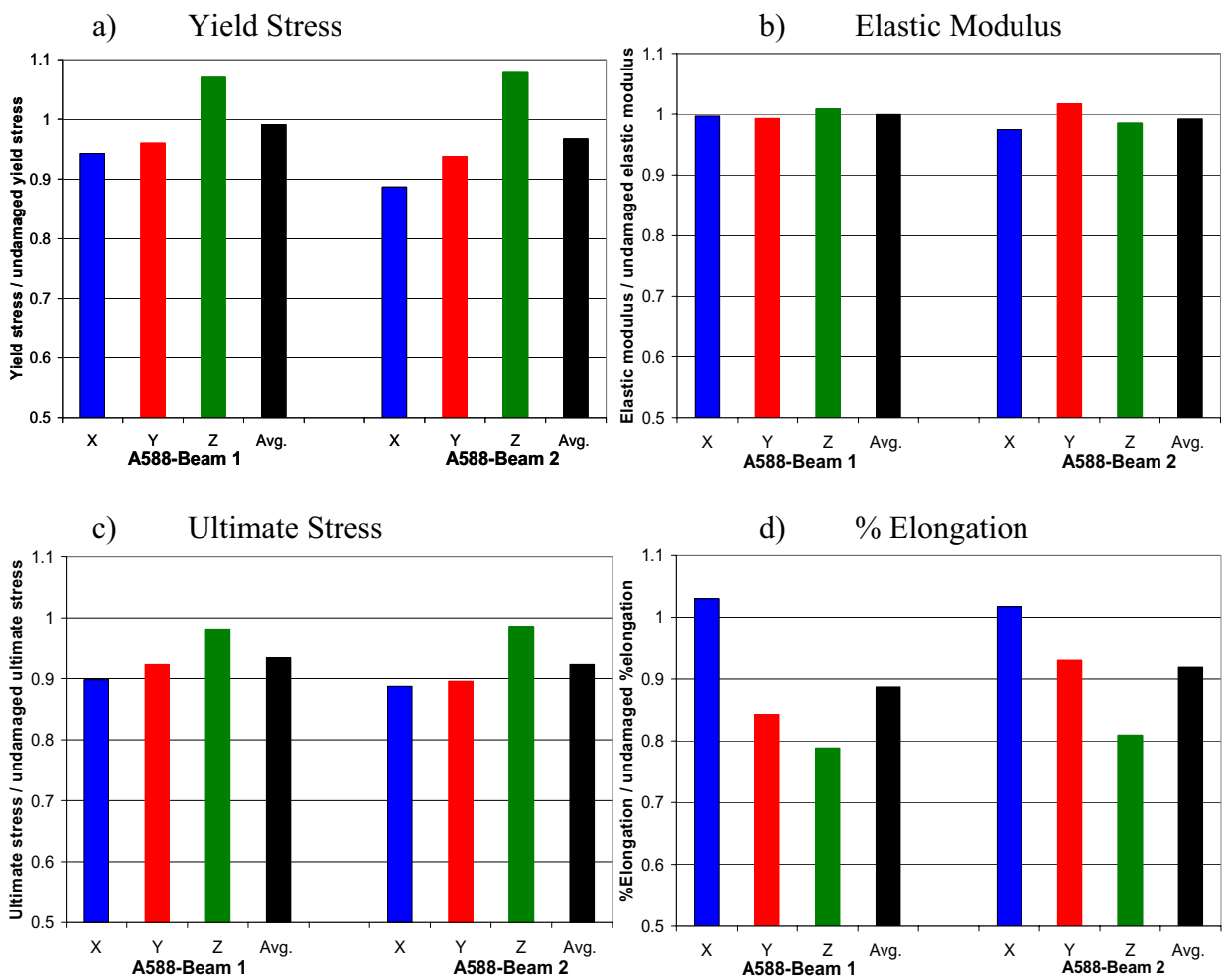

Figure 8.77
Normalized structural properties of damaged-repaired A588 steel

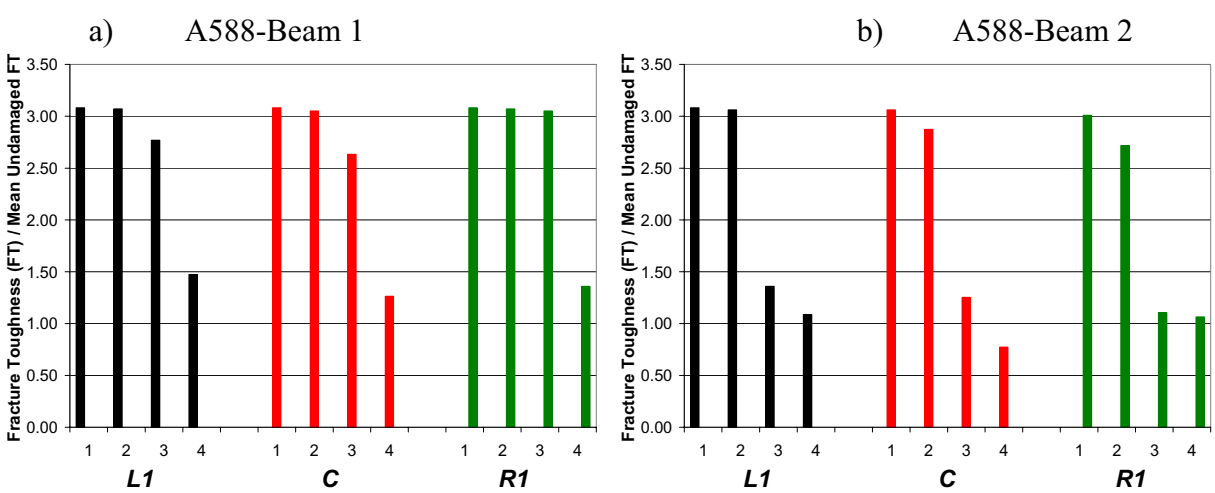

Figure 8.78
Normalized fracture toughness of damaged-repaired A588 steel

a) A588-Beam 1 b) A588-Beam 2

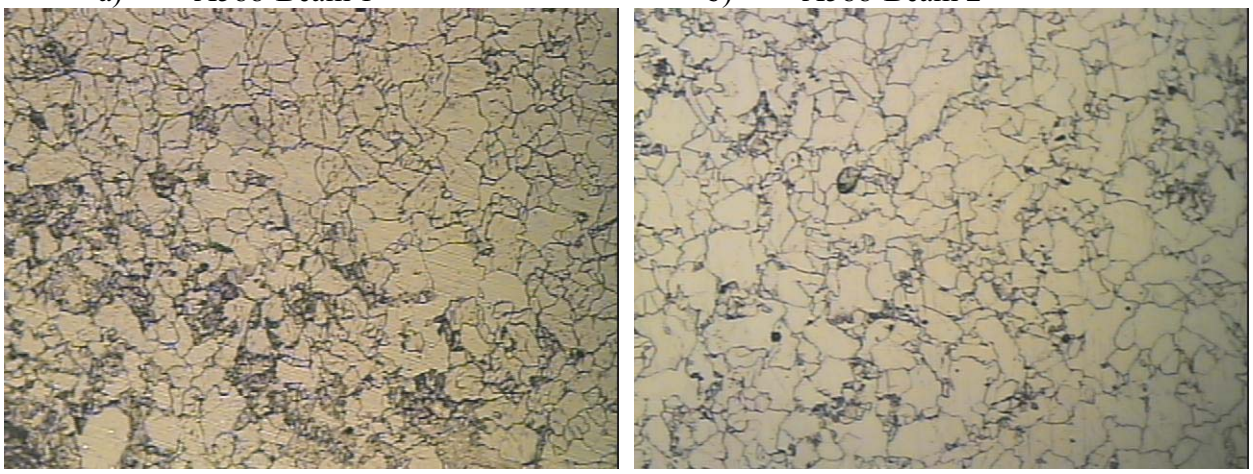

Figure 8.79
Microstructures of the damaged-repaired A588 experimental beam specimens (480X)

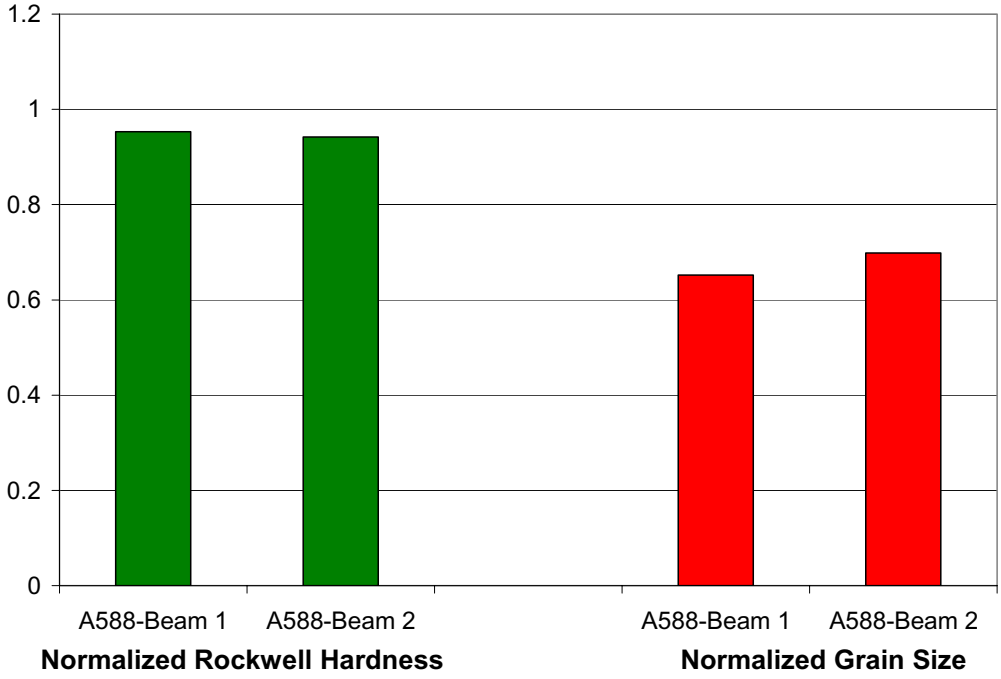

Figure 8.80
Normalized hardness and grain size of damaged-repaired A588 steel

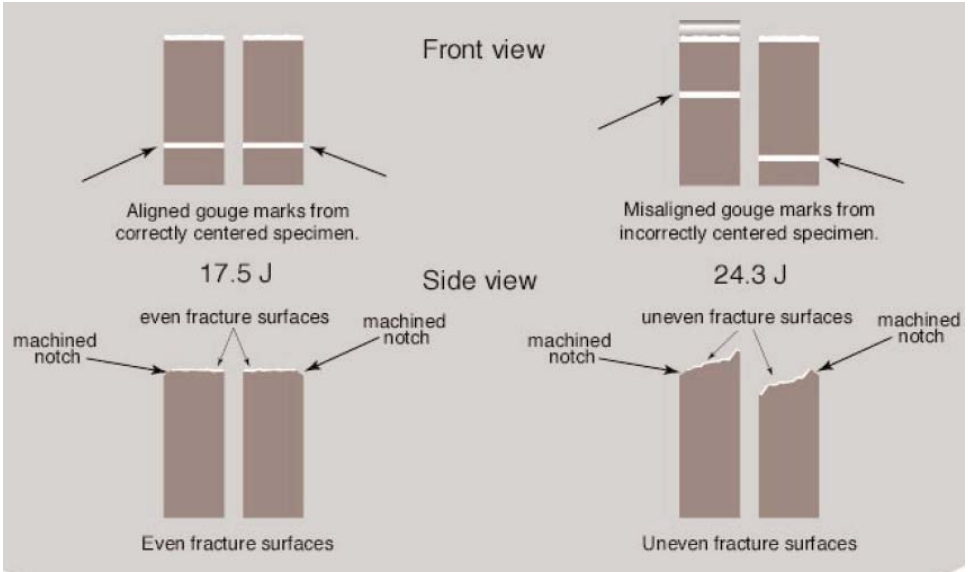

Figure 8.81
Broken orientation of off centered charpy specimens [*1*]

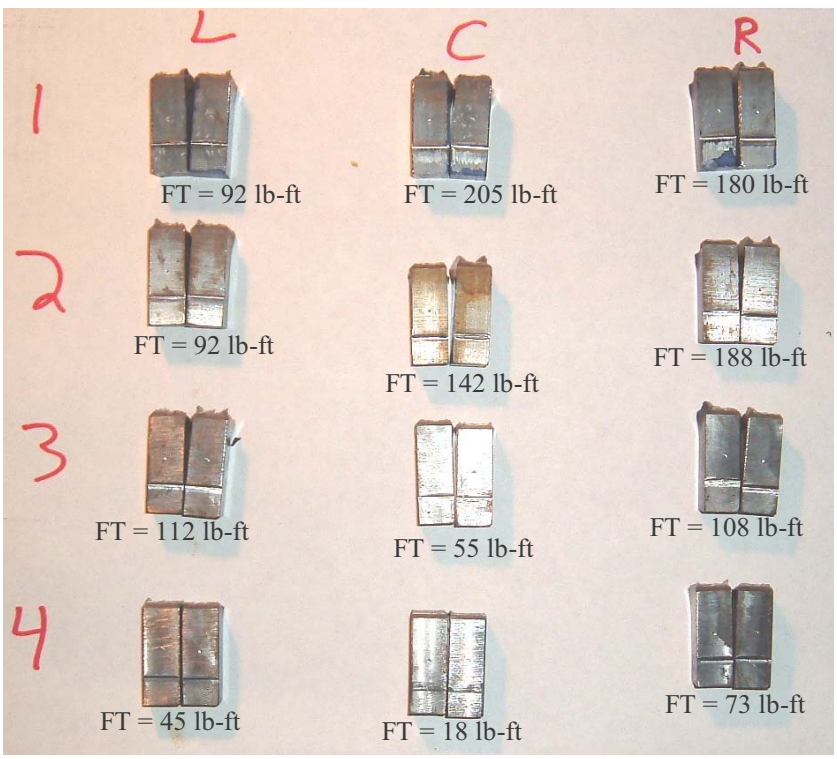

Figure 8.82
Charpy specimens from A36-Beam 2

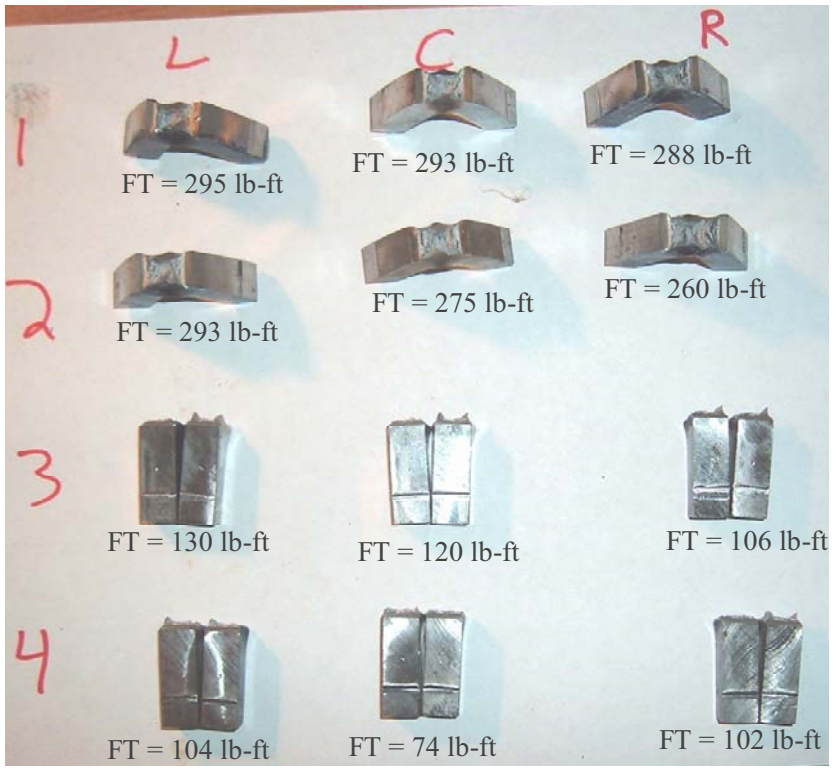

Figure 8.83
Charpy specimens from A588-Beam 2

(a) (b) (c)

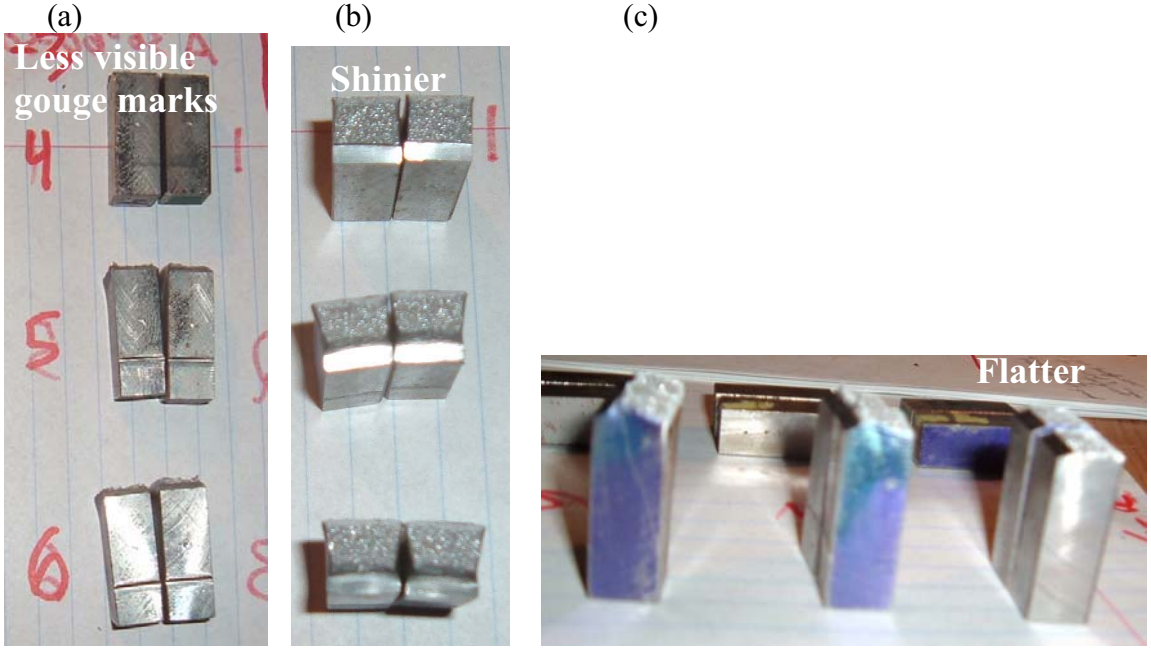

Figure 8.84
Illustration of broken specimens with lower fracture toughness (A36-30-70-3)

9 SUMMARY, CONCLUSIONS, RECOMMENDATIONS, AND FUTURE WORK

9.1 SUMMARY AND CONCLSIONS FROM TASK I

Task I, Literature Review and Survey, was summarized in Chapter 2. This task included three sub-tasks: (1) literature review; (2) Survey of various DOTs; and (3) analysis of the MI high load hits database.

A comprehensive review of existing literature on heat straightening and its effects on the structural properties of steel was provided as part of this report (see Section 2.1). The results indicate that significant research has been conducted on the heat straightening repair of damaged steel members. Most of this research has focused on: (a) the development of heat straightening repair techniques for damaged steel members, (b) the development of guidelines and recommendations for heat straightening repair, and (c) the effects of heat straightening on the structural properties of steel. Currently, there is a lack of lack of knowledge of the fundamental effects of multiple damage events followed by heat straightening repairs on the structural properties including the fracture toughness and microstructure of steel. This research project focused on developing fundamental knowledge to address this shortcoming.

State DOTs across the U.S. were surveyed to determine their current heat straightening procedures and guidelines. Twenty-two state DOTs responded to the survey. The results from this survey indicate that: (a) a majority (68%) of the surveyed DOTs do not have special provisions or guidelines for heat straightening; (b) there is significant variation in the heat straightening guidelines adopted by the state DOTs across the U.S.; (c) none of the surveyed state DOTs have provisions for multiple heat straightening; (d) a majority (54%) of the surveyed state DOTs believe that the combination of the damage magnitude and the number of repairs governs the maximum number of multiple heat straightening repairs; and (e) 100% of the surveyed state DOTs are interested in the results of this research project. More specific heat straightening guidelines were provided by six of the DOTs surveyed. The different guidelines were considered very similar.

The 1976-2001 Michigan high load hits database was analyzed to determine the steel and structure types that are damaged and repaired by heat straightening most frequently. The results from this database indicate that in Michigan, A7 and A373 are the steel types most frequently damage and repaired by heat straightening followed by A588, A36, and A572. The simply supported composite wide-flange steel beam is the type of structure most frequently damaged and repaired by heat straightening in Michigan. Eighty-two percent of damage-repair cases were either composite wide-flange steel beams or composite plate girders. The steel and structure types identified by the high-load hits database were considered for the decisions made in the experimental investigations conducted in this research project.

9.2 SUMMARY AND CONCLSIONS FROM TASK II

Task II, Review MDOT Heat Straightening Procedures, was discussed in Chapter 3. This task included: (a) three site visits to Michigan steel bridges being repaired by heat-straightening, and (b) review of MDOT's documented provisions for conducting heat-straightening in the field.

In all three site visits, the repairs were conducted on composite steel beams damaged by collisions with overheight trucks. This damage caused large out-of-plane displacements of the bottom flanges. In order to repair each beam, the Statewide Bridge Crew (SBC) first applied strip heats high on the web in 5 in. bands using a low restraining force of 6 kips and temperatures significantly below 1200 °F. According to the SBC, this process is used to straighten the web and soften the beam-to-concrete slab interface. However, since the heating temperatures were significantly below 1200 °F (close to 600-800 °F), we

believe that this step did not produce any beneficial movement. This step can be removed from the overall repair procedure, or the heating temperatures must be closer to 1200 °F to repair the web effectively.

After applying the web strip heats, the SBC increased the restraining force to 15 kips, and applied partial (half) depth Vee-heats to the bottom flange on the tension (elongated) side within the damage region. The Vee angles were computed to be approximately 50-55°. The Vee-heat temperatures were typically close to 1200 °F, but sometimes increased to values as high as 1400 °F. Towards the end of the repair procedure significant overheating of the steel (red-hot color of the steel) was observed at some locations. The temperatures were too high to be measured with the temperature device, which was limited to 1450 °F. In some cases, the SBC used a sledge hammer while the steel was hot to get additional movements. These improper practices were usually limited towards the end of the repair procedure.

The current MDOT heat-straightening provisions were reviewed. The comparisons relate well with what is suggested by the Federal Highway Admission (FWHA). Besides some of the improper practices mentioned above, the SBC usually followed the MDOT guidelines. The SBC did not use Vee angles of 10° and had a tendency to heat beyond 1200 °F. The MDOT provisions should be improved to provide specific guidelines for the magnitude of restraining force or stress used while heating to repair. The engineer should design and have more control over the heat straightening repair procedure.

9.3 SUMMARY AND CONCLSIONS FROM TASK III

Task III, Effects of Multiple Heat Straightening on the Structural Properties of Steel, was discussed in Chapters 4, 5, and 6. Ninety-one small scale specimens were subjected to multiple cycles of damage followed by heat straightening repair. The damage-repair parameters included in the study were the steel type, the initial damage strain (ε_d), the restraining stress (σ_r), the maximum heating temperature (T_{max}), and the number of damage-repairs (N_r). Structural properties included in the study were the elastic modulus (E), yield stress (σ_y), ultimate stress (σ_u), strain ductility, fracture toughness, hardness, and microstructure of steel. A summary of the specimen behavior during the damage and repair cycles was included in this report (see Chapter 5). The key findings from the material tests conducted on specimens fabricated from the damaged-repaired steel specimens are as follows:

9.3.1 A7 Steel

- Damage-heat straightening repair cycles do not have a significant influence on the yield stress, elastic modulus, ultimate stress, or surface hardness of A7 steel. Most of the damaged-repaired results are within ± 15% of the undamaged values.
- The percent elongation (ductility) of damaged-repaired A7 steel is usually within 80-90% of the undamaged percent elongations. However, for specimens subjected to five cycles, the percent elongation was approximately 55-60% of the undamaged value. Increasing the damage strain, the restraining stress, or the number of damage-repair cycles reduces the percent elongation significantly.
- The fracture toughness of damaged-repaired A7 steel decreases significantly with increase in the restraining stress or the number of damage-repair cycles.
  - The fracture toughness of specimens damaged to 30 ε_y reduces to 50% of the undamaged toughness after three damage-repair cycles.
  - The fracture toughness of specimens damaged to 60 ε_y and repaired with the lower restraining stress of 0.25 σ_y is greater than the undamaged toughness after three or five cycles. Increasing the restraining stress has an adverse effect on the fracture toughness, which decreases to 50% and 25% of the undamaged toughness after three and five cycles, respectively.

- The fracture toughness of specimens damaged to 90 ε_y is close to the undamaged toughness after three damage-repair cycles. Increasing the restraining stress reduces the toughness slightly.

A7 steel can undergo up to three damage-repair cycles without a drastic reduction in the material properties. The percent elongation values are small after five damage-repair cycles. The fracture toughness values are also reduced significantly after three damage-repair cycles. Hence, a limit of three damage-repair cycles is recommended for A7 steel. The use of lower restraining stresses is also recommended.

9.3.2 A588 steel

- Damage-heat straightening repair cycles do not have a significant influence on the yield stress, elastic modulus, ultimate stress, or surface hardness of A588 steel. Most of the damaged-repaired values are within ± 15% of the undamaged values.
- The percent elongation (ductility) of damaged-repaired A588 steel is approximately 80-90% of the undamaged elongation, which is quite reasonable and usually.
- The fracture toughness of damaged-repaired A588 steel is very good. In several cases, the fracture toughness of damaged-repaired specimens is greater than or close to the undamaged toughness.
  - The fracture toughness of damaged-repaired A588 specimens never decreases below 50% of the undamaged toughness (even after five damage-repair cycles).
  - Increasing the restraining stress reduces the fracture toughness of damaged-repaired A588 specimens significantly.
  - The fracture toughness of specimens repaired with 0.25 σ_y restraining stress is greater than or close of the undamaged toughness. Specimens repaired with 0.50 σ_y restraining stress have toughness close to or less than the undamaged toughness, but never less than 50% of the undamaged toughness.

A588 steel is extremely resilient material. It has excellent material properties after several damage-repair cycles. Hence, we recommend that A588 steel can undergo up to five damage-repair cycles, which was the limit of the experimental program. Lower restraining stresses are also recommended for repair.

9.3.3 A36 Steel

- Damage-heat straightening repair cycles do not have a significant influence on the yield stress, elastic modulus, ultimate stress, or surface hardness of A36 steel. Most of the damaged-repaired are within ± 15% of the undamaged values, and are acceptable according to AASHTO requirements.
- However, the percent elongation (ductility) of damaged-repaired A36 steel is quite low, approximately 66-95% of the undamaged percent elongation. The reduction in percent elongation is greater for specimens subjected to smaller damage strains. Overall, it seems that the smaller damage strain of ε_d=30ε_y had more adverse effects on the strength and ductility of A36 steel.
- The fracture toughness of damaged-repaired A36 steel is quite poor with respect to the undamaged toughness.
  - The mean fracture toughness of specimens damaged to 30 ε_y becomes less than 50% of the undamaged toughness after two damage-repair cycles.
  - The fracture toughness of specimens damaged to 60 ε_y becomes less than 50% of the undamaged toughness after three damage-repair cycles.

- The mean fracture toughness of specimens damaged to 90ε_y was found to have significant scatter. The lower bound of the 95% confidence interval reduces below 25% generally after three damage-repair cycles. Higher restraining stress is detrimental for these specimens.

Due to the poor fracture toughness values and the significant scatter in their measured values, we recommend no more than three damage-repair cycles for A36 steel. Lower restraining stresses are recommended for repairing the damage.

9.3.4 Overheated A36 Steel

- The results from the material tests indicate excellent material properties for damaged-repaired overheated A36 steel. The strength and fracture toughness of the material increased significantly. The percent elongation (ductility) decreased by approximately the same magnitude as A36 steel repaired with a maximum temperature of 1200 °F.
- Temperatures reaching 1600 °F are not recommended because the heat flux from the torch will cause surface damage and produce unwanted distortions.

We recommend that additional research should be conducted on different types of steel subjected to multiple damage-repair cycles with heating temperatures greater than 1200 °F. If the conclusions for overheated steel are validated with further investigations, then we recommend that A36 steel should be heat straightened with maximum heating temperatures close to 1400 °F. This will also allow several damage-repair cycles to the same beam without significant reduction in the material properties.

9.4 SUMMARY AND CONCLSIONS FROM TASK IV

Task IV, Effects of Multiple Heat Straightening on Large-Scale Steel Beams, was discussed in Chapters 7 and 8. Six beam specimens were subjected to three cycles of damage followed by heat straightening repair each. Two beams were fabricated from A7 steel, two were fabricated from A36 steel, and two were fabricated from A588 steel. The behavior of the beam specimens during the damage and repair cycles was discussed in detail in Section 8.1. The results of the material tests conducted on specimens from the damage-repaired beam specimens were presented and discussed in detail in Section 8.2. The major findings from the material tests were as follows:

9.4.1 A7 Beam Specimens

- Damage-heat straightening repair cycles do not have a significant influence on the yield stress, elastic modulus, ultimate stress, or surface hardness of A7 steel. Most of the damaged-repaired are within ± 15% of the undamaged values, and are acceptable according to AASHTO requirements.
- Damage-repair cycles reduce the percent elongation (ductility) of A7 steel. This reduction in ductility ranges from approximately 80%-95% of the undamaged material.
- The fracture toughness of A7-Beam 1 subjected to three damage-repair cycles at the smaller damage strain of 30 ε_y is much lower than the undamaged toughness. The beam has become unusable after three damage-repair cycles.
- The fracture toughness of A7-Beam 2 compares favorably with the undamaged toughness. However, some variability is seen in the results and the toughness of material closer to the flange-web junction (k-region) is much lower.

9.4.2 A36 Beam Specimens

- Damage-heat straightening repair cycles do not have a significant influence on the yield stress, elastic modulus, ultimate stress, or surface hardness of A36 steel heated to 1200 ^{o}F or 1400 ^{o}F. Most of the damaged-repaired are within ± 15% of the undamaged values, and are acceptable according to AASHTO requirements.
- Damage-repair cycles reduce the percent elongation (ductility) of A36 steel. For specimens subjected to 1200 °F, the reduction in ductility ranges from approximately 86%-94% of the undamaged material. The reductions in the percent elongation from the overheated steel were much more substantial. The reduction was found from 86% to as low as 67% of the undamaged material. The reasons for this reduction are not known.
- The overall fracture toughness of A36-Beam 1 is comparable to the undamaged toughness. However, significant variability exists in the toughness of A36-Beam 1. In fact, the toughness of specimens from the center Vee heat (*C*) is much lower (average 62%) than the undamaged toughness.
- The fracture toughness of damage-repaired overheated A36 steel increased. The increase ranges from 101-460% of the undamaged toughness. There was one low value (77% of undamaged toughness).
- The fracture toughness results of specimens removed from the center Vee heat (*C*) results in the lowest values. A general trend was noticed that the fracture toughness decreased as the specimens are removed closer to the web (away from the edge of the flange).

9.4.3 A588 Beam Specimens

- Damage-heat straightening repair cycles do not have a significant influence on the yield stress, elastic modulus, ultimate stress, or surface hardness of A588 steel. Most of the damaged-repaired are within ± 15% of the undamaged values, and are acceptable according to AASHTO requirements
- Damage-repair cycles increased slightly the percent elongation of the outmost (X) specimen and decreased the percent elongation of the middle (Y) and innermost (Z) specimens. Applying a higher external restraining moment had an insignificant effect on the resulting ductility.
- Damage-repair cycles increased the fracture toughness of A588 steel significantly. However, the fracture toughness values were smaller for charpy specimens loser to the flange-web junction (k-area region)
- From A588-Beam 1, Specimens 1, 2, and 3 (including L, C, and R) were found to be exceptionally high with values ranging from 263-308% of the undamaged mean. Specimen 4 was found to be moderately high with values ranging from 126-147% of the undamaged material.
- From A588-Beam 2, Specimens 1 and 2 (including L, C, and R) were found to be exceptionally high with values ranging from 272-308% of the undamaged mean. Specimens 3 and 4 ranged from 77-136% of the undamaged material. Thus, applying a higher external restraining stress reduces the fracture toughness.

9.5 FINAL CONCLUSIONS COMBINING TASKS III AND IV

The comparisons of the major findings from Tasks III and IV were presented in Section 8.3. The major findings from the comparisons of Tasks III and IV were as follows:

- *The results for A7 steel from Tasks III and IV compare favorably. Based on the fracture toughness results of Tasks III and IV, it is recommended that A7 steel beams should not be subjected to more than three damage-heat straightening repair cycles. Smaller damage strains are more detrimental to A7 steel as compared to larger damage strains.*
- *The results for A36 steel from Tasks III and IV compare favorably. Based on the fracture toughness results of Tasks III and IV, it is recommended that A36 steel beams should not be subjected to more than three damage-heat straightening repair cycles. Overheating the A36 steel during damage-repair improves its material properties and fracture toughness significantly.*
- *The results from Tasks III and IV for A588 steel compare favorably. A588 steel is an extremely resilient material that can undergo several (up to five) damage-repair cycles without significant adverse effects on the structural properties including fracture toughness. It is recommended that A588 steel beams can be subjected to several (up to five) damage-heat straightening repair cycles. Lower restraining stresses should be used preferably. However, higher restraining stresses can also be used without impacting the material properties adversely.*

9.6 FUTURE RESEARCH

This research project developed significant knowledge of the effects of multiple damage-heat straightening repair cycles on the structural properties of bridge steels. However, some observations were interesting and additional research is needed to further validate the conclusions as follows:

- Due to a limited source of available material, the lab-scale A7 specimens of Task III had a relatively low thickness causing significant curvature in the test area of specimens subjected to higher damage strains. The researchers suggest additional investigations should be conducted on A7 steel if thicker plates become available.
- The researchers highly strongly recommend additional research and experimental investigations of the effects of overheating on the structural properties and fracture toughness of bridge steels. Due to its relevance to MDOT and poor fracture toughness results when heated to 1200 °F, perhaps A7 should be the focus for future overheating investigations. Since the fracture toughness of A588 steel never decreased substantially after multiple damage-repair events, overheating steel grade may not be necessary.